

Dissertation
submitted to the
Combined Faculties of the Natural Sciences and Mathematics
of the Ruperto-Carola-University of Heidelberg, Germany
for the degree of
Doctor of Natural Sciences

Put forward by
Michael Rainer Rugel
born in: Munich, Germany
Oral examination: 21.11.2018

**On the formation and destruction
of molecular clouds
with the Galactic plane survey THOR**

Referees: Prof. Dr. Henrik Beuther
Prof. Dr. Cornelis P. Dullemond

Über die Entstehung und Auflösung von Molekülwolken mit dem Survey der galaktischen Ebene THOR

Die vorliegende Dissertationsschrift untersucht Eigenschaften von Molekülwolken im Zusammenhang mit dem THOR Survey (The H I, OH, Radio Recombination Line (RRL) survey of the Milky Way). Wir analysieren OH-Absorption bei 18 cm sowohl mit THOR, als auch mit Folgebeobachtungen. Hieraus leiten wir die Häufigkeiten von OH abhängig von molekularem Wasserstoff sowie der Gesamtanzahl aller Wasserstoffteilchen ab. Dabei finden wir: 1) Die OH-Häufigkeit sinkt mit höheren Säulendichte molekularen Wasserstoffs. 2) Aufgrund beträchtlicher atomarer Säulendichten bei niedrigen OH-Säulendichten ist die OH-Häufigkeit hinsichtlich der Gesamtanzahl aller Wasserstoffteilchen in Näherung konstant. 3) Wir finden OH-Komponenten, die mit Gas assoziiert sind, das entweder nicht überwiegend molekular oder "CO-dark" ist. Daraus folgern wir, dass OH ein potenzieller Indikator für diffuses Gas ist. Die Auswirkungen von Sternhaufen auf Molekülwolken betreffend finden wir Signaturen von Feedback in RRL-Emission in der Sternentstehungsregion W49A. Ein Vergleich zu den WARPFIELD Modellen (eindimensionale Modelle von Feedback-getriebenen Schalen) deutet an, dass Feedback noch nicht stark genug ist, um die Molekülwolke, aus der der Sternhaufen entstanden ist, aufzulösen. Außerdem, dass die Schale entweder dabei ist, zu re-kollabieren und neue Sterne zu bilden, oder bereits re-kollabiert ist. Dieses Ergebnis weist darauf hin, dass zumindest Teile der Sternentstehung in W49A von Feedback reguliert werden.

On the formation and destruction of molecular clouds with the Galactic plane survey THOR

This thesis investigates the properties of molecular clouds with THOR (The H I, OH and Radio Recombination Line (RRL) survey of the Milky Way). We analyze OH absorption at 18 cm within THOR and follow-up observations. We derive the abundance with respect to molecular hydrogen and the total number of hydrogen nuclei: 1) We find a decreasing OH abundance with increasing column density of molecular hydrogen. 2) Due to significant column densities of atomic hydrogen at low N_{OH} , the OH abundance with respect to N_{H} is approximately constant. 3) We detect OH components which are associated with gas that is not predominantly molecular or even CO-dark. We conclude that OH is a potential tracer for diffuse gas. Regarding the impact of star clusters on molecular clouds, we detect signatures of feedback in RRL emission in the star forming region W49A. A comparison to the WARPFIELD models (one-dimensional models of feedback-driven shells) indicates that feedback is not yet strong enough to disperse its molecular cloud and that the shell is either in process of re-collapsing to initiate a new event of star formation or has already re-collapsed. This suggests that at least parts of the star formation in W49A is regulated by feedback.

Contents

1	Introduction	1
1.1	Molecular cloud formation and destruction	2
1.1.1	The phases of the ISM	2
1.1.2	Observations of molecular gas	3
1.1.3	Molecular cloud assembly	3
1.1.4	Molecular cloud dispersal	4
1.2	Interfaces between ISM phases	5
1.3	OH as tracer of regions relevant to GMC formation	6
1.4	Ionized gas around star clusters with radio recombination lines	9
1.5	Questions addressed in this thesis	10
2	The THOR survey – an overview	11
2.1	The THOR survey - a motivation	11
2.1.1	THOR as a tracer of the cycle of matter of the ISM	11
2.1.2	A HI survey at comparable resolution as molecular gas surveys	12
2.2	Radio Interferometry – the VLA	12
2.3	Setup	13
2.3.1	Coverage	13
2.3.2	Setup of the mosaics	13
2.3.3	Integration	15
2.3.4	Spectral setup	15
2.4	Calibration	17
2.4.1	Calibration strategy	17
2.4.2	Pipeline calibration	17
2.4.3	Calibration details	18
2.5	Imaging & Deconvolution	19
2.5.1	Mosaicking algorithms	19
2.5.2	Imaging & Deconvolution in THOR	20
2.5.3	CASA tests: Flux dependence on the phase center of the mosaic	21
2.6	Further applications of the THOR data - Carbon α RRLs	23
2.7	Publications within the THOR collaboration	25
2.7.1	First-author publications	25
2.7.2	Publications as co-author	25
3	Characterization of the OH abundance with THOR	27
3.1	Introduction	27
3.2	Observations and data reduction	30

3.3	Results	32
3.3.1	Detection statistics	32
3.3.2	OH abundance	36
3.3.3	Satellite line transitions	45
3.3.4	Extended OH absorption: the example of W43	49
3.4	Discussion	54
3.4.1	Distribution of OH in the Galactic plane	54
3.4.2	OH as tracer of hydrogen gas	55
3.4.3	Comparison with OH column density measurements from other transitions	56
3.4.4	Extended OH absorption towards W43	57
3.5	Conclusions	59
4	OH high-sensitivity follow-up observations of THOR	65
4.1	Introduction	65
4.2	Observations	66
4.2.1	H I and OH follow-up observations	66
4.2.2	Optical depths of H I and OH	68
4.2.3	Archival CO observations	68
4.3	Analysis	70
4.3.1	Selection of components	70
4.3.2	Column densities	75
4.4	Results	76
4.4.1	Probing the optical depth of H I	76
4.4.2	Characteristics of OH detections	78
4.4.3	VLA follow-up observations in comparison to THOR	84
4.4.4	OH abundance with respect to molecular hydrogen	87
4.4.5	OH abundance with respect to the total number of hydrogen nuclei	89
4.5	Discussion	92
4.5.1	H I optical depths	92
4.5.2	OH abundance variations revisited	94
4.5.3	OH column densities in comparison to the Millennium survey	94
4.5.4	CO-dark gas	96
4.5.5	Future work	97
4.6	Conclusion	99
5	Stellar feedback in W49A with radio recombination lines	101
5.1	Introduction	101
5.1.1	Overview of W49A	102
5.1.2	Feedback and star formation in W49A	104
5.2	Observations and Methods	106
5.2.1	Radio recombination lines at 1.6–1.9 GHz	106
5.2.2	Archival CO observations	110
5.2.3	Gaussian line-fitting of the RRL data	110

5.3	Results	110
5.3.1	Spatial distribution of the RRL emission in comparison to other gas tracers	110
5.3.2	Shell-like distribution of RRL and CO emission around Cluster 1	111
5.3.3	Kinematics of RRLs and ^{13}CO	112
5.4	Stellar feedback models for W49A	114
5.4.1	Initial conditions	115
5.4.2	Models of stellar feedback indicate collapse of an initially expanding shell	116
5.5	Discussion	119
5.5.1	Dynamics of re-collapse in W49A	119
5.5.2	Effect of feedback on the molecular gas in W49A	120
5.5.3	Star formation rate and multiple generations of stars	121
5.5.4	W49A in comparison to the massive star-forming region 30 Doradus	123
5.5.5	Future investigations	124
5.6	Conclusions	125
6	Conclusions & Outlook	127
6.1	Conclusions	127
6.2	Outlook	129
6.2.1	Further characterization of the gas phase of OH	129
6.2.2	Satellite lines as indicators of physical properties of OH gas	130
6.2.3	Future surveys on OH and HI absorption observations	130
6.2.4	RRL emission in other regions	130
A	Supplementary material for Chapter 2	133
B	Supplementary material for Chapter 3	137
B.1	Detection of OH main line absorption – notes on individual sources	137
B.2	Estimation of the correlation between N_{OH} and N_{H_2}	138
B.3	Individual sources – transitions of the OH ground state	138
B.4	Individual sources - OH and HI optical depth and $^{13}\text{CO}(1 - 0)$ emission	142
B.5	OH absorption towards W43	142
C	Supplementary material for Chapter 4	153
C.1	Estimation of the correlation between N_{OH} and N_{H_2}	153
C.2	Details on the derivation of $N_{^{13}\text{CO}}$ for Sect. 4.5.3	153
C.2.1	Formalism	153
C.2.2	Column densities of ^{13}CO with T_{ex} derived from ^{12}CO observations	156
C.2.3	Derivation of N_{OH}	156
C.2.4	Systematic uncertainties	157
C.3	Overview plots of each transition	167
C.4	Tables	167

Contents

D Supplementary material for Chapter 5	169
Bibliography of own publications used in this thesis	173
Bibliography	175
Acknowledgements	183

Chapter 1

Introduction

Molecular clouds are seen as obscuration of the stars of the Milky Way (Fig. 1.1). They were first reported as “an opening, or hole” by William Herschel (Herschel 1785) and mapped with optical photography (e.g., Barnard 1910). The first molecule to be discovered in the interstellar medium, CH, was seen in optical stellar absorption spectra (e.g., Swings & Rosenfeld 1937; McKellar 1940). In the radio wavelength regime, the first molecule to be detected was OH (Weinreb et al. 1963). As molecular clouds are readily observable in dust and molecular line emission at infrared to millimeter wavelengths, large surveys of our Galaxy have been undertaken to detect, map, and characterize the molecular gas content of the Milky Way (e.g., Dame et al. 2001; Jackson et al. 2006; Schuller et al. 2009). Thousands of molecular clouds have been identified in our Galaxy to date – with some of them hosting stars and others are yet to form them (e.g., Miville-Deschênes et al. 2017).

Being the birthplace of stars, molecular clouds are of central importance for understanding the origins of the Sun, the Solar System, and for star formation in general. They consist of cold, dense gas and dust which can eventually begin to fragment and collapse under its own gravity to form stars. The average efficiency of this conversion from gas into stars has been found to be typically at 5–10% (e.g., McKee & Ostriker 2007). However, the precise physical processes that determine how efficient an individual molecular cloud is at forming stars are not entirely understood.

This thesis aims at contributing to the in-depth characterization of molecular clouds. In particular, the objects and cloud regions which are relevant for the understanding of the formation and destruction of molecular clouds are addressed. Molecular clouds form out of atomic gas and are destroyed by ionizing radiation, stellar winds, jets and outflows, and supernova explosions in star clusters which have formed inside the molecular clouds. Thus, this study analyzes the interaction of ionized, atomic, and molecular gas phases.

To observe the emission from these gas phases, we conducted the THOR survey (“The H_I, OH and Radio recombination line survey of the Milky Way” – a Galactic plane survey in the first quadrant of the Milky Way with the Very Large Array between 1 and 2 GHz; Beuther et al. 2016). This thesis focusses on the observations, analysis, and interpretation of the transitions of OH in the ground state, as well as the radio recombination lines. The following chapter expands on this motivation, highlights the questions addressed in this work, and marks the relevance of observations of OH absorption and radio recombination lines to the understanding of molecular cloud evolution. The observations of the THOR survey are explained in Chapter 2.

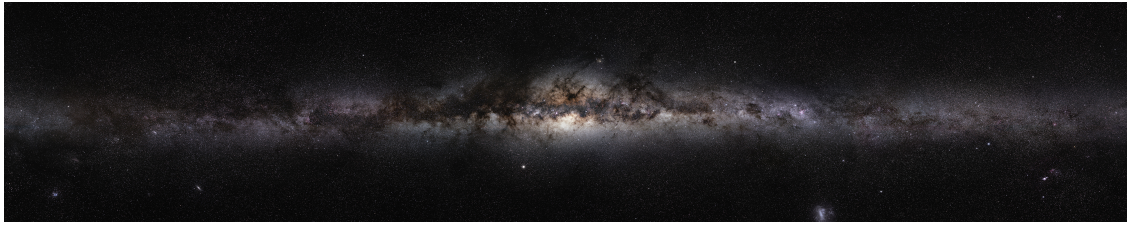


Figure 1.1: Optical photography of the Milky Way. (ESO/S. Brunier)

1.1 Molecular cloud formation and destruction

1.1.1 The phases of the ISM

In the current understanding, the ISM breaks up into several different phases (e.g., [Klessen & Glover 2016](#), and references therein). Four of them relate to hydrogen in either atomic or ionized form: *i*) The hot ionized medium (HIM), a very hot (10^6 K), low density (10^{-2} cm $^{-3}$), and fully ionized component; *ii*) the warm ionized medium (WIM), at temperatures of several thousand Kelvin, densities of a few tenth of cm $^{-3}$, and fully ionized; *iii*) the warm neutral medium (WNM), with similar temperatures and densities as the WIM, but predominantly neutral, with ionization fractions of around 0.1 (WIM and WNM can also be considered one single phase with different ionizations; [McKee & Ostriker 1977](#)); *iv*) the cold neutral medium (CNM) with temperatures of 50 – 100 K, densities of a few tens cm $^{-3}$, and low ionization fractions of 10^{-4} . This multi-phase model of the ISM has its origins in the “two-phase” model by [Field et al. \(1969\)](#), who found that, given the cooling and heating processes in the ISM, neutral gas can be in thermal equilibrium in two phases of distinct temperature and density, the WNM and the CNM. Both phases can coexist in pressure equilibrium, while gas at temperatures between the CNM and WNM is thermally unstable and will be driven to either of those by heating or cooling. The “two-phase” model has been subsequently extended by the phase of HIM, caused by hot, ionized gas emerging from supernovae explosions and stellar winds from massive stars (“three-phase” model; [McKee & Ostriker 1977](#)).

A fifth phase of the ISM considers molecular gas in the form of Giant Molecular Clouds (GMCs) which represent discrete clouds at temperatures of 10–20 K and high densities larger than 10^2 cm $^{-3}$ (e.g., [Klessen & Glover 2016](#), and references therein). Observational results indicate that most GMCs with masses above $10^4 M_{\odot}$ are gravitationally bound (e.g., [Heyer et al. 2001](#)) and are therefore distinct from CNM dynamics; it is under debate if parts of a GMC may be unbound (see review by, e.g., [McKee & Ostriker 2007](#)). Molecular gas also exists outside of GMCs, in clouds that are less dense and massive which may coexist with the CNM (and would be part of it), if the gas is not predominantly in molecular form and/or not self-gravitating (e.g., [Magnani & Shore 2017](#), and references therein). One type of cloud which falls into this category is often referred to as “diffuse” or “dark” and is likely to be bound by the pressure from the surrounding ISM (e.g., [Elmegreen 1993](#), and references therein). The definition of GMCs as a fifth phase of the ISM is not unique; for example, non-selfgravitating, molecular clouds were suggested

as a separate phase since, in common with the other phases, their own gravity is not the dominant force which determines their physical properties (e.g., [Magnani & Shore 2017](#)).

1.1.2 Observations of molecular gas

The boundaries of GMCs are not well defined. While being the most abundant molecule, molecular hydrogen (H_2) is not easily observable under typical conditions of GMCs due to the lack of dipole transitions. In consequence, the emission from other molecules or dust particles is used as a tracer of molecular gas, typically by invoking a conversion to molecular hydrogen derived from dedicated studies (e.g., [Frerking et al. 1982](#); [Pineda et al. 2008](#); [Bolatto et al. 2013](#)). The most frequent gas tracers are from extinction or emission by interstellar dust grains and CO emission. While observations of visual extinctions are frequently used in the study of nearby clouds, the Milky Way becomes opaque to stellar radiation at wavelengths in the visible within a few kiloparsec from the Sun. Dust emission at mid and far-infrared wavelengths is observable (e.g., [Schuller et al. 2009](#); [Planck Collaboration et al. 2011](#); [Molinari et al. 2016](#)) but lacks the spectroscopic information to study its kinematics. CO emission is a common tracer of molecular gas and has been used to systematically study GMCs with large surveys (e.g., [Dame et al. 2001](#); [Jackson et al. 2006](#)). As it is one of the most accessible tracers of molecular gas, it may be used to define molecular cloud boundaries, but this definition will intrinsically exclude regions in the outskirts of GMCs in which molecular hydrogen has already formed but CO is not yet present and/or its emission not detectable (e.g., [Klessen & Glover 2016](#); [Magnani & Shore 2017](#), see also Sect. 1.3).

1.1.3 Molecular cloud assembly

One of the most important questions in the realm of star formation is the actual transition of gas from the WNM to the CNM and the assembly of dense, cold (~ 10 K) molecular clouds in the CNM (~ 100 K). The conversion from WNM to CNM requires a compression of the gas which triggers a thermal instability and allows it to cool. Molecular clouds form by gathering column densities of gas or dust high enough to provide shielding from the interstellar radiation field, such that photodissociating radiation is effectively attenuated (see Sect. 1.2). While molecular clouds distinguish themselves as being molecular, the chemical transition from atomic to molecular hydrogen is a by-product in this process ([Glover & Clark 2012](#)) rather than a necessary condition for forming self-gravitating clouds.

The process of reaching such column densities is dynamic and different scenarios have been proposed (e.g., [Klessen & Glover 2016](#); [McClure-Griffiths et al. 2015](#), and references therein). Mass can be accumulated by collisions of mainly atomic clouds in the CNM which are either aggregated in spiral-arm potentials or pushed together by colliding superbubbles. GMCs may be formed in this model by accumulating the appropriate mass. However, this process may not be fast enough to form the cloud before star formation starts to disrupt it (see, e.g., [McKee & Ostriker 2007](#), for details) and a description of the ISM as a collection of separate cloud entities may not correspond to the ISM as it

is observed. Alternatively, “converging flows” in the WNM which are created by large-scale instabilities in the Galactic disk, may collide to form overdensities that lead to the transformation to cool gas (see above). Irrespective of the model assumed, H_2 will form in dense, cool atomic gas once enough shielding from interstellar radiation is provided (for references and more details on molecular cloud formation out of the WNM, see reviews by, e.g., [Klessen & Glover 2016](#); [McClure-Griffiths et al. 2015](#), and references therein).

The relevant part of the cloud, in which the transition from atomic to molecular hydrogen occurs, is at low visual extinctions. Here, one would expect kinematic signatures of convergence of different flows or of inflow of material onto a GMC. Therefore, to adequately study the formation of molecular clouds, it is necessary to observe molecular gas in these lower density regions. These may be largely inaccessible with standard tracers, such as CO, since it may not have formed yet. A candidate tracer molecule would need to be abundant prior to CO formation and closely linked to the presence of H_2 . A possible molecule is OH, which is investigated in detail in this thesis.

1.1.4 Molecular cloud dispersal

Star formation will occur once gravitational collapse has started in the densest and gravitationally unstable parts of GMCs. Of the total molecular gas mass, typically 5–10% is converted into stars, while the rest of the cloud mass is disrupted by feedback from the formed stars or star clusters. High-mass stars emit Lyman-continuum photons (i.e., radiation which can ionize atomic hydrogen) and ionize the gas which surrounds the star. These regions are called H II-regions (H II is the spectroscopic notation for ionized hydrogen) and are typically bound by an ionization front, beyond which hydrogen remains atomic, followed by a photodissociation region (see Fig. 1.2).

Stellar feedback generally implies energy or momentum deposition from radiation, stellar winds, jets and outflows, or supernova explosions on the ambient gas. The expansion of a thermally overpressured H II-region is considered as energy-driven expansion, where the heating of the gas can either be caused by ionization through stellar radiation or by shocked gas from stellar winds. Momentum-driven expansion is caused by radiation pressure (either directly, from FUV photons, or indirectly, from heated dust) and ram-pressure from stellar winds or supernovae. Each of these act in different phases of the expansion and their effectiveness is under dispute (see review by e.g., [Krumholz et al. 2014](#)). While often discussed in isolation, recent models indicate that their interplay is important; for example, momentum driven expansion depends on the density structure of the photodissociation region at the boundary with the surrounding cloud which, in turn, is shaped by stellar winds ([Rahner et al. 2017](#)).

These models (WARPFIELD; [Rahner et al. 2017](#)) study the effect of feedback of a star cluster on its parent GMC with one-dimensional models of feedback-driven shells. They show that it is necessary to incorporate all relevant types of feedback in such a description: ionizing radiation, stellar winds, and supernova explosions. As stated above, all of these processes have to be considered together. The shell is initially swept-up by a wind-bubble. After a phase of adiabatic expansion, due to wind-shocked gas, the expansion is governed by radiation and wind (and eventually also supernova) pressure counteracting

the gravity of the shell. The shell density structure during this evolution is given by the ram-pressure from stellar winds and supernova explosions (for a more detailed description of the models, see Sect. 5.4). The WARPFIELD models indicate that feedback shells can re-collapse in dense, massive clouds and form a second generation of stars. This proposes a new hypothesis on the formation of multiple generations of stars which have been detected in star clusters (for example in Orion Nebula Cluster, [Beccari et al. 2017](#); or in 30 Doradus, e.g., [Brandl et al. 1996](#); [Sabbi et al. 2012](#)). An application of WARPFIELD to observed clusters has been done by [Rahner et al. \(2018\)](#) for the 30 Doradus region and is shown for the Galactic starburst H II region W49A in Chapter 5.

Stellar feedback has assumed the role of triggering the formation of new stars across molecular clouds in some scenarios. There are different observational indicators, for example, the finding of a large number of coeval stars spread over a molecular cloud in the Carina nebula, with their formation likely being induced by a nearby supernova explosion (e.g., [Preibisch et al. 2002](#); [Preibisch & Zinnecker 2007](#)). Also, studies of the Hi-Gal survey (Herschel PACS and SPIRE observations of the Galactic plane; [Molinari et al. 2016](#)) showed the increased number of protostellar sources ([Thompson et al. 2012](#); [Kendrew et al. 2012](#); [Palmeirim et al. 2017](#)) and cold gas clumps ([Kendrew et al. 2016](#)) at the edges of infrared bubbles ([Churchwell et al. 2006, 2007](#); [Simpson et al. 2012](#)).

From a theoretical point of view, this was investigated in multiple studies (e.g., [Elmegreen & Lada 1977](#); [Whitworth et al. 1994a](#)). However, the precise effect of feedback on the ability of a molecular cloud to form stars has not always been clear and many approaches to model it have been taken, both analytically (e.g., [Whitworth et al. 1994b](#)) and with simulations (e.g., [Dale & Bonnell 2011](#); [Howard et al. 2014](#)). Studies have also shown that observational signatures of triggering may be intrinsically hard to find and to distinguish (e.g., [Dale et al. 2015](#)).

1.2 Interfaces between ISM phases

Ongoing cloud formation and dispersal manifest themselves in gas transitioning between phases dominated by atomic and molecular and, in the case of dispersal, by ionized hydrogen gas. The formation of molecular gas (e.g., [Klessen & Glover 2016](#), and references therein) in the Galaxy occurs on dust grains rather than in gas-phase chemistry (e.g., [Gould & Salpeter 1963](#)) while being destructed by photodissociation (e.g., [Stecher & Williams 1967](#)). With dust grains omnipresent in the ISM, the abundance of molecular hydrogen is regulated mainly by the interstellar radiation field, or better, by its attenuation. The presence of molecular hydrogen is therefore linked to certain column densities of gas and dust. The column density required for H₂ formation depends on the ratio of the strength of the interstellar radiation field to the density (e.g., [Klessen & Glover 2016](#)).

Shielding can be provided either by self-shielding of H₂ itself or by shielding of far-ultraviolet (FUV) photons by dust. Self-shielding means that the transitions of H₂ in the FUV, which initiate the photodissociation process, become optically thick. In typical ISM conditions with average interstellar radiation fields, self-shielding is more effective, such that molecular hydrogen dominates the gas phase at visual extinction of $A_V \sim 0.1 -$

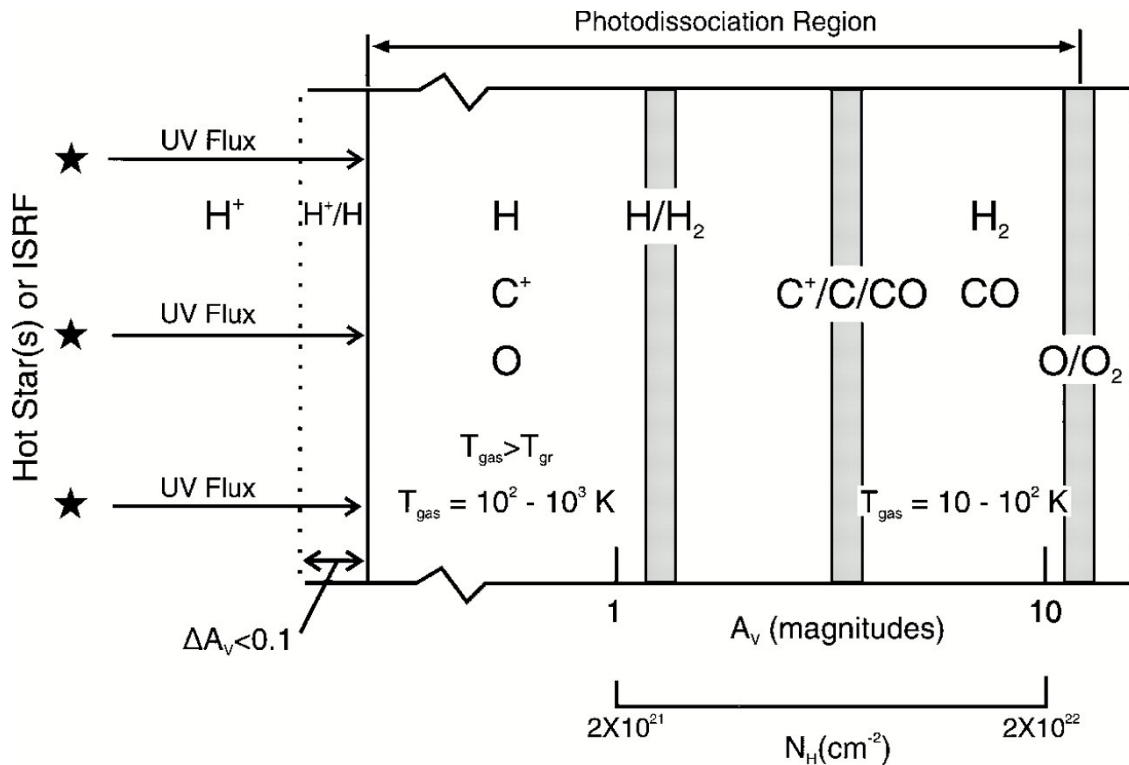


Figure 1.2: Photodissociation region – schematic view (Hollenbach & Tielens 1997). A_V indicates the attenuation of the incident radiation field. Reproduced from Hollenbach, D. J. & Tielens, A. G. G. M. 1997, Annual Review of Astronomy and Astrophysics, 35, 179.

0.2 or $N_{\text{H}} \sim 2 - 4 \times 10^{20} \text{ cm}^{-2}$ (Draine & Bertoldi 1996; Klessen & Glover 2016). In photodissociation regions, the radiation field is enhanced due to the proximity to stars. This leads to visual extinction by dust (A_V) being the most important process to attenuate photodissociation radiation (Fig. 1.2), such that the transition from atomic to molecular gas occurs at $A_V \sim 1 - 2$ or $N_{\text{H}} \sim 2 - 4 \times 10^{21} \text{ cm}^{-2}$ (e.g., Hollenbach & Tielens 1997).

1.3 OH as tracer of regions relevant to GMC formation

The hydroxyl radical, OH, is a possible tracer of diffuse regions¹ of molecular clouds. As these regions are important for the understanding of GMC formation (Sect. 1.1.3), OH shows the potential to render these regions accessible to observational studies. As OH is also present throughout dense molecular phases of the ISM (Heiles et al. 1993), a thorough characterization of its abundance at different densities and cloud depths is necessary.

OH is formed in the gas phase with ion-molecule chemistry. It is initiated by the cosmic-ray ionization of hydrogen to form H^+ , which proceeds to form O^+ in a charge

¹We will hereafter refer to “diffuse regions” of the ISM, wherever carbon is not yet dominantly bound in CO, i.e., regions with $A_V \lesssim 3$ (e.g., Snow & McCall 2006, and references therein).

transfer reaction with oxygen (e.g., [Tielens 2010](#), p. 297; see also [van Dishoeck et al. 2013](#)). O^+ then further reacts with H_2 to eventually form H_2O^+ and H_3O^+ , which can dissociatively recombine with an electron into OH and H_2O (see also Fig. 1.3). OH is destroyed by photodissociation or by reaction with C^+ to form CO^+ , HCO^+ , and CO. Once H_2 is abundant in well-shielded parts of the cloud, ion-molecule chemistry can also be initiated by cosmic-ray ionization of H_2 , leading to H_2^+ which reacts to H_3^+ and forms OH^+ by reaction with oxygen and then proceeds to form OH and H_2O as described above (e.g., [Tielens 2010](#), pp. 350, 355). In warm regions of the ISM ($> 100 - 300$ K), OH can be formed by neutral-neutral reactions of oxygen and H_2 to OH which can proceed further with H_2 to form H_2O . This transition is only active in high temperature environments (i.e., in shocks), due to the activation barrier of the neutral-neutral reactions ([Neufeld et al. 1995, 2002](#)). Lastly, photo-desorption of OH formed on grains or water ice from grains may also increase the OH abundance in the gas phase in dense regions ([Dulieu et al. 2013; Hollenbach et al. 2009, 2012](#)).

Observationally, the OH abundance has been found to be around 4×10^{-8} with respect to the column density of the total number of hydrogen nuclei ($N_H = 2N_{H_2} + N_{HI}$; [Crutcher 1979](#)) or around 1×10^{-7} with respect to molecular hydrogen ([Liszt & Lucas 1996, 2002](#)). More recent studies using the OH ground state transitions at far-infrared wavelengths found OH abundances largely in agreement with these earlier evaluations within large scatter (abundances with respect to molecular hydrogen of $10^{-8} - 10^{-7}$; [Wiesemeyer et al. 2012, 2016](#)). A tight correlation between OH emission at radio wavelengths and H_2 column density has also been indicated by [Xu & Li \(2016\)](#). Model calculations have largely been found in agreement with the observationally determined abundances (e.g., [van Dishoeck & Black 1986; Albertsson et al. 2014](#)).

Both observational and theoretical studies in the last decade indicate the existence of molecular gas which is not traced by standard molecular gas tracers such as CO (e.g., [Grenier et al. 2005; Planck Collaboration et al. 2011; Remy et al. 2018; Pineda et al. 2013; Langer et al. 2014; Wolfire et al. 2010; Smith et al. 2014](#)). This results in an underestimate of the molecular gas mass of our Galaxy. Also the dynamics of this ‘‘CO-dark’’ transition phase remain out of reach which are crucial to verify hypotheses on the emergence of molecular clouds, such as the formation of density enhancements by converging or colliding flows (see Sect. 1.1.3 and review by [Dobbs et al. 2014](#)).

OH is a promising tracer of the molecular content in this transition region. While being the first molecule to be detected at radio wavelengths ([Weinreb et al. 1963](#)) and subsequently being measured towards many lines of sight in our galaxy (e.g., [Goss 1968; Turner 1979](#)), there is increasing attention in recent literature for its potential to trace CO-dark gas (e.g., [Allen et al. 2015; Xu et al. 2016](#)). While these studies focussed on a confrontation with molecular gas tracers such as CO, some works indicate a relation between OH and atomic hydrogen gas in the surroundings of molecular clouds (e.g., [Wannier et al. 1993; Tang et al. 2017](#)). Also, OH has been found to be associated with [C II] emission ([Tang et al. 2017](#)) which, in turn, has been found to be a tracer of CO-dark gas (GOT C^+ survey; [Pineda et al. 2013](#)).

As seen above, the OH molecule can also be formed at higher extinctions, where hydrogen is already mainly molecular. This may either be initiated by cosmic ray ionization,

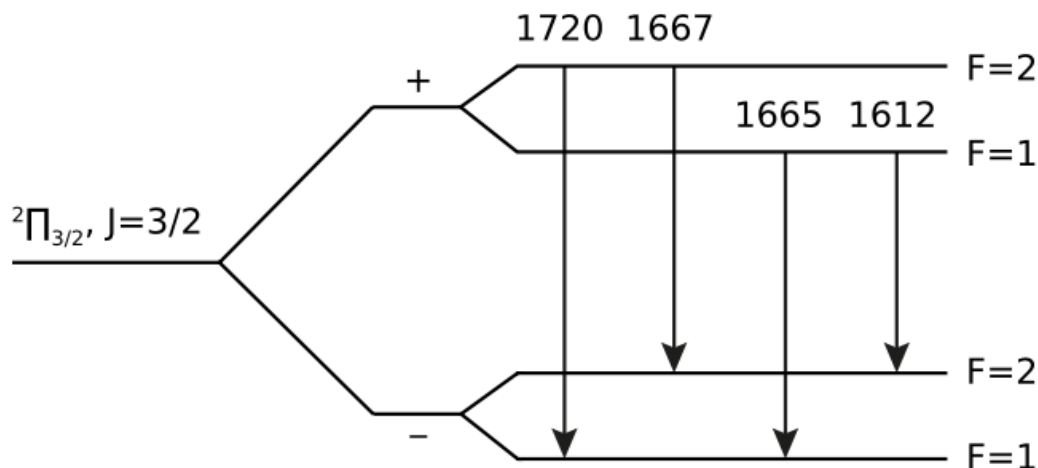


Figure 1.4: Energy levels and transitions in the OH ground state. Reproduced from Dawson, J. R., Walsh, A. J., Jones, P. A., et al. 2014, MNRAS, 439, 1596.

1.4 Ionized gas around star clusters with radio recombination lines

The boundary of an H II region (Sect. 1.1.4) with atomic gas (the ionization front, typically very sharp) is determined by the equilibrium between recombination of ionized hydrogen with electrons and the ionization of neutral hydrogen (e.g., [Wilson et al. 2009](#), eq. 14.5). The H II region is bound towards its surrounding molecular cloud by a photodissociation region (see Fig. 1.2 and Sect. 1.2). An ionized bubble is expected to show both velocity and density structures. It is filled with very hot gas in the innermost regions, with lower temperatures and increasing density towards the boundaries of the H II region (for an example of such a density profile, see fig. 6 in [Pellegrini et al. 2007](#)).

Ionized gas emission manifests itself as free-free emission from thermal bremsstrahlung. This continuum emission has both an optically thick and optically thin part, with the transition being determined by the electron temperature (T_e) and the “Emission measure” (EM), defined as $EM = \int n_e^2 ds$, where n_e is the electron density and the integral is performed over the line of sight (e.g., [Wilson et al. 2009](#), eq. 10.37). The continuum emission of the optically thin regime is directly given by the number of ionizing photons (e.g., [Rubin 1968](#)). In this study, the relevant frequencies are between 1–2 GHz, for which continuum emission may already be optically thick in some H II regions (i.e., with a spectral index between 0–2, depending on density structure; e.g., [Keto et al. 2008](#)). The strength of the continuum emission in that case is set by the electron temperature, the beam-filling factor of the source, and the distance to the emitting source.

A second tracer of ionized gas is line emission of atoms after recombination with its electron. The well-known optical Lyman, Balmer, Paschen, etc., series between low-order energy levels extend to the radio, where transitions between high-order quantum states

are visible. As these are observable at radio wavelengths (e.g., the $H\alpha 166$ transition at ~ 1.4 GHz), these are called radio recombination lines (RRLs). In this thesis, we discuss transitions arising from electrons cascading between energy levels with a difference in quantum number of $\Delta n = 1$. These are nominated $H\alpha$ transitions, with, i.e., the $H\alpha 166$ transition corresponding to photons emitted at the transition of electrons between the energy level $n + 1 = 167$ and $n = 166$.

Optical depths of the RRL emission are typically very low and their emission strength weak, with line-to-continuum ratios often $< 1\%$. Since they are seen at the same frequencies as the free-free continuum, their emission also depends on the optical depth of the continuum emission. If the continuum emission is optically thick at the same frequency, the RRLs will trace only parts of the ionized gas, in which also the continuum is optically thin.

This thesis concentrates on the kinematics of RRLs. While in practice, RRLs can also give valuable information on the electron temperatures, the electron density of the region, and, together with the continuum emission, the number of ionizing photons, these aspects are not discussed here but may be discussed in future works. For the purpose here, we investigate the morphology and kinematics of the $H\alpha$ RRLs in THOR, after stacking the lines at each velocity into a single image in order to improve the sensitivity. Their peak velocities, line widths, and relative strengths are used to investigate the spatial and kinematic structure of ionized gas in the star-forming region W49A in Chapter 5.

1.5 Questions addressed in this thesis

This thesis is focused on two aspects of the observational characterization of molecular clouds. First, it deals with the characterization of the OH molecule in molecular clouds, both diffuse and GMCs. Second, stellar feedback on molecular in GMCs is investigated with RRLs. With observations from the THOR survey (Chapter 2) and follow-up observations with the *Karl G. Jansky* Very Large Array (VLA; Perley et al. 2011), I address the following main questions:

- What is the abundance of OH with respect to atomic and molecular gas?
- Is OH a suitable tracer for CO-dark gas?
- What are the observational effects of stellar feedback, especially in RRL emission?
- How do models constrain the evolution of such feedback-driven shells?

After giving an overview of the THOR survey in Chapter 2, this thesis presents what can be learned on the OH abundance in molecular clouds with OH observations from THOR (Chapter 3) and with high resolution and high sensitivity OH absorption observations in selected regions of the Galactic Plane (Chapter 4). Chapter 5 presents how RRL emission shows signatures from ongoing stellar feedback which, together with models, give us information on how this influences star formation in the star-forming region W49A. The summary and outlook in Chapter 6 discuss possible directions on the future investigations with the THOR survey data and beyond.

Chapter 2

The THOR survey – an overview

Overview: *This chapter introduces the THOR survey and describes its motivation, the observational setup and the data reduction. Publications, to which I have contributed in this context, are listed in the end of the chapter.*

2.1 The THOR survey - a motivation

2.1.1 THOR as a tracer of the cycle of matter of the ISM

Matter in the interstellar medium (ISM) is subject to a cycle. As described in Chapter 1, molecular gas forms out of the atomic, cold neutral medium (see Sect. 1.1.3). Inside molecular clouds, stars are born in dense molecular clumps. Massive stars affect their surrounding gas cloud with ionizing radiation, winds, outflows or supernova explosions, eventually dispersing it entirely (see Sect. 1.1.4). New elements are injected into the ISM at the end of stellar lifetime, both by supernova explosions of massive stars, or winds from AGB stars on the asymptotic giant branch.

The THOR survey (The H_I, OH, Radio recombination line survey of the Milky Way) mapped the first quadrant of the Milky Way between 1–2 GHz. A variety of spectral lines as well as continuum emission from different astronomical objects in the ISM fall in this frequency range. The H_I spin-flip transition at 21 cm (1.4 GHz) is frequently observed to study atomic hydrogen. The four OH ground state transitions at 18 cm can be observed in absorption/emission to study molecular gas in various environments of the ISM (Sect. 1.3). Under certain conditions, they show stimulated emission (masers; e.g., Elitzur 1992). OH masers (e.g., Walsh et al. 2016) trace star-forming regions (at 1665 MHz and 1667 MHz, but also at 1612 MHz and 1720 MHz), evolved stars (1612 MHz; AGB-stars) and supernova remnants (1720 MHz). The continuum emission arises both in thermal (e.g., H II-regions) and non-thermal sources (e.g., supernova remnants). These processes can be classified according to the shape of their spectral energy distribution

between 1–2 GHz (the spectral index of the radiation; [Bihr et al. 2016](#); Wang et al., in press). Radio recombination lines (RRLs) give kinematic information on the ionized gas (see Sect. 1.4). To summarize, the emission spectrum between 1–2 GHz gives information on processes at numerous stages along the cycle of matter in the ISM.

2.1.2 A H I survey at comparable resolution as molecular gas surveys

In the last two decades, a number of Galactic plane surveys became publicly available which trace the molecular gas at angular resolutions of $\sim 20''$. Among these are surveys of dust emission at sub-mm (the ATLASGAL survey at $870\ \mu\text{m}$; [Schuller et al. 2009](#)) and far-infrared wavelengths (the Hi-GAL survey with *Herschel* between $60\text{--}600\ \mu\text{m}$; [Molinari et al. 2016](#)), as well as surveys of CO lines (the COHRS survey, [Dempsey et al. 2013](#); the CHIMPS survey, [Rigby et al. 2016](#); the FUGIN survey, [Umemoto et al. 2017](#)). Surveys that trace atomic gas with the H I 21 cm line were available only at lower angular resolution (e.g., the VGPS survey in the first quadrant of the Milky Way with an angular resolution of $60''$; [Stil et al. 2006](#)).

To study atomic and molecular gas at comparable angular scales, we conducted the THOR survey to observe the H I transition at 21 cm at an angular resolution of $20''$. A first data product of the new H I maps have been released and were presented in [Beuther et al. \(2016\)](#), which combines the H I surveys from THOR and VGPS, in order to be sensitive to both small and large angular scales. The WIDAR correlator at the *Karl. G. Jansky* Very Large Array (VLA) enables the simultaneous observation of continuum and other spectral lines – the OH ground state transitions and the RRLs, which are discussed in the following chapters. This chapter gives details on the calibration and imaging steps of the data reduction of THOR, as far as they apply in particular to the second half of the survey for which I led the calibration (for a comprehensive overview on the calibration and imaging in the THOR survey, see [Beuther et al. 2016](#)).

2.2 Radio Interferometry – the VLA

The VLA ([Perley et al. 2011](#); Fig. 2.1) consists of 27 antennas, arranged in the shape of a “Y”. Each pair of antennas forms a baseline of a certain length and direction with respect to the sky. The raw data from the VLA consists in complex visibilities, each of which describe the amplitude and phase of the signal after the interference of the signal from the two antennas of each baseline. Simply speaking, the visibility obtained from the interference from two antennas traces a well defined angular scale of intensity variations of the emission source. This scale is defined by the separation between the antennas, the baseline. With 351 possible baselines, the VLA can trace 351 different angular scales of the sky emission at each point in time.

The visibilities approximately resemble a Fourier transformation of the sky intensity. More precisely, a discrete Fourier transformation, due to the limited amount of baselines. The task of data-processing is to recover the true sky intensity from the set of measured

angular scales. This is obviously limited to the range of the scales probed. These are roughly given by the shortest and the longest baseline of the interferometer, corresponding to the largest and the smallest angular scale, respectively. Hence, the setup of the interferometer determines the angular resolution of the final image. In case of the VLA, the antennas are movable to allow for different antenna arrangements¹.

The sampling of angular scales obtained with an interferometric observation is usually expressed with the “*uv*-coverage”. The *uv*-coverage shows all sampled angular scales on the “*uv*-plane”, which can roughly be understood as the Fourier transformation of the sky (or image) plane (for more details, see, e.g., Thompson 1999). An example is shown in Fig. 2.4.

The following sections describe the setup of the observations in THOR to measure the visibilities, the steps of calibrating the visibilities as well as the recovery of the image of the astronomical source (i.e., its measured intensity distribution) from the visibilities.

2.3 Setup

2.3.1 Coverage

The THOR survey was observed at *L*-band (1 – 2 GHz) in C-configuration with the VLA between $l = 14.5^\circ$ and $l = 67.25^\circ$ in Galactic Longitude, as well as between $\pm 1.25^\circ$ in Galactic Latitude. The survey was structured in three parts (Fig. 2.2): A pilot study between $l = 29.2^\circ - 31.5^\circ$ (Program ID: 12A-161), the first half of the survey between $l = 14.5^\circ - 37.9^\circ$ and $l = 47.1^\circ - 51.2^\circ$ (Program ID: 13A-120), and the second half covering the remaining area between $l = 37.9^\circ - 67.25^\circ$ (Program ID: 14B-148). The survey was divided into tiles of 1.25° in Galactic Longitude (except the pilot region, which is one single tile), with a total of 20 and 21 tiles to cover the area of the first and second half of the survey, respectively. Each tile was observed separately in observation blocks of ~ 4 h. The observations were conducted in June 2012, June–July 2013 and October–December 2014.

2.3.2 Setup of the mosaics

Each tile was sampled by 45 pointings (59 pointings in the pilot survey), which were arranged in a hexagonal pattern in the pilot survey, and a rectangular pattern in the main survey (Fig. 2.3). The spacing between the pointings was such that each position was Nyquist-sampled at 1.4 GHz, i.e., covered by at least two pointings within the half-power beam size of the response pattern of an individual antenna. This allows for a uniform sensitivity pattern of the final mosaic in the HI observations, which was the main scientific goal of the survey.

¹The different antenna configurations of the VLA can be found here: <https://science.nrao.edu/facilities/vla/docs/manuals/oss/performance/resolution>



Figure 2.1: The *Karl G. Jansky* Very Large Array (VLA; Credit: Alex Savello).

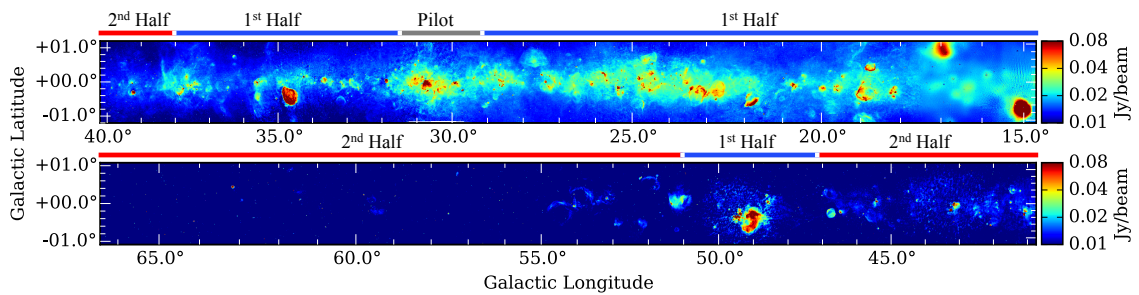


Figure 2.2: Survey coverage of the THOR survey. The image shows 1.4 GHz continuum emission from a combined image of the THOR and VGPS survey (Wang et al., in press). The survey parts are indicated on top of both panels – the pilot survey (*gray*), the first half (*blue*) and the second half (*red*).

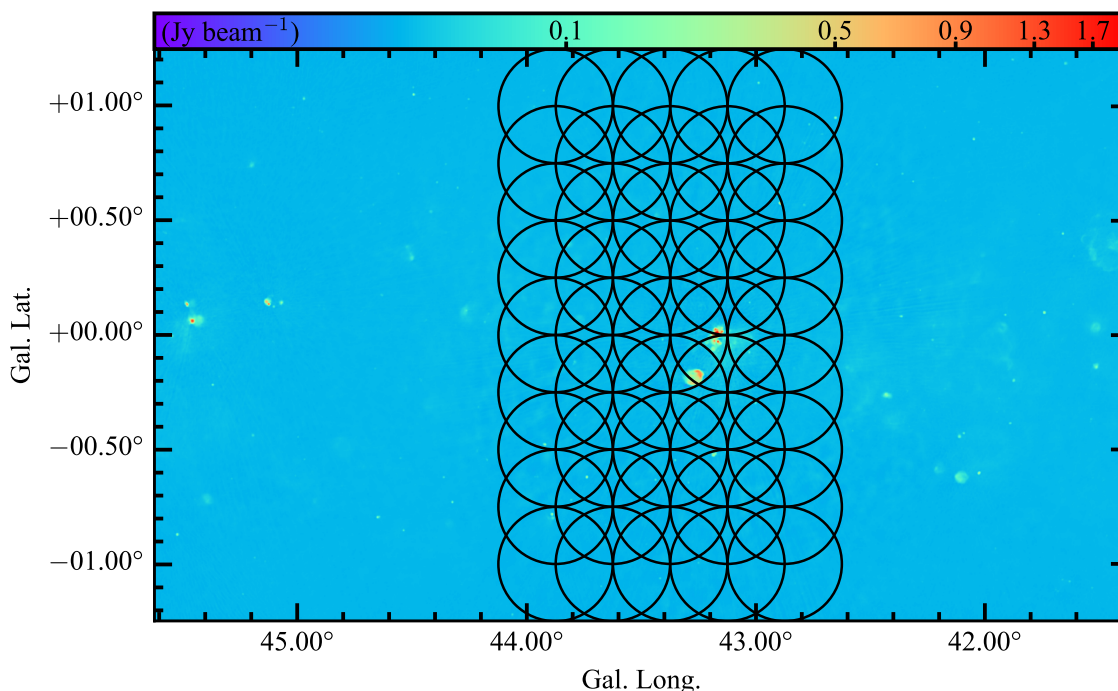


Figure 2.3: Mosaic setup of the THOR survey (first and second half). The *black circles* show the pointings of the survey tile towards $l = 43.5^\circ$. The background images shows 1.4 GHz continuum emission from THOR (Bühr et al. 2016; Wang et al., in press).

2.3.3 Integration

Each pointing was observed three times for ~ 2 min during the 4 hours of observations of one tile. The three observations of a single pointing were spread equidistantly in time over the observation block in order to improve the sampling of the uv -plane. In order to achieve an approximately uniform uv -coverage in each tile, the pointings were not visited sequentially, but different sides were iteratively observed. The typical uv -coverage of a pointing is shown in Fig. 2.4. While the total integration time per pointing was 5-6 min, the effective integration time at any given position was higher due to overlapping coverage by adjacent pointings.

2.3.4 Spectral setup

The spectral setup is listed in Table 2.1. Within L -band, we could place 8 continuum bands, 3 spectral windows for the 4 OH transitions, 1 spectral window for the H I transition and 18 spectral windows for the RRL transitions. The spectral setup of the survey differed slightly among the individual parts. The H I and OH transitions were observed at higher spectral resolution in the pilot survey, while the RRLs were observed at lower spectral resolution than in the remainder of the survey. The selection of RRLs was slightly modified after the pilot study and the first part of the survey, if they were strongly affected by radio frequency interference (for further details see also Beuther et al. 2016, table 1;

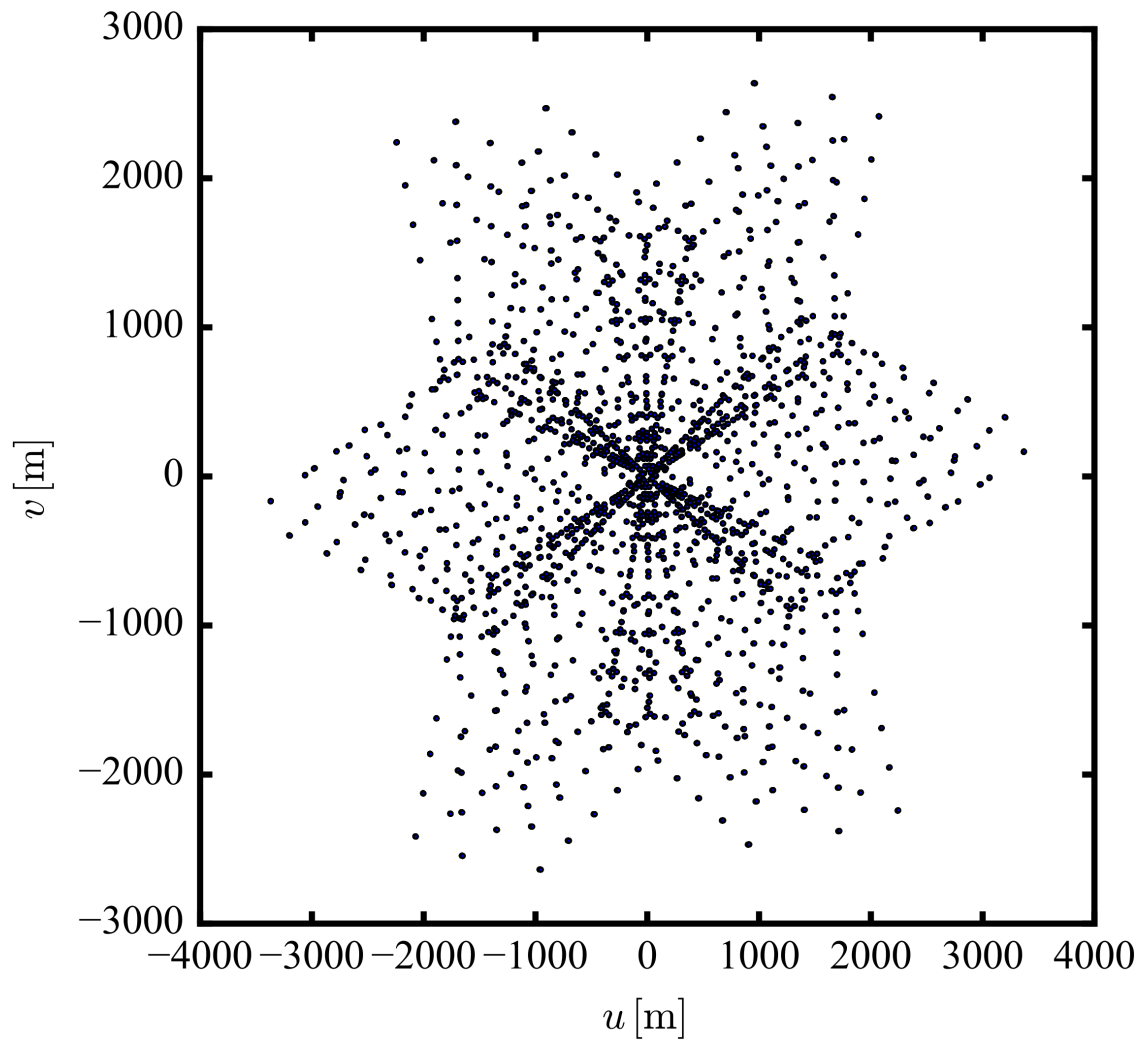


Figure 2.4: Typical uv -coverage of a survey pointing. The plot shows the uv -coverage of a pointing in the tile at $l = 43.5^\circ$.

for radio frequency interference (RFI), see Sect. 2.4.2).

While the H₁ and the OH transitions were observed at a spectral resolution of 0.8 and 1.5 km s⁻¹, respectively, the RRLs were observed with a wider channel width as the lines are significantly broader (20–40 km s⁻¹; see Chapter 5). The continuum bands were spaced such that they cover the entire range between 1–2 GHz.

2.4 Calibration

The calibration was performed using the standard VLA calibration pipeline. It performs flux, phase and bandpass calibration, as well as gain calibration in an iterative procedure. The pipeline applies initial flags as reported by the observatory (e.g., shadowing of antennas). It also uses automatic routines to identify RFI. For the first part of the survey, pipeline version 1.2.0 was used with CASA version 4.1.0. For the second part of the survey, we use pipeline version 1.3.1 with CASA version 4.2.2. Both versions used the same calibration scheme.

2.4.1 Calibration strategy

Each observation block (the observations of one tile of the survey) was structured in three parts. First, a strong quasar (3C286) was observed as flux calibrator for ~10 minutes. Together with a model of the source, this was used to set the absolute flux scale of the observations. The gain calibrator was observed repeatedly during the observation block for gain and phase stability every 10 science pointings. As gain calibrator, we used the source J1822-0938 for all tiles with $l < 39^\circ$ and J1925+2106 for $l > 39^\circ$.

2.4.2 Pipeline calibration

After an initial CASA pipeline run we verified that all antennas were functioning correctly. Since the calibrators are point sources, by definition, amplitude and gain calibration solutions are determined such that all calibrator baselines have the same amplitude and zero phase (i.e., is exactly at the center of the image) after application of the solutions (e.g., Fomalont & Perley 1999, p. 98). One sign of malfunction are strong outliers in flux or in phase. These indicate that for these baselines or antennas no suitable calibration solution could be found and therefore were manually flagged.

The main difficulty of observations at *L*-band is the removal of spurious signal from radio communications, e.g., from satellite communication or airport radar stations (Fig. 2.5). After the automatic flagging of the pipeline, some residual RFI was still present in the data.

We identified large spikes of RFI both spectrally and in time in the calibration sources, and removed the affected calibrator scans accordingly. We inspected the gain amplitude and phase solutions, and removed large outliers. artifacts affected single antennas or baselines. In rare cases, entire parts of the correlator were affected. Generally, however,

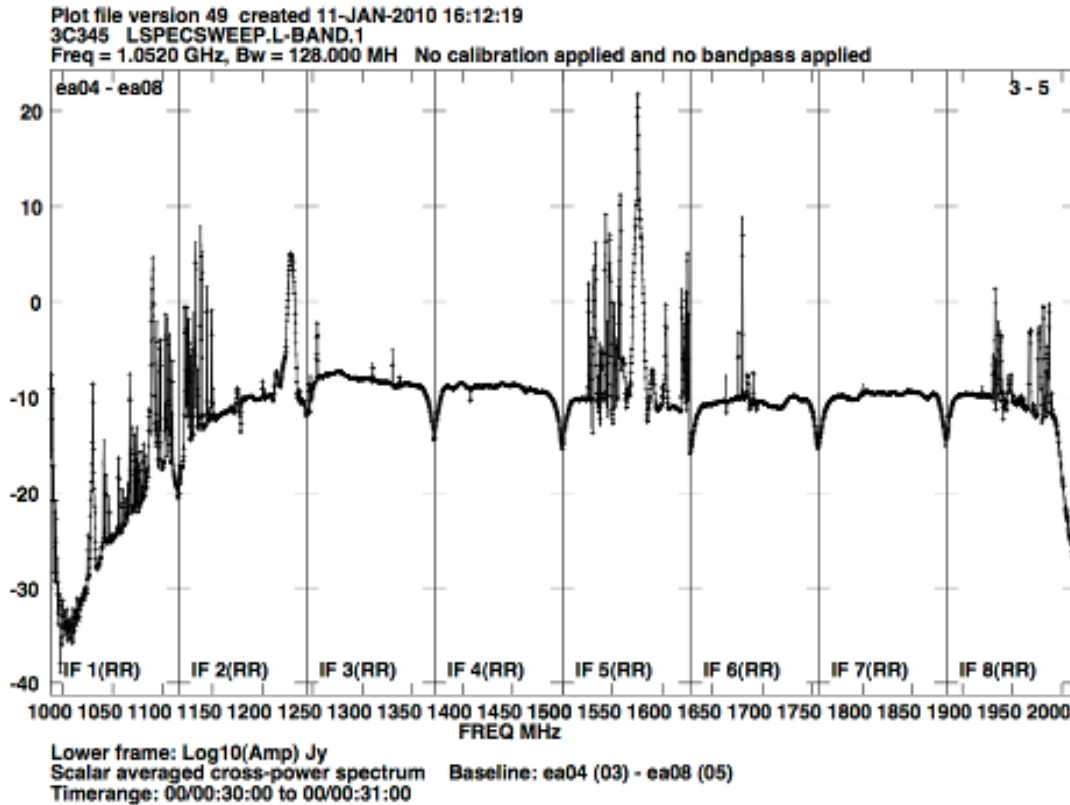


Figure 2.5: Radio Frequency Interference (RFI) between 1–2 GHz. Uncalibrated spectrum of one baseline in *L*-band (from <https://science.nrao.edu/facilities/vla/docs/manuals/obsguide/rfi>).

the VLA is very stable at *L*-band, such that especially the bandpass solutions were always of high quality, at least in spectral lines, which were not affected by RFI.

After application of these corrections, the pipeline was run a second time. We repeated the inspection and the second run of the pipeline, until all calibration solutions were satisfactory. Some spectral windows were heavily affected by RFI, and had to be discarded in the calibration process (e.g., the continuum spectral window “cont5” at 1565 MHz was flagged in all observations; other continuum and RRLs were in some cases heavily affected as well; see Fig. A.1 for details, and Table 2.1 for details on the frequency bands).

2.4.3 Calibration details

Additional modifications were made to the pipeline to optimize it for THOR. *i*) No “Hanning-smoothing” was applied, in order to preserve the original spectral resolution of the data. *ii*) Automatic RFI identification on the scientific targets was disabled in order to preserve spectral line observations. *iii*) The continuum bandpass shows strong drops in sensitivity towards 1 and 2 GHz (Fig. 2.5). This affected the continuum observations in the spectral windows “cont1” and “cont8”. As the pipeline often miss-interpreted these

drops as failed bandpass solutions, we decided to always flag the first 12 channels of “cont1” and the last 24 channels of “cont8”. *iv*) The gain calibrator of the second half of the survey shows substantial H I absorption. This may affect the gain calibration solutions of the H I observations. We therefore flag the channels 200–420 in all gain calibrator scans of the H I spectral window, and channels 24–25 in “cont4”.

2.5 Imaging & Deconvolution

This section discusses the method of creating an image with angular coordinates from the observed visibilities. This is usually done by gridding the visibilities on an image in Fourier space (the uv -plane), which is then inverted to an image in angular coordinates (the “image-plane”). A second step is necessary after inversion, since a point source in the inverted image usually shows a complicated structure of side-lobes (the “dirty” image), which arise due to the incomplete sampling of the uv -plane by the interferometer. These can be partially removed by deconvolving or “CLEANing” the image. In this process, emission sources in the final images are identified, fitted with a point spread function of the baseline configuration of the observations, and removed from the image. These steps are iterated until all emission is sufficiently removed. In the end, the fitted components are restored to the image, but with a 2D-Gaussian profile, which is determined from the central peak of the point spread function.

For THOR, we use the CASA task `clean` for imaging and deconvolution of the data. For spectral lines, this software conducts the imaging for every channel separately and adds the final images to one spectral line cube. For continuum observations, we use “multi-frequency synthesis” (e.g., [Sault & Conway 1999](#)), which combines all channels into one image of the continuum (accounting for frequency dependence). While these processes are handled well for single pointings, software implementation for mosaics of many pointings is difficult. We discuss different possibilities, and describe the method used for the THOR data.

2.5.1 Mosaicking algorithms

There are two principal ways of creating a mosaic from interferometric data. The visibilities of the mosaic can either be combined in the uv -plane, or in the image-plane, after separate inversion of each pointing. Both methods are described briefly in the following.

2.5.1.1 Mosaicking in the image-plane

Each pointing is imaged separately (i.e., inverted to image-space), such that an image for each pointing is created. These small images are simply arranged according to their image centers into one large image of the mosaicked region. This is fully implemented in the `clean` task of CASA. Similar as for cleaning a single pointing, CASA de-convolves the image in multiple steps. It iteratively searches for clean components, now in the dirty image of the entire mosaic, subtracts them in uv -space from the visibilities of each

pointing, and then inverts again each pointing and creates a new dirty image of the mosaic without the fitted emission components. This process is repeated until a user-specified number of iterations is reached, or the residual image is within a specified noise level (for details see, e.g., [Cornwell et al. 1999](#)).

2.5.1.2 Mosaicking in the uv -plane

All visibilities from all pointings are transformed in Fourier-space such that they are referenced to a common phase center (to the center of the large mosaic; this can be simply done by applying a phase-shift to all visibilities). The visibilities of all pointings are then gridded onto one single uv -plane, which is subsequently inverted to yield the dirty image of the mosaic. Hence, only one Fourier inversion is performed for the entire mosaic, instead of multiple inversions for each pointing separately. The task `clean` then performs a similar iterative search for clean components as for mosaicking in the image-plane, however always gridding all visibilities into one single uv -plane.

This method bears many possibilities, such as an implementation of a frequency-dependent correction for the attenuation of the antenna response towards the edges of each pointing, an implementation for multi-frequency synthesis also for mosaics, as well as accounting for wide-field corrections, which are necessary in the large images used in the THOR survey at L-band.

2.5.2 Imaging & Deconvolution in THOR

Since only recent versions of CASA implement mosaicking in the uv -plane (Sect. 2.5.1.2) correctly, which were not available when the bulk of the imaging for THOR was done, we performed all imaging with CASA version 4.2.2, which creates the mosaic in the image plane (Sect. 2.5.1.1). We tested this version in many ways, e.g., by comparing the fluxes of sources in the mosaics to the results obtained from imaging single pointings.

`Clean` in CASA version 4.2.2 accounts correctly for distortions arising from the large image size in THOR. While the sky plane is usually assumed to be co-planar to the telescope array, this approximation fails for the size of typical THOR mosaics ($3.75^\circ \times 2.5^\circ$), in comparison to maximum angular resolution of THOR of $10''$ - $20''$ (see eq. 2-29 [Thompson 1999](#)), which makes the widefield correction necessary for THOR. It is possible to perform the same way of cleaning also in the CASA versions starting from CASA 4.7.2 (the specific option in `clean` is `gridmode = 'widefield'`).

We tested and assisted in the debugging of many later versions after CASA 4.2.2, since mosaicking in the uv -plane has many advantages (see Sect. 2.5.1). One of the tests is shown in the following section. As it is also more difficult to implement, only recent versions provide reliable results for large images of L -band observations. A new implementation of this algorithm can create mosaics even from different antenna configurations, and is used in THOR for a future release of the HI data, which contains mosaics created by jointly imaging the C-configuration data from THOR and the D-configuration data from the VGPS survey (Wang et al., in prep.).

2.5.3 CASA tests: Flux dependence on the phase center of the mosaic

As mentioned above, considerable efforts were invested into ensuring the quality of the images done with mosaicking in the uv -plane. The type of problems were related to software implementation, which is difficult given such a complex code as CASA, and especially functions such as `clean`, which offer an enormous flexibility to deal with different types of imaging and deconvolution.

One of these problems was an apparent variation in the flux of sources in the mosaicked images to reference images of single pointings. After confirming that this was not a problem related to mosaicking in general, by verifying that mosaics made in CASA 4.2.2 with `gridmode='widefield'` (see Sect. 2.5.2) were consistent with the images of the reference pointings, we noted a dependence of flux strength with distance to the phase center of the mosaic in some later versions of CASA, and therefore went on to testing this in detail.

We chose a sub-region of VLA C-configuration continuum observations at 1.4 GHz and analyzed a mosaic of seven pointings. We created seven different images of the region, each time taking a different single pointing of the mosaic as phase center of the image. Seven point-like sources are selected in the image and are fitted with a 2D-Gaussian to determine their peak flux. An image to highlight the setup is shown in Fig. 2.6.

The images are cleaned with two versions of the imaging software CASA, version 4.2.2 and 4.5. The images created in CASA version 4.2.2 are created by selecting the option `gridmode=widefield` - according to the CASA cookbook and the program log-file, this selects `ftmachine = wproject`. The mosaic is then created in the image-plane (Sect. 2.5.1.1). We tested in the previous analyses that the source fluxes in mosaics created in this way compare well with the source flux extracted when imaging only a single pointing of the source in question and using standard clean procedures (`csclean`) in CASA.

CASA 4.5 was used in `imagermode = "mosaic"` with `ftmachine = "mosaic"`. This creates a mosaic in the uv -plane. As no distortions were visible in the resulting images, we assume that the built-in widefield correction was applied correctly. Identical tests were conducted with CASA 4.6.0, which yield identical results as CASA 4.5.0. Therefore we only report the results from CASA 4.5.0.

Using `imfit()` from CASA 4.5.0, 2D-Gaussians are fitted to small boxes around the sources indicated in Fig. 2.6. We calculate the angular separation to the respective phase center and compare the flux densities. To put the comparison on a comparable scale, Fig. 2.7 shows the percentile deviation of the flux in CASA 4.5 to CASA 4.2.2 of source 5 (see Fig. 2.6) in dependence of its distance to the phase center of each of the seven mosaics. We find a trend of decreasing peak flux with angular distance to the phase center. Up to a separation of 0.8° , the difference is not larger than 5%. In all cases, the deviation is below 10% within a separation of 1° .

As this trend can be seen in all tests, in CASA from versions 4.3 to 4.7.1, we strongly conjectured that this would be a software problem. In fact, it was found out later that a flux correction, which is used for going from the uv -plane to the image domain, was not included. The problem has been fixed as of rev 36997 (e.g., from release version

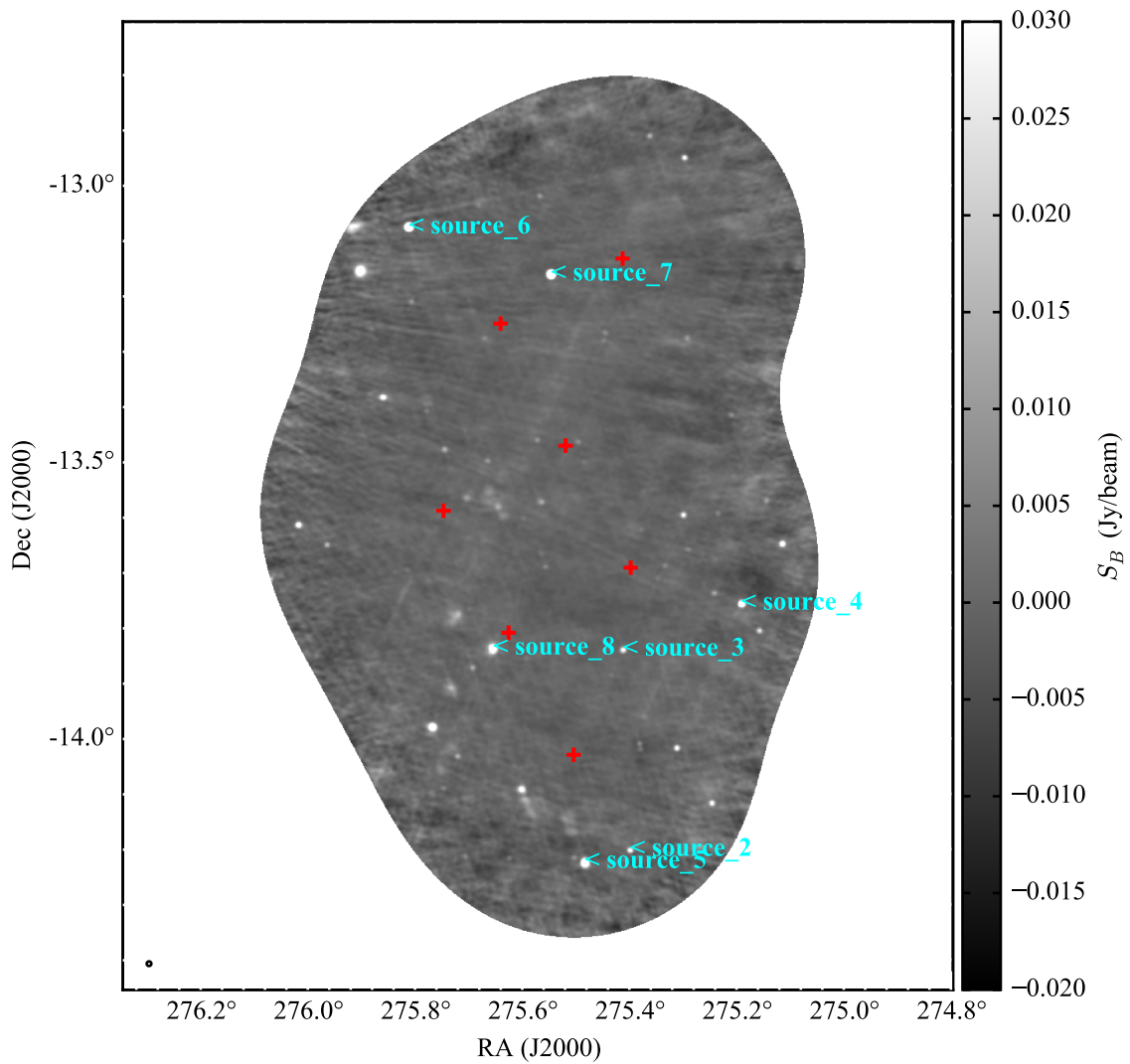


Figure 2.6: Setup for the test of the mosaicking algorithm of CASA in Sect. 2.5.3. The position of test sources is marked in *cyan*. *Red* crosses indicate the phase centers of the seven images used for the test. The background image shows 1.4 GHz emission.

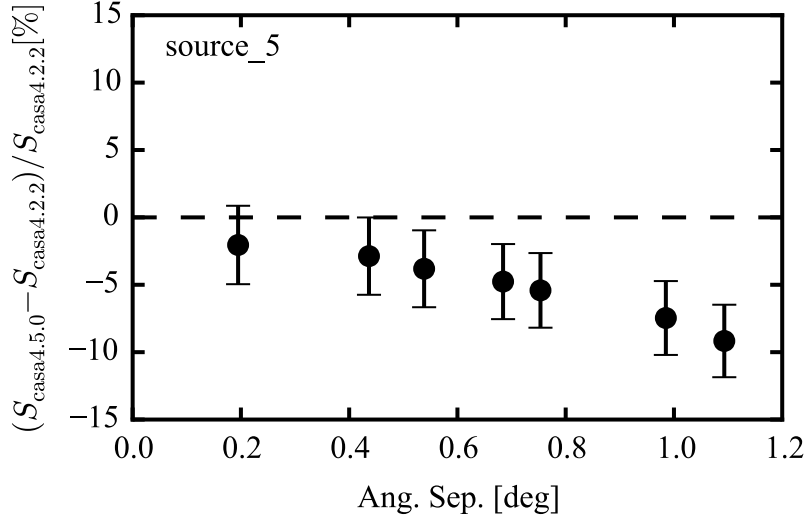


Figure 2.7: Relative deviation of the flux in CASA versions 4.5.0 and 4.2.2 vs. angular separation from phase center for continuum source 5. The test results of all sources are given in Fig. A.2.

CASA 4.7.2 on). As noted above, this release appeared after the bulk of the imaging was done. We therefore used CASA version 4.2.2 for all imaging (with mosaicking in the image-plane), which was verified to produce images with reliable fluxes.

2.6 Further applications of the THOR data - Carbon α RRLs

This section highlights shortly one other possibility of the application of the THOR data – the observations of carbon α RRLs. The RRLs of carbon typically arise from different regions in clouds as the RRLs of hydrogen, with different temperatures and densities. In the case of photodissociation regions (PDRs), the ionization front of carbon lies at higher visual extinctions than the hydrogen ionization front (see Fig. 1.2). They may therefore show distinct kinematic signatures from the hydrogen RRLs. The purpose of this section is to show – without further analysis – an example of capabilities of the THOR survey, which were not originally planned but may be of interest for future exploration (for further details on carbon RRLs, see e.g., [Hoang-Binh & Walmsley 1974](#)).

The carbon α RRLs are separated from the hydrogen α RRLs by a velocity shift of -150 km s^{-1} . The typical usable bandwidth after calibration for the RRLs ranges between 540 km s^{-1} at 1 GHz, and 270 km s^{-1} at 2 GHz. With the spectral windows of the RRLs centered on the hydrogen RRLs (Table 2.1), the carbon RRLs become observable from the H154 α transition on (for RRLs at frequencies of 1800 MHz or lower), assuming that the rest velocity of the source is at 0 km s^{-1} .

While initially looking for helium α RRLs, which are separated by -122 km s^{-1} from the H α transitions, we imaged the spectral windows of the RRLs around the star-forming regions W49A and W51 at the frequencies of the helium RRLs (see, e.g., table 1 in [Towle](#)

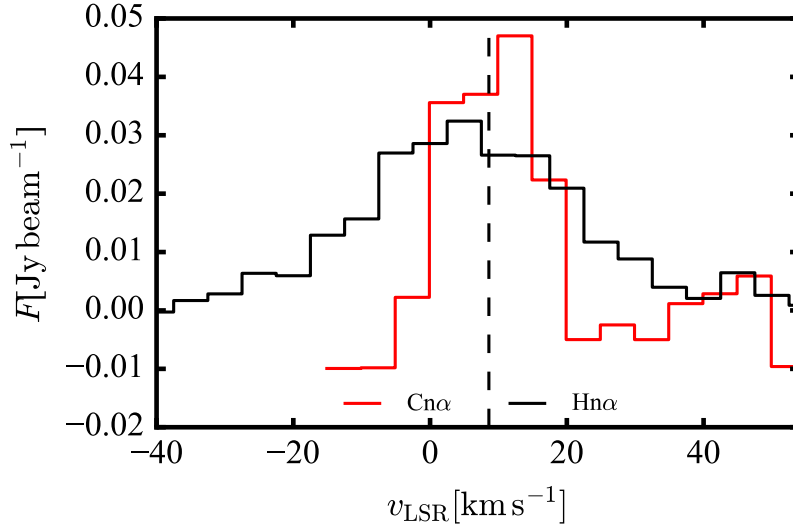


Figure 2.8: Carbon α RRLs in W49A. Emission of carbon α RRLs ($Cn\alpha$, at $40''$) and hydrogen α RRLs ($13''.8 \times 16''.8$) towards the peak of the 1.6 GHz continuum emission in W49A (Pos. 1 in Fig. 5.1).

et al. 1996). We followed the same steps for the reduction of the RRLs as described in Sect. 5.2.1, however smoothing the data to an angular resolution of $40''$ in order to increase sensitivity (see also, Beuther et al. 2016), and using only a smaller portion of the mosaic, as we were only interested in two particular regions.

The helium α RRL transitions were not significantly detected in any of the two regions, however, the carbon α RRLs were. Fig. 2.8 shows the emission of the carbon RRLs (at $40''$ resolution). It is shown together with the emission of $H\alpha$ RRLs presented in Chapter 5 (at a resolution of $13''.8 \times 16''.8$). Both spectra are extracted towards Pos. 1, which is indicated in Fig. 5.1. The carbon RRLs were stacked in velocity, with the carbon α transitions at orders $n = 165, 166, 168, 170, 171, 186$ included in the stacking process (the other transitions were either not fully included in the bandpass or affected by RFI).

We see in Fig. 2.8 that the carbon and hydrogen RRL transitions agree well in central velocity. The line widths of the carbon RRLs are significantly lower than the hydrogen RRLs. One reason is that they arise from significantly lower temperature regions ($T = 50 - 100$ K; e.g., Hoang-Binh & Walmsley 1974) as the hydrogen RRLs ($T \sim 10^4$ K; see Chapter 5).

While this short outlook does not attempt to present a complete analysis of the carbon RRLs by any means, it shows that there are further applications of the measurements conducted within the THOR survey. The carbon RRLs were also detected in W51, with other star forming regions remaining to be investigated.

2.7 Publications within the THOR collaboration

This section shortly lists the publications within the THOR collaboration, which I have led or in which I have participated.

2.7.1 First-author publications

- *OH absorption in the first quadrant of the Milky Way as seen by THOR*; Rugel, M. R., Beuther, H., Bihr, S., et al., A&A, in press. Chapter 3 is based on this publication.
- *Feedback in W49A diagnosed with Radio Recombination Lines and Models*; Rugel, M. R., Rahner, D., Beuther, H., et al., A&A, submitted. Chapter 5 is based on this publication.

2.7.2 Publications as co-author

The following papers made use of the THOR data. I contributed with comments on the manuscripts.

- *Radio continuum emission in the northern Galactic plane: sources and spectral indices from the THOR survey*; Wang, Y., Beuther, H., Rugel, M., et al. 2018, A&A, in press.
- *Confirmation Of Two Galactic Supernova Remnant Candidates Discovered By THOR*; Dokara, R., Roy, N., Beuther, H., [...], Rugel, M., et al. 2018, ApJ, accepted for publication.
- *Galactic supernova remnant candidates discovered by THOR*; Anderson, L. D., Wang, Y., Bihr, S, Rugel, M., et al. 2017, A&A, 605, A58
- *Large-scale Map of Millimeter-wavelength Hydrogen Radio Recombination Lines around a Young Massive Star Cluster*; Nguyen-Luong, Q., Anderson, L. D., Motte, F., [...], Rugel, M., et al. 2017, ApJL, 844, L25
- *The HI/OH/Recombination line survey of the inner Milky Way (THOR). Survey overview and data release 1*; Beuther, H., Bihr, S., Rugel, M., et al. 2016, A&A, 595, A32
- *Continuum sources from the THOR survey between 1 and 2 GHz*; Bihr, S., Johnston, K. G., Beuther, H., [...], Rugel, M., et al. 2016, A&A, 588, A97
- *A survey for hydroxyl in the THOR pilot region around W43*; Walsh, A. J., Beuther, H., Bihr, S., [...], Rugel, M. 2016, MNRAS, 455, 3494

Table 2.1: Spectral setup of the THOR survey (second half)

Spw	Transition	Frequency [MHz]	Nchan	Freq. Res. [kHz]	Vel. Res. [km s ⁻¹]	Freq. Bw. [MHz]	Vel. Bw. [km s ⁻¹]
0	cont1	1052	64	2000.000	570.3	128	36502
1	H186 α	1013.767	128	15.625	4.6	2	592
2	cont2	1180	64	2000.000	508.5	128	32542
3	H178 α	1156.299	128	15.625	4.1	2	519
4	H176 α	1196.028	128	15.625	3.9	2	502
5	H173 α	1259.150	128	15.625	3.7	2	477
6	H172 α	1281.175	128	15.625	3.7	2	468
7	H171 α	1303.718	128	15.625	3.6	2	460
8	H170 α	1326.792	128	15.625	3.5	2	452
9	H168 α	1374.601	128	15.625	3.4	2	436
10	H167 α	1399.368	128	15.625	3.3	2	429
11	Hr ^a	1420.406	512	3.906	0.8	2	422
12	H166 α	1424.734	128	15.625	3.3	2	421
13	H165 α	1450.716	128	15.625	3.2	2	414
14	H158 α^b	1651.541	128	15.625	2.8	2	363
15	cont3	1308	64	2000.000	458.7	128	29358
16	cont4	1436	64	2000.000	417.8	128	26741
17	cont5	1564	64	2000.000	383.6	128	24552
18	OH1612 ^a	1612.231	256	7.812	1.5	2	372
19	cont6	1692	64	2000.000	354.6	128	22695
20	OH1665/OH1667 ^a	1665.402	512	7.812	1.4	4	721
21	H156 α^b	1715.673	128	15.625	2.7	2	350
22	OH1720 ^a	1720.530	256	7.812	1.4	2	349
23	H155 α^b	1748.986	128	15.625	2.7	2	343
24	cont7	1820	64	2000.000	329.7	128	21099
25	H154 α^b	1783.168	128	15.625	2.6	2	336
26	H153 α^b	1818.246	128	15.625	2.6	2	330
27	H152 α^b	1854.250	128	15.625	2.5	2	324
28	cont8	1948	64	2000.000	308.0	128	19713

Notes: Column 1 denotes spectral window number. Column 4 denotes number of channels. Columns 5 and 6 denote frequency and velocity resolution, respectively. Columns 7 and 8 give the bandwidth in frequency and velocity. Note that channels at the edges of the bandpass are flagged during calibration, such that the effective bandwidth is approximately 10% smaller. For further details, see table 1 in (Beuther et al. 2016).

Footnotes: ^(a) Transitions used in Chapter 3. ^(b) Transitions used in Chapter 5.

Chapter 3

Characterization of the OH abundance with THOR

This chapter was published in a refereed journal as “OH absorption in the first quadrant of the Milky Way as seen by THOR”, M. R. Rugel, H. Beuther, S. Bihl, et al., A&A, in press, and was adapted for this thesis.

Overview: *In this Chapter, we evaluate the abundance of OH with respect to molecular hydrogen using OH absorption towards cm-continuum sources over the first Galactic quadrant from the THOR survey. OH absorption is found towards approximately 15% of these continuum sources. Most of the absorption occurs in molecular clouds that are associated with Galactic H II regions. The data indicate that the OH abundance decreases with increasing hydrogen column density. Towards the lowest column densities, we find sources that exhibit OH absorption but no ^{13}CO emission. We also present spatially resolved OH absorption towards the prominent extended H II-region W43.*

3.1 Introduction

As discussed in Chapter 1, most molecular gas is in the form of molecular hydrogen, H_2 , which is difficult to observe directly in the cold environments of molecular clouds. While CO is frequently used as a tracer of H_2 in the Milky Way (e.g., [Miville-Deschênes et al. 2017](#)), observational and theoretical studies suggest that a significant fraction of the molecular gas is not traced by CO (e.g., [Grenier et al. 2005](#); [Planck Collaboration et al. 2011](#); [Pineda et al. 2013](#); [Smith et al. 2014](#)). Therefore, a search for alternative molecular gas tracers is necessary.

As introduced in Sect. 1.3, OH is a potential tracer for molecular gas in transition regions. It was first detected by [Weinreb et al. \(1963\)](#) and was one of the earliest molecules studied in detail in many regions of the Galactic plane (e.g., [Goss 1968](#); [Turner 1979](#); [Dawson et al. 2014](#)), as it has easily-accessible ground state transitions at cm-wavelengths.

Recent high sensitivity studies found OH emission that extends beyond the molecular cloud envelope traced by CO surveys (e.g., [Allen et al. 2015](#); [Xu et al. 2016](#), using the GBT with 7'6 and the Arecibo telescope with 3' resolution, respectively). A detailed comparison of the “CO-dark” gas fraction and OH across a molecular cloud boundary in Taurus found OH to be present in “CO-dark” regions with $A_V < 1.5$ mag ([Xu et al. 2016](#)). Complementary studies show that OH is present in “partially atomic, partially molecular”, warm (~ 100 K) H I halos ([Wannier et al. 1993](#)), and show that its column density increases with increasing N_{HI} for $N_{\text{HI}} < 1.0 \times 10^{21} \text{ cm}^{-2}$ ([Tang et al. 2017](#)). Additionally, OH has also been found to be correlated with visual extinction in diffuse clouds ([Crutcher 1979](#), observed at 22' resolution with the 37m telescope of the Vermilion River Observatory). These results strongly suggest its presence in transition regions between atomic and molecular gas.

The OH abundance towards higher extinction regions is on the other hand of interest for the determination of magnetic field strengths from Zeeman splitting of OH absorption lines. To understand the gas densities at which OH traces the magnetic fields, precise knowledge of the OH abundance at different densities is indispensable. In particular, the behavior of the OH abundance in regions of higher density is not yet well understood, neither theoretically nor observationally (e.g., [Heiles et al. 1993](#)).

There are three different types of chemical reactions in molecular clouds that can influence the abundance of OH (e.g., [van Dishoeck et al. 2013](#)): Gas phase ion-neutral chemistry, important in diffuse and cold environments (“diffuse” chemistry), neutral-neutral chemistry, important for warm regions (>200 K), and grain surface chemistry, which depends on the strength of the radiation field and the temperature. The fractional abundance of OH is closely related to that of H₂O if diffuse chemistry or photodesorption of water from grains is dominant ([Hollenbach et al. 2012](#)). In high temperature environments, e.g., in shocks, this changes, favoring the formation of H₂O in the case of very high temperatures, unless strong ultraviolet radiation is present to photo-dissociate H₂O and thus to increase the amount of OH in the gas phase (e.g., [Neufeld et al. 2002](#); [van Dishoeck et al. 2013](#)).

The fractional OH abundance has been found to be constant for $A_V < 7$ mag and hydrogen nuclei number densities of $n \lesssim 2500 \text{ cm}^{-3}$ (e.g., [Crutcher 1979](#)). Typical values for the OH abundance with respect to total hydrogen nuclei column density are $X_{\text{OH}} \sim 4.0 \times 10^{-8}$ ([Goss 1968](#); [Crutcher 1979](#); [Heiles et al. 1993](#)), and with respect to molecular hydrogen column density $X_{\text{OH}} \sim 1.0 \times 10^{-7}$ (e.g., [Liszt & Lucas 2002](#)). Other studies exist, however, which also found higher values for the OH abundance, i.e. of a few $\times 10^{-7}$ in molecular cloud boundaries, with a decreasing trend towards $X_{\text{OH}} \sim 1.5 \times 10^{-7}$ at visual extinctions $A_V \geq 2.5$ mag ([Xu et al. 2016](#)). Once molecular cloud regions fall into the line-of-sight where UV radiation is attenuated, the OH abundance is no longer expected to be constant ([Heiles et al. 1993](#), and references therein). Models predict the depletion of oxygen bearing species from the gas phase in the absence of photodesorption of water ice, which occurs at $A_V \sim 6$ mag, depending on the strength of the radiation field ([Hollenbach et al. 2012](#)).

The transitions investigated in this chapter are the Λ doubling transitions of the OH ground state, the $^2\Pi_{3/2}; J = 3/2$ state. The transitions at 1665 MHz and 1667 MHz (“main

lines”) are 5 and 9 times stronger than the satellite transitions at 1612 MHz and 1720 MHz (“satellite lines”; e.g., [Elitzur 1992](#)). While the satellite lines are easily anomalously excited, e.g., through ambient infrared radiation (that is, are subject to population inversion and show non-thermal, maser emission), it requires higher densities to anomalously excite the main lines, which are mostly also found to be optically thin (e.g., [Goss 1968](#); [Crutcher 1979](#); [Heiles et al. 1993](#)). Observations of OH transitions at 1665 MHz and 1667 MHz in absorption against strong cm-continuum sources therefore provide a possibility to determine the optical depth of the OH ground state transitions directly (e.g., [Goss 1968](#); [Stanimirović et al. 2003](#)).

Strong maser emission from OH 1665 and 1667 MHz has also been found, predominantly towards high mass young stellar objects, but also towards evolved stars (e.g., [Argon et al. 2000](#)). They are pumped by the strong far infrared field emitted by the warm ($T \sim 150$ K) dust in their host stars’ dense ($\sim 10^7$ cm $^{-3}$) envelopes (e.g., [Cesaroni & Walmsley 1991](#)). In the course of the THOR survey (The H I, OH, Recombination line survey of the Milky Way; [Beuther et al. 2016](#)) many such OH masers have been detected (see, e.g., [Walsh et al. 2016](#)), but are not the topic of the present chapter.

The determination of OH column densities from hyperfine ground state absorption observations requires an assumption regarding the excitation temperature of the transitions. The OH excitation temperature of the main lines depends on the volume density and ionization fraction, and only weakly on the kinetic temperature (e.g., [Guibert et al. 1978](#)). The critical density ($n_{\text{crit}} = A_{\text{ul}}/\gamma_{\text{ul}}$; A_{ul} is the Einstein coefficient for spontaneous emission and γ_{ul} the collisional deexcitation rate coefficient), a measure of when collisional processes dominate the deexcitation of the upper energy levels of a transition, is typically found around $n_{\text{crit}} \sim 0.5$ cm $^{-3}$ for the OH transitions at 1665 MHz and 1667 MHz. The transitions are typically found to be subthermally excited, with excitation temperatures of $T_{\text{ex}} = 5 - 10$ K (e.g., [Colgan et al. 1989](#)). The reason for this is that densities much higher than n_{crit} are needed for thermalization. These densities exceed those typical of boundary regions of molecular clouds ($n \leq 10^3$ cm $^{-3}$). Firstly, once stimulated emission and absorption of the cosmic microwave background are included, the effective critical density required for the collisional and radiative deexcitation rates to balance is $n \gtrsim 10^3$ cm $^{-3}$ (e.g., [Wannier et al. 1993](#)). Secondly, the small energy separation of the OH lines ($E_u/k \sim 0.1$ K) makes the lines harder to thermalize for any given T_{kin} , such that $n \gtrsim 10^3$ cm $^{-3}$ are required to thermalize the lines even if stimulated emission and absorption are not taken into account.

Within the THOR survey, we observed the ground state OH transitions at a high angular resolution of $20''$ and compared our results to those obtained from tracers of atomic and molecular gas at comparable angular resolution across the first quadrant of the Milky Way. The present chapter addresses two aspects of the OH data: The detection statistics of OH main line absorption and the utility of the OH ground state transitions as molecular and atomic gas tracers based on comparisons of column densities and kinematic properties.

The chapter is structured as follows: In Section 3.2, we present the observations and delineate the use of ancillary data. Section 3.3 gives the results that are discussed in Section 3.4. The conclusions are provided in Section 3.5.

3.2 Observations and data reduction

We have mapped the four OH ground state transitions in the first quadrant of the Milky Way with the Karl G. Jansky Very Large Array (VLA) in C-configuration. The observations are part of the large program THOR (see Chapter 2 for more details), with data taken over several observational periods, mapping between $l = 14.5^\circ$ and $l = 67.25^\circ$, $|b| \leq 1.1^\circ$. Here we present OH observations in absorption for the entire survey region and include the OH absorption data in the pilot study of 4 square degrees around the star-forming region W43, which have already been presented in Walsh et al. (2016). As the observing strategy was discussed in Chapter 2, we will restrict the discussion of the THOR data in this chapter to the OH absorption observations.

The OH satellite line transitions, located at 1.612231 and 1.720530 GHz (Schöier et al. 2005; Offer et al. 1994), were observed with two 2-MHz-wide spectral windows. The two main line transitions at 1.665402 and 1.667359 GHz were observed in one 4-MHz-wide spectral window for $l = 29.2^\circ - 31.5^\circ$, $l = 37.9^\circ - 47.1^\circ$ and $l = 51.2^\circ - 67.0^\circ$. The rest of the survey coverage was mapped in the 1.665-GHz transition alone, using a 2-MHz-wide spectral window. Channel widths for all transitions are 3.9 kHz ($\sim 0.7 \text{ km s}^{-1}$) in the pilot study ($l = 29.2^\circ - 31.5^\circ$, $|b| \leq 1.1^\circ$) and 7.8 kHz ($\sim 1.4 \text{ km s}^{-1}$) for the rest of the survey. The channel width of the OH transitions was chosen to be equivalent to the simultaneously-conducted H I observations, which in turn were following the spectral resolution of the existing H I Very Large Array Galactic Plane Survey (VGPS; Stil et al. 2006) for comparability. All data have been taken at a total integration time per pointing of 5–6 min, split into 3 observations of equal time to improve the uv -coverage.

The data were calibrated with the CASA calibration pipeline, and the solutions were iterated after removing data of individual baselines and antennas in time ranges in which these contain artifacts. Using CASA¹, data were continuum-subtracted and gridded on a common velocity grid of 1.5 km s^{-1} resolution, and subsequently inverted and deconvolved with the CASA task `clean`. The line free channels were cleaned separately to obtain the continuum at 1666 MHz for the 1665/1667 MHz transitions. These continuum data were used for the later analysis for consistency in calibration.

The angular resolution of the data is between $12''.7 \times 12''.4$ and $18''.7 \times 12''.5$, depending on the transition and on the elevation of the source at the time of observation. We regrid all data to the Galactic coordinate system and smooth all data to a resolution of $20'' \times 20''$. The noise is typically about 10 mJy beam^{-1} at a velocity resolution of 1.5 km s^{-1} , except for areas around strong emission sources.

The $^{13}\text{CO}(1-0)$ observations employed as tracer for the molecular gas are taken from GRS (Galactic Ring Survey, Jackson et al. 2006) and for two sources (G60.882–0.132 and G61.475+0.092) that lie beyond $l = 60^\circ$ from the Exeter FCRAO CO survey (Mottram & Brunt 2010). Both datasets were taken with a single dish telescope having a $46''$ FWHM beamsize. All data have been converted to main-beam temperature (T_{mb}) using a beam efficiency of $\eta = 0.48$ (Jackson et al. 2006). The H I 21 cm absorption gives column densities of the atomic gas and the data are also from THOR (Bihl et al. 2015;

¹<http://casa.nrao.edu>; version 4.2.2

Beuther et al. 2016). As the H I spectral cubes ($20'' \times 20''$ resolution) were imaged without continuum subtraction, the continuum is extracted from the line-free channels in the provided spectral cubes and used later to derive the line-to-continuum ratio. All datasets are gridded on the same coordinate system as the 1666 MHz continuum image.

A continuum catalog was extracted from the narrow band continuum maps at 1666 MHz with a spatial resolution of $20'' \times 20''$ with the source finding algorithm blobcat (Hales et al. 2012). The noise maps were created using the residual maps that have been produced during deconvolution (see also Bühr et al. 2016). To verify the completeness of the catalog, it was matched to the continuum source catalog of the THOR survey for sources with $F_{\text{cont}} \geq 0.1 \text{ Jy beam}^{-1}$, which was derived from 128-MHz-wide spectral windows and therefore has higher sensitivity (Bühr et al. 2016, Wang et al., in prep.). One continuum source, G30.854+0.151, which was not detected in the narrow-band catalog due to strong sidelobes from a nearby continuum source, was subsequently added to the detections, and the flux from the broadband continuum catalog was used for quantitative analysis in the following.

For the quantitative comparison of OH and H I absorption to $^{13}\text{CO}(1-0)$ emission in Section 3.3.2, the spatial resolution of the OH, H I and continuum datacubes is degraded to match the resolution of $^{13}\text{CO}(1-0)$ data at $46''$. For simplicity, the deconvolved images are smoothed with a Gaussian kernel in the image plane. The relevant quantity for absorption measurements in Sect. 3.3.2 is the ratio of absorption line to continuum. While the baselines of the VLA in C-configuration sample angular scales of $46''$, the actual scales probed depend intrinsically on the emission structure of the continuum source. Scales of $46''$ are only probed for continuum emission extending at least $46''$ in angular size. For inhomogeneous emission, patches of stronger continuum emission will have a larger contribution to the line-to-continuum ratio. With this general consideration regarding absorption measurements, smoothing the data to $46''$ resolution gets closest to the scales probed by ^{13}CO emission. An example of an extended OH absorption map at $20'' \times 20''$ resolution is provided for the star forming complex W43 in Sect. 3.3.4.

To minimize the introduction of systematic errors, the continuum is derived from line-free channels and thus has the same uv-coverage and calibration as the spectral line data. The median noise in the smoothed spectral line cubes is at $0.013 \text{ Jy beam}^{-1}$, with variations between $0.008 \text{ Jy beam}^{-1}$ and $0.020 \text{ Jy beam}^{-1}$ (see also gray lines in Fig. 3.3). An example spectrum of all transitions is shown in Fig. 3.1.

To address extended OH absorption in W43 (e.g., Smith et al. 1978; Motte et al. 2014), we employ the full resolution OH 1667 MHz data ($20'' \times 20''$). It is compared to APEX observations of $870 \mu\text{m}$ dust emission from the ATLASGAL² survey (Schuller et al. 2009; Contreras et al. 2013; Urquhart et al. 2014) and IRAM $\text{C}^{18}\text{O}(2-1)$ emission from the literature (Carlhoff et al. 2013). Both datasets were smoothed to the same spatial resolution and the $\text{C}^{18}\text{O}(2-1)$ emission to the same spectral resolution as the OH data.

²http://atlasgal.mpifr-bonn.mpg.de/cgi-bin/ATLASGAL_DATABASE.cgi

3.3 Results

3.3.1 Detection statistics

The OH main line transitions at 1665 MHz and 1667 MHz are searched for absorption features at the locations of peaks in the continuum maps at 1666 MHz. Absorption lines which are detected at a signal-to-noise level larger than 4 are classified as detections. In total, significant OH absorption is found against 42 continuum sources (Fig. 3.2).

As OH absorption can occur at multiple velocities due to clouds along the line of sight, in total we find absorption in both main lines in 59 velocity components. Of these, we find 30 and 17 velocity components exclusively in the 1665 MHz and 1667 MHz OH ground state transitions, respectively, and 12 in both lines, matching in velocity. We detect a higher number of OH 1665 MHz transitions, because the 1667 MHz transition was observed only around W43, during the pilot study, and during the second part of the THOR survey (see section 3.2). Conversely, we sometimes find OH features in the 1667 MHz transition that have no counterparts in the 1665 MHz transition. This is expected, as the statistical weight of this transition is roughly twice as large, hence at a given sensitivity, optical depths and column densities twice as low can be probed. Examples of these are absorption at 7.0, 51.0 and 67.5 km s⁻¹ towards G29.935–0.053 (Fig. 3.1).

The continuum sources with detections are listed in Table 3.1. The spectra of the detected absorption lines are displayed in Figs. B.4 - B.10.

3.3.1.1 Sensitivity of the survey

The weakest continuum source with OH absorption has a continuum flux density of 0.1 Jy beam⁻¹. As shown in Fig. 3.3, stronger continuum sources are more sensitive to lower OH column densities. Therefore, the fraction of continuum sources that exhibit OH absorption is dependent on the continuum source strength (which sets the 4 σ detection threshold, τ_{\min}): There are 291 continuum sources above a flux density of 0.1 Jy beam⁻¹ at 20'' \times 20'' ($\tau_{\min} \sim 0.5$), of which 42 show OH absorption lines (14.4%). Above 1.0 Jy beam⁻¹ ($\tau_{\min} \sim 0.04$), 13 of 29 LOS have OH absorption lines (44.8%), while above 2.0 Jy beam⁻¹ ($\tau_{\min} \sim 0.02$), 3 out of 4 LOS (75.0%; this value should be taken with caution due to small number statistics). The cumulative detection fraction therefore is an increasing function of the continuum strength.

The reason for this increase is the dependence of the sensitivity of the optical depth (τ) on the strength of the continuum source:

$$\tau = -\ln\left(\frac{F_{\text{line}}}{F_{\text{cont}}} + 1\right), \quad (3.1)$$

where F_{line} is the continuum subtracted OH absorption spectrum and F_{cont} the continuum emission. Contributions from OH emission to the observed signal are neglected, assuming the distribution of OH is smooth enough for emission to be filtered out by the interferometric observations and due to the small OH excitation temperatures in comparison to the continuum emission (see sect. 3.3.2.1 for a more detailed discussion). While the OH tran-

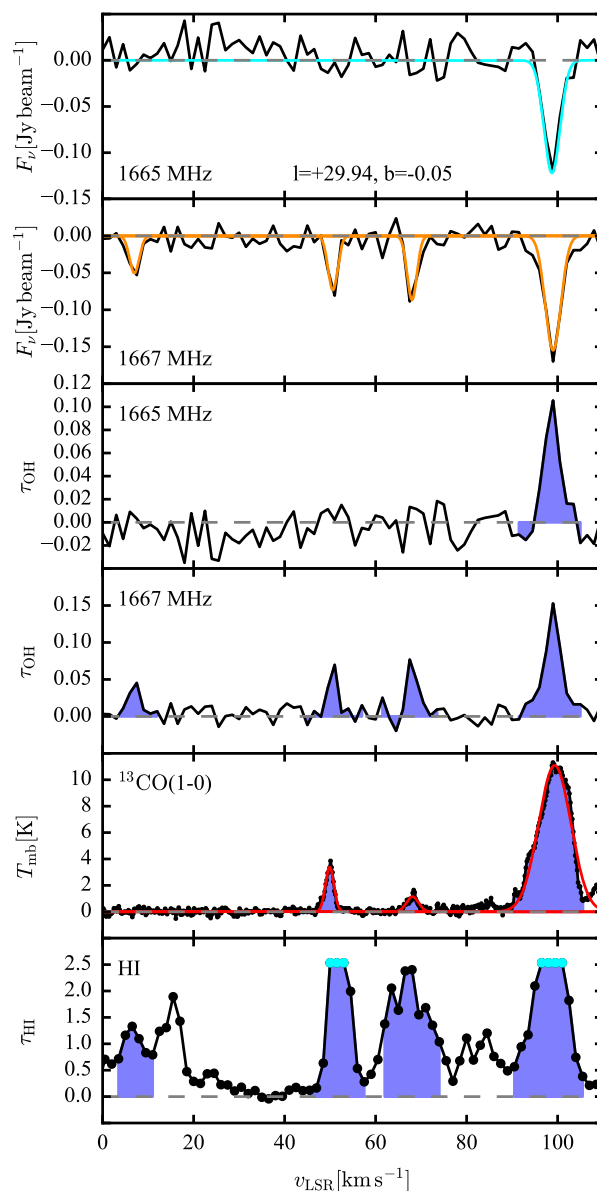


Figure 3.1: Example spectra and optical depths at $l=+29.935^\circ$, $b=-0.053^\circ$ (at $46''$ resolution). The topmost two panels show 1665 MHz and 1667 MHz absorption features. The fitted Gaussian profiles for the 1665 MHz line (cyan) and 1667 MHz line (orange) are overlaid. The two middle panels show the optical depth of the 1665 MHz and 1667 MHz transitions. The second panel from the bottom shows emission of $^{13}\text{CO}(1-0)$ in main-beam temperature (T_{mb}), overlaid with a fitted Gaussian profile (red). The lowermost panel shows H I optical depth as measured from the absorption spectra. Lower limits (cyan dots) are given for saturated bins. The blue shaded area in the lower four panels denotes the area of the transitions, from which the column densities are determined.

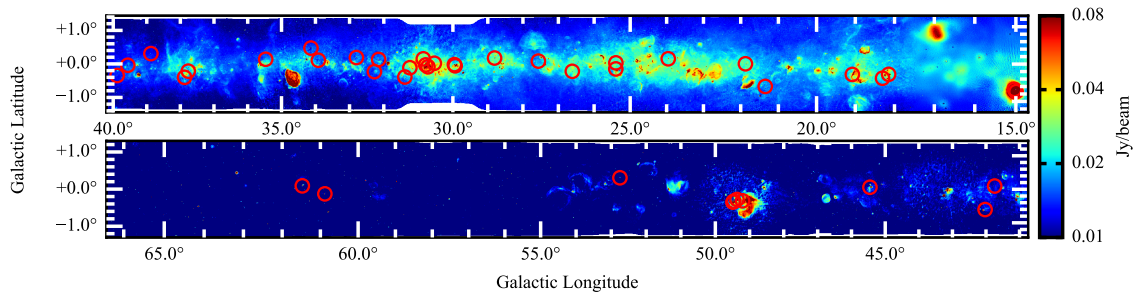


Figure 3.2: Detections of OH absorption at 1665 and 1667 MHz (red circles) overlotted on continuum emission at 1.4 GHz from the combined THOR and VGPS data (Beuther et al. 2016, Wang et al., in press).

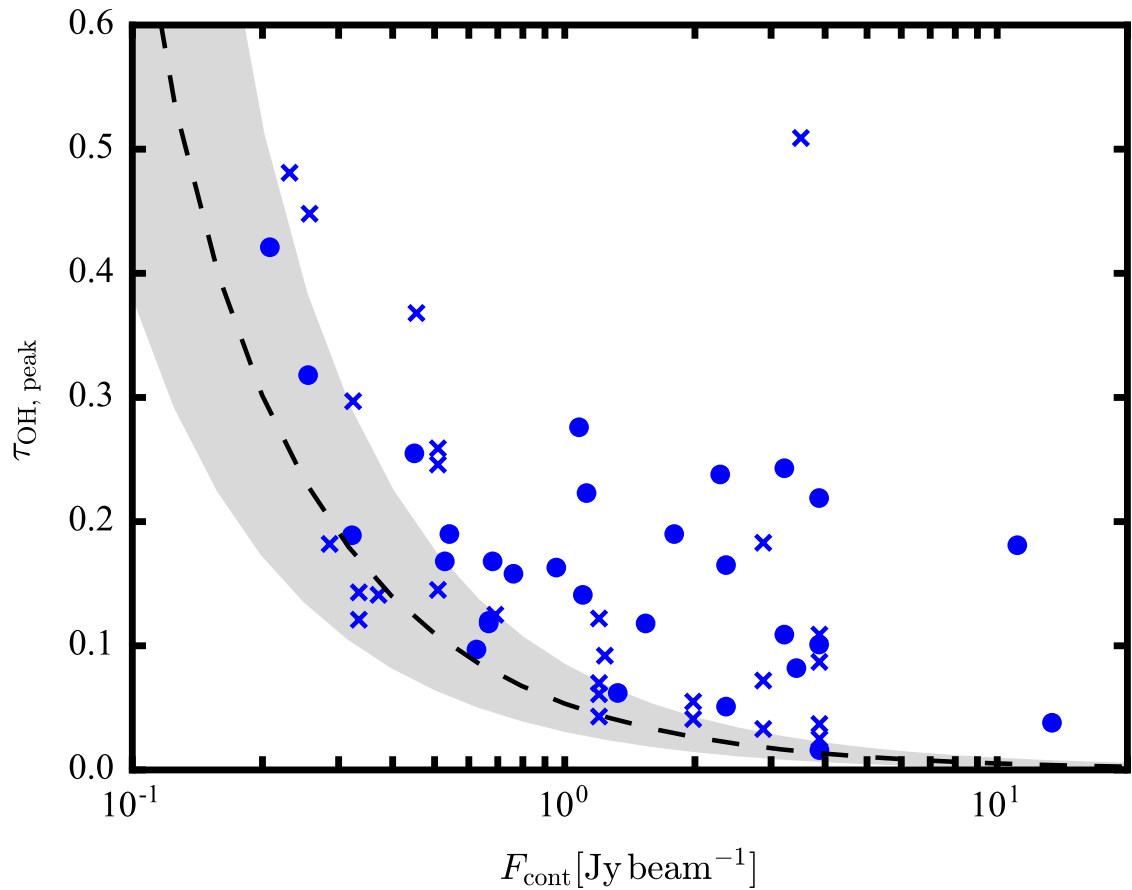


Figure 3.3: Peak optical depth of the 1665-MHz transition (circles) and the 1667-MHz transition (crosses) versus continuum flux density at $46''$. The sensitivity in OH optical depth is indicated by an average $4\text{-}\sigma$ detection limit (black dashed curve). Variations in the detection limit among sightlines are indicated by the gray shaded area.

sitions are mapped at rather uniform noise, the noise in OH optical depth, and therefore its sensitivity, is inversely proportional to continuum flux.

The OH ground state main lines show maser emission against many of the strong continuum sources. Non-detection of absorption lines is therefore not indicative of absence of OH in these lines of sight, but points to OH having different excitation conditions. Such regions typically have high dust temperatures and local densities ($T_{\text{dust}} > 80$ K, $n_{\text{H}_2} > 10^5 \text{ cm}^{-3}$; e.g., [Cesaroni & Walmsley 1991](#), [Guibert et al. 1978](#), [Csengeri et al. 2012](#), [Elitzur 1992](#), and references therein).

Artifacts also influence some of the spectra. This can be due to increased noise caused by residual radio frequency interference (RFI), which should be minor, as the data have been closely inspected for RFI prior to imaging. Also, strong line emission of non-thermal origin can leave various traces. At the position of a maser, adjacent channels are affected by Gibbs ringing, which is a recurring pattern in velocity of emission and absorption. If the maser emission is strong, channel maps around the peak velocity of the emission can be affected by increased noise levels and sidelobes. In the case of W51 Main (e.g., [Ginsburg et al. 2012](#); G49.488–0.380 in this work), for example, it is difficult to discern negative sidelobes from true absorption. Absorption is present in this region as it is different from the shape of the interferometry pattern. Both, however, overlap and therefore a quantitative analysis of the affected velocity channels is not possible.

3.3.1.2 H II region associations

In order to classify the continuum sources, we compare their location and the velocity of the detections to the emission from Radio Recombination Lines (RRLs) as reported in the WISE³ catalog of H II-regions ([Anderson et al. 2014](#)). The spatial selection criterium is overlap with the H II-regions using their angular sizes as reported in the WISE catalog. Since typical velocity differences between H II regions and associated molecular gas are lower than 10 km s^{-1} ([Anderson et al. 2009, 2014](#)), we use this as criterium for association in velocity.

For completeness, we also search the RRL observations in THOR ([Beuther et al. 2016](#)) and catalogs of dense molecular gas tracers associated with compact and ultracompact H II regions (e.g., NH_3 , HCO^+ ; ATLASGAL survey; [Urquhart et al. 2013](#); [Contreras et al. 2013](#); [Urquhart et al. 2014](#)). While not adding new sources, counterparts of many OH detections could be found also in these datasets.

To confirm the presence H II-regions, we obtain information on the spatial extent and the spectral index of the continuum sources from the THOR continuum source catalog ([Bühr et al. 2016](#); Wang et al. in prep.). As H II regions would be located in our Galaxy, they are likely to be spatially resolved within THOR. The spectral index between 1 and 2 GHz helps to distinguish between thermal (with a spectral index of $\alpha \gtrsim -0.1$) and non-thermal emission sources (with a spectral index of $\alpha \sim -1$). Most of the continuum sources with RRL counterparts show thermal emission and are spatially resolved.

In total, 47 OH absorption components have its origin in molecular gas that is associ-

³<http://astro.phys.wvu.edu/wise/>

ated with H II regions in position and velocity, which represent 80% of all detections (see discussion in Sect. 3.4.1). We find that 38 out of 42 of the cm-continuum sources, against which the detections occur, show evidence of being H II regions. Three of the four other continuum sources are likely to be of extragalactic origin, as they are spatially unresolved and show non-thermal emission.

Twelve velocity components in the 1665 MHz and 1667 MHz transitions, of which 4 are detected in both, originate from clouds that are not associated with H II regions. Neither RRL emission in the WISE catalog, nor dense molecular gas tracers are reported at the same v_{LSR} . The peak optical depth is lower than seen for sources associated with H II regions. Accordingly, these absorption features are likely to originate from foreground, potentially diffuse clouds.

3.3.1.3 Distribution of sources in the Galactic plane

The distribution of OH absorption detections is strongly concentrated towards the Galactic midplane (Figs. 3.4 and 3.5), while relatively few detections are made at $|b| > 0.5^\circ$. This follows the distribution of resolved Galactic continuum sources as a function of Galactic latitude (e.g., Bihl et al. 2016). Figure 3.5 is slightly skewed towards negative Galactic latitudes. This may be due to the sun being located above the true galactic plane, while the sun is located at $b=0.0^\circ$ in the Galactic coordinate system (Blaauw et al. 1960; Ragan et al. 2014). Depending on the distance of the object and the assumptions used to determine the physical location of the galactic plane, sources which lie, e.g., in the Scutum–Centaurus Arm have galactic latitudes of $b = [-0.4^\circ, -0.1^\circ]$ (see discussion in, e.g., Goodman et al. 2014), which agrees well with the observed extent of the source distribution towards lower Galactic latitudes.

The histogram of sources versus Galactic longitude (Fig. 3.4) reflects the Galactic structure, with a peak in the number of OH absorption sources at longitudes $l = 30^\circ$ and 50° , which are the tangential points of the Scutum and Sagittarius spiral arms, respectively (e.g., Reid et al. 2014). This confirms that most of the continuum background sources, against which OH absorption is seen, are of Galactic origin, as already indicated by the large number of H II regions in our sample.

3.3.2 OH abundance

3.3.2.1 Line integrals

The OH column density is derived from the integrated optical depth in the main line transitions under the assumption that all molecules are in the four sublevels of the ground state arising from the Λ doubling and hyperfine structure (e.g., Elitzur 1992). The derived column densities are listed in Table 3.3.

Optical depths are computed from the line-to-continuum ratio. Contributions from large-scale emission are assumed to be filtered out by the interferometer. The emission term in the radiative transfer equation which includes the excitation temperature is therefore negligible ($T_{\text{line}} = (T_{\text{ex}} - T_{\text{cont}})(1 - e^{-\tau})$; where T_{line} and T_{cont} can be derived in Raleigh-

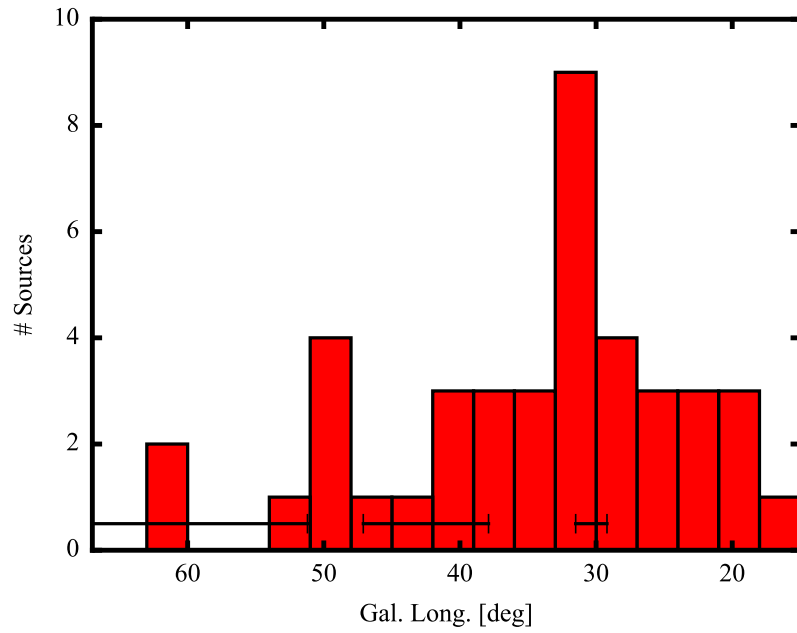


Figure 3.4: Number of continuum sources with OH absorption detections versus Galactic longitude. The 1665 MHz transition was observed over the entire region of the survey. The coverage of the 1667 MHz transition is indicated by the black bars.

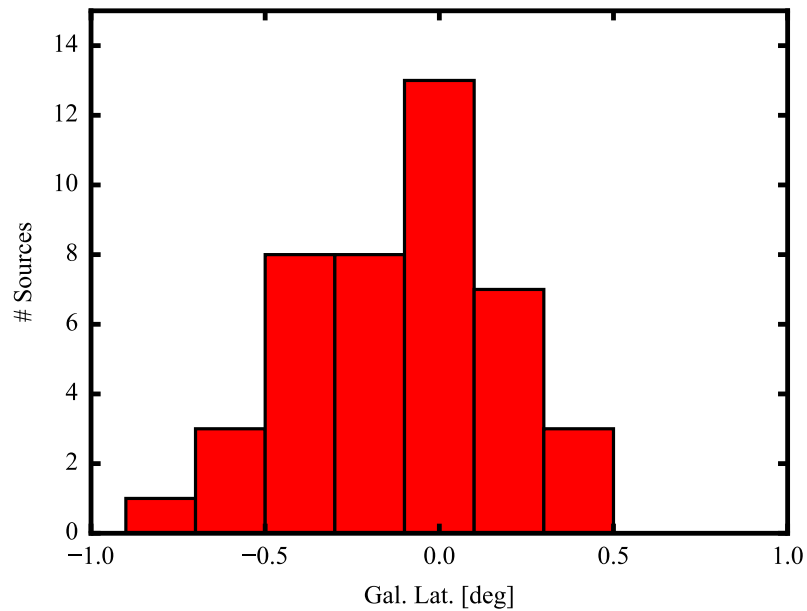


Figure 3.5: Number of continuum sources with OH absorption detections versus Galactic latitude.

Jeans approximation from the continuum-subtracted line flux and the continuum flux, F_{line} and F_{cont}). Even if this assumption did not hold true, at excitation temperatures of about $T_{\text{ex}} = 5 - 10$ K, the approximation $T_{\text{cont}} \gg T_{\text{ex}}$ underestimates the optical depth for a $5\text{-}\sigma$ detection by less than $\ll 10\%$ at $20''$ resolution and for sources with $F_{\text{cont}} > 0.5 \text{ Jy beam}^{-1}$ at $46''$ resolution. For weaker sources which show detectable extended continuum emission, the underestimation would be between 6-16% after smoothing to $46''$.

The integrated optical depth is determined by summation over all spectral bins of the absorption feature. The $^{13}\text{CO}(1-0)$ emission is integrated over the same velocity range. If a corresponding $^{13}\text{CO}(1-0)$ feature exists that is broader than the OH feature, the velocity range is chosen to enclose the $^{13}\text{CO}(1-0)$ feature (see Fig. 3.1). For lines that have no $^{13}\text{CO}(1-0)$ detection counterpart, $3\text{-}\sigma$ upper limits are given for integrated emission and all derived quantities, under the assumption of an average line width of 4.0 km s^{-1} of the detected ^{13}CO emission (Table 3.3).

Similarly, we derive the optical depth of HI from the line-to-continuum ratio, and give lower limits in the case of saturated absorption. A saturated channel is defined here as observed flux that is within $3\text{-}\sigma$ of the zero level. This value is then used to calculate the lower limit (see cyan circles in the lowermost panel of Fig. 3.1). Analogously to the discussion above on τ_{OH} , emission in principle also affects the HI optical depth, but is likely to be filtered out here. For this reason, we do not attempt to correct for it, but note that the integrated optical depth here always represents a lower limit.

3.3.2.2 OH column density

The OH column density is inferred for each main line separately, under the assumption that all OH molecules are in the ground state, $^2\Pi_{3/2}(J = 3/2)$. The OH column density is given by (e.g., Stanimirović et al. 2003)

$$\frac{N_{\text{OH}}}{T_{\text{ex}}} = \frac{C_0}{f} \int \tau dv, \quad (3.2)$$

where N_{OH} is the total OH column density in cm^{-2} , T_{ex} the excitation temperature in Kelvin, $C_0 = 4.0 \times 10^{14} \text{ cm}^{-2} \text{ K}^{-1} \text{ km}^{-1} \text{ s}$ for the 1665 MHz transition and $C_0 = 2.24 \times 10^{14} \text{ cm}^{-2} \text{ K}^{-1} \text{ km}^{-1} \text{ s}$ for the 1667 MHz transition (e.g., Goss 1968; Turner & Heiles 1971; Stanimirović et al. 2003, calculated using Einstein coefficients from Turner 1966). The filling factor f describes the solid angle fraction of the continuum source that is covered by the OH cloud. We assume that $f = 1$. The 1667 MHz transition is expected to be detected at higher signal-to-noise than the 1665 MHz transition because of its larger statistical weight, and therefore the 1667 MHz transition is used for further analysis whenever available. The calculated $\frac{N_{\text{OH}}}{T_{\text{ex}}}$ ratios are given in Table 3.3.

The excitation temperatures of the OH transitions cannot be derived independently from their optical depth, as local thermal equilibrium between the levels of the two main lines is not necessarily given, and thus the excitation temperatures of both main lines may be different (e.g., Crutcher 1979; Dawson et al. 2014). A determination of both T_{ex} and τ is in principle possible if additional emission observations were obtained at a posi-

tion slightly offset from the continuum source. The OH emission is not detectable in the present dataset, as the OH emission is expected to be dominated by warm gas (e.g., [Wanier et al. 1993](#)) that varies on scales larger than the interferometric observations presented here. Hence, emission is filtered out. Observations of transitions to higher rotational levels of OH are not available for most sources and would require detailed modelling to constrain the excitation conditions of the hyperfine transitions in the ground state, which is beyond the scope of this chapter. We therefore assume an excitation temperature from the literature in order to determine OH column densities (e.g., [Stanimirović et al. 2003](#)).

The excitation temperatures of the OH main lines have been found to differ relative to each other by 0.5 – 2.0 K (e.g., [Goss 1968](#); [Crutcher 1979](#); [Dawson et al. 2014](#)). This has also been seen in models (e.g., [Guibert et al. 1978](#)). The level populations may also be affected by radiative pumping ([Csengeri et al. 2012](#); [Wiesemeyer et al. 2016](#)). Previous investigations reported excitation temperatures for the OH main line transitions between 3 and 10 K (e.g., [Goss 1968](#); [Turner 1973](#); [Crutcher 1977](#); [Colgan et al. 1989](#); [Li & Goldsmith 2003](#); [Bourke et al. 2001](#); [Yusef-Zadeh et al. 2003](#)). We therefore assume a uniform excitation temperature of $T_{\text{ex}}(1665) = 5$ K for the 1665 MHz transition, which in principle can be higher by up to about a factor of two for OH gas associated with H II regions. We consider this in the systematic uncertainties (see Sect. 3.3.2.5). For transitions in which both main lines are detected, the medians of the column density distributions of each main line are offset. A better agreement between the samples is reached for a slightly higher excitation temperature for the 1667 MHz line of $T_{\text{ex}}(1667) = 6.7$ K. We therefore adopt this value for the OH 1667 MHz transition in the following, while using $T_{\text{ex}}(1665) = 5$ K in the OH 1665 MHz transition.

3.3.2.3 H₂ column density

As proxy for H₂, we use ¹³CO emission. Kinematically, ¹³CO is related to the OH gas. The line widths of the OH main lines and ¹³CO are compared in Fig. 3.6. The channel spacing of 1.5 km s⁻¹ in the OH observations poses a limit of 2.5 km s⁻¹ on the narrowest resolved line width for OH lines, while the full spectral resolution of 0.21 km s⁻¹ is used for ¹³CO to disentangle different velocity components. Excluding the unresolved OH lines, the line widths of both tracers are found to be correlated⁴. In some cases, the ¹³CO emission features larger line widths than OH. One possible explanation is that larger parts of the molecular cloud contribute to the ¹³CO antenna temperature than to the OH absorption. For many continuum sources, only OH absorption from scales less than 46'' is recovered. As emission from within the entire beam contributes to the ¹³CO antenna temperature, the ¹³CO emission may average over larger parts of the cloud. Similarly, if the continuum source is located within the molecular cloud, ¹³CO emission contains information from all cloud depths (if not optically thick), while only parts of the cloud between the continuum source and the observer affect the OH absorption (see also sect. 3.3.2.5). Depending on the velocity substructure of the cloud on scales smaller than the beam and along the line

⁴This sample of 15 datapoints is described by a Pearson's correlation coefficient $\rho = 0.8$ at a statistical significance of $\approx 3\sigma$.

of sight, this can lead in both cases to larger line widths in the ^{13}CO emission than in the OH absorption.

The column density of ^{13}CO is determined from the integrated line profile ($\int T_{\text{mb}} dv$) under the assumption that the gas is optically thin (e.g., [Wilson et al. 2009](#), eq. 15.37):

$$N(^{13}\text{CO}) \approx 3.0 \times 10^{14} \frac{\int \frac{T_{\text{mb}}}{\text{K}} dv}{1 - \exp(-5.3/T_{\text{ex}})} \text{cm}^{-2}. \quad (3.3)$$

Average excitation temperatures of ^{13}CO in molecular clouds are typically between 10–15 K, with values of up to 25 K in some cases (e.g., [Pineda et al. 2010](#); [Nishimura et al. 2015](#); [Frerking et al. 1982](#); [Anderson et al. 2009](#)). We select an excitation temperature towards the upper end of this range of $T_{\text{ex}} = 20$ K, as most of the OH detections are associated with H II regions. To account for possibly lower excitation temperatures, we assume an uncertainty of a factor of two on T_{ex} , which results in an uncertainty of approximately a factor of two for $N_{^{13}\text{CO}}$.

The column density of molecular gas is determined by assuming a constant ^{13}CO abundance relative to molecular hydrogen molecules of $N_{\text{H}_2}/N_{^{13}\text{CO}} = 3.8 \times 10^5$ ([Bolatto et al. 2013](#); [Pineda et al. 2008](#)). Uncertainties in this estimate due to optical thickness of ^{13}CO or local variations in the $^{13}\text{CO}/^{12}\text{CO}$ ratio ([Szűcs et al. 2016](#)) are discussed in Sect. 3.3.2.5. If the $^{13}\text{CO}(1-0)$ emission is not detected, we report upper limits for both N_{H_2} and N_{H} and lower limits on X_{OH} .

3.3.2.4 H I column density

To derive the H I column density, we assume a spin temperature ($= T_{\text{ex}}$) of $T_{\text{spin}} \sim 100$ K ([Bihl et al. 2015](#)). The H I column density is given by (e.g., [Wilson et al. 2009](#))

$$N_{\text{H I}} = 1.8224 \times 10^{18} \frac{T_{\text{spin}}}{\text{K}} \int \tau(v) \left(\frac{dv}{\text{km s}^{-1}} \right) \text{cm}^{-2}. \quad (3.4)$$

Since the optical depth is a lower limit here (see sect. 3.3.2.1), the H I column density is a lower limit as well. As T_{spin} may vary for individual regions by a factor of two, these limits are subject to a systematic uncertainty of the same factor.

In the following, we determine the OH abundance, X_{OH} , both in terms of the column density of molecular hydrogen, N_{H_2} , and in terms of the total column density of hydrogen nuclei, which includes both atomic and molecular hydrogen, $N_{\text{H I}}$ and N_{H_2} . N_{H} is given by $N_{\text{H}} = N_{\text{H I}} + 2N_{\text{H}_2}$. The lower limits on $N_{\text{H I}}$ yield upper limits on X_{OH} . The derived quantities from this section are listed in Table 3.3.

3.3.2.5 Systematic uncertainties

The systematic uncertainties of X_{OH} , N_{H_2} and N_{H} are estimated as follows. The $N_{\text{H}_2}/N_{^{13}\text{CO}}$ ratio varies within molecular clouds and may be affected by global changes in the ^{13}C isotope abundance with Galactocentric radius. First, the scatter of $N_{\text{H}_2}/N_{^{13}\text{CO}}$ measurements has been found to be up to a factor of two within individual clouds (e.g., in Perseus;

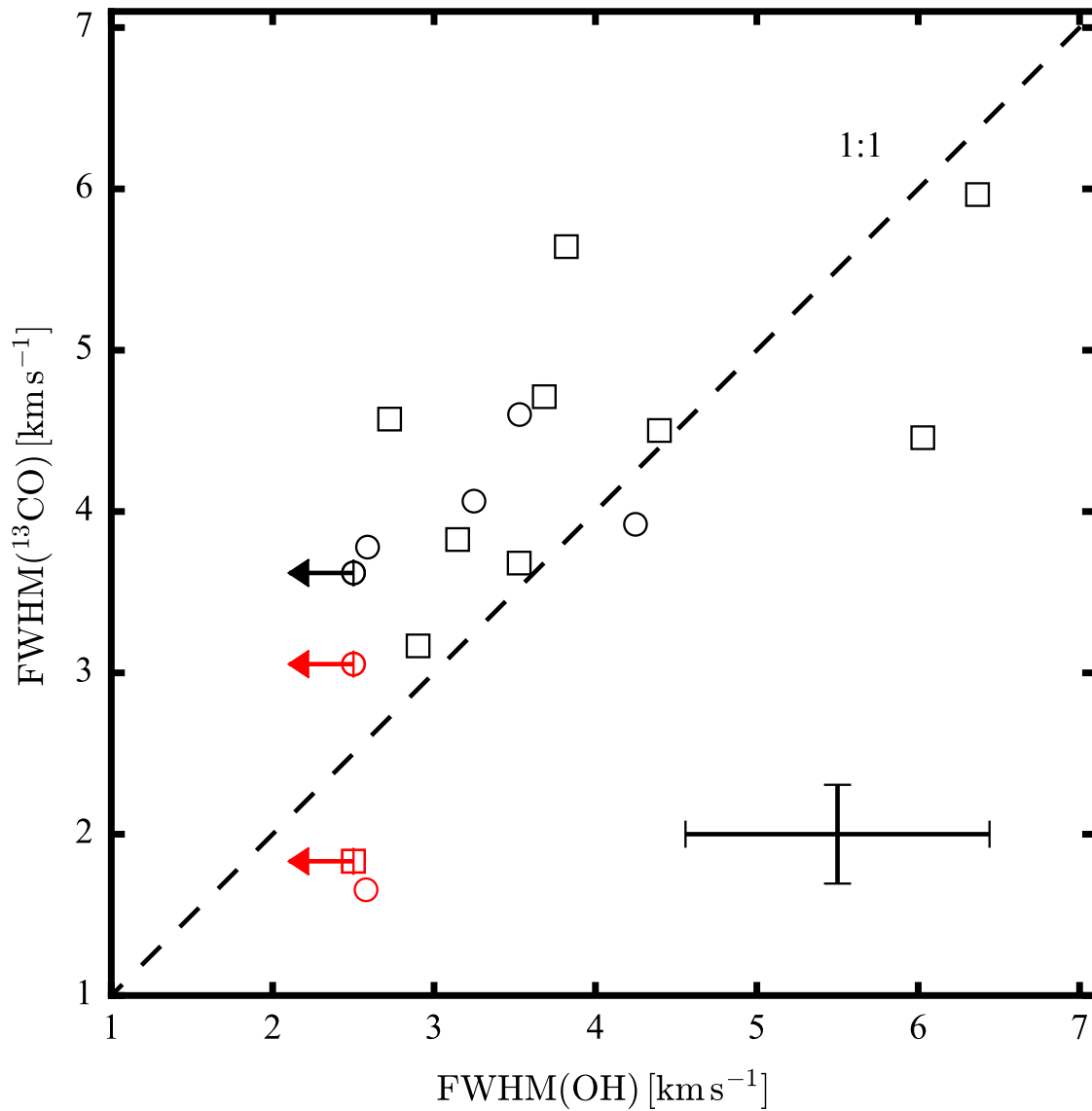


Figure 3.6: Comparison of FWHM of OH and ¹³CO(1-0) lines. OH line widths of the 1665 MHz transition (squares) are used whenever the 1667 MHz transition (circles) was not available. Detections associated with H II regions are drawn in black, others in red. Arrows indicate spectrally unresolved lines. The dashed line indicates a 1:1 correlation. The bars in the lower right-hand corner of the figure indicate typical errors in both quantities.

Pineda et al. 2008). We assume that this inflicts an uncertainty of a factor of two on N_{H_2} . Second, the conversion used here has been determined in nearby Gould Belt clouds, but the $^{12}\text{C}/^{13}\text{C}$ isotope ratio increases with Galactocentric radius (Milam et al. 2005). With absorption sources located at Galactocentric radii between $R_{\text{gc}} = 3 - 10$ kpc, we assume that global variations in the ^{13}C isotope abundance introduce an additional uncertainty of a factor of two on N_{H_2} .

As described above, the assumptions regarding the excitation temperatures of OH, $^{13}\text{CO}(1-0)$ and H I are likely to be valid within a factor of two as well. These result in a combined uncertainty of approximately a factor of 3.5 in N_{H_2} and N_{H} , and a factor of four in X_{OH} . As the H I absorption saturates in most cases, we can only determine lower limits to $N_{\text{H I}}$.

Also, some of the $^{13}\text{CO}(1 - 0)$ emission may be optically thick and give lower limits on N_{H_2} , and therefore upper limits on X_{OH} . While N_{H_2} as derived from ^{13}CO may also be underestimated due to chemical effects (e.g., Szűcs et al. 2016), the derived H_2 column densities have been compared with column densities derived from $870\mu\text{m}$ dust emission (ATLASGAL), and we find reasonable agreement also towards high column densities within a factor of two.

At low CO column densities, molecular cloud regions may be traced that contain a significant fraction of “CO-dark” H_2 . This means that the column density of H_2 would be underestimated and the OH abundance overestimated. The amount of “CO-dark” gas depends on the environment, i.e., on metallicity and the strength of the external radiation field. This makes a quantitative correction difficult, but the effect may influence detections for which H_2 and H I column densities are comparable.

Geometrical uncertainties should also be considered. For the sake of simplicity, they are mentioned here only briefly, because they are difficult to quantify. First, the ^{13}CO emission may trace molecular gas that is not accessible by the OH absorption observations. OH absorption occurs in material between the observer and a continuum source, while material at any distance along the sightline contributes to the ^{13}CO emission if optically thin. Most of the OH absorption detections are associated in velocity with the continuum source itself and by our definition separated from the continuum source by less than 10 km s^{-1} . Assuming that the OH and ^{13}CO gas, as well as the H II-region are part of the same molecular cloud, a fraction of the ^{13}CO emission emerges from behind the continuum source as seen by the observer. This fraction depends on the structure of the molecular cloud and the relative position of the continuum source. For example, 50% of the ^{13}CO emission will come from behind the H II region, if it is embedded in the middle of a spherically symmetric molecular cloud. No OH absorption can be measured for this part of the cloud, and the OH abundance will be underestimated. Velocity shifts between the different tracers in our data ($<2\text{ km s}^{-1}$) indicate that at least some sources are affected by this. As we cannot constrain the structure of the cloud and quantify this effect, we choose not to correct for it here.

Second, crowded regions may contain multiple, overlapping H II-regions, which contribute to the observed continuum flux, if the continuum emission is optically thin. If OH absorption occurs along the line of sight in between such continuum sources, the observed continuum will overestimate the true continuum incident on the absorbing cloud. There-

fore, the optical depth of OH would be underestimated. This is likely to affect lines of sight towards galactic continuum sources that are located in crowded regions, such as the tangent points of spiral arms (G29, W43 and W51).

3.3.2.6 OH vs. H₂ column density

OH and H₂ column densities are shown in Fig. 3.7. N_{OH} is derived from the 1667 MHz transition (circles) if available, and from the 1665 MHz transitions in the rest of the cases (squares). The absorption features are separated by color into regions that are associated (black) or not associated (red) with H II regions.

To investigate the correlation between N_{OH} and N_{H_2} , we perform a linear regression in log-space, $\log(N_{\text{OH}}) = m \times \log(N_{\text{H}_2}) + t$, to determine the slope m . The uncertainties are dominated by the systematic errors, i.e. possible variations of N_{OH} and N_{H_2} by a factor of 2 and 3.5, respectively (see Sect. 3.3.2.5). To properly take into account their impact on the correlation, we estimate the distribution of slopes m given these uncertainties and the stochastic measurement errors. We do not include upper limits. We sample the *posterior* distribution of m by performing linear regressions on multiple, artificial representations of the data, which are inferred from the uncertainty distributions of the measurements.

We create a large number of artificial datasets ($n_{\text{datasets}} = 10^5$). Each artificial dataset has the same number of points as our measured sample, but instead of containing the measurements itself, each point is replaced by randomly drawing an artificial datapoint from the uncertainty distribution. We also “bootstrap” each of these simulated datasets, i.e. randomly assigning weights to the points to reduce the importance of each individual measurement. From the linear regression on each of these artificial datasets, we obtain a distribution of slopes with median and 16%-, 84%-percentiles of $m = 0.33^{+0.14}_{-0.13}$ (see also Fig. B.1). The green line in Fig. 3.7 shows the median slope.

We interpret this result as an indication of a weak, sublinear correlation between N_{OH} and N_{H_2} . A direct proportionality between the two parameters is unlikely, given the distribution of slopes. The sublinear relation between N_{OH} and N_{H_2} yields a decreasing OH abundance ($X_{\text{OH}} = N_{\text{OH}}/N_{\text{H}_2}$), as discussed in the following sections. The analysis shows that a correlation is present in the data, but for tighter constraints, follow-up studies are needed to provide more data and/or to decrease the systematic uncertainties.

3.3.2.7 OH abundance at different hydrogen column densities

Fig. 3.8 shows the OH abundance in terms of the molecular hydrogen column density ($X_{\text{OH}} = N_{\text{OH}}/N_{\text{H}_2}$) versus N_{H_2} . The literature value for $X_{\text{OH}} = N_{\text{OH}}/N_{\text{H}_2} \approx 1 \times 10^{-7}$ is plotted as a dashed gray line, and the right axis shows the data in terms of this value (e.g., Guelin 1985; Langer & Graedel 1989; van Langevelde et al. 1995; Liszt & Lucas 1999, 2002). The OH abundance is found to be anti-correlated with N_{H_2} over the range of probed cloud depths ($8 \times 10^{20} \text{ cm}^{-2} < N_{\text{H}_2} < 5.8 \times 10^{22} \text{ cm}^{-2}$). Above $N_{\text{H}_2} > 1.9 \times 10^{22} \text{ cm}^{-2}$ ($A_V \sim 20 \text{ mag}$)⁵, most of the abundances are lower than the literature value, while the

⁵Assuming $N_{\text{H}}/(A_V/R_V) = 5.8 \times 10^{21} \text{ cm}^{-2} \text{ mag}^{-1}$ (Bohlin et al. 1978) and the average ISM value for the total-to-selective extinction of $R_V = 3.1$, the total hydrogen column density can be related to visual

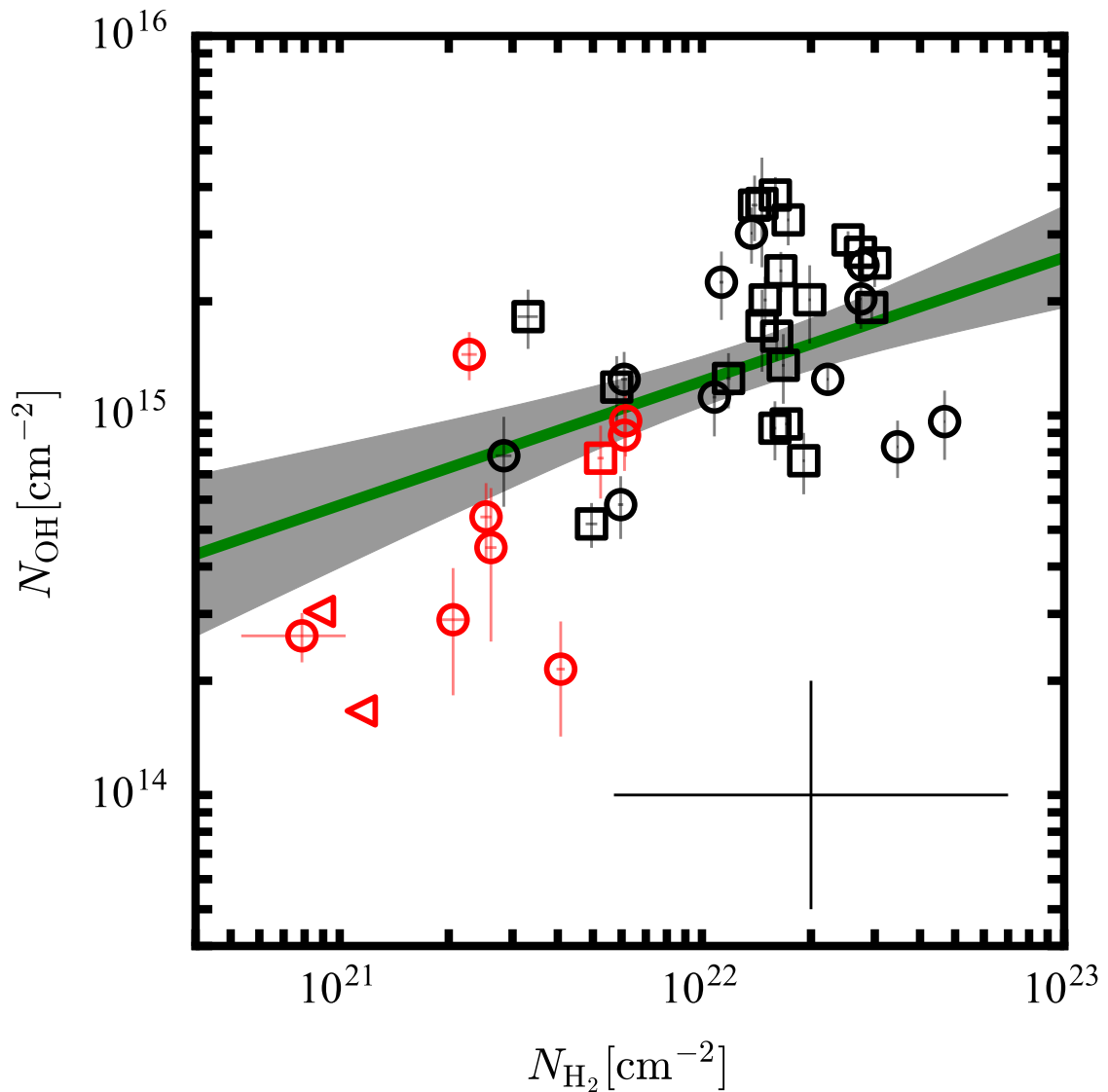


Figure 3.7: Comparison of the OH column density from the 1665 MHz (squares) and 1667 MHz transitions (circles) to that of H_2 as inferred from $^{13}\text{CO}(1-0)$ emission. Column densities from absorption features overlapping in velocity with H II regions (black) and with no such counterpart (red) divide the plot into regions with higher and lower hydrogen column densities. Triangles denote upper limits on N_{H_2} as determined from $^{13}\text{CO}(1-0)$ non-detections. The green line is the result of parameter estimation of a correlation between N_{OH} and N_{H_2} , using errors on x and y axes and not including upper limits. The gray shaded regions shows the 16%- and 84%-percentiles. The black error bars in the lower right corner show the systematic errors.

abundances at lower H_2 column densities are slightly higher.

We use the $H\text{I}$ absorption data as lower limit for the column density of atomic hydrogen, and show the OH abundance with respect to the total number of hydrogen nuclei in Fig. 3.9. While the overall trend is similar to that seen in Fig. 3.8, the atomic hydrogen content probed along the line-of-sight is comparable to molecular hydrogen for a few detected components with low molecular hydrogen column densities (e.g., for G29.935–0.053 at 7.0 km s^{-1} and G29.957–0.018 at 8.0 km s^{-1}).

We see a clear anti-correlation between X_{OH} and N_{H_2} for OH associated with $H\text{II}$ regions (black). Measurements which are not associated (red), follow this trend in Fig. 3.8. In the abundance with respect to all hydrogen nuclei ($N_{\text{OH}}/N_{\text{H}}$) in Fig. 3.9, this trend appears not to be present in the red data points, since the lowest data points have significant contribution from atomic hydrogen. As the $H\text{I}$ column densities are lower limits, the abundances are upper limits, favoring an even shallower trend of X_{OH} in this N_{H} column density regime. As mentioned in Sect. 3.3.2.5, also the fraction of “CO-dark” H_2 may be significant for most of the detections which are not associated with $H\text{II}$ regions and the lowest of the measurements associated with $H\text{II}$ regions, which would place them at higher N_{H_2} (and N_{H}) and lower X_{OH} in Figs. 3.8 and 3.9.

The red data points fall into similar ranges of visual extinction as probed by many earlier studies. The OH abundance for visual extinctions of $A_V < 7\text{ mag}$ has been reported in the literature to be constant at $X_{\text{OH}} = N_{\text{OH}}/N_{\text{H}} = 4 \times 10^{-8}$ (e.g., Goss 1968; Crutcher 1979). The median OH abundance for this group of points here is $X_{\text{OH}}(N_{H_2}) = 1.6 \times 10^{-7}$ with a scatter of $\Delta X_{\text{OH}} = 0.27\text{ dex}$ and $X_{\text{OH}}(N_{\text{H}}) = 6.0 \times 10^{-8}$ and a scatter of $\Delta X_{\text{OH}} = 0.22\text{ dex}$.

3.3.3 Satellite line transitions

Satellite lines of the OH ground state transitions are rarely found in local thermodynamic equilibrium with the main line transitions. While the main lines are seen in absorption, the satellite lines can be anomalously excited and may show conjugate emission and absorption, often at equal strength (e.g., towards G18.303–0.390 and G25.396+0.033; see Fig. B.2). Table 3.4 catalogs conjugate satellite transitions found in this survey. The qualitative satellite line behavior reflects the physical conditions of the gas, such that we can use this to estimate OH column densities for a subsample of sources.

Emission in the 1612 MHz transition with absorption in the 1720 MHz transition is found in 14 instances. Emission in the 1720 MHz transition with absorption in the 1612 MHz transition occurs in three cases (e.g., towards G32.798+0.190 at 90 km s^{-1} ; see Table 3.4).

Satellite line reversal, i.e., the transition from absorption to emission (or vice versa) across the line, is seen along 3 lines of sight. Both satellites mirror each other: At lower velocities, the 1720 MHz line is in emission, while the 1612 MHz line is in absorption. At a certain velocity, the behavior reverses. This is found in the following cases in this work: G19.075–0.288 at 67.5 km s^{-1} , G32.798+0.190 at 14.0 km s^{-1} , G49.369–0.302 at

extinction as $N_{\text{H}} = 1.9 \times 10^{21}\text{ cm}^{-2}\text{ mag}^{-1} \times A_V$. For large column densities ($N_{H_2} \gg 5 \times 10^{21}\text{ cm}^{-2}$) we assume the contribution of atomic hydrogen to be negligible, i.e., $N_{\text{H}} \approx 2 \times N_{H_2}$.

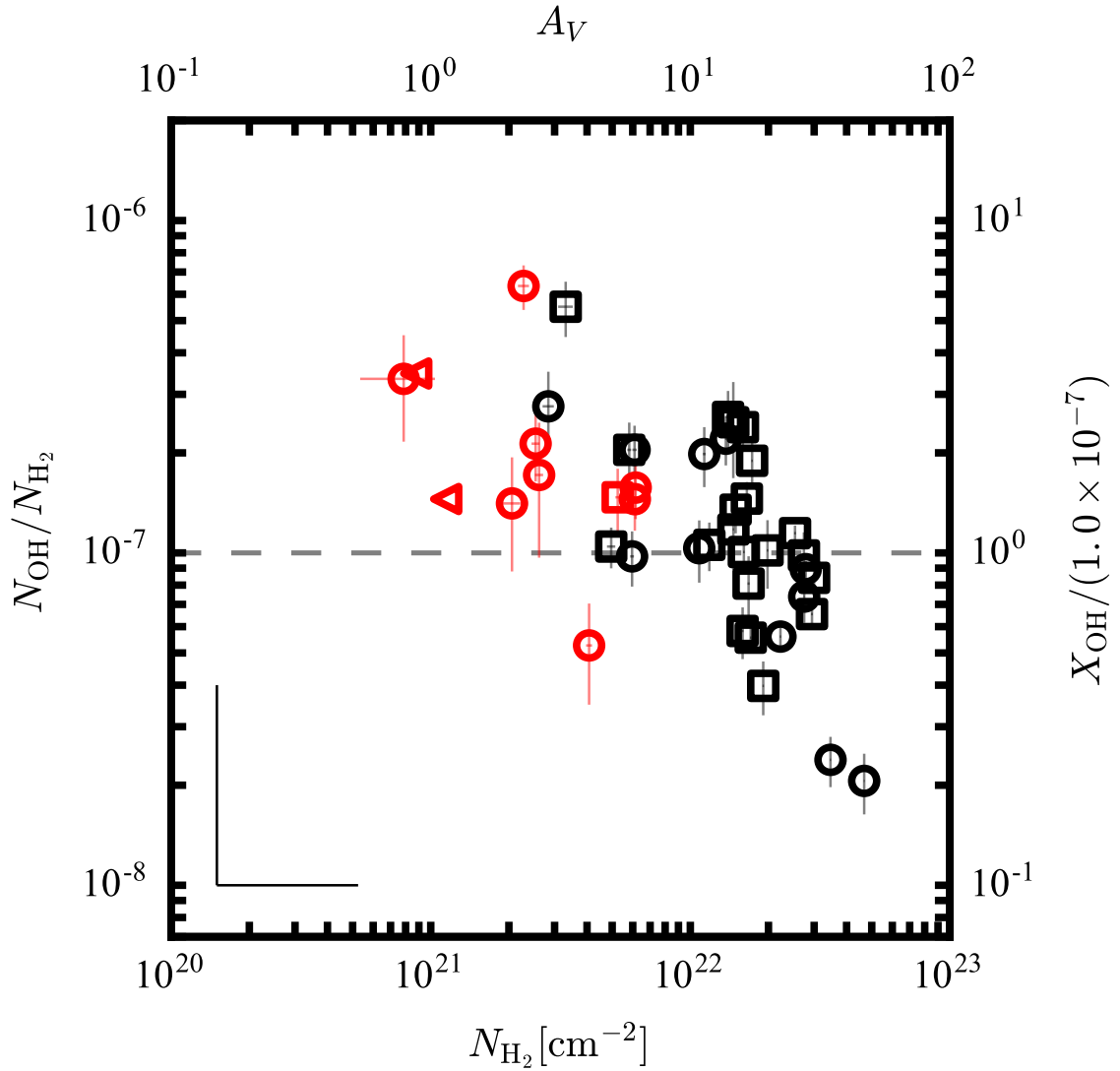


Figure 3.8: OH abundance $X_{\text{OH}} = N_{\text{OH}}/N_{\text{H}_2}$ vs. N_{H_2} . N_{OH} is inferred from 1665 MHz (squares) or 1667 MHz absorption (circles) and N_{H_2} from $^{13}\text{CO}(1-0)$ emission. Absorption features associated with H II regions are shown in black; those not associated are shown in red. Triangles denote upper limits on N_{H_2} (inferred from the non-detection of ^{13}CO). The right axis shows the OH abundance in units of literature (molecular) OH abundance of 1×10^{-7} (e.g., Liszt & Lucas 1999, 2002, indicated also by the dashed gray line). The black error bars in the lower left corner show the systematic errors (only the upper halves of the error bars are shown here).

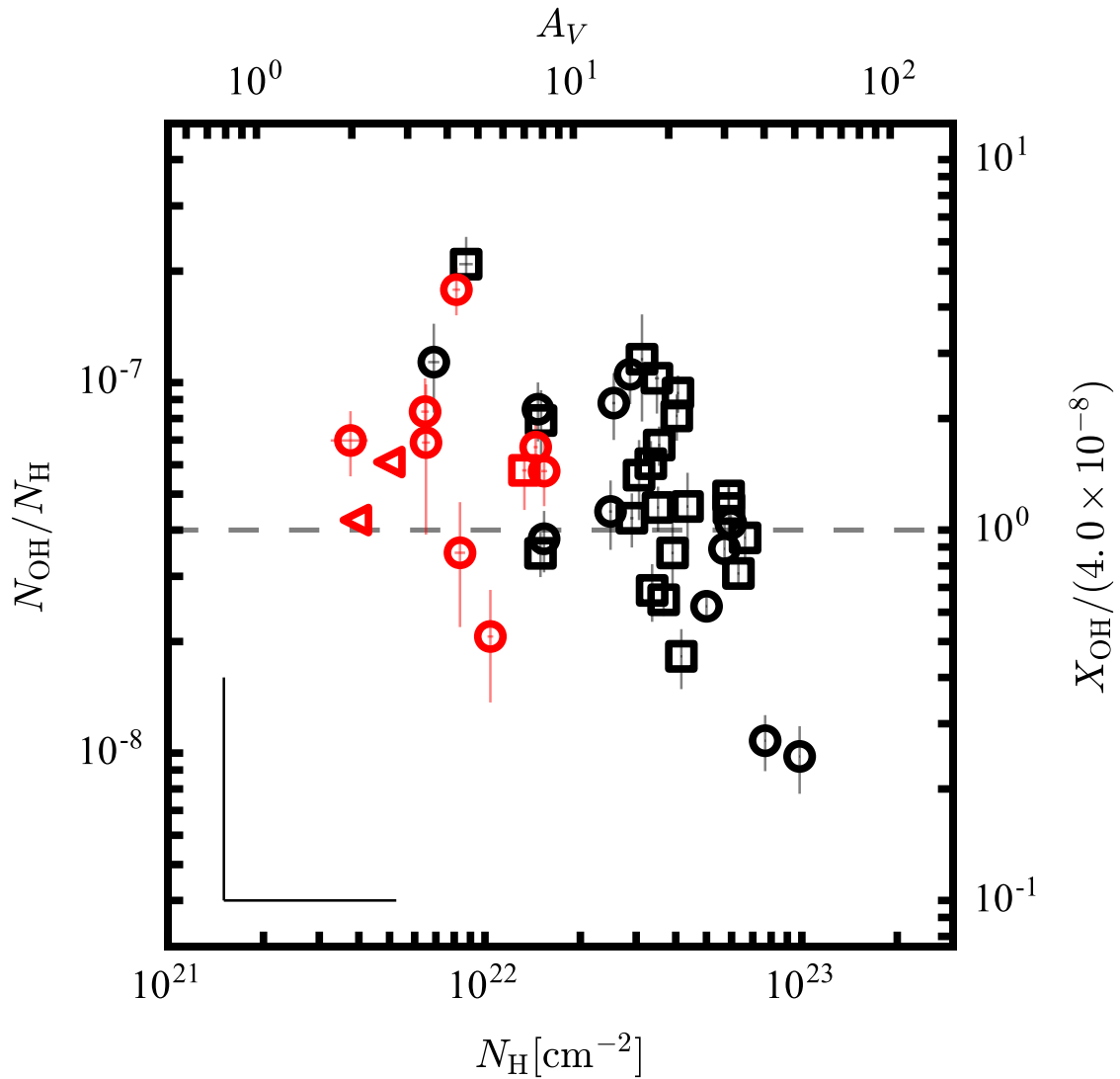


Figure 3.9: OH abundance $X_{\text{OH}} = N_{\text{OH}}/N_{\text{H}}$ vs. N_{H} . The total column density of hydrogen nuclei, N_{H} , is inferred from $^{13}\text{CO}(1-0)$ emission and H I absorption. As the H I column density represents lower limits, the OH abundances represent upper limits. Colors and symbols are as in Fig. 3.8. The right axis shows the OH abundance in units of the typical OH abundance in diffuse clouds of 4×10^{-8} (Crutcher 1979, indicated also by the dashed gray line).

63.5 km s⁻¹. Lines of sight, for which the full reversal profile is not detected in both satellite lines, but which are indicative of this behavior, are: G29.935–0.053 at 98.5 km s⁻¹, for which reversal in the 1612 MHz transition is detected, but the 1720 MHz line is seen only in absorption at higher velocities, and not detected in emission at lower velocities. Towards G37.764–0.215 at 65.0 km s⁻¹, G49.206–0.342 at 63.5 km s⁻¹ and G49.369–0.302 at 49.5 km s⁻¹, 1612 MHz absorption is seen at low velocities without conjugate emission in the 1720 MHz transition, while at higher velocities, the 1720 MHz transition is in absorption without conjugate emission in the 1612 MHz transition.

In the other cases, the satellite lines are not detected or only one transition of the two is detected. Indication of absorption in both lines can be seen in G61.475+0.092 at +21.2 km s⁻¹, with the satellite line strengths differing from each other, as is expected since the lines are typically not in local thermal equilibrium.

The conjugate emission and absorption of the satellite lines has been noted in previous studies (e.g., Goss 1968; Crutcher 1977; van Langevelde et al. 1995; Brooks & Whiteoak 2001; Dawson et al. 2014), and is the result of overpopulation of either the F=1 or the F=2 hyperfine energy levels of the ground state and mutual depletion of the others (e.g., Elitzur 1992, §9.1). As the satellite lines are transitions with $|\Delta F| = 1$, they are affected by the relative population changes, while the main line transitions with $|\Delta F| = 0$ may not be affected by this particular inversion mechanism.

There are different pumping mechanisms that may be responsible for the population inversion (see discussion in, e.g., Frayer et al. 1998). In all cases, transitions from higher rotational levels to the ground state need to become optically thick (e.g., Elitzur 1992; van Langevelde et al. 1995): If the infrared transitions from either the $^2\Pi_{3/2}(J = 5/2)$ or the $^2\Pi_{1/2}(J = 1/2)$ states into the ground state become optically thick, the 1720 MHz or the 1612 MHz transition, respectively, is seen in inversion. If both transitions are optically thick, inversion of the 1612 MHz transition is seen. As the transitions from the $^2\Pi_{3/2}(J = 5/2)$ excited state become optically thick at lower N_{OH} than from the $^2\Pi_{1/2}(J = 1/2)$ state, there exists a typical OH column density at which the transition from 1720 MHz to 1612 MHz inversion takes place. This has been used and modeled by van Langevelde et al. (1995) for a molecular cloud heated by a background H II region and satellite line reversal was found to take place at $\approx 1 \times 10^{15} \text{ cm}^{-2} \text{ km}^{-1} \text{ s}$.

Assuming this geometry also for the sources in this sample, this model provides a possibility to estimate N_{OH} . The column density depends on the velocity dispersion of the gas ($N_{\text{OH}} \approx \Delta v \times 1 \times 10^{15} \text{ cm}^{-2} \text{ km}^{-1} \text{ s}$). As we have no direct measure of the line width at the velocity of the reversal of the inversion we use as approximation the full width of half maximum of the 1665 MHz main. The transition occurs at $N_{\text{OH}} \approx 7.4 \times 10^{15} \text{ cm}^{-2}$ for G19.075–0.288, at $N_{\text{OH}} \approx 1.2 \times 10^{16} \text{ cm}^{-2}$ for G32.798+0.190 and at $N_{\text{OH}} \approx 4.4 \times 10^{15} \text{ cm}^{-2}$ for G49.369–0.302.

We compare the estimates for G32.798+0.190 and G49.369–0.302 to N_{OH} derived from the main lines in Sect. 3.3.2. G19.075–0.288 is omitted here, as the reversal velocity does not match the velocity of the maximum optical depth of the 1665 MHz transition (Fig. B.2). For G32.798+0.190 and G49.369–0.302, N_{OH} determined from the main lines is a factor of 3–4 lower than the estimate from the satellite lines. The line width used for the N_{OH} estimate from the satellite lines could be an overestimate if multiple components

are blended into the feature. Alternatively, the discrepancy could be an indication of higher main line excitation temperatures than the assumed $T_{\text{ex}}(1665) = 5$ K. To match the estimates from the satellite lines, excitation temperatures of $T_{\text{ex}} \approx 15 - 20$ K would be required.

A similar discrepancy has been noted in [Xu et al. \(2016\)](#), who find lower OH column densities than needed to reproduce the observed emission in the 1612 MHz transition. They attribute this to other excitation mechanisms, such as collisional excitation in shocks (e.g., [Pihlström et al. 2008](#)), which are also not taken into account in the model by [van Langevelde et al. \(1995\)](#).

Recently, employing non-LTE modeling of all four 18 cm OH emission lines, [Ebisawa et al. \(2015\)](#) have used the relative intensities of main-line and 1720 MHz emission and 1612 MHz absorption in the Heiles Cloud 2 and ρ Oph to derive kinetic temperatures that are significantly higher in translucent than in dark molecular regions. This indicates that OH appears to be able to probe the interface between molecular and warmer atomic material. Such an analysis is beyond the scope of the present chapter, but can be included in a future study.

3.3.4 Extended OH absorption: the example of W43

Spatially resolved OH absorption is seen against a subsample of the continuum sources (examples of these are the Galactic H II regions M17, G18.148–0.283, G37.764–0.215, G45.454+0.060 and G61.475+0.092). This allows for a comparison of column density and kinematic structure in different physical regimes: The ionized gas phase is traced by continuum emission and RRLs, the cold neutral medium is traced by H I absorption and the molecular gas regime is traced by different CO isotopologues and far-IR continuum emission. We present the star-forming region W43, as an example of what can be learned from this data.

W43 is one of the largest molecular cloud complexes in our Galaxy. It is located at the intersection of the Scutum–Centaurus spiral arm with the Galactic bar, is actively forming stars at a high rate and is dynamically complex (e.g., [Nguyen Luong et al. 2011](#); [Motte et al. 2014](#); [Bühr et al. 2015](#)). It is composed of multiple sub-regions, most prominently the W43-main and W43-south regions, which themselves break down into smaller regions of molecular gas (e.g., [Carlhoff et al. 2013](#)). In W43-main, complex structure is also indicated by the high H I column densities (e.g., [Liszt 1995](#); [Motte et al. 2014](#); [Bühr et al. 2015](#)), which suggests the presence of several molecular clouds along the line-of-sight ([Bialy et al. 2017](#)).

Different evolutionary stages of stars and clouds coexist and appear to be influencing each other: An OB cluster at the center of W43-main, which contains Wolf-Rayet stars, includes a strong source of ultraviolet photons (e.g., [Smith et al. 1978](#); [Blum et al. 1999](#)); these provide the ionization and heating of the central H II region (e.g., [Reifenstein et al. 1970](#); [Lester et al. 1985](#)). There is evidence for a second generation of star formation, indicated by clumps of dense gas and ultra-compact H II regions (e.g., [Motte et al. 2003](#); [Bally et al. 2010](#); [Beuther et al. 2012](#)), which conveys the picture of gas compression driven by the central H II regions (e.g., [Blum et al. 1999](#); [Balsler et al. 2001](#)). In the

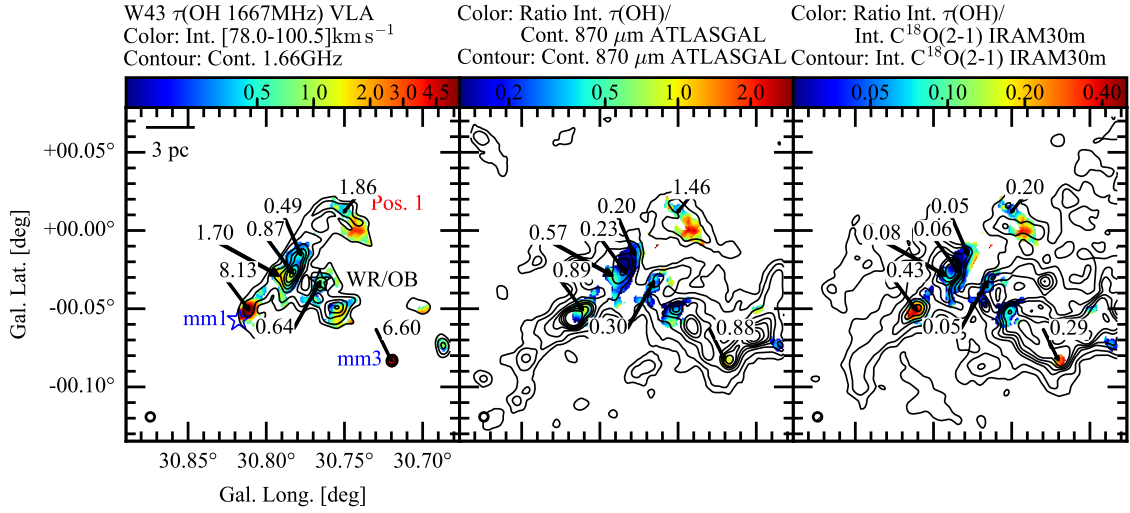


Figure 3.10: Comparison of $\tau(\text{OH } 1667 \text{ MHz})$, dust continuum emission at $\lambda = 870 \mu\text{m}$, and $\text{C}^{18}\text{O}(2-1)$ emission in the W43 star-forming region. In the left panel, the integrated optical depth of the OH 1667 MHz transition between 78.0 and 100.5 km s^{-1} is displayed in colors. For each pixel, only channels that are detected at a $3\text{-}\sigma$ level contribute to the integrated τ -map. It is overlaid with contours of the 18 cm continuum emission (black, at levels of $0.1, 0.2, 0.4, 0.6, 0.8, 1.0, 1.25, 1.5$ and $1.75 \text{ Jy beam}^{-1}$). The middle panel shows the ratio of the integrated $\tau(\text{OH})$ map to $870 \mu\text{m}$ ATLASGAL emission (Schuller et al. 2009), which traces dense gas (the dust emission is overlaid in black contours, at levels of $0.5, 1.0, 2.0, 3.0, 4.0, 5.0, 7.0$ and $10.0 \text{ Jy beam}^{-1}$). The right panel shows the ratio of $\tau(\text{OH})$ to $\text{C}^{18}\text{O}(2-1)$ emission (Carlhoff et al. 2013), integrated over the same velocity range (the velocity integrated $\text{C}^{18}\text{O}(2-1)$ emission is overplotted in black contours at levels of $6, 9, 13, 15, 17, 19, 23 \text{ K km s}^{-1}$). All data have been smoothed to a common resolution of $20''$, corresponding to spatial scales of 0.5 pc . In the left panel, the central Wolf-Rayet/OB cluster is marked by a black star, while the dense clumps MM1 and MM3 (Motte et al. 2003) are marked by blue stars. The upper end of the T-bar-shaped continuum emission is marked as Pos. 1 for easier reference in the text. For readability, the values of the ratio are displayed for selected positions in the figure.

environment of W43-main, pre-stellar cores manifest higher gas temperatures than in quiescent regions due to the heating by the central cluster, possibly affecting the number of stars formed in the future (Beuther et al. 2012). Adding to the complexity of the region, observations of molecular and ionized gas tracers revealed several velocity gradients and substructures of different morphologies (e.g., Liszt 1995; Balser et al. 2001; Carlhoff et al. 2013). The gas streams on global scales in molecular and atomic gas indicate that the H to H_2 conversion is ongoing (Motte et al. 2014). Dynamical interaction between clouds has been investigated on smaller scales with SiO emission, which possibly emerges from low velocity shocks in mm-emission peaks (e.g., Nguyen Luong et al. 2013; Louvet et al. 2016).

The extended OH absorption in W43 is displayed in the left panel of Fig. 3.10, in which the optical depth has been integrated between $78.0\text{--}100.5 \text{ km s}^{-1}$ and all maps are shown at an angular resolution of $20'' \times 20''$, corresponding to a spatial scale of 0.5 pc at

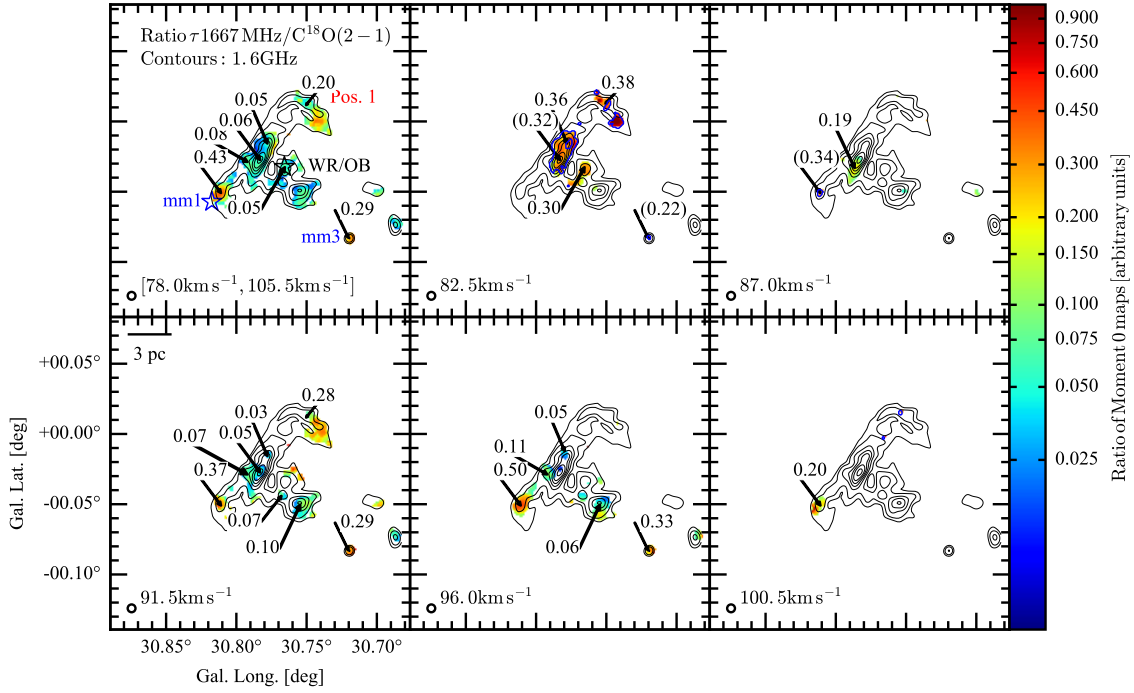


Figure 3.11: Ratio of integrated $\tau(\text{OH } 1667 \text{ MHz})$ absorption and $\text{C}^{18}\text{O}(2-1)$ emission in W43. The top-left panel is the same as the rightmost panel in Fig. 3.10 and is shown for orientation. The other panels show the ratio of $\tau(\text{OH } 1667 \text{ MHz})$ and $\text{C}^{18}\text{O}(2-1)$ at the indicated velocities after binning three channels of 1.5 km s^{-1} width. Overlaid on all panels are contours of 18 cm continuum emission (black, in levels of 0.1, 0.2, 0.4, 0.6, 0.8, 1.0, 1.25, 1.5 and $1.75 \text{ Jy beam}^{-1}$). The 1667 MHz optical depth has been masked at $3\text{-}\sigma$ detection levels in the original OH absorption data. For pixels with no C^{18}O emission counterpart, $3\text{-}\sigma$ detection limits have been used, and are indicated by blue contours. The ratio is quoted in brackets for these locations.

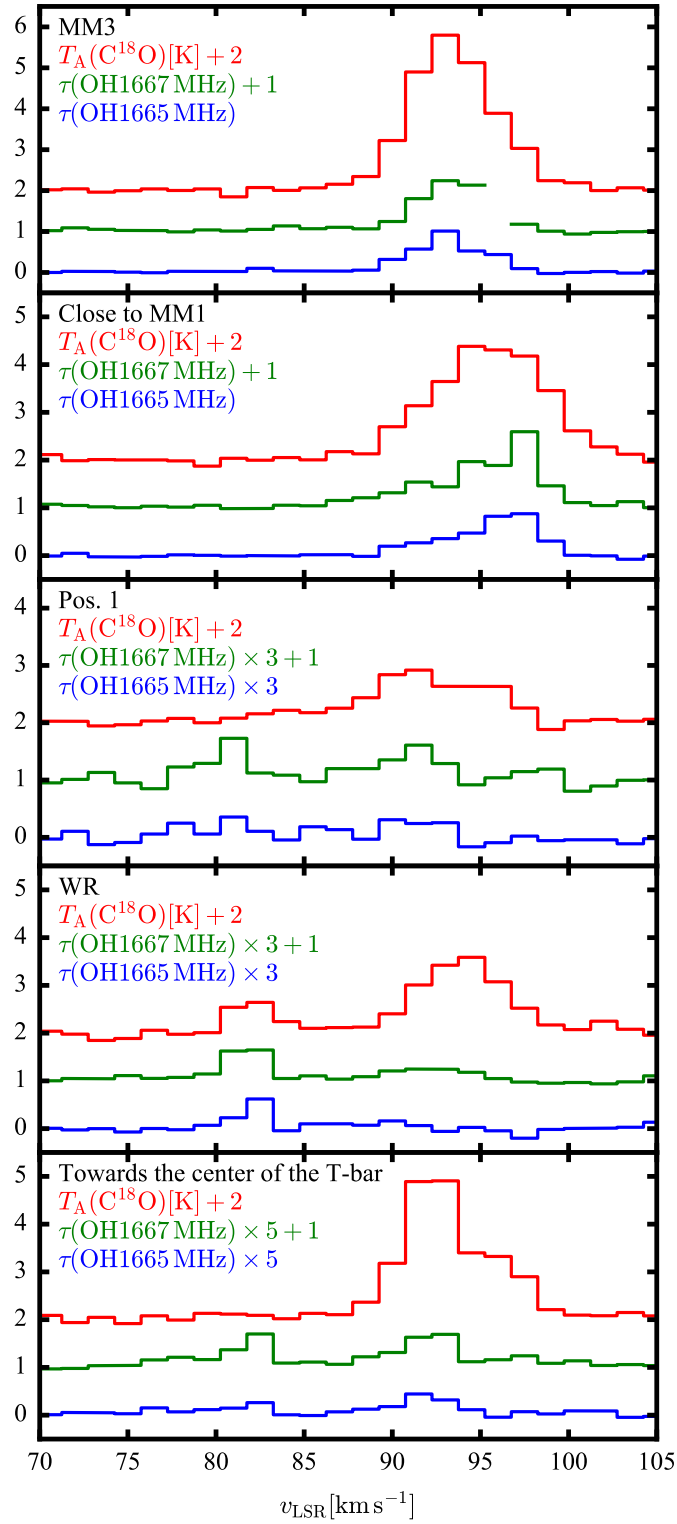


Figure 3.12: Spectra of τ_{OH} in the 1665 and 1667 MHz lines, as well as of emission in $\text{C}^{18}\text{O}(2-1)$ line. The spectra are extracted towards positions MM1, MM3⁶, WR and "Pos. 1" as indicated in Figs. 3.10 and 3.11, as well as towards the central part of the T-bar. Towards MM3, the channel at 96 km s^{-1} of the OH 1667 MHz absorption is masked because of sidelobes of close-by maser emission.

a distance of 5.5 kpc (Zhang et al. 2014). Intrinsically, absorption is seen towards strong continuum emission peaks, as the sensitivity to find absorption increases with continuum emission strength. However, the strongest integrated optical depth peaks do not coincide with continuum emission peaks, but are seen towards the mm dust emission sources MM1 and MM3⁶ (nomenclature taken from Motte et al. 2003). The integrated OH absorption varies by a factor of 3 around the central H II region, and is higher by an order of magnitude towards the outer parts of the T-shaped continuum emission: At MM3 and towards MM1, the total line-of-sight column density is approximately $7 \times 10^{15} \text{ cm}^{-2}$ and $9 \times 10^{15} \text{ cm}^{-2}$, respectively while the column density is between $0.5 - 2 \times 10^{15} \text{ cm}^{-2}$ around the central H II region, assuming an excitation temperature of $T_{\text{ex}} = 5 \text{ K}$ in both cases.

Fig. 3.10 compares the optical depth of the OH 1667 MHz transition to ATLASGAL 870 μm dust emission (Schuller et al. 2009) and to C¹⁸O(2–1) emission (Carlhoff et al. 2013). The middle panel displays the ratio of integrated OH optical depth to 870 μm dust emission, while the right panel displays the ratio to integrated C¹⁸O(2–1) emission. Both the OH and C¹⁸O(2–1) data have been integrated between 78.0 km s^{-1} and 100.5 km s^{-1} . For the OH optical depth only such pixels contribute to the integral that are significantly detected in the absorption data. The value of the ratio maps are shown for relative comparison of different parts of the region, motivated by the hypothesis that all the tracers are optically thin and hence contribute linearly to the column density of the species (the optical thickness of the tracers is discussed further in sect. 3.4.4). Thus, the ratios quoted here represent no physical quantity directly but their variation across the map can be indicative either of OH abundance or excitation variations.

The integrated C¹⁸O and 870 μm emission are shown as contours in Fig. 3.10. There are enhancements towards the central continuum source, towards MM1 and MM3 in both tracers. The strongest peak in the C¹⁸O emission is towards the central part of the T-bar, and is slightly offset from the peak of the continuum emission. The ATLASGAL emission peaks more strongly towards MM1 and MM3. At MM1, continuum emission and C¹⁸O emission are slightly shifted away from the 870 μm emission.

Within the central part of the T-bar, the ratio of OH optical depth to C¹⁸O emission is around 0.05, and slightly higher on the left side of the central continuum peak. This is similar in the 870 μm emission, where the ratio is between 0.2–0.3, and by a factor of 2 higher on the side facing MM1. The ratio is around a factor of 4–9 higher against the MM1 and MM3 sources in both tracers. This increase is slightly higher for the ratio to C¹⁸O emission than to 870 μm emission, which is consistent with the stronger increase of the 870 μm emission towards these sources. Against “Pos. 1”, however, the ratio to ATLASGAL 870 μm emission is by a factor of ~ 5 higher than in the central continuum emission region. The increase in this ratio is also seen in the C¹⁸O emission.

In order to understand this comparison better, Fig. 3.11 shows the ratio of OH optical depth and C¹⁸O in velocity ranges of 4.5 km s^{-1} (after binning three channels of 1.5 km s^{-1}). Between 81.0 and 84.0 km s^{-1} , OH absorption is seen against the central H II

⁶At MM3, the OH 1667 MHz absorption is affected by side lobes of close-by maser emission at 96 km s^{-1} . To determine the moment maps shown in Figs. 3.10 and 3.11, we interpolated over the channel at 96 km s^{-1} in lines of sight close to MM3. For clarity, this channel is masked in Fig. 3.12.

region and “Pos. 1”. $C^{18}O$ is significantly detected only in few locations, and we include upper limits in the plot (encircled by blue contours). Ratios are found between 0.3 and 0.4. A similar ratio is seen between 90 km s^{-1} and 93.0 km s^{-1} towards MM3, MM1 and “Pos. 1”. In this velocity range, however, the OH ratio at the center of the T-bar is rather low, between 0.03 and 0.1. The ratio increases for MM1 towards 0.5 between 94.5 and 97.5 km s^{-1} .

To conclude, variations in OH to $C^{18}O$ ratio are seen also when refining the integration interval. There seem to be two regimes – the central part of the H II region exhibits a ratio of ~ 0.05 , while for other locations and other velocities, we find a ratio of ~ 0.3 . At lower velocities, also the central part of the H II region is seen at ratios of ~ 0.3 . This is further discussed in Section 3.4.4.

3.4 Discussion

3.4.1 Distribution of OH in the Galactic plane

Recent single-dish observations of the OH ground state transitions find OH to be extended over wide areas in the Galactic plane (Dawson et al. 2014). The number of absorption detections found in this work is at first glance small relative to the number of cm-continuum sources available in the Galactic plane (e.g., Bihl et al. 2016) and needs to be discussed in terms of the varying sensitivity limit with continuum source strength.

We detect OH absorption mostly against extended Galactic cm-continuum background sources that show a spectral index in agreement with that of free-free emission from H II regions. The lower number of detections of OH in diffuse clouds not associated with H II regions is likely due to the sensitivity limits indicated in Fig. 3.3. While we do detect OH absorption at a variety of optical depths below $\tau \leq 0.2$ at continuum flux density $> 1 \text{ Jy beam}^{-1}$, at lower continuum surface brightness the sensitivity is not high enough to detect sources with $\tau \leq 0.05 - 0.1$. As the majority of the continuum sources have a flux density $< 1 \text{ Jy beam}^{-1}$, we pick up largely absorption at higher optical depths. The increase of the relative number of detections with strength of the continuum source is a further indication that some of the diffuse OH gas (e.g., Dawson et al. 2014) remains undetected for this group of sources.

As diffuse clouds are typically found to have low optical depths (e.g., Liszt & Lucas 1996), we are therefore biased towards higher column densities. As comparison, according to Dickey et al. (1981) using the Nancay telescope at $3'.5$ resolution, OH optical depths in diffuse clouds have been found to be approximately 0.05 in a 1 km s^{-1} channel in the 1667 MHz transition. Higher optical depths were found by, e.g., Goss (1968), Yusef-Zadeh et al. (2003) or Stanimirović et al. (2003). OH gas was associated with the Galactic continuum sources, H II regions or supernova remnants (SNR). The detections presented here match more with the latter categories.

3.4.2 OH as tracer of hydrogen gas

In section 3.3.2, we compared the OH abundance to the column densities of molecular hydrogen and hydrogen nuclei (hydrogen atoms and molecules). These comparisons are shown in Figs. 3.8 and 3.9. OH abundance is found to be decreasing with increasing hydrogen column density. The OH column density is not directly proportional to molecular column density. Therefore, the OH columns densities span a smaller dynamic range than molecular hydrogen. This also indicates that OH traces only specific ranges of molecular cloud column densities.

At any given hydrogen column density, the OH abundance shows variations of a factor of two, which is within the systematic uncertainties. The median value of the OH abundance with respect to N_{H_2} is 1.3×10^{-7} . Within the systematic uncertainties of a factor of 4, this is in agreement with the values reported in the literature, $N_{\text{OH}}/N_{\text{H}_2} = 1 \times 10^{-7}$ (e.g., Liszt & Lucas 2002).

A constant OH abundance with respect to N_{H} , as reported by, e.g., Crutcher (1979), can be reproduced - albeit with large scatter - for OH absorption with visual extinctions below $A_V \approx 10 - 20$. A median abundance of $X_{\text{OH}}(N_{\text{H}}) \approx 6.1 \times 10^{-8}$ is found for $A_V < 20$. We include atomic hydrogen, as OH may be present in transition regions that contain significant amounts of atomic hydrogen (e.g., Xu et al. 2016; Tang et al. 2017). The H I column density affects the OH abundances at the lowest molecular hydrogen column densities probed, when both are of similar strength. X_{OH} may even be lower in this regime, since the $N_{\text{H I}}$ measurements are lower limits and the N_{H_2} column densities may be underestimated, if the ‘‘CO-dark’’ gas fraction is significant (see Sect. 3.3.2.5).

Crutcher (1979) finds an abundance of $X_{\text{OH}} = 4.0 \times 10^{-8}$, in a range of visual extinction of $A_V = 0.4 - 7$ (see also review by Heiles et al. 1993), which is within the errors of our results. These results are based on studies of nearby molecular clouds (Perseus, Ophiuchus and Taurus), the SNR W44 and line-of-sight observations against extragalactic continuum sources, therefore mainly including observations towards diffuse molecular/translucent clouds (e.g., Snow & McCall 2006) that probably have environments similar to those of clouds that are not associated with H II regions in the sample presented here.

Above visual extinctions of $A_V \approx 10 - 20$, some OH abundances are found to be lower than the literature abundance, which is in agreement with theoretical predictions (e.g., Heiles et al. 1993). Oxygen to form OH at these extinctions is likely to be removed from the gas phase by the formation of CO and through the formation of water and its subsequent freeze-out onto grains. Far ultraviolet (FUV) radiation may counteract this removal: Models of photon dominated regions (PDRs) indicate that the local abundance of OH peaks between cloud depths of $A_V \approx 3 - 7$ (e.g., Hollenbach et al. 2009, 2012). According to Hollenbach et al. (2009), the abundance of water in these regions depends on the photodesorption of water ice from dust grains, and OH forms by photodissociation of water in the gas phase. Both water and hydroxyl gas phase abundances thus depend on the flux of the far ultraviolet (FUV) radiation, and decrease once the FUV radiation is efficiently attenuated deeper inside the cloud. As N_{OH} in this work represents a line-of-sight averaged density, OH from more embedded regions in the molecular cloud may contribute less to N_{OH} than ^{13}CO does to N_{H_2} , which may yield a decrease in the line-of-

sight averaged OH abundance.

Another possibility for the low OH abundances at high visual extinctions is that the OH excitation temperatures could be higher, approaching the kinetic temperatures in denser and warmer regions of the star forming molecular clouds in our sample. An excitation temperature of, e.g., 20 K would place most of the lowest measured OH abundances at $X_{\text{OH}} \sim 1 \times 10^{-7}$ in Fig. 3.8. As many OH abundances at lower N_{H_2} lie above this value, the trend in Fig. 3.8 is likely to persist but to be less steep if higher excitation temperatures at higher N_{H_2} were assumed. This effect is difficult to assess from our data alone, as the excitation temperature cannot be determined independently of the optical depth. Hence, more detailed modelling or targeted observations would be necessary to resolve this ambiguity.

3.4.3 Comparison with OH column density measurements from other transitions

In this section, we briefly discuss results on the OH column density that had been inferred from observations of other OH transitions. Section 3.3.3 described the morphologies of the satellite line transitions inside the OH ground state. In three regions, reversal of the 1612 MHz transition from absorption to emission and of the 1720 MHz transition from emission to absorption has been seen. As discussed in Section 3.3.3, the column density at the transition velocity was inferred using modeling results from [van Langevelde et al. \(1995\)](#). The column densities appear to be by a factor of 3-4 higher than the value inferred from the main lines. As an excitation temperature of 5 K was assumed for the OH ground state transitions, this discrepancy could be remedied by assuming an excitation temperature of 15 – 20 K, where values up to ~ 15 K have been found also in previous works ([Colgan et al. 1989](#)).

Additionally, rotational transitions in the far infrared wavelength regime (e.g., [Wiesemeyer et al. 2012](#); [Csengeri et al. 2012](#)) or electronic transitions in the optical regime (e.g., [Weselak et al. 2010](#)) can be used to study the OH column density. The crossmatch with our sample yields a match only for G49.488–0.380 with the source W51e2 in [Wiesemeyer et al. \(2016\)](#). However, the column density at velocities at which OH is detected in this work, is not reported, as the ${}^2\Pi_{3/2} J = 5/2 \leftarrow 3/2$ transitions at 2.5 THz saturate between 50 – 80 km s⁻¹.

The OH abundances determined here agree within our systematic uncertainty with the abundances inferred from optical and infrared transitions ([Weselak et al. 2010](#); [Wiesemeyer et al. 2016](#)). Figure 3.13 compares the OH abundances determined here with OH abundances derived from the THz transitions at different lines of sight by [Wiesemeyer et al. \(2016\)](#). Within the sensitivity limits of our survey, for abundances using HF as tracer of H₂, good agreement is seen between both datasets. This is also true for abundances using CH as tracer of H₂, although some points are present between $N_{\text{H}_2} \approx 6-10 \times 10^{21}$ cm⁻², which show lower abundance, but are still within uncertainties. Also, for low H₂ column densities, our measurements appear to be sensitivity limited (some measurements from [Wiesemeyer et al. \(2016\)](#) fall below the sensitivity limits indicated in Fig. 3.13). This comparison affirms the conclusion from Sect. 3.4.1 that the sample of OH absorption pre-

sented here indeed is biased towards high N_{OH} . Conversely, some continuum sources are strong enough to reveal OH absorption in more diffuse molecular cloud regions. Albeit the large systematic uncertainties of X_{OH} here, Fig. 3.13 shows that the variations in OH abundance at any given N_{H_2} persist when using alternative methods to measure N_{OH} and N_{H_2} , which are possibly less prone to systematics.

3.4.4 Extended OH absorption towards W43

As W43 is structured in a complicated way, and OH chemistry and excitation may vary strongly in different environments, there may be multiple explanations for variations in the ratios of OH optical depth to C^{18}O and $870\mu\text{m}$ emission. For example, there are temperature gradients present in the entire region, which may affect the dust emission.

The peak optical depth of the 1667 MHz transition is typically at $\tau < 1$ in W43. Exceptions are MM1 and MM3, for which optical depth peaks of $\tau_{1667} \sim 1.2$ indicate that the line becomes optically thick (Fig. 3.12). For MM1, the 1665 MHz transition peaks at $\tau_{1665} \sim 0.6$. Therefore, the ratio of the main lines ($\tau_{1667}/\tau_{1665} \approx 2.0$) is within errors of the expected ratio for LTE excitation of 1.8. For MM3, the ratio of the main lines is closer to unity with $\tau_{1665} \sim 1.0$, indicating that the transitions are not in LTE. As we have no probe of the excitation temperatures, this cannot be further assessed here. We note, however, that deviations from LTE in the OH hyperfine ground state transitions appear to be a common phenomenon (e.g., Li et al. 2018).

In order to minimize the chance of the CO tracers to become optically thick, we choose data from the $\text{C}^{18}\text{O}(2-1)$ transition. Optical thickness even of this transition cannot be ruled out in the entire region, and it will trace regions at higher densities than the $^{13}\text{CO}(1-0)$ used in the rest of the analysis. However, in order to investigate variations on a $20''$ scale (0.5 pc) in W43, these data provide information about the molecular gas at matching spatial resolution. As the datasets presented here cannot constrain whether these variations are due to abundance variations or differences in the excitation behavior, we limit the discussion to a qualitative description of the results.

In Figure 3.11, the enhancement in the OH to C^{18}O ratio around 82.5 km s^{-1} coincides with a peak in radio recombination lines (see velocity distribution of H92 α in fig. 6 of Balser et al. 2001 or of cm-RRLs from THOR in fig. 2 of Nguyen-Luong et al. 2017). At this velocity, possibly a photon-dominated, partly ionized region of the cloud is seen, in which models of photon-dominated regions predict the peak of the OH abundance (e.g., Hollenbach et al. 2012).

The OH 1667 MHz to C^{18}O ratios in the center of W43-main at $90\text{--}93 \text{ km s}^{-1}$ are found to be lower (≤ 0.1 ; Fig. 3.11, bottom left panel). This may be due to different physical or chemical conditions of the OH gas, which are difficult to disentangle in a crowded region like W43. Alternatively, this can be a consequence of systematically underestimating the OH optical depth. As described in Sect. 3.3.2.5, the measured continuum is higher than the true continuum incident on the OH gas, if H II-regions contribute to the continuum emission, which lie between the absorbing cloud and the observer.

This geometry is likely to be present here. The continuum emission at the Wolf-Rayet/OB cluster originates from the H II-region, which emits RRLs between $80\text{--}90 \text{ km s}^{-1}$.

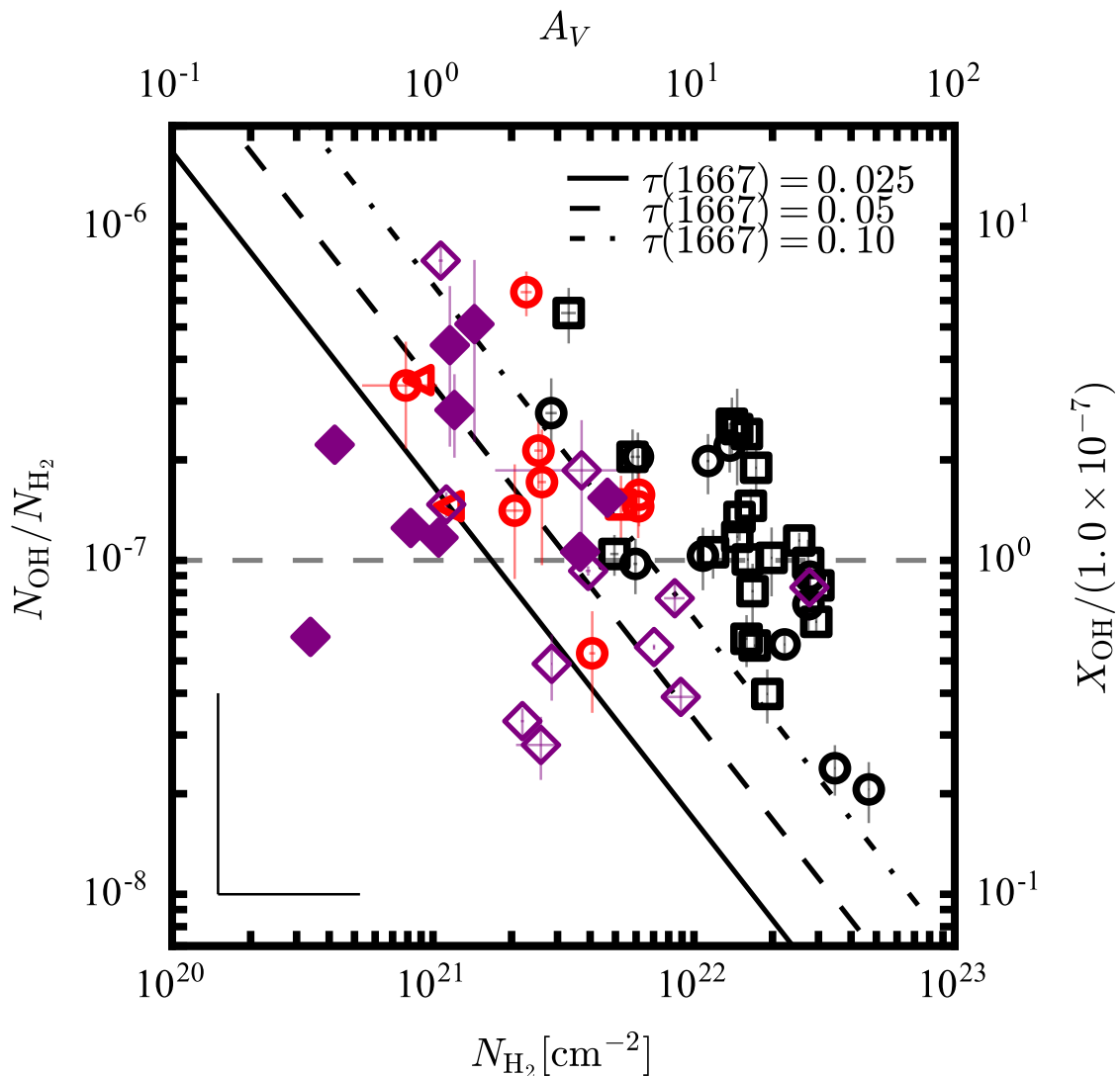


Figure 3.13: Comparison of the OH molecular abundances from this work to abundances measured in Wiesemeyer et al. (2016). Data, symbols and systematic uncertainties as in Fig. 3.8. Measurements from table 4 of Wiesemeyer et al. (2016) are overplotted as purple diamonds. Filled diamonds use HF as proxy for the H₂ column density. Empty diamonds use CH. If both HF and CH measurements are available, OH measurements are drawn twice. Black diagonal lines indicate sensitivity limits of X_{OH} for typical 4- σ limits on optical depth in the OH main lines and assuming a line width of 2.5 km s⁻¹ (The detection limits of $\tau = 0.025, 0.05$ and 0.1 are achieved for continuum sources stronger than $F_{\text{cont}} = 2.10, 1.05$ and 0.53 Jy beam⁻¹, respectively).

At the T-bar, the RRLs peak between 90–100 km s⁻¹, or even at higher velocities close to MM1. Since H II-regions are expanding, gas at lower velocities may be located closer to the observer than higher velocities gas. Absorbing OH gas at 90–100 km s⁻¹ would therefore lie between two H II-regions and its measured optical depth can be lower than the true value.

The distribution of absorption in OH and emission in C¹⁸O is in agreement with this scenario. In Figure 3.12, we show spectra of both molecules at different positions. Towards the central Wolf-Rayet cluster, only absorption at 82 km s⁻¹ is present, while not detected between 90–95 km s⁻¹ in spite of the presence of C¹⁸O emission. Towards the center of the T-bar, absorption becomes visible in both velocity ranges. How much and at which lines of sight the optical depth is influenced by this effect, depends on the fractional contribution of each H II-region to the continuum emission. A quantitative assessment of this is beyond the scope of this work.

Close to MM1, the peak of the OH absorption occurs between 96 and 97.5 km s⁻¹. The average velocity of the MM1 complex has been found to be at 98 km s⁻¹ (Nguyen Luong et al. 2013) and more resolved observation in HCN(1-0) and SiO(2-1) emission show peaks between 97 and 94 km s⁻¹, respectively, when going from MM1 towards the center of W43-main (Louvet et al. 2016). Louvet et al. indicate low velocity shocks in this region. While this needs to be confirmed, such shocks may produce temperatures that can enhance the OH abundance by activating neutral-neutral chemistry (Neufeld et al. 2002). However, the presence of additional, enhanced UV radiation may be required to produce OH, as neutral-neutral chemistry at high temperatures typically leads to water production (e.g., van Dishoeck et al. 2013). Near MM3 we see emission over a large range of velocities, with a clear peak in optical depth at 93 km s⁻¹ in the 1665 MHz line, in agreement with N₂H⁺ and SiO peaks at the same velocity (Nguyen Luong et al. 2013).

3.5 Conclusions

This work gives an overview on the OH absorption against strong continuum background sources as inferred from the THOR survey. This is the first survey-style analysis with the VLA over a significant fraction of the inner Milky Way in the range between $l = 15^\circ$ and $l = 67^\circ$. We detect 59 distinct absorption features against 42 continuum background sources. Most of the absorption is found against Galactic H II regions. We discuss the detection limit in terms of the continuum source strengths.

- Using ¹³CO(1-0) as tracer for N_{H_2} , we compare the OH abundance ($N_{\text{OH}}/N_{\text{H}_2}$) at different N_{H_2} . The OH abundance decreases with increasing hydrogen column density, especially for OH detections in molecular clouds that are associated with H II regions. This can be due to probing cloud regions where the OH in the gas phase is significantly depleted, although varying excitation conditions may provide an alternative explanation. The median abundance is found at $N_{\text{OH}}/N_{\text{H}_2} \sim 1.3 \times 10^{-7}$, in agreement within errors with previous studies.
- At low column densities, the atomic hydrogen fraction of the gas along the line-of-

sight becomes comparable to molecular hydrogen. The OH abundance ($N_{\text{OH}}/N_{\text{H}}$) is found to decrease with increasing total hydrogen nucleus column density for $A_{\text{v}} > 20$, but for lower extinction lines of sight, the data are consistent with a constant abundance having median value $N_{\text{OH}}/N_{\text{H}} \sim 6.1 \times 10^{-8}$.

- Extended OH absorption is seen against W43. The OH absorption is compared to ancillary data of $870\ \mu\text{m}$ and C^{18}O emission. At an angular resolution of $20'' \times 20''$, we find variation in the ratios of OH optical depth to emission in $870\ \mu\text{m}$ and C^{18}O , especially towards mm emission sources in the region.

Studies of OH provide a unique insight into the physical conditions of the ISM, particularly the transition between diffuse gas and molecular clouds. This first unbiased interferometric survey is a contribution to the characterization of the variation of OH absorption properties throughout the Galaxy. This work may provide a starting point for theoretical and observational follow-up studies with deeper observations at higher velocity resolution (see, e.g., Chapter 4), to expand the sample towards fainter sources with narrower line widths, and in combination with other observational data to resolve the physical conditions of the OH gas, and the molecular content of the diffuse gas surrounding molecular clouds.

Table 3.1: Lines of sight with detections of OH 1665/1667 MHz absorption.

Name	RA (J2000) (^h ^m ^s)	Dec. (J2000) ([°] ['] ^{''})	F_c		Ext.	α	OH velocities ($\frac{\text{km}}{\text{s}}$)	Ass. H II	H II-region
			$\frac{\text{Jy}}{\text{beam}}$ (20'')	$\frac{\text{Jy}}{\text{beam}}$ (46'')					
G14.490+0.021	18 16 46.666	-16 20 33.15	0.2	0.2	1	+0.0	(23.1)	(1)	G014.489+00.020
G14.996-0.738	18 20 33.756	-16 15 22.46	1.1	3.4	1	+0.7	21.8	1	G015.035-00.677; M17; S45
G15.033-0.679	18 20 25.129	-16 11 43.00	3.4	13.4	1	+0.7	12.9	1	G015.035-00.677; M17; S45
G18.148-0.283	18 25 01.009	-13 15 30.78	0.4	1.1	1	+0.1	56.4	1	G018.144-00.286
G18.303-0.390	18 25 42.284	-13 10 18.26	0.8	1.1	1	+0.4	(27.2), 32.2, (36.2)	(1), 1, (1)	G018.305-00.391
G19.075-0.288	18 26 48.526	-12 26 28.66	0.4	0.7	1	+0.4	64.6	1	G019.066-00.281; W39
G21.347-0.629	18 32 20.815	-10 35 11.37	1.0	1.0	0	+0.0	56.1	0	
G21.874+0.007	18 31 02.524	-09 49 30.49	0.5	0.6	1	+0.3	21.8	1	G021.870+00.010
G23.956+0.150	18 34 25.303	-07 54 46.37	0.9	1.3	1	+0.6	80.0	1	G023.956+00.152
G25.396+0.033	18 37 30.623	-06 41 16.38	0.3	0.4	1	+0.4	-12.1	1	G025.396+00.034
G25.397-0.141	18 38 08.202	-06 45 58.85	1.6	2.4	1	+0.8	67.1, 94.5	1, 1	G025.383-00.177
G26.609-0.212	18 40 37.495	-05 43 19.00	0.2	0.2	1	+0.3	-33.2	1	G026.610-00.212a
G27.563+0.084	18 41 19.379	-04 44 17.57	0.1	0.1	1	+0.2	86.0	1	G027.562+00.084
G28.806+0.174	18 43 16.959	-03 35 28.97	0.3	0.7	1	+0.1	79.8, 103.5	0, 1	G028.801+00.174
G29.935-0.053	18 46 09.525	-02 41 27.54	0.5	1.2	1	+0.1	7.0, 50.6, 68.0, 98.9	0, 0, 0, 1	G029.945-00.039; G29
G29.957-0.018	18 46 04.241	-02 39 19.25	1.4	2.0	1	+0.9	8.0, 99.8	0, 1	G029.945-00.039; G29
G30.535+0.021	18 46 59.359	-02 07 26.40	0.5	0.7	1	+0.6	(43.7, 49.4), 91.6	(1, 1), 1	G030.539+00.024
G30.720-0.083*	18 47 41.713	-02 00 23.48	0.4	-	0	+1.0	93.6	1	G030.782-00.028; W43
G30.783-0.028	18 47 36.898	-01 55 30.26	1.3	3.9	1	+0.3	77.9, 81.9, 87.1 92.1, 98.6	1, 1, 1 1, 1	G030.782-00.028; W43
G30.854+0.151	18 47 06.546	-01 46 49.14	0.1	0.3	1	-0.1	95.4	1	G030.852+00.149a
G31.242-0.110	18 48 44.821	-01 33 14.65	0.4	0.5	1	+0.5	19.6, 79.2, 83.7	1, 0, 0	G031.239-00.108
G31.388-0.383	18 49 59.195	-01 32 56.04	1.2	1.2	0	-0.9	18.1	0	
G32.151+0.132	18 49 32.499	-00 38 05.79	0.4	0.5	1	+0.4	93.8	1	G032.160+00.130
G32.272-0.226	18 51 02.358	-00 41 24.22	0.3	0.3	1	+0.2	22.6	1	G032.272-00.226
G32.798+0.190	18 50 31.084	-00 01 56.81	1.2	1.5	1	+1.0	12.8	1	G032.960+00.276
G32.928+0.607	18 49 16.315	00 16 23.85	0.2	0.3	1	+0.4	(-33.9)	(1)	G032.928+00.607
G33.915+0.110	18 52 50.381	00 55 29.56	0.6	0.8	1	+0.5	(95.3, 101.5), 106.3	(1, 1), 1	G033.910+00.110
G34.132+0.471	18 51 57.102	01 16 58.86	0.4	0.5	1	+0.2	33.8	1	G034.133+00.471
G35.467+0.139	18 55 34.169	02 19 11.16	0.2	0.3	1	+0.6	77.0	1	G035.470+00.140
G37.764-0.215	19 01 02.118	04 12 03.76	0.4	1.1	1	+0.1	63.4	1	G037.760-00.200
G37.874-0.399	19 01 53.641	04 12 52.52	1.3	1.8	1	+0.5	61.0	1	G037.870-00.400; W47
G38.876+0.308	19 01 12.538	05 25 44.28	0.2	0.2	0	+0.8	-16.3	1	G038.875+00.308
G39.565-0.040	19 03 43.340	05 52 55.41	0.4	0.5	0	-0.9	23.2	0	
G39.883-0.346	19 05 24.156	06 01 28.52	0.2	0.3	0	+0.8	56.9	1	G039.883-00.346
G41.741+0.097	19 07 15.655	07 52 42.12	0.3	0.3	1	+0.3	14.2	1	G041.740+00.100
G42.027-0.604	19 10 18.252	07 48 32.39	0.3	0.4	1	-1.0	65.1	0	
G45.454+0.060	19 14 21.188	11 09 12.92	1.4	2.9	1	+0.4	56.0, 59.4, 64.9	1, 1, 1	G045.454+00.059; K47
G49.206-0.342	19 23 00.834	14 16 50.73	0.8	2.3	1	+0.2	65.3	1	G049.205-00.343; W51
G49.369-0.302	19 23 11.204	14 26 37.06	1.5	3.2	1	+0.5	50.9, 62.9	1, 1	G049.384-00.298; W51
G49.459-0.353	19 23 32.908	14 29 55.71	1.9	3.9	1	+1.3	62.0, 68.6	1, 1	G049.490-00.381; W51
G49.488-0.380	19 23 42.119	14 30 41.99	4.0	11.1	1	+1.3	65.9	1	G049.490-00.381; W51
G52.753+0.334	19 27 32.385	17 43 27.32	0.3	0.3	1	+0.1	12.1, 45.2	1, 0	G052.757+00.334
G60.882-0.132	19 46 20.621	24 35 17.59	0.2	0.3	1	+0.0	22.3	1	G060.883-00.133; S87
G61.475+0.092	19 46 48.189	25 12 47.06	2.1	3.5	1	+0.5	(5.9), 21.1	(0), 1	G061.477+00.094; S88

Notes: The source name is constructed from the Galactic coordinates at which the peak of the continuum emission measured at 20'' resolution occurs. The columns F_c denotes the flux density at the given coordinates for an angular resolution of 20'' and 46''. The column "Ext." denotes whether the source is resolved (*I* for resolved, *O* for unresolved sources), and the column α is the L-band spectral index, defined as $I(\nu) \propto \nu^\alpha$, which are both taken from [Bühr et al. \(2016\)](#) and Wang et al. (in prep.). The central velocities of detected OH main line absorption are summarized in column 8 "OH velocities" (tentative, 3- σ components are listed in brackets in column 8 and 9). Association in position and velocity with an H II region is indicated with *I* in column 9. Criteria for the association are a smaller angular separation from the H II region than its radius, and a velocity difference of less than 10 km s⁻¹. The name of the H II regions are obtained from the WISE catalog of H II-regions ([Anderson et al. 2014](#)).

Footnotes: (*) Used 20'' resolution data only in order not to blend OH absorption with adjacent maser.

Chapter 3 Characterization of the OH abundance with THOR

Table 3.2: Line properties of OH 1665/1667 MHz absorption and $^{13}\text{CO}(1-0)$ emission.

Name	OH 1665 MHz					OH 1667 MHz					$^{13}\text{CO}(1-0)$				Ass.	Int. Range	Notes	
	v	Δv	F_{peak}	τ_{peak}	$\int \tau dv$	v	Δv	F_{peak}	τ_{peak}	$\int \tau dv$	v	Δv	$T_{\text{mb,p}}$	$\int T_{\text{mb}} dv$			H II	[km s $^{-1}$]
	[km s $^{-1}$]	[km s $^{-1}$]	[Jy beam $^{-1}$]	[km s $^{-1}$]	[km s $^{-1}$]	[km s $^{-1}$]	[km s $^{-1}$]	[Jy beam $^{-1}$]	[km s $^{-1}$]	[km s $^{-1}$]	[km s $^{-1}$]	[km s $^{-1}$]	[K]	[K km s $^{-1}$]				
G14.490+0.021	23.1	2.9	-0.06	0.34 ^a	<1.35	-	-	-	-	-	-	-	-	-	(1)	[+19.4, +27.1]	2(OH)	2(OH)
G14.996-0.738	21.8	4.0	-0.28	0.08	0.37	-	-	-	-	-	-	-	-	-	1	[+16.0, +28.0]	1	1
G15.033-0.679	12.9	5.4	-0.49	0.04	0.21	-	-	-	-	-	-	-	-	-	1	[+7.0, +16.6]	1	1
G18.148-0.283	56.4	3.5	-0.22	0.22	0.81	-	-	-	-	-	-	-	-	-	1	[+51.2, +61.0]	1665	1665
G18.303-0.390	27.2	4.3	-0.04	0.03 ^a	- ^b	-	-	-	-	-	-	-	-	-	(1)	-	3(OH)	3(OH)
	32.2	2.5	-0.15	0.14	0.47	-	-	-	-	-	-	-	-	-	1	[+27.0, +38.0]	4(CO)	1665
	36.2	2.5	-0.02	0.02 ^a	- ^b	-	-	-	-	-	-	-	-	-	(1)	-	3(OH)	3(OH)
G19.075-0.288	64.6	7.4	-0.11	0.17	1.35	-	-	-	-	-	-	-	-	-	1	[+56.9, +75.0]	4(OH)	1665
G21.347-0.629	56.1	2.5	-0.15	0.16	0.47	-	-	-	-	-	-	-	-	-	0	[+48.0, +58.6]	1665	4(CO)
G21.874+0.007	21.8	8.8	-0.08	0.10	1.01	-	-	-	-	-	-	-	-	-	1	[+15.5, +27.0]	5(OH)	1665
G23.956+0.150	80.0	5.5	-0.08	0.06	0.38	-	-	-	-	-	-	-	-	-	1	[+74.9, +86.1]	4(CO)	1665
G25.396+0.033	-12.1	2.7	-0.10	0.25	0.80	-	-	-	-	-	-	-	-	-	1	[-15.1, -8.9]	1	1
G25.397-0.141	67.1	5.3	-0.12	0.05	0.26	-	-	-	-	-	-	-	-	-	1	[+61.4, +72.5]	4(CO)	1665
	94.5	5.8	-0.35	0.17	0.96	-	-	-	-	-	-	-	-	-	1	[+88.0, +105.0]	4(CO,OH)	1665
G26.609-0.212	-33.2	2.5	-0.07	0.42	0.77	-	-	-	-	-	-	-	-	-	1	[-37.6, -29.9]	1	1
G27.563+0.084	86.0	2.5	-0.06	0.61	1.81	-	-	-	-	-	-	-	-	-	1	[+78.0, +89.0]	5(OH)	1665
G28.806+0.174	79.8	2.5	-0.08	0.12	0.39	-	-	-	-	-	-	-	-	-	0	[+76.4, +83.0]	4(CO)	1665
	103.5	3.8	-0.07	0.12	0.38	-	-	-	-	-	-	-	-	-	1	[+98.0, +115.0]	1665	4(CO)
G29.935-0.053	-	-	-	<0.14	-	7.0	2.5	-0.05	0.04	0.11	-	-	-	<2.34	0	[+2.0, +12.0]	2(CO)	1667
	-	-	-	<0.15	-	50.6	2.5	-0.08	0.06	0.14	49.9	2.2	3.39	8.32	0	[+47.0, +53.0]	5(CO)	1667
	-	-	-	<0.14	-	68.0	2.5	-0.09	0.07	0.19	68.1	3.1	1.15	4.20	0	[+61.0, +74.0]	5(CO)	1667
	98.8	4.3	-0.12	0.10	0.47	99.0	4.1	-0.16	0.12	0.64	99.4	8.3	11.09	95.48	1	[+90.0, +105.6]	4(CO)	1667
G29.957-0.018	8.2	2.7	-0.06	0.03	0.07	7.8	2.6	-0.11	0.05	0.17	7.4	1.7	1.31	1.61	0	[+2.0, +13.0]	1667	1667
	-	-	-	- ^c	-	99.8	5.1	-0.08	0.04	0.19	98.0	7.2	13.33	101.98	1	[+93.0, +107.0]	4(CO)	4(CO)
G30.535+0.021	-	-	-	- ^c	-	43.7	4.7	-0.05	0.07 ^a	- ^b	-	-	-	-	1	-	2(OH)	2(OH)
	-	-	-	- ^c	-	49.4	3.5	-0.04	0.06 ^a	0.57	47.7	4.4	4.96	42.44	1	[+33.0, +54.0]	2(OH)	2(OH)
G30.720-0.083 [*]	91.0	5.6	-0.06	0.11	0.67	92.1	5.4	-0.08	0.12	0.74	91.9	6.4	3.57	22.10	1	[+86.9, +98.0]	5(OH)	1667
G30.783-0.028	93.1	5.8	-0.25	0.80	- ^c	94.1	5.8	-0.34	1.29	- ^c	94.0	9.2	8.36	73.81	1	[+87.0, +101.0]	7	7
	-	-	-	-	-	77.9	3.4	-0.13	0.04	- ^b	-	-	-	-	1	-	3(OH)	3(OH)
	81.6	6.3	-0.14	0.02	0.20	82.2	2.5	-0.44	0.11	0.39	81.9	5.6	2.30	12.18	1	[+79.0, +85.6]	4(CO)	1667
	87.1	2.7	-0.06	0.02	- ^b	-	-	-	-	-	-	-	-	-	1	-	3(OH)	3(OH)
	92.0	3.5	-0.25	0.07	0.39	92.2	3.5	-0.32	0.09	0.55	93.3	8.7	7.41	70.82	1	[+85.0, +103.0]	4(CO)	1667
	98.3	3.4	-0.07	0.01	- ^b	98.8	4.2	-0.10	0.03	- ^b	104.9	5.6	1.78	- ^b	1	-	3(OH)	3(OH)
G30.854+0.151	95.5	2.9	-0.14	0.52	1.36	95.3	3.2	-0.16	0.63	2.01	95.5	4.1	6.72	27.98	1	[+91.0, +98.5]	1667	1667
G31.242-0.110	-	-	-	-	-	19.6	2.6	-0.12	0.26	0.83	20.8	3.8	3.33	12.45	1	[+15.0, +23.0]	1667	1667
	79.4	4.1	-0.07	0.15	0.57	78.9	2.5	-0.11	0.25	0.65	78.8	4.0	3.09	12.57	0	[+75.0, +81.8]	4	1667
	-	-	-	-	-	83.7	2.5	-0.07	0.14	0.30	84.0	2.4	1.96	5.34	0	[+81.7, +87.1]	4	1667
	-	-	-	-	<0.29	17.9	2.5	-0.11	0.09	0.20	-	-	-	<1.79	0	[+15.0, +22.0]	2(CO)	1667
G31.388-0.383	18.4	2.5	-0.08	0.06	0.17	-	-	-	-	-	-	-	-	-	1	[+88.0, +101.0]	1665	1665
G32.151+0.132	93.8	6.0	-0.10	0.19	1.20	-	-	-	-	-	94.4	4.5	7.24	33.72	1	[+18.0, +27.0]	4(CO)	1665
G32.272-0.226	22.6	4.6	-0.06	0.19	0.91	-	-	-	-	-	22.4	5.7	1.20	6.76	1	[+0.0, +25.0]	1665	1665
G32.798+0.190	12.8	11.8	-0.17	0.12	1.45	-	-	-	-	-	15.1	7.4	6.61	51.69	1	[-41.0, -28.0]	1	1
G32.928+0.607	-33.9	2.9	-0.05	0.21 ^a	0.64	-	-	-	-	-	-	-	-	-	1	[+92.0, +96.5]	2(OH)	2(OH)
G33.915+0.110	95.3	3.4	-0.04	0.06 ^a	0.16	-	-	-	-	-	-	-	-	<2.28	1	[+96.5, +104.0]	2(OH)	2(OH)
	101.5	2.9	-0.06	0.08 ^a	0.28	-	-	-	-	-	-	-	-	<2.28	1	[+103.4, +113.0]	1665	1665
	106.3	2.7	-0.11	0.16	0.46	-	-	-	-	-	107.5	4.6	6.80	32.47	1	[+28.0, +39.5]	1665	1665
G34.132+0.471	33.8	3.1	-0.08	0.17	0.59	-	-	-	-	-	35.1	3.8	2.93	11.88	1	[+74.0, +80.1]	1665	1665
G35.467+0.139	77.0	2.9	-0.07	0.32	0.86	-	-	-	-	-	77.4	3.2	8.73	29.92	1	[+56.5, +69.5]	4	1665
G37.764-0.215	63.4	4.3	-0.32	0.28	1.64	-	-	-	-	-	61.5	5.6	3.29	35.33	1	[+52.5, +67.5]	5(OH)	1665
G37.874-0.399	61.0	10.1	-0.31	0.19	1.91	-	-	-	-	-	61.4	7.2	4.29	32.56	1	[-20.0, -13.0]	1	1
G38.876+0.308	-16.4	2.9	-0.07	0.38	1.03	-16.1	4.1	-0.08	0.48	1.79	-	-	-	-	1	[+17.0, +28.0]	1667	1667
G39.565-0.040	23.4	2.8	-0.10	0.24	0.66	23.1	2.5	-0.15	0.37	0.96	23.4	3.1	1.25	4.65	0	[+50.5, +63.5]	1667	1667
G39.883-0.346	56.9	4.8	-0.05	0.23	1.23	56.9	3.5	-0.09	0.45	1.50	58.7	4.6	4.60	23.11	1	[+10.0, +14.2]	5(OH)	1667
G41.741+0.097	14.4	8.2	-0.04	0.17	0.47	13.9	4.3	-0.05	0.18	0.52	13.4	2.9	2.44	5.79	1	[+62.0, +71.0]	4(CO)	1667
G42.027-0.604	-	-	-	-	<0.33	65.1	3.5	-0.05	0.14	0.59	65.5	3.9	3.02	12.48	0	-	3(OH)	3(OH)
G45.454+0.060	-	-	-	-	-	56.0	7.2	-0.17	0.07	- ^b	-	-	-	-	1	-	4(CO)	1667
	59.3	4.1	-0.19	0.07	- ^c	59.5	2.5	-0.38	0.18	0.83	58.9	5.9	8.02	45.42	1	[+53.2, +62.3]	3(OH)	3(OH)
	-	-	-	-	-	64.9	8.2	-0.09	0.03	- ^c	-	-	-	-	1	-	1665	1665
G49.206-0.342	65.3	6.4	-0.52	0.24	1.79	-	-	-	-	-	65.7	6.0	4.31	28.54	1	[+44.5, +57.5]	1665	1665
G49.369-0.302	50.9	4.4	-0.75	0.24	1.26	-	-	-	-	-	51.1	4.5	11.71	61.22	1	[+56.5, +69.5]	4	1665
	62.9	5.2	-0.33	0.11	0.63	-	-	-	-	-	61.1	2.3	4.11	24.18	1	[+55.0, +65.0]	4	1665
G49.459-0.353	62.0	7.4	-0.36	0.10	0.68	-	-	-	-	-	61.1	8.2	4.55	34.25	1	[+65.0, +73.0]	1665	1665
	68.6	3.7	-0.81	0.22	1.01	-	-	-	-	-	68.6	4.7	7.47	40.51	1	[+63.0, +72.5]	4	4
G49.488-0.380	65.9	2.5	-1.89	0.18	0.48	-	-	-	-	-	67.8	4.0	6.13	44.89	1	[+11.5, +18.5]	7	7
G52.753+0.334	13.6	2.9	-0.02	0.07 ^a	<0.35	10.6	4.8	-0.04	0.12	0.31	15.2	2.3	2.86	7.22	1	[+43.0, +47.0]		

Table 3.3: Derived quantities from OH 1665/1667 MHz and H I absorption and $^{13}\text{CO}(1-0)$ emission.

Name	v_{OH} [km s ⁻¹]	$N_{\text{OH}1665}/T_{\text{ex}}$ [$\times 10^{14}$ cm ⁻² K]	$N_{\text{OH}1667}/T_{\text{ex}}$ [$\times 10^{14}$ cm ⁻² K]	$v^{13}\text{CO}$ [km s ⁻¹]	$N^{13}\text{CO}$ [$\times 10^{16}$ cm ⁻²]	N_{H_2} [$\times 10^{21}$ cm ⁻²]	N_{H_1} [$\times 10^{21}$ cm ⁻²]	Notes	$X_{\text{OH}}(N_{\text{H}})$ [$\times 10^{-7}$]	$X_{\text{OH}}(N_{\text{H}_2})$ [$\times 10^{-7}$]
G14.490+0.021	23.1	$<5.4 \pm 2.4^a$	–	–	–	–	>1.3	2(OH)	–	–
G14.996–0.738	21.8	1.5 ± 0.4	–	–	–	–	>6.3	1	–	–
G15.033–0.679	12.9	0.8 ± 0.2	–	–	–	–	>4.6	1	–	–
G18.148–0.283	56.4	3.2 ± 0.4	–	55.5	4.2	16.1	>3.0	1665	>0.5	1.0
G18.303–0.390	27.2	– ^b	–	–	–	–	–	3(OH)	–	–
	32.2	1.9 ± 0.2	–	33.0	4.5	17.1	>2.5	1665	>0.3	0.6
	36.2	– ^b	–	–	–	–	–	3(OH)	–	–
G19.075–0.288	64.6	5.4 ± 0.9	–	65.1	7.2	27.4	>4.1	1665	>0.5	1.0
G21.347–0.629	56.1	1.9 ± 0.3	–	56.2	2.8	10.7	>3.3	4(CO)	–	–
G21.874+0.007	21.8	4.0 ± 0.6	–	22.3	3.9	14.9	>3.5	1665	>0.6	1.3
G23.956+0.150	80.0	1.5 ± 0.3	–	79.6	5.0	19.1	>3.5	1665	>0.2	0.4
G25.396+0.033	–12.1	3.2 ± 0.6	–	–	–	–	>1.3	1	–	–
G25.397–0.141	67.1	1.0 ± 0.1	–	66.5	1.3	5.0	>5.1	1665	>0.3	1.0
	94.5	3.9 ± 0.3	–	96.3	7.7	29.4	>4.2	1665	>0.3	0.7
G26.609–0.212	–33.2	3.1 ± 1.3	–	–	–	–	>1.5	1	–	–
G27.563+0.084	86.0	7.2 ± 2.3	–	85.8	3.9	14.6	>2.0	1665	>1.2	2.5
G28.806+0.174	79.8	1.5 ± 0.3	–	80.6	1.4	5.3	>2.8	1665	>0.6	1.5
	103.5	1.5 ± 0.6	–	104.8	5.4	20.4	>2.5	4(CO)	–	–
G29.935–0.053	7.0	$<0.6 \pm 0.2$	0.2 ± 0.1	–	<0.3	<1.1	>1.6	1667	>0.4	1.5
	50.6	$<0.6 \pm 0.2$	0.3 ± 0.1	49.9	1.1	4.1	>2.3	1667	>0.2	0.5
	68.0	$<0.6 \pm 0.2$	0.4 ± 0.2	68.1	0.5	2.1	>4.2	1667	>0.3	1.4
	98.9	1.9 ± 0.5	1.4 ± 0.3	99.4	12.3	46.8	>4.9	1667	>0.1	0.2
G29.957–0.018	8.0	0.3 ± 0.1	0.4 ± 0.1	7.4	0.2	0.8	>2.2	1667	>0.7	3.3
	99.8	– ^c	0.4 ± 0.1	98.0	13.1	49.9	>4.5	4(CO)	–	–
G30.535+0.021	43.7	– ^c	– ^b	–	–	–	–	2(OH)	–	–
	49.4	1.1 ± 0.5	1.3 ± 0.4	47.7	5.5	20.8	>4.0	2(OH)	–	–
	91.6	2.7 ± 0.5	1.7 ± 0.4	91.9	2.8	10.8	>3.3	1667	>0.4	1.0
G30.720–0.083	93.6	– ^c	– ^c	94.0	9.5	36.1	>4.4	7	–	–
G30.783–0.028	77.9	–	– ^b	–	–	–	–	3(OH)	–	–
	81.9	0.8 ± 0.1	0.9 ± 0.2	81.9	1.6	6.0	>3.4	1667	>0.4	1.0
	87.1	– ^b	–	–	–	–	–	3(OH)	–	–
	92.1	1.5 ± 0.3	1.2 ± 0.2	93.3	9.1	34.7	>7.2	1667	>0.1	0.2
	98.6	– ^b	– ^b	104.9	–	–	–	3(OH)	–	–
G30.854+0.151	95.4	5.4 ± 0.9	4.5 ± 0.8	95.5	3.6	13.7	>1.3	1667	>1.1	2.2
G31.242–0.110	19.6	– ^c	1.9 ± 0.3	20.8	1.6	6.1	>2.5	1667	>0.8	2.0
	79.2	2.3 ± 0.4	1.4 ± 0.3	78.8	1.6	6.2	>2.1	1667	>0.7	1.6
	83.7	$<1.1 \pm 0.3$	0.7 ± 0.3	84.0	0.7	2.6	>1.3	1667	>0.7	1.7
G31.388–0.383	18.1	0.7 ± 0.2	0.5 ± 0.1	–	<0.2	<0.9	>3.2	1667	>0.6	3.5
G32.151+0.132	93.8	4.8 ± 0.6	–	94.4	4.3	16.5	>2.4	1665	>0.7	1.5
G32.272–0.226	22.6	3.6 ± 0.6	–	22.4	0.9	3.3	>2.1	1665	>2.1	5.5
G32.798+0.190	12.8	5.8 ± 0.3	–	15.1	6.7	25.3	>8.1	1665	>0.5	1.1
G32.928+0.607	–33.9	2.5 ± 1.1^a	–	–	–	–	>2.8	1	–	–
G33.915+0.110	95.3	0.6 ± 0.2^a	–	–	<0.3	<1.1	>0.6	2(OH)	–	–
	101.5	1.1 ± 0.2^a	–	–	<0.3	<1.1	>1.5	2(OH)	–	–
	106.3	1.9 ± 0.3	–	107.5	4.2	15.9	>1.9	1665	>0.3	0.6
G34.132+0.471	33.8	2.4 ± 0.5	–	35.1	1.5	5.8	>3.4	1665	>0.8	2.0
G35.467+0.139	77.0	3.4 ± 0.8	–	77.4	3.9	14.6	>1.3	1665	>0.6	1.2
G37.764–0.215	63.4	6.6 ± 0.9	–	61.5	4.6	17.3	>5.7	1665	>0.8	1.9
G37.874–0.399	61.0	7.6 ± 0.9	–	61.4	4.2	15.9	>8.8	1665	>0.9	2.4
G38.876+0.308	–16.3	4.1 ± 0.7	4.0 ± 0.6	–	–	–	>1.7	1	–	–
G39.565–0.040	23.2	2.6 ± 0.4	2.2 ± 0.3	23.4	0.6	2.3	>3.6	1667	>1.8	6.4
G39.883–0.346	56.9	4.9 ± 1.0	3.4 ± 0.7	58.7	3.0	11.3	>2.9	1667	>0.9	2.0
G41.741+0.097	14.2	1.9 ± 0.7	1.2 ± 0.3	13.4	0.7	2.8	>1.2	1667	>1.1	2.8
G42.027–0.604	65.1	$<1.3 \pm 0.4$	1.3 ± 0.3	65.5	1.6	6.1	>3.1	1667	>0.6	1.5
G45.454+0.060	56.0	–	– ^b	–	–	–	–	3(OH)	–	–
	59.4	– ^c	1.9 ± 0.2	58.9	5.9	22.2	>5.5	1667	>0.2	0.6
	64.9	–	– ^c	–	–	–	–	3(OH)	–	–
G49.206–0.342	65.3	7.2 ± 1.4	–	65.7	3.7	14.0	>6.9	1665	>1.0	2.6
G49.369–0.302	50.9	5.0 ± 0.7	–	51.1	7.9	30.0	>6.2	1665	>0.4	0.8
	62.9	2.5 ± 0.4	–	61.1	3.1	11.8	>5.4	1665	>0.4	1.1
G49.459–0.353	62.0	2.7 ± 0.6	–	61.1	4.4	16.8	>5.5	1665	>0.3	0.8
	68.6	4.0 ± 0.9	–	68.6	5.2	19.8	>3.9	1665	>0.5	1.0
G49.488–0.380	65.9	1.9 ± 0.4	–	67.8	5.8	22.0	>4.7	4	–	–
G52.753+0.334	12.1	$<1.4 \pm 0.4^a$	0.7 ± 0.3	–	0.9	3.5	>2.1	7	–	–
	45.2	$<1.3 \pm 0.3^a$	0.8 ± 0.2	44.5	0.7	2.5	>1.4	1667	>0.8	2.1
G60.882–0.132	22.3	2.8 ± 0.7	3.0 ± 0.5	22.4	7.2	27.5	>2.1	1667	>0.4	0.7
G61.475+0.092	5.9	$<0.12 \pm 0.03$	0.1 ± 0.03^a	6.6	0.03	0.12	>1.6	2(OH)	–	–
	21.1	4.9 ± 0.2	3.7 ± 0.2	21.6	7.3	27.8	>4.0	1667	>0.4	0.9

Notes: $N_{\text{OH}1665\text{MHz}}/T_{\text{ex}}$, $N_{\text{OH}1667\text{MHz}}/T_{\text{ex}}$ and N_{H_1} are determined from the integrated optical depth (Table 3.2; see text for the conversions used). The velocity in Col. 2 is the mean of the center velocities of the OH 1665 MHz and OH 1667 MHz absorption. The column density of molecular hydrogen, N_{H_2} , is derived from ^{13}CO emission (for assumptions and conversions see text). $X_{\text{OH}}(N_{\text{H}})$ is defined as $N_{\text{OH}}/N_{\text{H}}$, with $N_{\text{H}} = N_{\text{H}_1} + 2N_{\text{H}_2}$, while $X_{\text{OH}}(N_{\text{H}_2})$ is the ratio $N_{\text{OH}}/N_{\text{H}_2}$. Notes and footnotes are as in Table 3.2.

Table 3.4: Conjugate inversion and anti-inversion of satellite lines

Name	1612	1720	v [km/s]
G18.303-0.390	E	A	31.5
G19.075-0.288	A	E	58.5
	R	R	67.5
	E	A	70.0
G25.396+0.033	E	A	-12.0
G25.397-0.141	E	A	96.0
G29.935-0.053	A	-	97.0
	R	-	98.5
	E	A	100.0
G29.957-0.018	E	A	100.5
G30.535+0.021	E	A	45.0
G30.535+0.021	A	E	92.0
G30.720-0.083	E	A	93.0
G30.783-0.028	E	A	82.0
G32.151+0.132	E	A	94.5
G32.798+0.190	A	E	12.0
	R	R	14.0
	E	A	18.0
G32.798+0.190	A	E	90.0
G33.915+0.110	E	A	105.0
G37.764-0.215	A	-	62.5
	R	R	65.0
	-	A	67.5
G37.874-0.399	E	A	58.5
G38.876+0.308	E	A	-16.5
G39.883-0.346	E	A	57.0
G41.741+0.097	E	A	14.0
G49.206-0.342	A	-	65.0
	R	-	66.0
	E	A	68.0
G49.369-0.302	A	-	49.0
	R	-	49.5
	E	A	53.0
G49.369-0.302	A	E	62.5
	R	R	63.5
	E	A	65.0
G49.459-0.353	A	E	69.0
G60.882-0.132	E	A	22.5

Notes: Columns 2 and 3 indicate conjugate absorption (*A*) and emission (*E*) of the OH 1612 MHz and OH 1720 MHz transitions. The corresponding velocity is given in column 4. In some cases, 1612 MHz absorption and 1720 MHz emission transform into 1612 MHz emission and 1720 MHz absorption at higher velocities. For this kind of profile we give three entries: the central velocities of absorption and emission as well as the velocity, at which the reversal (*R*) of the line profile occurs. This is defined here as the velocity at which the satellite lines are equal. Components of the reversal profile that are not detected significantly are indicated by a horizontal dash.

Chapter 4

OH high-sensitivity follow-up observations of THOR

This chapter will be submitted for publication in the Astronomy & Astrophysics journal, M. R. Rugel, et al., to be submitted

Overview: *This chapter discusses VLA follow-up observations of OH and H₁ towards three of the continuum sources from Chapter 3. With higher sensitivity, we probe deeper in both OH and H₁ absorption, leading to a sample of lower column densities of OH that complement the THOR sample. Also, we are able to measure higher H₁ optical depths. Many of the OH features are in regimes that are not dominated by molecular gas, with two detections of OH without ¹²CO(1-0) emission counterparts.*

4.1 Introduction

As discussed in Chapter 1, there is convincing evidence from independent observations and simulations that substantial fractions of molecular gas in the ISM are not sampled by typical gas tracers, such as CO emission (e.g., [Grenier et al. 2005](#); [Pineda et al. 2013](#); [Wolfire et al. 2010](#); [Smith et al. 2014](#)). The fraction of the dark molecular component has been found to be around 30% ([Pineda et al. 2013](#); [Grenier et al. 2005](#); [Wolfire et al. 2010](#)), with higher fractions in diffuse clouds than in dense molecular ones ([Langer et al. 2014](#)). This dark molecular gas is important for understanding molecular cloud formation (Chapter 1). The best method to trace molecular gas in the transition region from atomic to molecular gas is a subject of active research.

As elaborated in Chapters 1 and 3, studies indicate that OH may be a good tracer for gas these regions. The CO-dark gas is located observationally between visual extinctions of $A_V = 0.2 - 0.3$ mag and $A_V = 1.5 - 3$ mag ([Grenier et al. 2005](#); [Paradis et al. 2012](#); [Xu et al. 2016](#); [Remy et al. 2018](#)), and at slightly lower magnitudes in the simulations of [Wolfire et al. \(2010\)](#). There exist different conventions for the definition of dark, or CO-

dark, gas. Dark gas has been defined as the difference between the column density of gas which is traced in γ -ray or dust emission and gas components which are measured by CO, H I and ionized gas tracers (e.g., Grenier et al. 2005). Dark gas may also indicate regions in which ^{12}CO is not yet optically thick (e.g., Wolfire et al. 2010) or not observable at the sensitivity of standard surveys (e.g., Allen et al. 2015), such as the $^{12}\text{CO}(1-0)$ CfA survey of the Galaxy (Dame et al. 2001). Other definitions require sensitivities in CO emission which go beyond those of standard surveys (e.g., Li et al. 2018; Donate & Magnani 2017). OH has been found in such regions. Xu et al. (2016) found OH in low-extinction parts of the Taurus molecular cloud with high CO-dark gas fractions. Other studies noted the detection of OH at similar extinctions in different clouds (e.g., Crutcher 1979) or beyond the sensitivities of the CfA survey (Allen et al. 2015). A comparison to very deep CO integrations yielded OH detections without CO-emission counterparts (Li et al. 2018).

With the THOR survey we characterized OH column densities between $N_{\text{OH}} \approx (2 - 40) \times 10^{14} \text{ cm}^{-2}$, at hydrogen column densities of $N_{\text{H}} \geq 4 \times 10^{21} \text{ cm}^{-2}$ ($A_V \gtrsim 2$). Many studies of diffuse clouds predict optical depths of OH of $\tau \leq 0.1$ (e.g., Dickey et al. 1981; Liszt & Lucas 1996). With the main sources of OH absorption in THOR (Chapter 3) being associated with H II regions and their giant molecular clouds (GMCs), the majority of sources were found at higher optical depths $\tau \geq 0.1$, while only detecting a small number of diffuse cloud components at lower optical depths. It is therefore natural to extend our sample to higher sensitivity, with the prospect of extending the sample of OH detections from THOR (Chapter 3) to the lower optical depths.

Another result of Chapter 3 was that the atomic gas content in GMCs is intrinsically difficult to measure, as the H I 21 cm line saturates (see also Bihl et al. 2015). H I turns optically thick, with the determination of lower limits on the H I column density as the only remaining option. Higher sensitivities are necessary to trace even higher optical depths.

It is for this reason that we observed three continuum sources from the THOR survey at higher sensitivity with the *Karl G. Jansky* Very Large Array (VLA), in the four OH ground state transitions and the H I 21 cm line. The observations were conducted at increased spectral resolution, to investigate the kinematic substructure of the molecular and atomic gas, and to capture narrow OH absorption components ($\Delta v \lesssim 1 \text{ km s}^{-1}$; e.g., Goldsmith & Li 2005).

The observations are presented in Section 4.2, the analysis method is described in Sect. 4.3. The results are stated in Sect. 4.4 and discussed in Sect. 4.5. Section 4.6 summarizes our findings.

4.2 Observations

4.2.1 H I and OH follow-up observations

We observed three continuum sources from the THOR survey with the VLA in C-configuration at higher sensitivity. We selected three continuum sources with a continuum flux of about 1 Jy beam^{-1} (see Table 4.1 for details). One of the continuum source is an H II-region

Table 4.1: Continuum sources discussed in this chapter

Source	Source (THOR)	l °	b °	RA. (^h ^m ^s)	Dec. (° ' ")	$F_{\text{cont}}(1.4 \text{ GHz})$ [Jy beam ⁻¹]	Angular resolution H I – OH 1720 MHz
G21	G21.347–0.629	21.347	–0.629	18 32 20.9	–10 35 11.4	0.9	17".2×12".8 – 14".0×10".7
G29	G29.957–0.018	29.957	–0.018	18 46 04.2	–02 39 19.3	1.0	16".1×13".8 – 13".3×11".4
G31	G31.388–0.383	31.388	–0.383	18 49 59.2	–01 32 56.0	1.3	15".1×13".8 – 12".8×11".5

Notes: Columns 3 and 4 show Galactic coordinates, Columns 5 and 6 the Equatorial coordinates (Epoch J2000). Column 7 shows the continuum flux as derived from line-free channels. Column 8 denotes the angular resolution of H I (lowest frequency transition) and of OH 1720 MHz (highest frequency transition).

(G29, with spectral indices of $\alpha = 0.9$; see Table 3.1; Wang et al., 2018, in press.) and two are extragalactic (G21 and G31; with $\alpha = 0.0$ and $\alpha = -0.9$). They are among the brightest sources in the THOR survey with OH absorption detections (Table 3.1). The sources were selected because they are either showing OH absorption components accompanied by weak (G29) or non-detected (G31) ¹³CO(1-0) emission, or to complement the sample with extragalactic sources to trace diffuse molecular gas along the line of sight in the Galactic plane (G21).

The spectral setup was chosen similar to the THOR survey (Sect. 2.3.4). We used several spectral windows at *L*-band to cover the H I and OH transitions, as well as six continuum bands (the latter are not discussed in this work). We observed the H I 21 cm transition at 1420 MHz, and the OH transitions at 1612 MHz and 1720 MHz with 2-MHz-wide bands, as well as the 1667 MHz and 1665 MHz transitions in one 4-MHz-wide band. The channel width was chosen at 0.488 kHz, corresponding to 0.1 km s⁻¹ at 1420 MHz and slightly smaller for the OH transitions. The observations were conducted in 8 nights between June and August 2017, with a total integration time of 7 h for G21, 4 h for G29 and 3 h for G31. The observation blocks lasted 2-3 h, with 10-20 minutes spent on bandpass (calibration source: 3C286) and gain calibration (calibration source: J1822-0938) each.

For calibration, we used the CASA¹ calibration pipeline. We inspected the data for antenna and baseline artifacts (see Chapter 2). The data were imaged and deconvolved using the CASA task `clean`. We cleaned the data (without continuum subtraction) in two different ways: First, with 0.5-km s⁻¹-wide channels over a range from –100 km s⁻¹ to 160 km s⁻¹. Second, we created image cubes for all OH transitions at a resolution of 0.2 km s⁻¹ for velocity ranges which showed absorption in one of the two OH main lines (OH 1665 MHz and OH 1667 MHz).

We obtained angular resolutions between 17".2×12".8 and 12".8×11".5. The noise in a 0.5-km s⁻¹-wide channel is between 0.004–0.008 Jy beam⁻¹ (depending on source, transition and dataset; see Tables 4.1 and C.2 for details). For the H I transition, this corresponds to a noise in brightness temperature of 13–20 K.

¹<http://casa.nrao.edu>; version 4.7.2; pipeline version 1.3.11

4.2.2 Optical depths of H I and OH

We convert the H I and OH transitions to optical depth using (see Eq. (3.1) and discussion in Sect. 3.3.1.1)

$$\frac{F_{\text{line}}}{F_{\text{cont}}} = e^{-\tau}, \quad (4.1)$$

with F_{line} the flux of the spectral line without continuum subtraction, F_{cont} the continuum flux and τ the optical depth. The continuum was derived from the absorption-free channels. In this equation, we assumed that for both H I and OH the contribution to the observed flux from emission is negligible as it is filtered out by the interferometer. Implications of this assumption, in particular on the H I optical depth, and possibilities to improve it, are discussed in Sect. 4.5.5.

In case of saturated channels in the H I transition, we calculate a lower limit on the optical depth by assuming a minimum H I absorption depth at the $3\text{-}\sigma$ noise level above zero. The uncertainties in the τ spectra are $\sigma(\tau) = 0.004 - 0.008$ (see Table C.2 for details). All transitions are shown in Figure 4.1.

4.2.3 Archival CO observations

To estimate the kinematics and column densities of molecular gas, we use archival CO observations from three surveys. $^{13}\text{CO}(1\text{-}0)$ observations are obtained from the Galactic Ring Survey (GRS; Jackson et al. 2006). As described in Sect 3.2, it has a half-power beam width of $46''$, and we correct all data for a main-beam efficiency of $\eta_{\text{mb}} = 0.48$. Also, we use $^{12}\text{CO}(1\text{-}0)$, $^{13}\text{CO}(1\text{-}0)$ and $\text{C}^{18}\text{O}(1\text{-}0)$ transition maps from the FUGIN survey (FOREST Unbiased Galactic plane Imaging survey with the Nobeyama 45-m telescope; Umemoto et al. 2017), and for G31 from a similar survey with the Purple Mountain Observatory (PMO; Y. Wang, private communication).

For G21 and G29, we use the GRS $^{13}\text{CO}(1\text{-}0)$ transition to determine the kinematics and the column density of CO. The data cubes are smoothed to an angular resolution of $46''$ to match the observations from GRS. The $^{12}\text{CO}(1\text{-}0)$, $^{13}\text{CO}(1\text{-}0)$ and $\text{C}^{18}\text{O}(1\text{-}0)$ emission from FUGIN (at $46''$ resolution) are shown for comparison. The $^{12}\text{CO}(1\text{-}0)$ emission from the FUGIN survey is also used to derive the excitation temperature T_{ex} of $^{13}\text{CO}(1\text{-}0)$ for comparison of the results of this Chapter to the study of Li et al. (2018) in Sect. 4.5.3 (see Appendix C.2.2 for more details). Both surveys are used at their native spectral resolution of 0.21 km s^{-1} and 0.65 km s^{-1} for GRS and FUGIN, respectively.

For G31, we choose observations from PMO as comparison for the CO(1-0) isotopologues, as the FUGIN survey shows artifacts at that particular position. As the PMO observations are at an angular resolution of $55''$, we also smooth the data from the GRS survey to an angular resolution of $55''$. Furthermore, to increase sensitivity, we smooth all spectra to a spectral resolution of 0.65 km s^{-1} (with the exception of Feature 7 at -4 km s^{-1} in G31, for which the PMO data are used at their full spectral resolution of 0.17 km s^{-1} for the kinematic analysis; see also Fig. C.7). We use the PMO observations for the analysis of both kinematics and column density, as GRS has limited velocity coverage and does

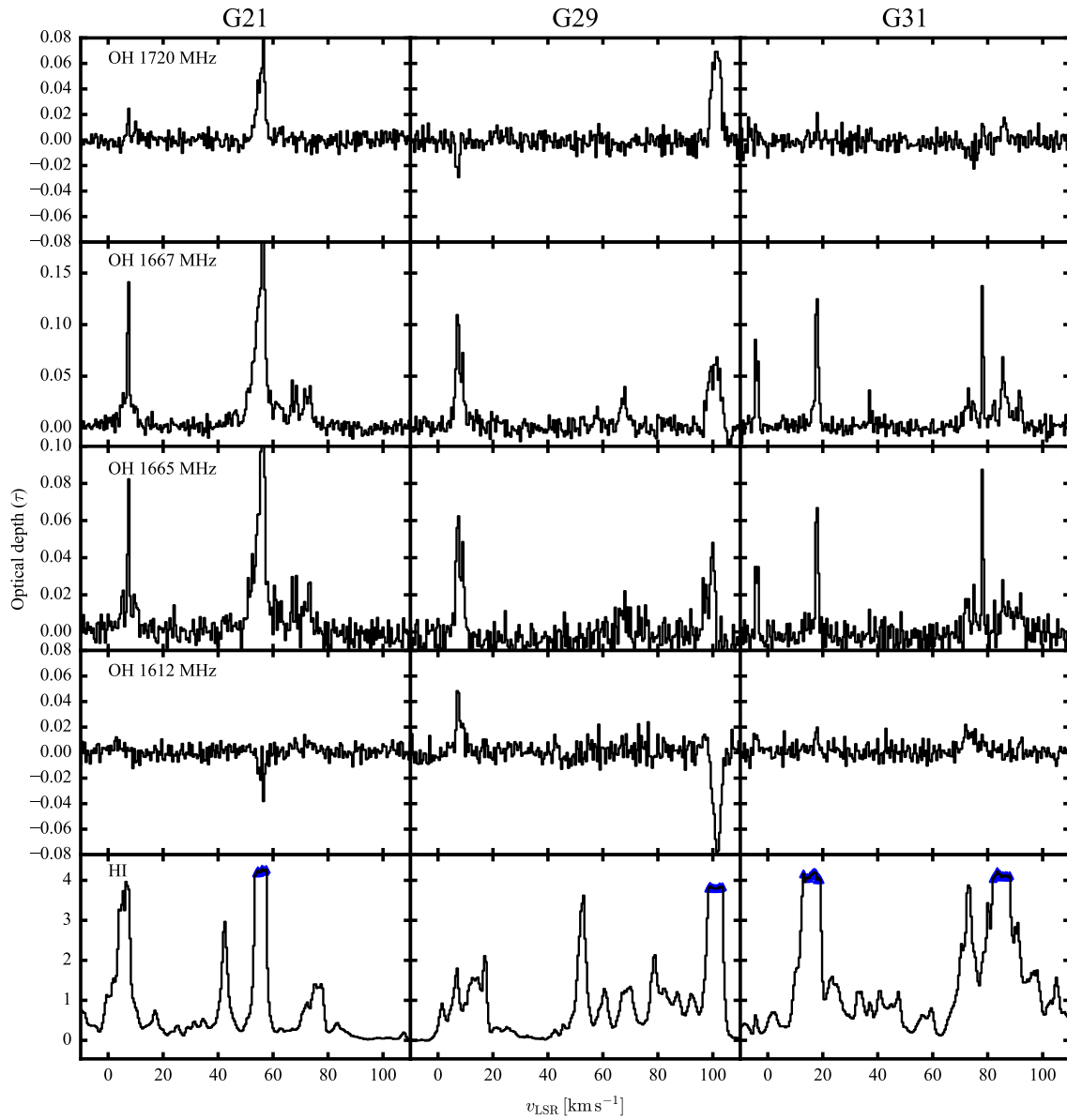


Figure 4.1: Overview of the optical depth of all OH transitions and the HI 21 cm line towards the three lines of sight G21, G29 and G31 (see Table 4.1 for further details on the sources). Negative optical depths imply that a transition is masing.

not cover all emission components (-4.95 km s^{-1} to 134.9 km s^{-1} ; see Table 4.2).

The absolute temperature scale of $^{13}\text{CO}(1-0)$ emission maps are in good agreement with the GRS survey (as tested for several positions in the maps). The spectra for the following analysis have been extracted from the same pixel as the OH absorption after gridding all image cubes to the same coordinate grid as the OH maps. The noise in all maps is listed in Table 4.2.

The beam sizes of all CO emission maps are larger than that of the OH absorption. Determining the CO emission on matching scales as the absorption is intrinsically difficult. As the continuum sources are unresolved here (in case of G29, at least the strongest emission component is not resolved), the size of the angular resolution of the OH observations is only an upper limit on the true source size, which determines the scale on which absorption occurs. While this is not a problem for the absorption observations itself, as Eq. (4.1) only depends on the ratio of the line to the continuum flux and therefore eventual filling factors cancel, it would be necessary to know the actual source size to provide adequate measurements of the CO emission.

From a practical point of view, the FUGIN data in its original form is provided as a resolution of $20''$, but at significantly lower sensitivity than GRS. As this is a detection experiment, we are interested in the highest possible sensitivity, and therefore smooth all datacubes to a half-power beam width of the GRS data at $46''$ (G21 and G29) and $55''$ (G31). The concern of different angular resolutions can be somewhat alleviated by the fact that our main targets are diffuse clouds, which may have more smoothly varying density distributions, than, e.g., dense cores in molecular clouds. Of course, the general discrepancy remains, which can only be remedied with more sensitive observations at higher angular resolution.

4.3 Analysis

4.3.1 Selection of components

For better overview, we divide the three lines of sight in 10 “features”, each of which contains one or multiple velocity components. The features are roughly defined as isolated groups in velocity of OH absorption components. Inside one feature, the components overlap and are sufficiently closely spaced, such that it is necessary to decompose them together into multiple Gaussian velocity components. All features are shown in Figs. 4.2, C.2–C.10.

We use two approaches to characterize the OH and H I absorption and the CO emission, to obtain both integrated spectra as well as peak optical depths and line widths from fitting the spectrum with Gaussians.

In the first approach, we identify peaks in the OH absorption spectrum, and define velocity ranges around these. These ranges are either defined by the optical depth falling below the $\sim 1\text{-}\sigma$ noise threshold (the choice is done by eye, but this approximately captures the procedure), or by reaching the minimum in optical depth between two absorption components. Within this range, the peak optical depth is given by the velocity bin with

Table 4.2: Noise characteristics of archival CO observations

Source	Transition	Survey	Δv km s ⁻¹	HPBW "	v_{\min} km s ⁻¹	v_{\max} km s ⁻¹	$\sigma(T_{\text{mb}})$ K
G21	¹² CO(1-0)	FUGIN	0.65	46.0	-99.67	+199.98	0.42
G21	¹³ CO(1-0)	FUGIN	0.65	46.0	-99.67	+199.98	0.23
G21	¹³ CO(1-0)	GRS	0.21	46.0	-4.95	+134.89	0.22
G21	C ¹⁸ O(1-0)	FUGIN	0.65	46.0	-99.67	+199.98	0.22
G29	¹² CO(1-0)	FUGIN	0.65	46.0	-99.67	+199.98	0.39
G29	¹³ CO(1-0)	FUGIN	0.65	46.0	-99.67	+199.98	0.24
G29	¹³ CO(1-0)	GRS	0.21	46.0	-4.95	+134.89	0.24
G29	C ¹⁸ O(1-0)	FUGIN	0.65	46.0	-99.67	+199.98	0.23
G31	¹² CO(1-0)	PMO	0.65	54.8	-99.67	+199.97	0.13
G31	¹³ CO(1-0)	PMO	0.65	54.8	-99.67	+199.98	0.08
G31	¹³ CO(1-0)	GRS	0.65	54.8	-4.95	+134.9	0.05
G31	C ¹⁸ O(1-0)	PMO	0.65	54.8	-99.98	+150.03	0.08
G31 ^a	¹² CO(1-0)	PMO	0.16	54.8	-100.00	+150.01	0.34
G31 ^a	¹³ CO(1-0)	PMO	0.17	54.8	+149.93	-99.96	0.20
G31 ^a	C ¹⁸ O(1-0)	PMO	0.17	54.8	+150.03	-99.98	0.20

Notes: The noise is given in main beam temperature T_{mb} .

Footnotes: (a) Higher spectral resolution was used for G31, feature 7, at -4 km s⁻¹.

the highest optical depth. The integrated optical depth is determined by summing over all optical depths within the range, multiplied by the channel width. The same velocity range is applied to the remaining spectral lines to determine integrated and peak emission. The results are shown in Table 4.3.

In the second approach, we model the optical depth (in case of OH and H I absorption) and emission (for the CO transitions) with a composition of Gaussian components. While the selection of the number of components has been done by eye, it roughly corresponds to creating a model such that the residual is indistinguishable from the noise, as well as excluding components that are unreasonably broad.

Gaussian components across different transition lines are associated in peak velocity to compare kinematic properties. Heavily blended lines, for which such an attribution is ambiguous or not possible at all, are excluded from the association (e.g., Fig. C.10).

The results of both approaches are shown graphically in Figs. 4.2, C.2–C.10. The parameters of the Gaussian decomposition of the OH spectra, together with the results for the CO and H I transitions, are listed in Table 4.4.

Table 4.3: Results of the integration of optical depth and emission line spectra

Source	Feature	OH 1667				OH 1665				¹² CO(1-0)				¹³ CO(1-0)				¹⁸ O(1-0)				H1	
		v_{mid} [km s ⁻¹]	Width [km s ⁻¹]	$\int \tau dv$ [km s ⁻¹]	τ_p	$\int \tau dv$ [km s ⁻¹]	τ_p	D	$\int T_{\text{mb}} dv$ [K km s ⁻¹]	$T_{\text{mb}}^{\text{int}}$ [K]	D	$\int T_{\text{mb}} dv$ [K km s ⁻¹]	$T_{\text{mb}}^{\text{int}}$ [K]	D	$\int T_{\text{mb}} dv$ [K km s ⁻¹]	$T_{\text{mb}}^{\text{int}}$ [K]	D	$\int \tau dv$ [km s ⁻¹]	τ_p				
G21	1	+7.4	+2.2	+0.144±0.007	+0.138	+0.075±0.006	+0.080	F	+9.3±0.5	+5.8	G	+1.0±0.2	+1.0	F	<1.3	<0.7	F	+7.07±0.27	+3.96				
	2	+56.5	+2.5	+0.488±0.007	+0.403	+0.329±0.006	+0.315	F	+22.2±0.5	+9.8	G	+9.7±0.2	+5.3	F	+2.9±0.3	+1.8	F	>10.62	>4.28				
	3	+66.6	+2.2	+0.047±0.005	+0.053	+0.023±0.005	+0.027	F	+2.2±0.5	+1.6	G	<1.3	<0.7	F	<1.3	<0.7	F	+0.64±0.01	+0.29				
G29	3	+68.8	+2.1	+0.049±0.005	+0.050	+0.023±0.004	+0.037	F	<3.9	<1.3	G	<1.3	<0.7	F	<1.3	<0.7	F	+0.60±0.01	+0.36				
	3	+73.5	+7.4	+0.127±0.010	+0.047	+0.062±0.008	+0.034	F	+16.1±1.0	+2.7	G	<1.3	<0.7	F	+1.5±0.5	+0.7	F	+7.55±0.04	+1.40				
	4	+6.5	+3.9	+0.176±0.009	+0.115	+0.107±0.009	+0.070	F	+12.9±0.6	+4.8	G	+2.1±0.2	+1.3	F	<1.3	<0.7	F	+4.82±0.04	+1.80				
G31	4	+9.7	+2.6	+0.076±0.008	+0.075	+0.048±0.007	+0.057	F	+2.5±0.5	+2.7	G	<1.4	<0.7	F	<1.3	<0.7	F	+2.11±0.02	+0.93				
	5	+67.5	+9.0	+0.108±0.014	+0.045	<0.038	<0.040	F	+22.1±1.0	+6.0	G	+4.3±0.3	+1.8	F	<1.3	<0.7	F	+7.97±0.04	+1.34				
	6	+102.4	+5.2	+0.199±0.007	+0.078	-0.093±0.011	+0.058	F	+100.8±0.7	+21.3	G	+30.5±0.3	+7.8	F	+5.6±0.4	+1.9	F	>16.73	>3.84				
G31	7	-4.8	+1.5	+0.063±0.006	+0.078	+0.024±0.004	+0.045	P ^u	+0.4±0.2	+1.5	P ^u	<1.1	<0.6	P ^u	<1.2	<0.6	P ^u	+0.58±0.01	+0.63				
	7	-3.5	+0.9	+0.039±0.004	+0.074	+0.030±0.004	+0.040	P ^u	+0.8±0.1	+1.2	P ^u	+0.3±0.1	+0.7	P ^u	<1.2	<0.6	P ^u	+0.41±0.00	+0.52				
	8	+17.5	+5.0	+0.183±0.007	+0.127	+0.091±0.008	+0.087	P	+7.1±0.2	+2.5	P	+1.1±0.1	+0.4	P	<0.5	<0.2	P	>19.85	>4.20				
	9	+37.0	+2.0	+0.020±0.003	+0.035	<0.023	<0.024	P	<1.2	<0.4	P	<0.4	<0.2	P	<0.5	<0.2	P	+1.60±0.01	+0.95				
	10	+71.9	+4.8	+0.069±0.007	+0.045	+0.025±0.008	+0.028	P	+7.8±0.2	+2.4	P	+0.6±0.1	+0.3	P	<0.5	<0.2	P	+13.93±0.21	+3.87				
	10	+75.5	+2.4	+0.040±0.005	+0.037	+0.022±0.006	+0.028	P	+5.1±0.2	+2.1	P	+0.7±0.1	+0.3	P	<0.5	<0.2	P	+4.96±0.05	+2.42				
	10	+78.1	+2.8	+0.118±0.006	+0.128	+0.069±0.006	+0.076	P	+3.4±0.2	+1.4	P	+0.7±0.1	+0.3	P	<0.5	<0.2	P	+4.71±0.04	+2.22				
	10	+81.8	+3.7	+0.050±0.006	+0.037	<0.024	<0.025	P	+5.7±0.2	+1.8	P	<0.4	<0.2	P	<0.5	<0.2	P	>14.67	>4.22				
	10	+85.1	+2.8	+0.092±0.005	+0.068	+0.033±0.006	+0.030	P	+4.2±0.2	+1.8	P	<0.4	<0.2	P	<0.5	<0.2	P	>10.31	>4.17				
	10	+92.0	+3.5	+0.057±0.006	+0.042	<0.024	<0.026	P	+6.8±0.2	+2.3	P	+1.0±0.1	+0.4	P	<0.5	<0.2	P	+7.31±0.07	+2.94				

Notes: Columns 2 and 3 denote center and width of the integration range, respectively. Column ‘D’ denotes if the FUGIN (‘F’), the GRS (‘G’) or the PMO (‘P’) survey data was used to determine the integrated CO emission.

Footnotes: (a) channel width: 0.17 km s⁻¹.

G21 Feature 1

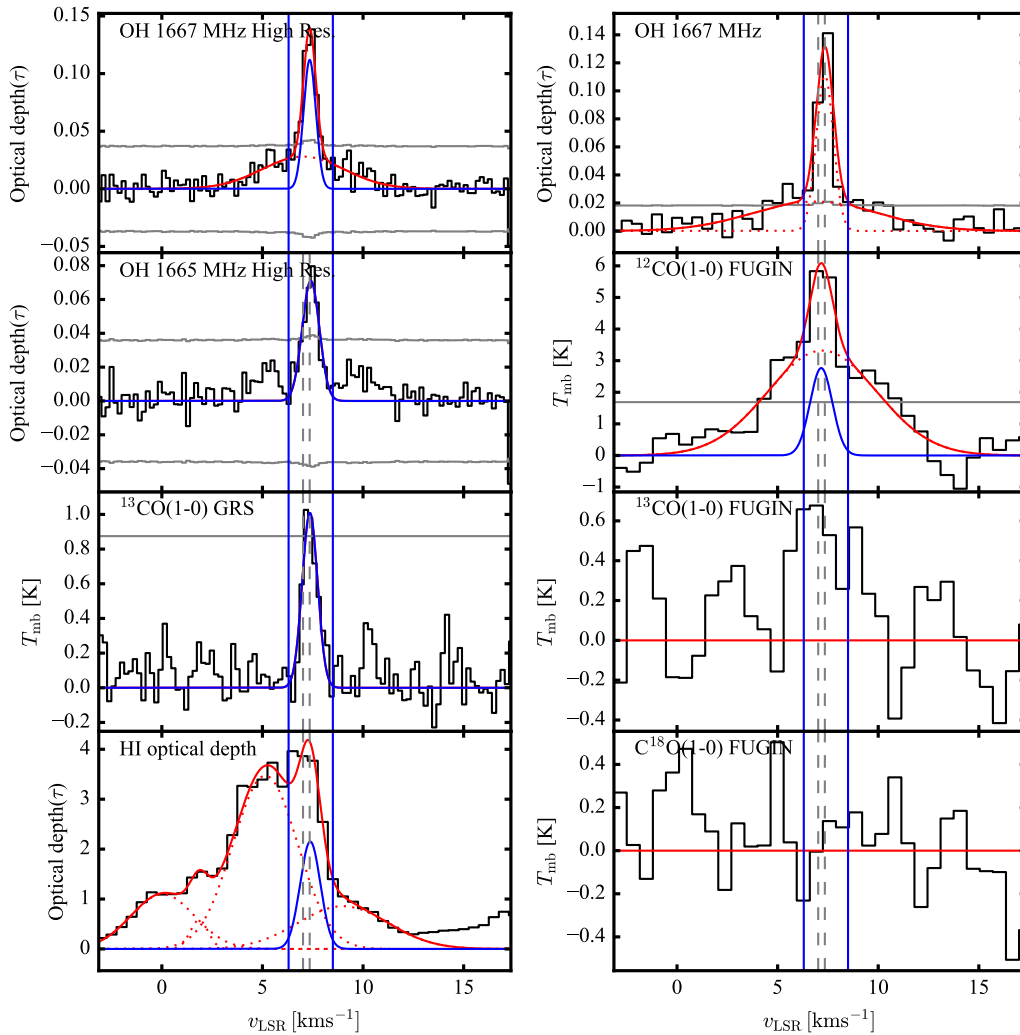


Figure 4.2: Gaussian decomposition of the OH absorption spectra towards Feature 1 in G21. (from the top:) The left column shows OH 1667 MHz and OH 1665 MHz optical depth with a channel width of 0.2 km s^{-1} , as well as the GRS $^{13}\text{CO}(1-0)$ transition and the H I optical depth. The right column shows the OH 1667 MHz absorption with a channel width of 0.5 km s^{-1} and the FUGIN $^{12}\text{CO}(1-0)$, $^{13}\text{CO}(1-0)$ and $\text{C}^{18}\text{O}(1-0)$ emission, at a channel width of 0.65 km s^{-1} and after smoothing to an angular resolution of $46''$. The 4σ level of the noise is shown as gray line (if not shown, all emission is below $< 4\sigma$). The red spectrum shows the composite model of each transition, consisting of multiple Gaussians highlighted by dashed red lines. The central velocity of the Gaussian components in the OH 1667 MHz transition at 0.2 km s^{-1} resolution (upper left panel) is shown in the other panels as gray, dashed line. Associated Gaussian components in velocity are shown in blue. The integration ranges of each subcomponent are based on the extents of the OH component in velocity, and is adopted subsequently in the other transitions (shown as blue, solid lines).

Table 4.4: Kinematic properties of OH absorption

Source	Feature	Flags	Transition	Survey	Nc	Center	Amplitude	FWHM	Gaus. Int.	Min. Res.
						[km s ⁻¹]	[K] ^a	[km s ⁻¹]	[K km s ⁻¹] ^b	[km s ⁻¹]
G21	1	0	¹² CO(1-0)	FUGIN	2	+7.2±0.1	2.767±0.518	1.3±0.3	3.837±1.194	1.3
	1	0	¹³ CO(1-0)	GRS	1	+7.4±0.1	1.009±0.150	0.9±0.2	0.965±0.219	0.4
	1	0	H ₁	VLA	5	+7.4±0.1	2.152±0.237	1.2±0.1	2.717±0.399	1.0
	1	0	OH1665	VLA	1	+7.4±0.0	0.071±0.006	1.0±0.1	0.076±0.010	0.4
	1	0	OH1667	VLA	2	+7.3±0.0	0.112±0.008	0.7±0.1	0.086±0.010	0.4
G21	2	0	¹³ CO(1-0)	GRS	2	+54.3±0.1	2.802±0.111	5.3±0.2	15.709±0.797	0.4
	2	1	H ₁	VLA	2	+55.3±0.0	3.194±0.073	4.9±0.0	16.510±0.399	1.0
	2	0	OH1665	VLA	2	+55.2±0.1	0.064±0.003	5.2±0.2	0.357±0.019	0.4
	2	0	OH1667	VLA	2	+55.1±0.1	0.112±0.003	5.7±0.1	0.680±0.024	0.4
G21	2	0	¹³ CO(1-0)	GRS	2	+56.2±0.0	3.463±0.179	1.8±0.1	6.697±0.514	0.4
	2	0	C ¹⁸ O(1-0)	FUGIN	1	+56.3±0.1	1.664±0.176	2.0±0.2	3.597±0.580	1.3
	2	0	OH1665	VLA	2	+56.4±0.0	0.216±0.006	0.8±0.0	0.186±0.008	0.4
	2	0	OH1667	VLA	2	+56.4±0.0	0.278±0.008	0.9±0.0	0.254±0.011	0.4
G21	3	0	OH1665	VLA	2	+66.9±0.1	0.026±0.005	0.8±0.2	0.022±0.006	0.4
	3	0	OH1667	VLA	3	+66.9±0.1	0.045±0.006	0.8±0.1	0.041±0.008	0.4
G21	3	0	OH1665	VLA	2	+68.6±0.1	0.031±0.006	0.6±0.1	0.018±0.005	0.4
	3	0	OH1667	VLA	3	+68.5±0.1	0.034±0.005	1.2±0.2	0.045±0.011	0.4
G21	3	1	¹² CO(1-0)	FUGIN	3	+73.6±0.3	2.575±0.184	7.0±0.6	19.303±2.211	1.3
	3	0	H ₁	VLA	5	+72.1±0.1	0.769±0.041	3.5±0.2	2.861±0.213	1.0
	3	0	OH1667	VLA	3	+72.5±0.2	0.032±0.003	3.8±0.4	0.128±0.017	0.4
G29	4	0	¹² CO(1-0)	FUGIN	6	+7.2±0.1	4.638±0.247	3.3±0.2	16.355±1.329	1.3
	4	2	¹³ CO(1-0)	FUGIN	1	+7.0±0.1	1.575±0.230	1.3±0.2	2.184±0.479	1.3
	4	0	¹³ CO(1-0)	GRS	1	+7.4±0.1	1.273±0.124	1.6±0.2	2.188±0.325	0.4
	4	0	H ₁	VLA	12	+6.7±0.0	1.675±0.025	2.5±0.1	4.379±0.267	1.0
	4	0	OH1665	VLA	2	+7.2±0.1	0.059±0.005	1.7±0.2	0.106±0.016	0.4
G29	4	0	OH1667	VLA	2	+7.2±0.0	0.099±0.006	1.6±0.1	0.172±0.017	0.4
	4	0	OH1665	VLA	2	+9.1±0.1	0.044±0.007	1.0±0.2	0.044±0.011	0.4
	4	0	OH1667	VLA	2	+9.0±0.1	0.065±0.007	0.9±0.1	0.063±0.011	0.4
	5	0	¹² CO(1-0)	FUGIN	6	+67.2±0.1	6.189±0.248	3.3±0.2	21.518±1.319	1.3
G29	5	0	¹³ CO(1-0)	GRS	1	+67.1±0.1	1.380±0.100	2.5±0.2	3.648±0.403	0.4
	5	0	H ₁	VLA	8	+68.3±0.2	1.211±0.186	5.6±0.3	7.177±1.189	1.0
	5	0	OH1667	VLA	1	+67.6±0.2	0.030±0.003	3.0±0.4	0.094±0.017	1.0
	6	1	¹² CO(1-0)	FUGIN	6	+102.6±0.1	18.294±0.860	4.9±0.3	95.388±7.963	1.3
G29	6	2	¹³ CO(1-0)	FUGIN	2	+102.4±0.1	5.833±0.147	5.1±0.3	31.470±1.808	1.3
	6	1	¹³ CO(1-0)	GRS	4	+101.7±0.1	4.073±0.935	1.6±0.2	6.884±1.732	0.4
	6	1	C ¹⁸ O(1-0)	FUGIN	2	+99.8±0.5	1.254±0.183	9.1±0.9	12.203±2.118	1.3
	6	1	OH1667	VLA	3	+101.7±0.3	0.058±0.004	3.2±0.5	0.197±0.032	0.4
	7	0	¹² CO(1-0)	PMO	2	-4.1±0.1	1.101±0.392	0.4±0.2	0.439±0.247	0.3
G31	7	0	H ₁	VLA	5	-4.3±0.0	0.550±0.006	1.7±0.0	0.981±0.015	1.0
	7	0	OH1665	VLA	2	-4.4±0.1	0.039±0.007	0.6±0.2	0.026±0.009	0.4
	7	0	OH1667	VLA	2	-4.5±0.0	0.081±0.008	0.7±0.1	0.061±0.011	0.4
	7	0	¹³ CO(1-0)	PMO	1	-3.8±0.1	0.718±0.163	0.5±0.1	0.377±0.131	0.4
G31	7	0	OH1665	VLA	2	-3.6±0.1	0.039±0.006	0.7±0.2	0.028±0.010	0.4
	7	0	OH1667	VLA	2	-3.6±0.0	0.066±0.008	0.6±0.1	0.041±0.009	0.4
	8	0	¹² CO(1-0)	PMO	1	+18.0±0.1	2.415±0.089	2.9±0.1	7.413±0.419	1.3
	8	0	¹³ CO(1-0)	PMO	1	+17.6±0.2	0.414±0.056	2.5±0.4	1.097±0.228	1.3
G31	8	0	OH1665	VLA	1	+17.9±0.0	0.071±0.005	1.1±0.1	0.084±0.009	0.4
	8	0	OH1667	VLA	1	+17.9±0.0	0.123±0.004	1.3±0.1	0.168±0.009	0.4
	9	0	H ₁	VLA	7	+37.4±0.0	0.791±0.011	2.0±0.0	1.678±0.044	1.0
	9	0	OH1667	VLA	1	+36.9±0.0	0.034±0.005	0.4±0.1	0.014±0.003	0.4
G31	10	1	H ₁	VLA	6	+73.1±0.1	2.972±0.176	2.2±0.2	7.008±0.782	1.0
	10	1	OH1667	VLA	7	+72.8±0.2	0.026±0.003	2.8±0.5	0.076±0.017	0.4
G31	10	1	¹³ CO(1-0)	PMO	2	+78.6±0.3	0.307±0.056	2.8±1.1	0.919±0.402	1.3
	10	1	H ₁	VLA	6	+78.3±0.2	1.819±0.199	2.2±0.4	4.266±0.951	1.0
	10	1	OH1665	VLA	1	+78.1±0.0	0.083±0.006	0.8±0.1	0.070±0.008	0.4
	10	1	OH1667	VLA	7	+78.1±0.0	0.123±0.005	0.9±0.0	0.113±0.007	0.4
G31	10	1	¹³ CO(1-0)	PMO	3	+91.8±0.4	0.359±0.052	3.1±0.9	1.189±0.369	1.3
	10	1	¹³ CO(1-0)	GRS	6	+91.3±0.8	0.435±0.079	4.0±3.2	1.872±1.542	1.3
	10	1	OH1667	VLA	7	+91.7±0.1	0.032±0.004	1.5±0.2	0.051±0.010	0.4

Notes: This table shows Gaussian components of the OH 1667 MHz optical depth which have been crossmatched to components in either the OH 1665 MHz, the ¹³CO(1-0), the ¹²CO(1-0) or the H₁ lines. Column 3 denotes flagged values: (0) not flagged; (1) flagged due to line-blending; (2) observation of transition from different dataset was used. Column 6 indicates the number of components used in the Gaussian fit (only the relevant component is shown). Column 10 denotes the integral of the Gaussian component, and Col. 11 the minimum resolvable FWHM.

Footnotes: (a) dimensionless for the OH/H₁ optical depth; (b) [km s⁻¹] for the OH/H₁ optical depth.

4.3.2 Column densities

4.3.2.1 Derivation of N_{OH}

We derive the OH column density analogously to Sect. 3.3.2. Since both main lines are observed for all three lines of sight, and the 1667 MHz transition has higher statistical weight, we only use the 1667 MHz transition to determine the column density of OH, as for a given sensitivity in τ the 1667 MHz transition probes lower column densities. In order to compare to the results from Chapter 3, we use the same assumption on the excitation temperature of this OH transition, i.e., $T_{\text{ex}} = 6.7$ K (Sect. 3.3.2.2), and compute the column density using Eq. (3.2).

4.3.2.2 Derivation of N_{HI}

We use the optical depths of HI, which were derived in Sect. 4.2.2 assuming that all emission is filtered out by the interferometer, such that the absorption spectrum is given by the attenuation of the radiation of the background source alone. We derive the HI column density analogously to Section 3.3.2, Eq. (3.4). An independent assessment of the spin temperature is beyond the scope of this chapter, and may be subject of future studies (see Sect. 4.5.5). Here, we assume a spin temperature of the absorption HI gas of $T_S = 100$ K (e.g., [Bühr et al. 2015](#), and discussion therein).

4.3.2.3 Derivation of $N_{^{13}\text{CO}}$ and N_{H_2}

To compare the results of the high-resolution observations to the results obtained in Chapter 3, we derive N_{H_2} from $^{13}\text{CO}(1-0)$ emission and provide results with the same assumptions on the CO excitation as in Sect. 3.3.2.3. This was done in the optically thin approximation (Eq. C.10), using an excitation temperature for the $^{13}\text{CO}(1-0)$ transition of $T_{\text{ex}} = 20$ K (motivated by the association of the majority of molecular gas with star-forming regions in Chapter 3). The integrated emission of the $^{13}\text{CO}(1-0)$ transition is listed in Table 4.3. We estimate the upper limits on $N_{^{13}\text{CO}}$ (and on N_{H_2}) in case of non-detections with a Gaussian of an amplitude of $3 \times \sigma(T_{^{13}\text{CO}})$ and a FWHM of 1.8 km s^{-1} (see Sect. 4.4.2.3). A conversion factor to molecular hydrogen of $N_{\text{H}_2} = 3.8 \times 10^5 \times N_{^{13}\text{CO}}$ was applied (see Sect. 3.3.2.3; [Bolatto et al. 2013](#); [Pineda et al. 2008](#)). These results are presented in Table 4.5.

4.3.2.4 Systematic uncertainties

We assume the same systematic uncertainties on column densities as in Chapter 3, because we use the same excitation assumptions. For clarity, as described in Sect. 3.3.2.5, the assumed, systematic uncertainties are of a factor of two in N_{OH} , a factor of 3.5 in N_{H_2} and a factor of 4 in OH abundances $X_{\text{OH}}(N_{\text{H}_2}) = N_{\text{OH}}/N_{\text{H}_2}$ and $X_{\text{OH}}(N_{\text{H}}) = N_{\text{OH}}/N_{\text{H}}$ (see Sect. 4.4.4 and 4.4.5).

Table 4.5: Abundances and column densities of OH

Source	Feature	v [km s ⁻¹]	N_{OH} [$\times 10^{14}$ cm ⁻²]	$N_{^{13}\text{CO}}$ [$\times 10^{15}$ cm ⁻²]	N_{H_2} [$\times 10^{21}$ cm ⁻²]	$N_{\text{H I}}$ [$\times 10^{21}$ cm ⁻²]	$X_{\text{OH}}(N_{\text{H}_2})$ [$\times 10^{-7}$]	$X_{\text{OH}}(N_{\text{H I}})$ [$\times 10^{-7}$]
G21	1	+7.4	2.16±0.10	1.23±0.20	0.47±0.08	1.29±0.05	4.61±0.77	0.97±0.08
	2	+56.5	7.32±0.10	12.53±0.20	4.76±0.08	>1.94	1.54±0.03	0.64±0.02
	3	+66.6	0.70±0.08	<1.62	<0.62	0.12±0.00	>1.13	>0.52
	3	+68.8	0.73±0.08	<1.62	<0.62	0.11±0.00	>1.18	>0.54
	3	+73.5	1.90±0.14	<1.62	<0.62	1.38±0.01	>3.09	>0.73
G29	4	+6.5	2.64±0.14	2.77±0.28	1.05±0.11	0.88±0.01	2.50±0.29	0.88±0.08
	4	+9.7	1.14±0.11	<1.79	<0.68	0.38±0.00	>1.68	>0.65
	5	+67.5	1.62±0.21	5.53±0.43	2.10±0.17	1.45±0.01	0.77±0.12	0.29±0.04
	6	+102.4	2.98±0.10	39.33±0.33	14.95±0.13	>3.05	0.20±0.01	0.09±0.00
G31	7	-4.8	0.95±0.08	<1.48	<0.56	0.11±0.00	>1.69	>0.77
	7	-3.5	0.58±0.06	0.45±0.10	0.17±0.04	0.08±0.00	3.41±0.87	1.39±0.30
	8	+17.5	2.74±0.11	1.39±0.18	0.53±0.07	>3.62	5.19±0.72	0.59±0.05
	9	+37.0	0.30±0.04	<0.58	<0.22	0.29±0.00	>1.35	>0.41
	10	+71.9	1.04±0.11	0.77±0.17	0.29±0.07	2.54±0.04	3.56±0.88	0.33±0.04
	10	+75.5	0.59±0.07	0.91±0.13	0.35±0.05	0.90±0.01	1.71±0.33	0.37±0.05
	10	+78.1	1.77±0.08	0.88±0.13	0.34±0.05	0.86±0.01	5.26±0.82	1.15±0.09
	10	+81.8	0.75±0.09	<0.58	<0.22	>2.67	>3.40	>0.24
	10	+85.1	1.38±0.08	<0.58	<0.22	>1.88	>6.29	>0.60
	10	+92.0	0.85±0.09	1.25±0.15	0.48±0.06	1.33±0.01	1.78±0.28	0.37±0.04

Notes: These values were derived with the same excitation conditions of Chapter 3: $T_{\text{ex}}(\text{OH } 1667 \text{ MHz}) = 6.7 \text{ K}$, $T_{\text{ex}}(^{13}\text{CO}) = 20 \text{ K}$ and $T_{\text{ex}}(\text{H I}) = 100 \text{ K}$. The column density averaged abundances are defined as $X_{\text{OH}}(N_{\text{H}_2}) = N_{\text{OH}}/N_{\text{H}_2}$ and $X_{\text{OH}}(N_{\text{H I}}) = N_{\text{OH}}/N_{\text{H I}}$.

4.4 Results

4.4.1 Probing the optical depth of H I

Figure 4.3 shows the H I optical depths from THOR and the VLA follow-up observations. The H I absorption features at $\tau \leq 2$ agree well. There are only slight differences. Three velocity bins between 20 and 45 km s⁻¹ towards G31, as well as one velocity bin at 18 km s⁻¹ in G29, show slightly deeper absorption in the THOR data. Otherwise, both spectra agree well in this optical depth regime.

This is especially reassuring, since features that were barely spectrally resolved in THOR can be well distinguished as true absorption features. Examples are the peaks towards G29 at 7 km s⁻¹ and 18 km s⁻¹. While no new substructure is revealed in the unresolved H I components, this can be used in the interpretation of the H I optical depth spectra of THOR in the future.

The second result is the higher optical depth which can be probed here. The median maximum optical depth in the follow-up data are τ_{max} of 4.1, 3.8 and 4.1 for G21, G29 and G31, respectively. The THOR data, has maximum optical depths of 2.6, 2.8, and 3.3, respectively, which corresponds to an increase of 20–60 % in the maximum optical depths. Using Eq. (3.4), with a spin temperature of 100 K, this corresponds to a maximum column density per 1-km s⁻¹-wide channel of $N_{\text{H I}} \sim 7.5 \times 10^{20} \text{ cm}^{-2} \text{ km}^{-1} \text{ s}$.

We further note that some features which saturated in the THOR data, are not saturated in the VLA follow-up data. This is the case for the features at 5 km s⁻¹ and 42 km s⁻¹ towards G21, which are associated with the near side of the Sagittarius and the Scutum

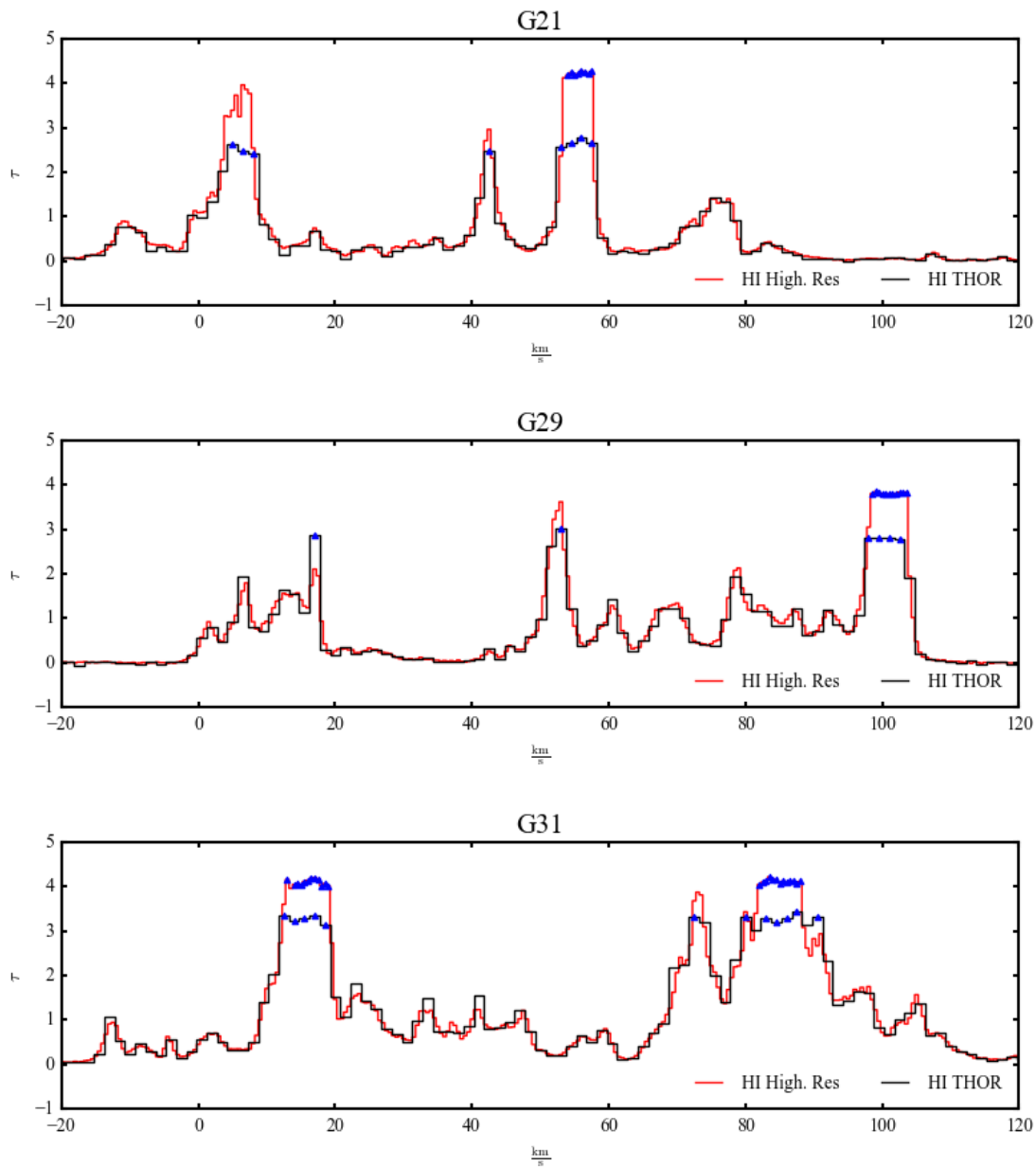


Figure 4.3: Optical depths derived from H I absorption spectra. The panels show the three lines of sight which were observed in the VLA follow-up study (*red*), in comparison to the results obtained with THOR (*black*). Blue triangles denote saturated absorption channels (i.e., completely absorbed continuum emission within the noise of the observations).

arm, respectively (as determined by the bayesian distance calculator from the BeSSeL survey²; Reid et al. 2016). For G29, the optical depth at 56 km s⁻¹ is detected in the VLA follow-up observations, which can also be attributed to the near side of the Scutum arm, given the distance of ≈ 6 kpc to the continuum source (e.g., Pratap et al. 1999; Russeil et al. 2011). In G31, the optical depth between 70–80 km s⁻¹ is now resolved, a feature attributed to the near side of the Scutum arm.

Some H I spectra are saturated even in the VLA follow-ups: For G21 between 53–60 km s⁻¹ (near side of Scutum arm), for G29 at 100 km s⁻¹ (likely associated with the H II region G29.96-0.02 itself), and for G31 between 12–20 km s⁻¹ (near side of Sagittarius arm) and 80–90 km s⁻¹ (near side of Scutum arm). If different sightlines are compared for each spiral arm, both the Sagittarius and Scutum arms show saturated and non-saturated absorption. Saturation of the H I absorption therefore is not specifically associated with a certain spiral arm. The H I absorption features share two similarities. First, the width in velocity (the difference between the maximum and minimum velocity of the channels, which saturate), over which the spectrum saturates is very similar in all cases, and is typically of $(v_{\text{sat}}^{\text{max}} - v_{\text{sat}}^{\text{min}}) \approx 6$ km s⁻¹. Second, for most lines that are not saturated in the VLA follow-up, but were in THOR, the FWHM is narrow (with a Gaussian FWHM of $\Delta v \sim 3-4$ km s⁻¹; the absorption in G21 between 3–10 km s⁻¹ is broader, but may contain multiple components).

4.4.2 Characteristics of OH detections

This section characterizes the detection statistics, the environment, the excitation and the kinematics of the OH 1667 MHz absorption components.

4.4.2.1 Detection statistics

We find 23 distinct OH components in the OH 1667 MHz transition from Gaussian fits in the three lines of sight (second approach in Sect. 4.3.1). The optical depth of the VLA follow-up study mainly traces low optical depths of $\tau = 0.02 - 0.15$ (Fig. 4.4), which correspond to typical optical depths found for diffuse molecular gas (e.g., Dickey et al. 1981; Liszt & Lucas 1996).

Two components are clearly associated with GMCs, and possibly also with gas around H II regions directly. This is G29 between 95–110 km s⁻¹ and G21 at 56.4 km s⁻¹. At both velocities, emission of C¹⁸O is detected (Figs. C.2 and C.6). This is a clear indication of the presence of dense gas. For G29, this narrow component at 56.5 km s⁻¹ is not present in the ¹²CO, likely due to optical thickness. The ¹³CO emission peak in GRS is slightly flattened which may point to optical thickness also in the ¹³CO emission peak. In fact, it has an optical depth of $\tau_{^{13}\text{CO}} = 0.8$ (see Table 4.5), indicating that it is almost optically thick. In contrast, the C¹⁸O transition is optically thin with an optical depth of $\tau_{\text{C}^{18}\text{O}} = 0.2$.

OH absorption/emission at velocities of 95–110 km s⁻¹ in G29 agree well with the velocity of the H II region itself. This indicates that the OH gas may be affected by the

²<http://bessel.vlbi-astrometry.org/bayesian>

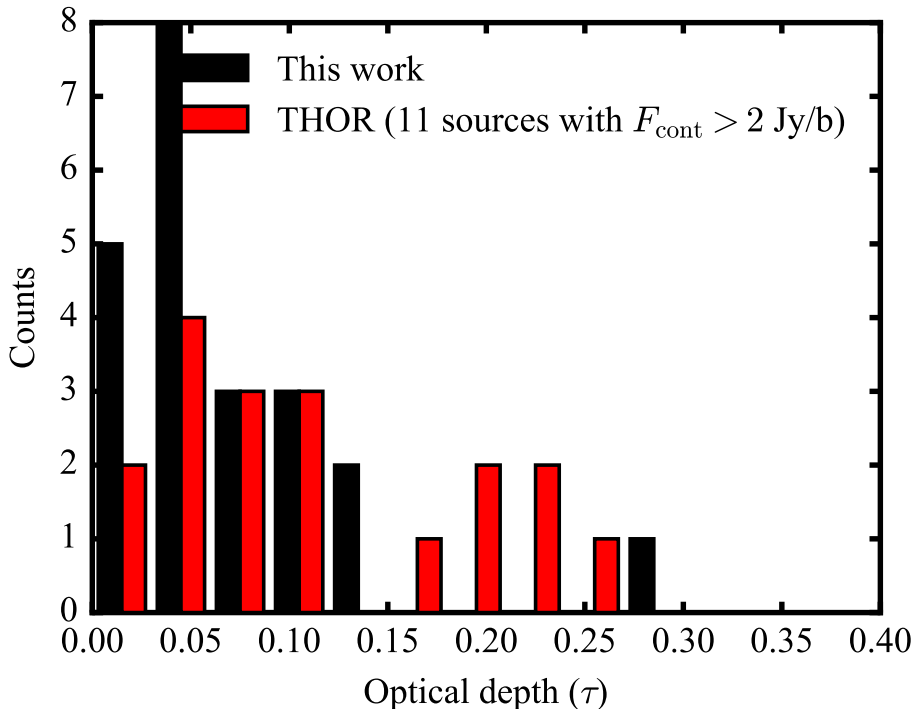


Figure 4.4: Histogram of peak optical depths of the OH 1667 MHz transition in the VLA follow-up observations (*red*), and the OH 1665/1667 MHz transitions from THOR (*black*). The sources from THOR were selected to have similar sensitivity as the VLA follow-up observations ($\tau_{\min} \sim 0.02$ per 1.5 km s^{-1} channel in this case). This sensitivity limit roughly corresponds to sources with continuum strengths larger than 2 Jy beam^{-1} at $46''$ (see Sect. 3.3.1.1).

enhanced infrared-radiation and dynamics of the star forming site. For G21, a first cross-match with the H II region catalog WISE (Anderson et al. 2014) did not yield any nearby sources – follow-up searches are necessary to determine the presence of young stellar sources. The effect of the nearby star formation on the OH transitions is discussed in the next section.

The rest of the components are likely to be associated with diffuse cloud material. They show ^{12}CO and/or ^{13}CO , but no C^{18}O emission. Some of them are not significantly detected in CO emission. When investigating all spectra in fixed velocity ranges (first approach in Sect. 4.3.1; Table 4.3), 8 of 19 features do not show evidence of significant ^{13}CO emission. Towards two locations even ^{12}CO is not detected (G21 at 68 km s^{-1} and G31 at 37 km s^{-1} ; Figs. C.3–C.9). We take this as evidence for the lack of dense gas at these velocities and refer to them as diffuse components.

4.4.2.2 OH excitation

From their statistical weights, both OH main line transitions are expected to have an optical depth ratio of $\tau_{1667\text{MHz}}/\tau_{1665\text{MHz}} = 1.8$, if they are in local thermal equilibrium (LTE). In order to test if this holds for our sample, the peak optical depths of the OH 1665 and 1667 MHz transitions are plotted against each other in Fig. 4.5. We choose all

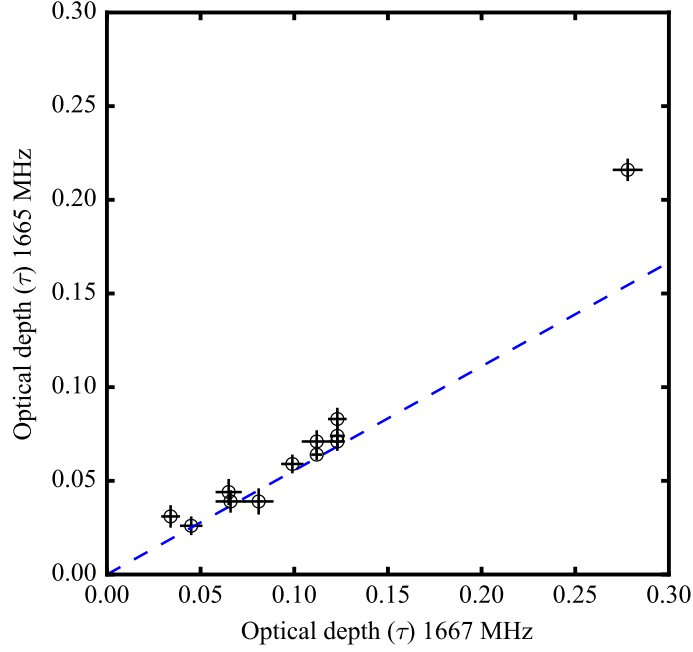


Figure 4.5: Comparison of peak OH optical depths of the OH 1665 MHz and OH 1667 MHz transitions. The errorbars indicate 1- σ uncertainties. The *blue dashed line* indicates the LTE ratio of $\tau_{1667\text{MHz}}/\tau_{1665\text{MHz}} = 1.8$.

velocity components that have been modelled with Gaussians in both the OH transitions (Table 4.4). As comparison, the LTE ratio is drawn as blue dashed line.

The majority of the datapoints agree with the LTE main line ratio with the median of all datapoints at 1.7 (LTE ratio is at 1.8). Five out of twelve points deviate from it within 1- σ uncertainties towards higher OH 1665 MHz optical depths than the expected LTE ratio, and only one within 3- σ uncertainties. Both OH components, which have been associated with dense gas in the previous section show strong deviations from the LTE value. The strongly deviating ratio of 1.3 corresponds to the G21 component at 56.4 km s^{-1} . For G29 at 101.5 km s^{-1} , the OH 1665 MHz is masing, i.e., has a negative optical depth ($\tau = -0.29$). The alteration of the excitation conditions is potentially due to the presence of strong infrared emission or shocks. At least for G29, these could be caused by the associated H II region.

Apart from these outliers, the optical depth ratios are within LTE, and, if any, only small deviations are found. In both the number of sources affected and the size, these deviations appear less severe than the results presented in Li et al. (2018) for the Millennium sample. They find that most of the sources show deviations from the LTE ratio, a few of them also stronger than the strongest deviation here of the G21 component at 56.4 km s^{-1} . The other difference to be noted is that we do not find deviations to higher ratios, i.e., to higher $\tau_{1667\text{MHz}}$ or lower $\tau_{1665\text{MHz}}$ than expected, while a few sources in Li et al. (2018) have higher ratios. It needs to be noted that their comparison was based on 1- σ variations. If a 3- σ threshold was applied, the number of deviations would significantly decrease. However, as seen already in this sample, the environment affects the excitation conditions

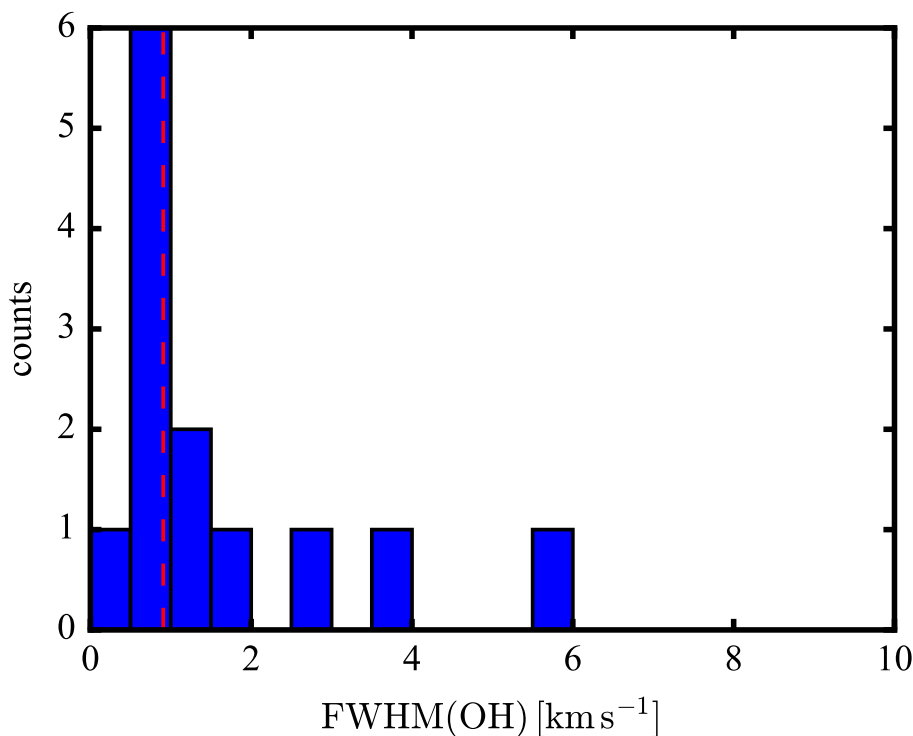


Figure 4.6: Histogram of measured OH 1667 MHz line widths which have been matched to either the OH 1665 MHz line, a CO transition or to H I absorption. The *red dashed line* indicates the median of the sample.

of OH. The difference may be found in the larger sample of OH detections in the Millennium survey. Thus it potentially samples a larger variety of excitation conditions and finally main line ratios.

4.4.2.3 OH kinematics

We investigate the width of the OH, CO and H I spectral lines to estimate the velocity distributions of the particles in the absorbing/emitting gas.

Line widths of OH: The distribution of those OH 1667 MHz components, which are associated with other gas tracers (either OH 1665 MHz, CO or H I; see Sect. 4.3.1 and all unflagged OH 1667 MHz components in Table 4.4), contains 13 components and is shown in Fig. 4.6. It has a median FWHM of 0.9 km s^{-1} and a long tail with components of up to 6 km s^{-1} .

OH is present in both narrow ($<2 \text{ km s}^{-1}$) and broader components ($>2 \text{ km s}^{-1}$), e.g., G21 at 7 km s^{-1} (Fig. 4.2) and at 55 km s^{-1} (Fig. C.2). At least the second feature indicates that two different densities are traced. The narrow component has been discussed Sect. 4.4.2.1. The broad component is traced by ^{12}CO and ^{13}CO and is absent in C^{18}O , which indicates lower densities. Both components are potentially connected if they arise from a site of star formation, with the broad component indicative of a molecular outflow

(e.g., Beuther et al. 2002).

In the case of the G21 component at 7 km s^{-1} , the narrow line is traced by ^{13}CO (only in the GRS spectrum, not detected in the FUGIN data), while the broader, weak component in the OH 1667 MHz line (detected at $4\text{-}\sigma$ in the low-resolution OH spectrum), has a counterpart in ^{12}CO emission only.

Line widths of ^{13}CO and H I: The median of the ^{13}CO line widths which have been matched to the OH components is 1.8 km s^{-1} (7 components) and the median of the H I line widths is 2.2 km s^{-1} (6 components).

Component-by-component comparison: We compare the line widths of the OH 1667 MHz transition with the line width of ^{13}CO in Fig. 4.7. We find that 5 out of 7 sources align well with a 1:1 correlation, while two sources show CO line widths, which are larger than OH by $\sim 1 \text{ km s}^{-1}$. Due to the limited sample size, we decided not to statistically determine the correlation. The fact that the majority of the sources agree in line width is an indication that both tracers probe gas at similar conditions. For the components G31 at 17 km s^{-1} and G21 at 56.5 km s^{-1} , the line widths of CO are higher than of OH. There are also other, narrower OH components, which are not detected in CO, such as the component towards G31 at 37 km s^{-1} . This indicates that, while some OH components trace the same gas as CO, other, more narrow components in OH may be associated with less turbulent gas than ^{13}CO .

The line width of H I is compared to the OH 1667 MHz line widths in Fig. 4.8. Apart from one case (G21 at 72.5 km s^{-1}), the H I component always has a higher line width than OH. It has to be noted that there is considerably higher uncertainty on the decomposition of the H I spectrum than on the OH spectrum due to its complexity. The higher line widths can be an indication of H I tracing either warmer material or of blending of extended cloud material with intrinsic velocity differences.

Non-thermal line widths: The non-thermal contribution to the line width is given as (assuming that the underlying velocity distribution is Gaussian),

$$\Delta v_{\text{nonthermal}} = \sqrt{v_{\text{measured}}^2 - v_{\text{thermal}}^2} = \sqrt{v_{\text{measured}}^2 - \left(\frac{2kT_{\text{kin}}}{m}\right)}, \quad (4.2)$$

with $v_{\text{nonthermal}}$ the non-thermal, v_{measured} the measured, v_{thermal} the thermal line width, which depends on T_{kin} the kinetic temperature, m the mass of the atom/molecule and k the Boltzmann constant. The line widths in all transitions are mostly non-thermal, assuming maximum kinetic gas temperatures of 130 K for the atomic (corresponding to a line width 1.5 km s^{-1}) and 50 K for the molecular gas components (corresponding to a line width of 0.22 km s^{-1} for OH and 0.17 km s^{-1} for CO). For the ^{13}CO and OH lines, the thermal line widths give negligible contributions to the observed line width, such that the observed line width is equal to the non-thermal line width within 0.1 km s^{-1} . The thermal contribution to the line width of H I is significantly larger.

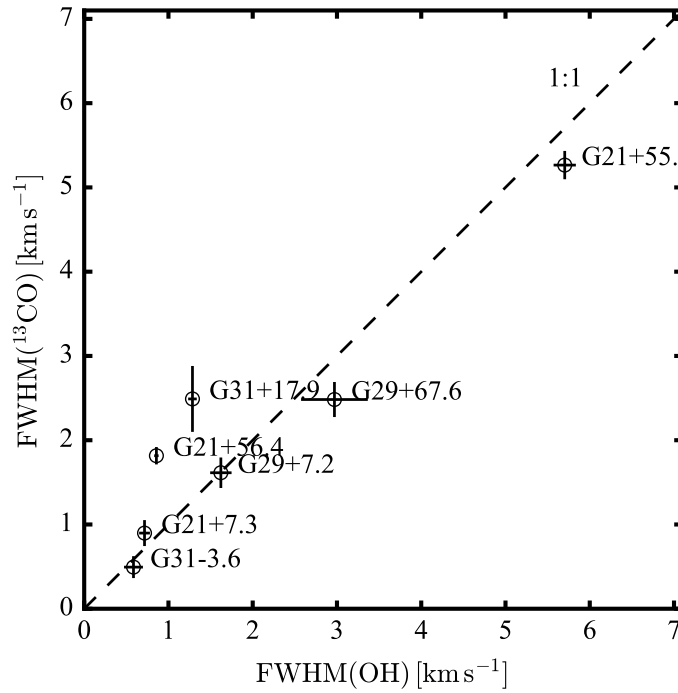


Figure 4.7: Comparison of the $^{13}\text{CO}(1-0)$ and OH 1667 MHz line widths for the seven associated components. The *dashed line* indicates the location of equal line widths in both transitions.

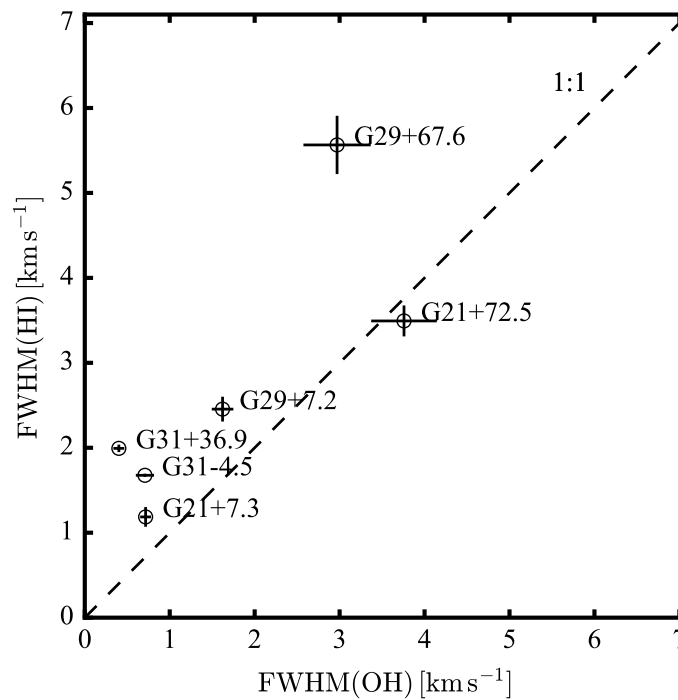


Figure 4.8: Comparison of H I and OH 1667 MHz line widths for the six associated components. The *dashed line* indicates the location of equal line widths in both transitions.

An indication for OH and H I absorption arising from the same parcel of gas is that they share similar kinetic temperatures. In order to test this, we assume that OH and H I have the same kinetic temperature and vary it, such that their non-thermal line widths are equal. Reasonable estimates for T_{kin} are only found for G21 at 7.3 km s^{-1} , with $T_{\text{kin}} = 57 \text{ K}$ and $v_{\text{nonthermal}} = 0.68 \text{ km s}^{-1}$. This temperature is in excellent agreement with (warm) OH temperatures found in outskirts of molecular clouds (60 K; Ebisawa et al. 2015). The line width of ^{13}CO is higher but within uncertainties of the OH transition. This suggests that OH, H I and CO are tracing gas with similar properties for this component.

For the component towards G21 at 72.5 km s^{-1} , OH and H I lines agree but are clearly non-thermal. Reason could be blending of multiple components along the line of sight, as indicated in the OH 1667 MHz spectrum at low spectral resolution (Fig. C.3).

For the other four components, the estimated kinetic temperatures are significantly higher than typical OH gas temperatures (the next closest kinetic temperatures to $T_{\text{kin}} \sim 60 \text{ K}$ are G31 at -4.5 km s^{-1} with 150 K and G29 at $+7.2 \text{ km s}^{-1}$ with 220 K). Therefore, either the H I absorption traces considerably warmer gas than OH or non-thermal contributions to the line widths are significantly higher than those of the OH (or CO) gas. Both suggest that for these four components the H I absorption traces additional layers of gas which are not contributing to the OH absorption.

4.4.3 VLA follow-up observations in comparison to THOR

4.4.3.1 OH optical depth

To compare the distribution of the OH optical depths of the VLA follow-up observations we the THOR survey, we compare the optical depths with lines of sight in THOR with similar sensitivity. We select absorption spectra from THOR with a continuum strength of above 2 Jy beam^{-1} , which corresponds roughly to a $4\text{-}\sigma$ level of 0.02 (see Sect. 3.3.1.1). We plot the histogram of both samples in Fig. 4.4.

We see a similar distribution of optical depths between $\tau = 0.03$ and 0.12 in both datasets. On the high end of the distribution, the THOR data has 6 detections with optical depths between $\tau = 0.15$ and 0.3, while the VLA follow-up data shows only one detection.

The discrepancy at high optical depths likely arises from a selection effect. The THOR data contains many more detections associated with molecular gas from H II-regions than the VLA follow-up. The high τ_{OH} are typically associated with molecular gas in the vicinity of H II regions, which is likely to be denser than diffuse molecular clouds. Consistent with this association, the only VLA follow-up measurement which falls in this range of optical depths is associated with dense gas (Sect. 4.4.2.1). The lower number of high optical depths is therefore likely due to the lower number of gas components in the VLA follow-up sample, which is associated with H II-regions.

For lower optical depths than 0.03, there are more features in the follow-up survey than in THOR, which is mainly because of two reasons. First, the cut in detection limit in the THOR survey was only approximate. Second, the velocity resolution of the new VLA data is better, such that narrower components can be detected. In conclusion, the optical depths in both samples are found in agreement, as long as selection effects due to the

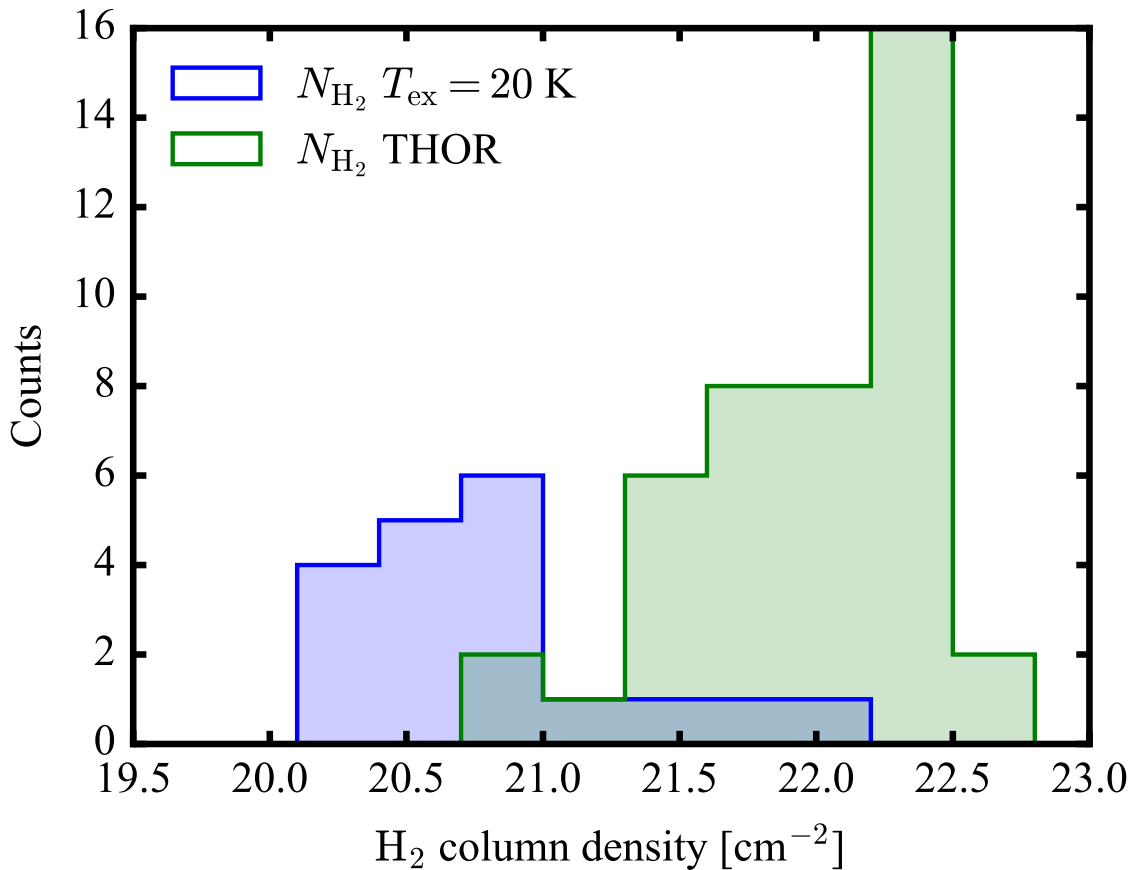


Figure 4.9: H₂ column densities as derived from ¹³CO(1-0) emission of this work (*blue*) and THOR (*green*). Upper limits on the H₂ column density are treated as detections.

environment of the gas are taken into account.

4.4.3.2 Distributions of N_{H_2}

The selection effects become more evident when comparing the distributions of N_{H_2} for all OH measurements in THOR and in the VLA follow-up. Figure 4.9 shows that the H₂ column densities probed in the VLA follow-up complement the THOR dataset at lower column densities. The bulge of the distribution of column densities in THOR reaches down to $N_{\text{H}_2} = 2 \times 10^{21} \text{ cm}^{-2}$, while only a small numbers of velocity components exceed this value in the VLA follow-up sample.

The data presented here extends to lower N_{H_2} of $N_{\text{H}_2} = 1 - 4 \times 10^{20} \text{ cm}^{-2}$. It also needs to be noted, that many of these detections are upper limits derived from ¹³CO(1-0), and are included in this histogram with the value of the upper limit. The true H₂ content of these components cannot be determined with certainty. The non-detection of ¹³CO(1-0) indicates lower column densities, but H₂ may still be present, if regions are traced which contain significant fractions of CO-dark gas.

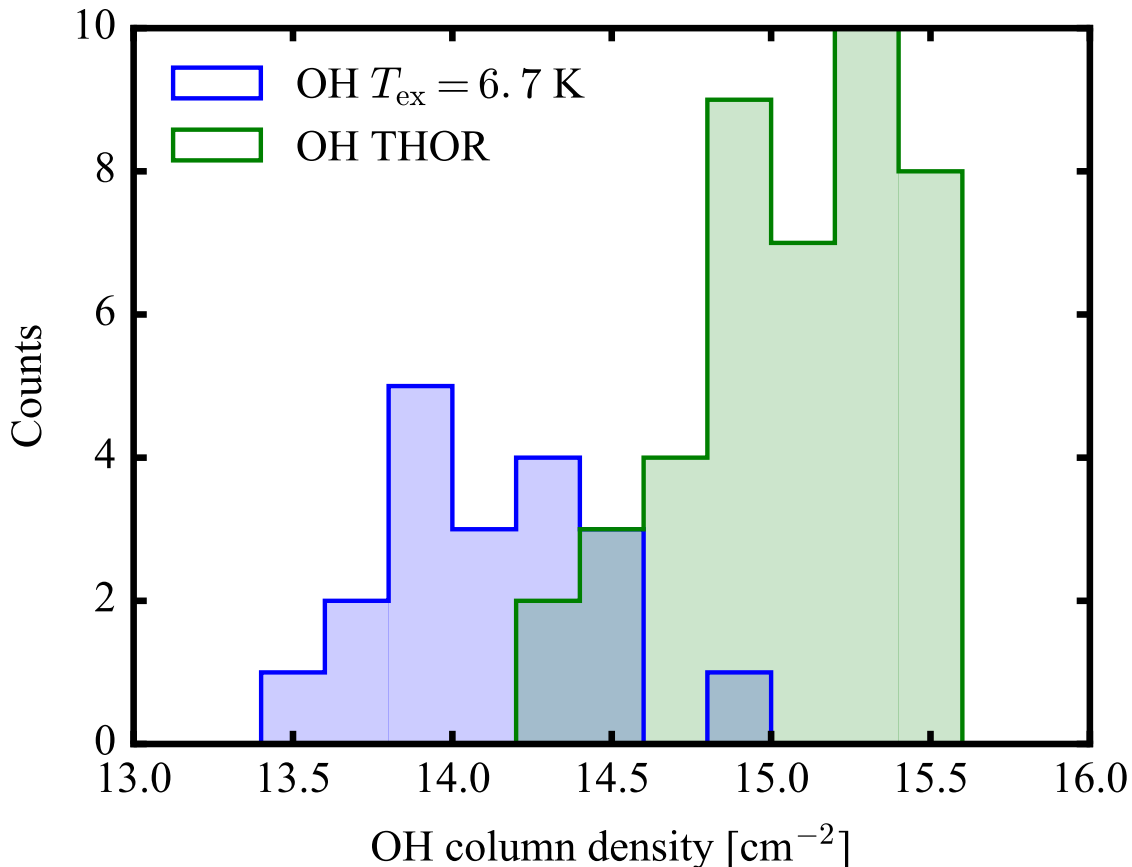


Figure 4.10: OH column densities of this work (*blue*) and THOR (*green*).

4.4.3.3 Distributions of N_{OH}

The distributions of the OH column densities for both samples are also affected by the selection effects indicated in the previous two paragraphs. In Fig. 4.10, we compare the distribution of N_{OH} investigated with the VLA follow-up observations with N_{OH} from THOR (Chapter 3). While both investigations span an order of magnitude in column density, the follow-up observations complement the THOR sample ($N_{\text{OH}} \sim 10^{14.5-15.5}$) to lower N_{OH} ($N_{\text{OH}} \sim 10^{13.5-14.5}$).

The OH column densities derived from the VLA follow-up observations extend to lower values due to the higher sensitivity of the new VLA observations, and also due to the higher spectral resolution. Components such as towards G31 at 37 km s^{-1} would not have been detected at lower resolution - even at the spectral resolution of the high resolution OH data (0.2 km s^{-1}), it is not resolved. Also, the OH 1667 MHz transition was only observed in the second half of the THOR survey, and therefore the sensitivity for a given column density was effectively lower in the first half of the THOR survey (Sect. 3.2). For the follow-up observations, all four OH ground state transitions were observed.

4.4.4 OH abundance with respect to molecular hydrogen

4.4.4.1 N_{OH} vs. N_{H_2}

The lower N_{OH} and N_{H_2} in the VLA follow-up allow us to extend the correlation analyzed in Sect. 3.3.2.6. We combine the follow-up observations with the THOR dataset and fit a linear correlation in logarithmic space to N_{OH} and N_{H_2} . As described in Sect. 3.3.2.6, we account for systematic uncertainties with the same method of sampling the posterior distribution of the slope m and do not include measurements with upper limits on the H_2 column density.

The resulting relation of $\log(N_{\text{OH}})$ vs. $\log(N_{\text{H}_2})$ has a slope of $m = 0.52^{+0.09}_{-0.09}$. It is shown in Fig. 4.11, together with the data. Appendix C.1 gives details on the posterior distribution of m . The slope is steeper than the fit of the THOR data alone ($m = 0.33$), but still excludes a linear relation beyond the 3σ confidence interval.

4.4.4.2 $X_{\text{OH}}(N_{\text{H}_2})$ vs. N_{H_2}

In order to investigate variations of the OH abundance at different N_{H_2} , we plot both quantities against each other. The column density averaged OH abundance is given by $X_{\text{OH}} = N_{\text{OH}}/N_{\text{H}_2}$. It is shown in Fig. 4.12, together with the data from THOR (Sect. 3.3.2.7).

The OH abundance is slightly decreasing with increasing N_{H_2} . Since the relation between $\log(N_{\text{OH}})$ and $\log(N_{\text{H}_2})$ is sublinear, the trend seen here is statistically significant. The detection limit decreased in the new observations, both due to better sensitivity and higher spectral resolution, which allows us to identify more narrow features. The OH absorption features with $N_{\text{H}_2} < 2 \times 10^{21} \text{ cm}^{-2}$ lie above the literature abundance ratio of $X_{\text{OH}} = 1 \times 10^{-7}$ (Liszt & Lucas 2002), but most of them within the systematic uncertainties.

Triangles in Fig. 4.12 denote non-detections of ^{13}CO emission and therefore an upper limit on N_{H_2} and a lower limit on $X_{\text{OH}}(\text{H}_2)$. As also discussed in Sect. 3.3.2.5, it is possible that these components emerge from gas in which the H_2 fraction is significant, but which is not shielded sufficiently such that ^{13}CO can form. The actual H_2 column density may therefore be higher than the upper limit on N_{H_2} . Thus, the actual H_2 column density could be lower, equal or even higher than the estimates given here. It is for this reason that they are not indicated as formal upper limits and highlighted in gray.

The lowest value in $X_{\text{OH}}(N_{\text{H}_2})$ from the VLA follow-up sample is towards G29 at 102.4 km s^{-1} . One of the two sources from the THOR sample at similar low OH abundances ($X_{\text{OH}}(N_{\text{H}_2}) \approx 0.2 \times 10^{-7}$) is at similar velocity and direction. G29.935-0.053 at 97.8 km s^{-1} is located just south from it (w.r.t. Galactic coordinates). Both show deviations from LTE - for G29 at 102.4 km s^{-1} , the OH 1665 MHz transition shows maser emission (see also Sect. 4.4.2.2), while for G29.935-0.053 at 97.8 km s^{-1} , the ratio of the OH mainlines is significantly lower than the LTE ratio of 1.8 km s^{-1} (see Fig. B.6). This potentially affects the OH column densities, but a closer investigation would require detailed radiative transfer modelling, which is beyond the scope of this work. The third feature at this low OH abundance, G30.783-0.028 at 94.0 km s^{-1} , consists of three weak OH components associated with one broad ^{13}CO component. They were combined to

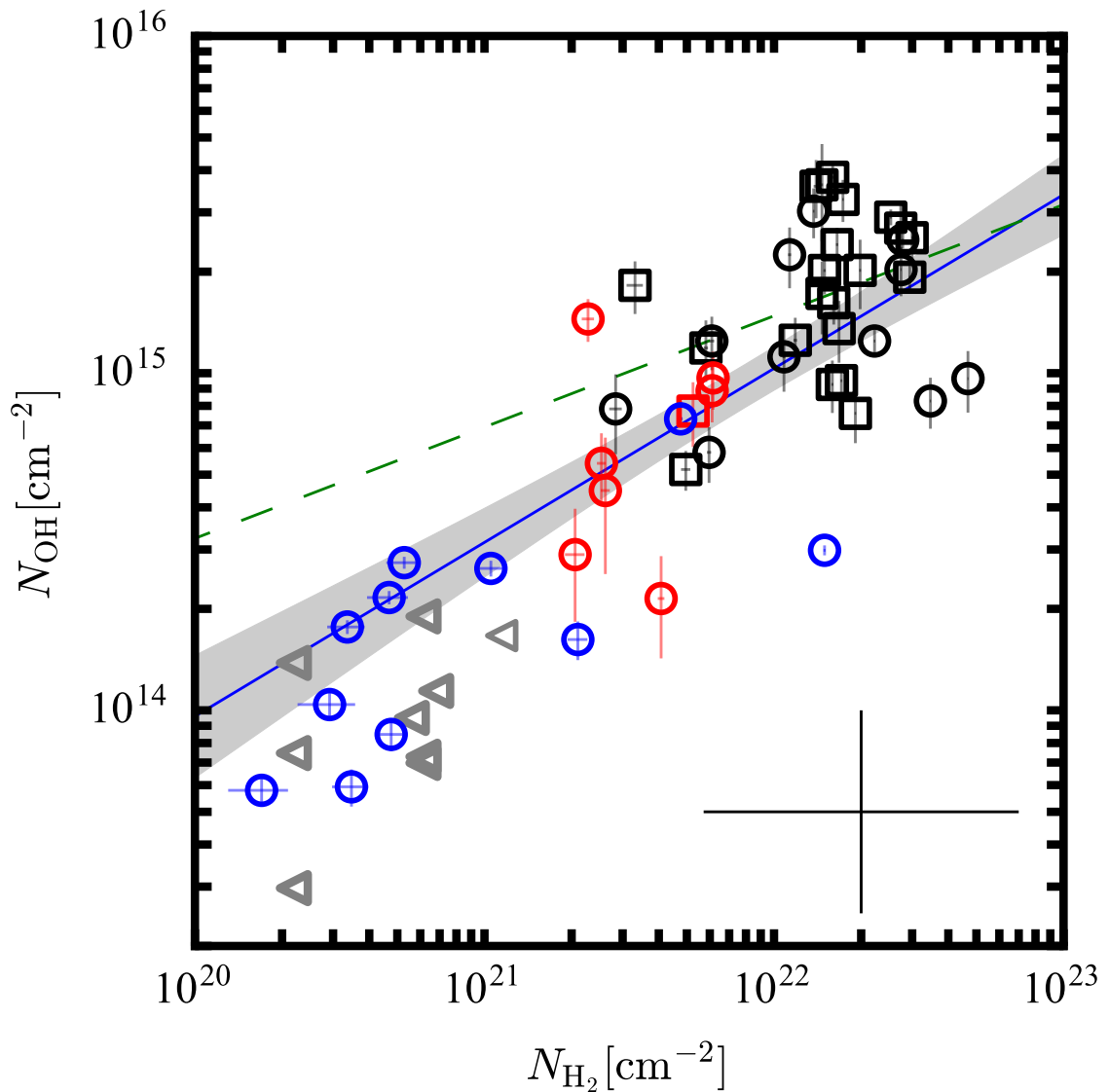


Figure 4.11: Column densities of OH and H₂ in comparison (see also Fig. 3.7). The plot shows both the results from the OH high-resolution observations presented in this chapter (*blue*), and the results from the THOR survey (Chapter 3; in *black* or *red*, depending on if associated with H II regions or not). Upper limits on N_{H_2} , as determined from $N_{13\text{CO}}$, are highlighted with *triangles* pointing to the left. The results of fitting a linear correlation in logarithmic space to the THOR data alone is shown as *dashed green line*. The relation obtained by fitting the combined THOR and VLA follow-up data is shown as *solid black line* (16%- and 84%-percentiles are shown as *gray area*). The systematic uncertainties are shown in the *lower-right corner* of the plot.

one average OH abundance measurement, as a decomposition of the ^{13}CO emission is ambiguous in this case. It is possible that emission from molecular gas contributes to the ^{13}CO feature which is not related to the OH absorption. If this was the case, the average OH abundance would be an underestimation of the true abundance. In summary, the three datapoints with low OH abundance in Fig. 4.12 are potentially influenced by radiative transfer effects or blending, which cannot be further assessed here. For consistency, they were included in the study in Chapter 3 and are incorporated here to present an unbiased survey of all OH absorption features. These effects may be accounted for with more advanced selection criteria on the entire sample in a future analysis.

4.4.5 OH abundance with respect to the total number of hydrogen nuclei

4.4.5.1 N_{OH} vs. N_{HI}

In contrast to the THOR sample, at many OH components the H I absorption spectrum does not saturate. For these, it is possible to obtain an estimate of the maximum value of τ . The column densities of atomic hydrogen, N_{HI} (see Section 4.3.2.2), represent estimates rather than lower bounds (with possible systematic uncertainties, as possible emission contributions to the absorption spectrum were not accounted for; Sect. 4.5.5).

Figure 4.13 shows the comparison of N_{OH} and N_{HI} . Non-saturated H I detections (circles) are located between $N_{\text{HI}} = 5 \times 10^{20} - 2 \times 10^{21} \text{ cm}^{-2}$. There is potentially a weak correlation between OH and H I present over this low-column density range, but, given the systematic uncertainties, it is likely not to be significant.

The maximum OH column density, for which H I has not yet reached saturation, is similar for both VLA follow-up and THOR ($N_{\text{OH}} \approx 3 \times 10^{14} \text{ cm}^{-2}$). Between $N_{\text{HI}} = 1 \times 10^{21} - 1 \times 10^{22} \text{ cm}^{-2}$, the H I column densities approach saturation. The OH column densities increase without any H I measurements being located at $N_{\text{HI}} > 1 \times 10^{22} \text{ cm}^{-2}$. While the VLA follow-up and the THOR data agree in the general location of the saturation limit, the first saturated H I absorption occurs at slightly higher N_{HI} in the VLA follow-up ($N_{\text{HI}} \approx 1.8 \times 10^{21} \text{ cm}^{-2}$) than in the THOR data ($N_{\text{HI}} \approx 1.2 \times 10^{21} \text{ cm}^{-2}$). This agrees roughly with the increase in the saturation level of τ_{HI} due to the higher sensitivity of the VLA follow-up observations (Sect. 4.4.1).

4.4.5.2 $X_{\text{OH}}(N_{\text{H}})$ vs. N_{H}

We note from Table 4.5 that for at least half of the OH components in the VLA follow-up observations, N_{HI} , or upper limits on N_{HI} , exceed N_{H_2} . This implies that OH absorption occurs in gas with significant fractions of atomic gas. Therefore, we investigate here the OH abundance with respect to the total number of hydrogen nuclei ($N_{\text{H}} \equiv 2 \times N_{\text{H}_2} + N_{\text{HI}}$).

Following Sect. 3.3.2.7, we combine the H I column density estimates from Sect. 4.3.2.2 with the H_2 column density estimates from ^{13}CO to obtain an estimate of N_{H} . The column density averaged OH abundance is then given as $X_{\text{OH}} = N_{\text{OH}}/N_{\text{H}}$ (Table 4.5). Figure 4.12 shows the derived values for X_{OH} at their corresponding N_{H} .

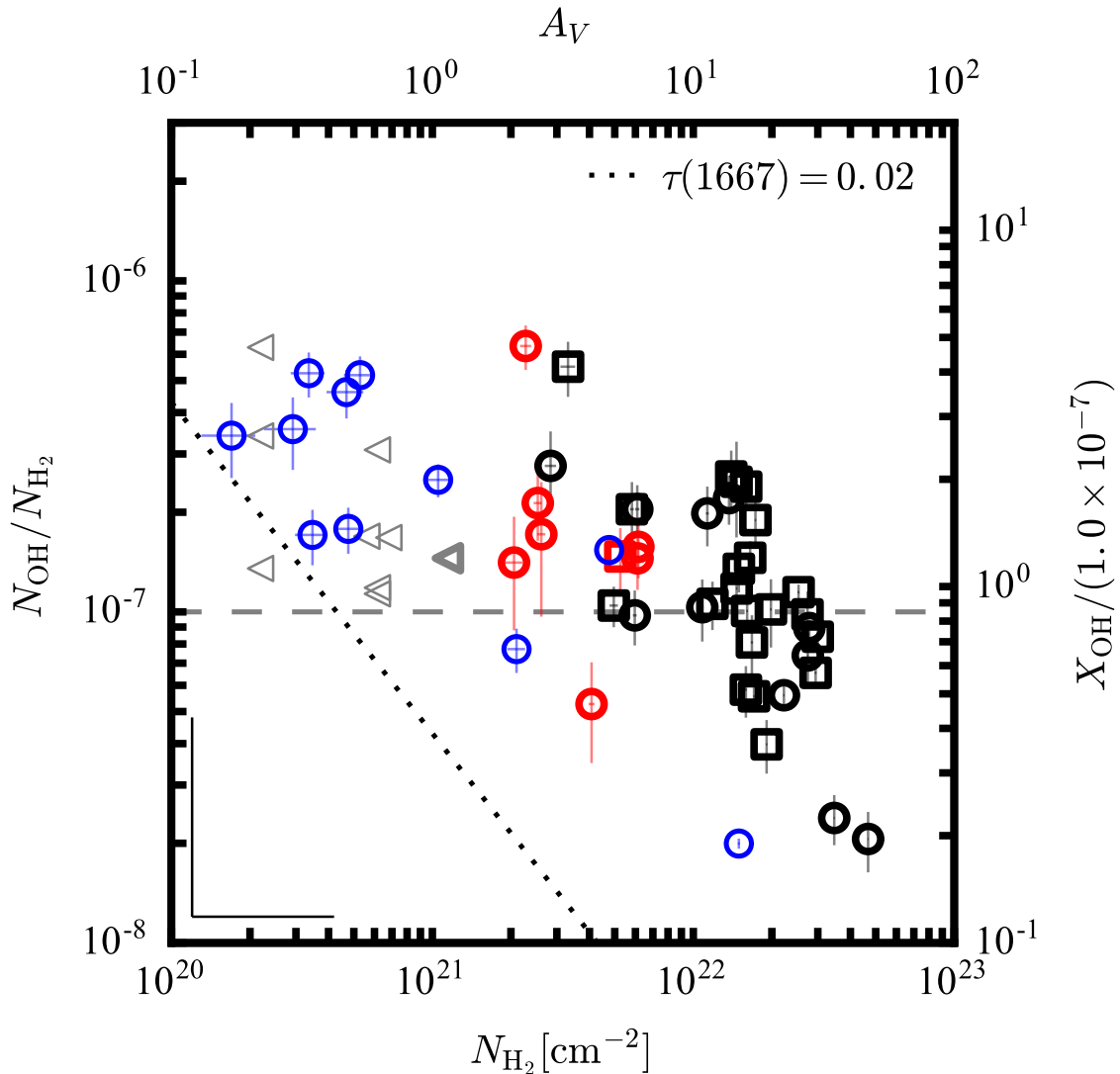


Figure 4.12: Column density averaged abundance of OH with respect to N_{H_2} , $X_{\text{OH}} = N_{\text{OH}}/N_{\text{H}_2}$, vs. N_{H_2} (see also Fig. 3.8). The plot shows both the results from the OH high-resolution observations presented in this chapter (*blue*), and the results from the THOR survey shown in Chapter 3 (in *black* or *red*, depending on if associated with H II regions or not). Upper limits on N_{H_2} , as determined from $N_{13\text{CO}}$, are highlighted with *triangles* pointing to the *left*. The *dotted black line* marks the detection limits of the VLA follow-up survey. The *dashed gray line* denotes the literature abundance of $X_{\text{OH}}(N_{\text{H}_2}) \sim 1.0 \times 10^{-7} \text{ cm}^{-2}$ (Liszt & Lucas 1996, 2002). The systematic uncertainties are shown in the *lower left corner* (for purposes of display, only the upper part of the errorbars is shown).

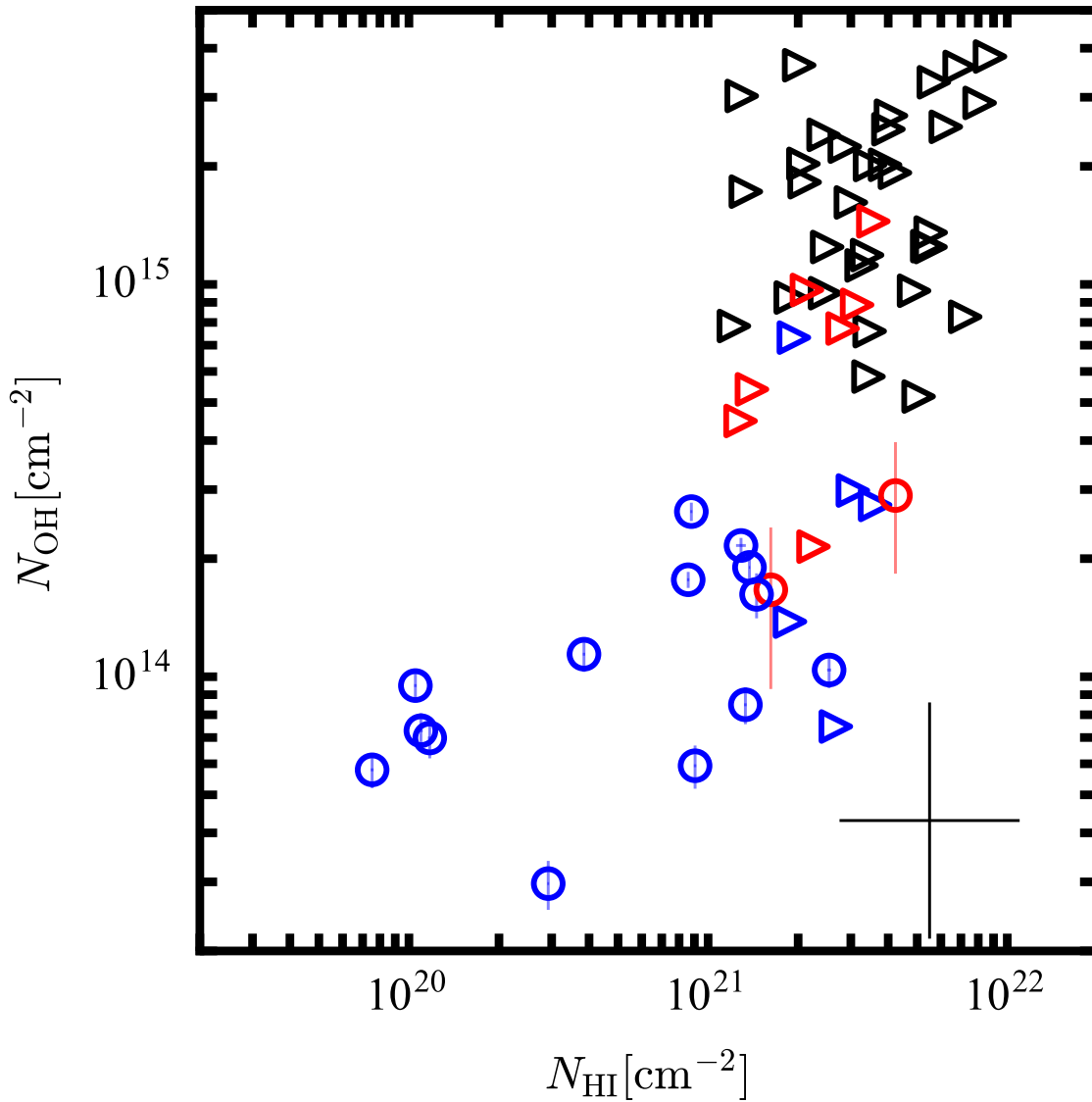


Figure 4.13: Column density of OH and H I in comparison. The plot shows both the results from the OH high-resolution observations presented in this chapter (*blue*), and the results from the THOR survey (in *black* or *red*). Components, in which the H I optical depth saturates in one or more velocity bins, are denoted as triangles. The systematic uncertainties are shown in the *lower-right corner*.

The OH abundance appears to be constant with large scatter between $X_{\text{OH}} \sim 2 - 10 \times 10^{-8}$. A statistical analysis of this relation would need to include lower limits on H I and upper limits on H₂, which is beyond the scope of this Chapter. The median of all derived values shown in Fig. 4.12 (including values with lower limits on H I and upper limits on H₂) is $X_{\text{OH}} = 4.8 \times 10^{-8}$, with a standard deviation in $\log(X_{\text{OH}})$ of 0.3 dex (corresponding to variations of a factor of two in X_{OH}). We note that this agrees well with a typical literature abundance of $\sim 4.0 \times 10^{-8}$ (Crutcher 1979).

4.5 Discussion

4.5.1 H I optical depths

The H I optical depth of the VLA follow-up observations improves the optical depth correction of H I measurements in GMCs. As shown in, e.g., Bihl et al. (2015) for the star-forming complex W43, the H I mass is underestimated by a factor of 2.4 when assuming the H I emission to be optically thin. In the optically thin approximation, the H I column density scales linearly with the measured brightness temperature (e.g., Wilson et al. 2009, eq. 13.17), while higher optical depths can be accounted for by a correction factor of $F_{\text{corr}} = \tau / (1 - e^{-\tau})$ (e.g., Wilson et al. 2009, p. 336; Bihl et al. 2015, eq. 9). With maximum optical depths of $\tau_{\text{max}} = 4.1$ in the VLA follow-up measurements, the H I column densities determined in the optically thin limit would need to be corrected by a factor of four. In the case of the three velocity ranges in which H I saturates (Fig. 4.3), this also implies an increase of 20–60 % in the correction as compared to the one derived from THOR for these three sources.

While τ_{max} increased, it needs to be stressed that in case of saturation of the H I absorption, the H I optical depths remain lower limits. It may therefore be asked, how much sensitivity would be needed to probe the full H I content. The increase in sensitivity revealed two different types of features, which were saturated in the THOR data. Narrow components (with a FWHM of 3–4 km s⁻¹), which do not saturate in the VLA follow-up ($\tau_{\text{max}} \lesssim 4$), and broader components, which saturate in both datasets on velocity ranges of $\sim 6 - 7$ km s⁻¹ (the width over which the spectra saturate). It needs to be investigated if this is a common pattern also in other parts of the THOR data.

The optical depth for the velocity features with saturated absorption cannot be determined from our data. For this small number of four absorption features, the saturation is always associated with a spiral arm or GMC, but the same spiral arm is not saturating in all spectra. This is not surprising, as considerable variations are expected and seen in the H I content along spectral arms (e.g., Dame et al. 2001). The strong saturation is therefore likely to be simply due to high column densities in H I. One possibility to estimate the expected optical depth would be a comparison with simulations of gas distributions in spiral galaxies. This is beyond the scope of this thesis.

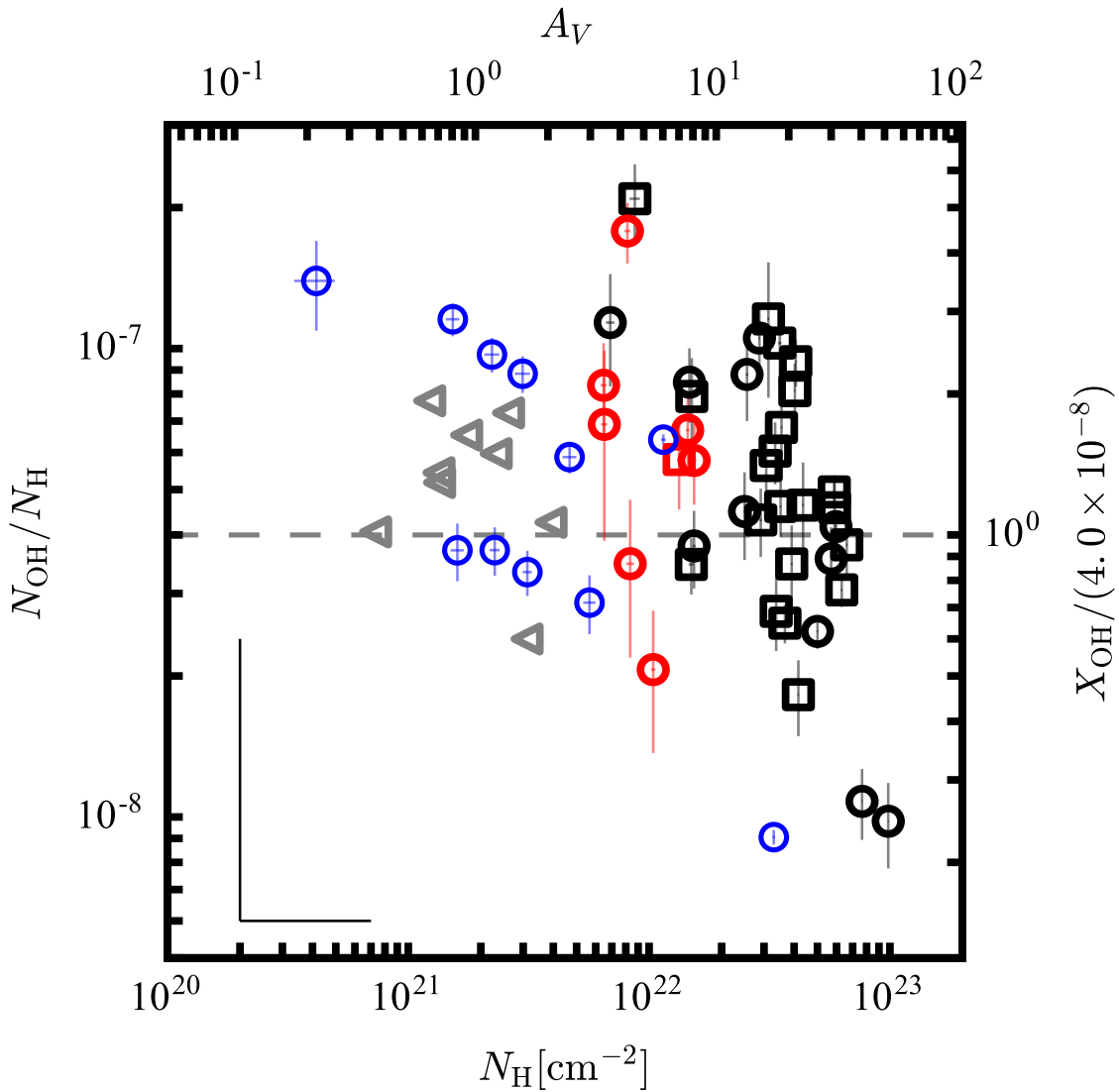


Figure 4.14: Column density averaged abundance of OH with respect to N_{H} , $X_{\text{OH}} = N_{\text{OH}}/N_{\text{H}}$, vs. N_{H} (see Fig. 3.9). N_{H} is the total number of hydrogen nuclei, $N_{\text{H}} = 2 \times N_{\text{H}_2} + N_{\text{H}}$. The plot shows both the results from the OH high-resolution observations presented in this chapter (*blue*), and the results from the THOR survey (in *black* or *red*). Upper limits on N_{H_2} , as determined from $N_{13\text{CO}}$, are highlighted with *triangles* pointing to the *left*. The *dashed gray line* indicates the literature abundance of $X_{\text{OH}}(N_{\text{H}}) \sim 4.0 \times 10^{-8}$ (Crutcher 1979). The systematic uncertainties are shown in the *lower left corner* (only the upper half of the error bars are shown for better display).

4.5.2 OH abundance variations revisited

The analysis of this chapter shows that the VLA follow-up observations detect many more OH absorption features at lower optical depths than found in the THOR survey (Chapter 3). The comparison to CO emission indicates that these are also associated with lower column densities of molecular gas. The survey reaches typical optical depths found in diffuse clouds (e.g., Dickey et al. 1981; Colgan et al. 1989; Liszt & Lucas 1996), while the comparison to even more sensitive observations suggests that the sample is still sensitivity-limited (see Sect. 4.5.3).

The comparison between N_{OH} and N_{H_2} as well as the investigation of $X_{\text{OH}}(N_{\text{H}_2})$ confirm the results of the analysis from Chapter 3 (Sect. 4.4.4). A statistical analysis of the combined VLA follow-up and THOR datasets updates the relation between $\log(N_{\text{OH}})$ and $\log(N_{\text{H}_2})$. It confirms that it is sub-linear (Fig. 4.11), however at a steeper slope of $m = 0.52^{+0.09}_{-0.09}$. The abundance ratio $X_{\text{OH}}(N_{\text{H}_2})$ is therefore still decreasing with N_{H_2} (Fig. 4.12), but less pronounced.

The analysis of $X_{\text{OH}}(N_{\text{H}})$, the column density of all hydrogen nuclei along the line of sight, strengthens the results from Chapter 3 (Sect. 4.4.5; Fig. 4.14). The abundance $X_{\text{OH}}(N_{\text{H}})$ appears to be constant within the systematic uncertainties at a median of $X_{\text{OH}} = 4.8 \times 10^{-8}$, when compared at different N_{H} between $N_{\text{H}} = 1 \times 10^{21} - 7 \times 10^{22} \text{ cm}^{-2}$, however shows a large spread (0.3 dex). This was indicated by the analysis of the THOR dataset (Sect. 3.3.2.7) and holds up with the VLA follow-up observations added.

Two sources of systematic uncertainty could not be accounted for (as discussed also in Chapter 3). The contribution of CO-dark gas is unknown, which would move the datapoints at low N_{H_2} diagonally to the lower right in the comparison of $X_{\text{OH}}(N_{\text{H}_2})$ vs. N_{H_2} (Fig. 4.12). This would lead to an even shallower decreasing trend. However, the amount of CO-dark gas is unknown and it is not clear if and how many cloud components would be affected (see also discussion in Sect. 4.5.3).

The second systematic uncertainty is the contribution of HI to N_{H} at large hydrogen column densities. Figure 4.13 hints at a correlation between N_{OH} and N_{HI} (however likely not statistical significant), which is also seen in the study by Tang et al. (2017). As shown in Sect. 4.4.5.1, the HI column density saturates above $N_{\text{HI}} = 1 \times 10^{21} - 1 \times 10^{22} \text{ cm}^{-2}$. As the optical depth is only a lower bound in these cases, N_{H} may be underestimated and $X_{\text{OH}}(N_{\text{H}})$ overestimated for values at high N_{H} . While this could in principle introduce a trend in Fig. 4.14, at high N_{H_2} we are likely to predominantly probe regions with a high molecular gas fraction. Hence, we assume this effect to be minor.

4.5.3 OH column densities in comparison to the Millennium survey

A comparison of the OH measurements presented in this chapter yields good agreement with the analysis obtained towards extragalactic continuum sources in the field of view of the Arecibo telescope, while the OH absorption measurements from the THOR survey appear to trace regions of higher OH column density. Li et al. (2018) evaluated OH absorption observations towards continuum sources which were observed with the Mil-

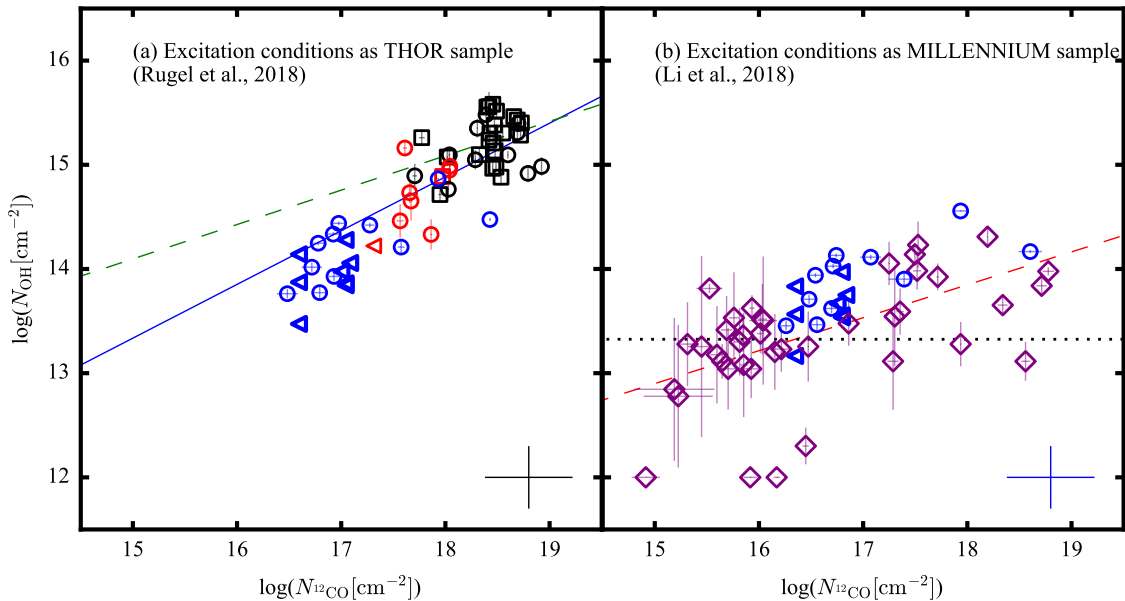


Figure 4.15: OH vs. ^{12}CO column density (as derived from the OH 1667 MHz transition and from ^{13}CO). The *left panel* shows the measurements from the THOR survey (in *black* and *red*) and from the VLA follow-up observations (*blue*) using excitation conditions as in Chapter 3 and 4. The fit results for $\log(N_{\text{OH}})$ vs. $\log(N_{\text{H}_2})$ are shown after converting to $N_{^{12}\text{CO}}$ (see text), both from the THOR sample alone (*dashed green line*) and from the VLA follow-up sample combined with THOR (*solid blue line*). The *right panel* shows the measurements from the VLA follow-up sample (*blue*), at excitation conditions as described in Appendix C.2.2, which are similar to those of the Millennium survey. Their OH 1667 MHz measurements are shown in *purple*; upper limits on $N_{^{12}\text{CO}}$ from their figure 9 are not shown (Li et al. 2018). The relation between $\log(N_{\text{OH}})$ vs. $\log(N_{^{12}\text{CO}})$ from Li et al. (2018) is shown as *dashed red line*. An approximate $3 - 5\sigma$ detection limit of the VLA follow-up survey is shown as *dotted black line*.

lennium survey of H I (Heiles & Troland 2003).

As they compare N_{OH} directly to $N_{^{12}\text{CO}}$, we convert our measurements of $N_{^{13}\text{CO}}$ by using the same isotope ratio as in Li et al. (2018) of $^{12}\text{C}/^{13}\text{C} = 68$. In the *left panel*, the THOR OH data and the VLA follow-up observations are shown using excitation conditions as assumed in Chapter 3 and for the preceding analysis in this chapter, and as such is similar to Fig. 4.11, but for a shift in y -direction due to the conversion of N_{CO} to N_{H_2} . In the *right panel*, we compare the VLA follow-up observations to the sample of Li et al. (2018), using similar excitation conditions for both OH and ^{13}CO as in their sample (the derivation is described in Appendix C.2).

A comparison of the THOR data in the *left panel* with the Millennium data in the *right panel*, of Fig. 4.11, shows that the THOR sample traces generally higher OH column densities at a given $N_{^{12}\text{CO}}$, beyond systematic uncertainties. Interestingly, the relation between N_{OH} and N_{H_2} , which was determined from the THOR data alone (*left panel, red-dashed line*), matches the relation determined from the Millennium sample well in slope after conversion to $N_{^{12}\text{CO}}$, but is shifted to higher N_{OH} by slightly more than an order of magnitude. A possible explanation for this difference could be the different

environment traced by many of the THOR measurements at high N_{OH} . These are mainly associated with H II regions, which may affect the chemistry and/or the excitation of OH. It is, however, not clear if a separation in two groups of OH sources is justified. The relation fitted to both THOR and VLA follow-up observations (*blue* line in the *left* panel) agrees within uncertainties with most of the Millennium detections at $\log(N_{12\text{CO}}) < 16$.

Focussing on the *right* panel, we note that the OH absorption observations from the VLA follow-up observations fit well into the scatter of the observations of the Millennium survey. They follow the trend between N_{OH} and $N_{12\text{CO}}$, which was derived from the Millennium data, but fall slightly above it. Likely reason for this is that our observations are sensitivity limited (*dotted* line in the *right* panel). The VLA follow-up observations appear to be consistent with the dataset from Li et al. (2018). This is re-assuring, as both predominantly trace OH in similar conditions of gas which are not associated with star formation, i.e., diffuse molecular clouds.

It should be noted that there are systematic differences between both methods of observation, which may explain at least parts of the differences in column density. The OH dataset from Li et al. (2018) was observed with the Arecibo telescope, which has a beam width of 3', while the angular resolution of the VLA follow-up observations is $\sim 15''$. The Millennium survey accounts for the contribution of the emission across the entire telescope beam to the absorption spectrum by measuring the emission in positions offset from the source. With these offset positions, they model the expected emission at the position of the continuum source. For smoothly varying emission on scales similar to the Arecibo beam, this technique may estimate the emission contribution well, while emission on smaller scales is less well accounted for and may lead to artificially low optical depths in the Millennium sample in some regions.

4.5.4 CO-dark gas

CO shows significant emission in most velocity ranges which were used for integration of the OH emission (see Table 4.3). Of these, 17 out of 19 show ^{12}CO emission and 11 out of 19 ^{13}CO emission of OH absorption in velocity. Though based on a small sample, we find the ^{13}CO and OH line widths to be predominantly similar (Sect. 4.4.2.3 and Fig. 4.7, whenever Gaussian components from both tracers could be associated with each other). In case of $^{13}\text{CO}(1-0)$ detection, it is therefore likely that OH traces similar gas along the line of sight.

The comparison to the H I line widths is less clear. While Sect. 4.4.2.3 indicates two components in which H I, OH and CO emerge from gas with similar properties, the H I line width was larger in the four other components of the comparison. The strongest caveat in this comparison is that the H I line widths were determined by modelling complex absorption spectra with many Gaussian components, which are likely to be affected by blending. For this reason, we could compare only six components. The fact that we find two components for which the line widths agree indicates that H I and OH gas can coexist. A more accurate determination of the relation between both gas tracers is left for further studies with larger sample sizes.

We find two cases of ‘‘CO-dark’’ gas with neither ^{12}CO nor ^{13}CO emission. Non-

detections in ^{13}CO are found more frequently, with 8 non-detections in 19 velocity ranges. Both findings indicate that OH can be detected in regions without ^{12}CO and/or ^{13}CO detection.

When comparing the results from this work to the results from [Li et al. \(2018\)](#), we note that the CO emission observations from the GRS, PMO and FUGIN are likely to be sensitivity limited, with the PMO dataset used here being a factor of 5 and 7 less sensitive than the ^{12}CO and ^{13}CO observations conducted with the same telescope in [Li et al. \(2018\)](#), respectively. As such, we reach the zone noted in their figure 9 as “dark molecular gas threshold” ($14.8 < \log(N_{\text{CO}}) < 15.8$), which contains an order of magnitude higher CO column densities than their “dark molecular gas” region ($\log(N_{\text{CO}}) < 14.8$).

Our results for the total column density of hydrogen nuclei confirm that some of our measurements are at low enough visual extinction to trace regimes where CO is not strongly abundant, and atomic hydrogen is significant compared to H_2 column density derived from the CO measurements (see also Sect. 4.4.5). About eight OH detections have visual extinctions of $A_V \lesssim 1$, while theoretical studies indicate that CO starts to be efficiently self-shielded at about $A_V \sim 1$ (e.g., [Wolfire et al. 2010](#)). Also, for at least some of them, the H I content becomes similar to H_2 content as derived from ^{13}CO detections or upper limits. This VLA follow-up sample to THOR therefore certainly approaches parts of molecular clouds which are diffuse, in the sense that they are not yet dominated by molecular gas.

4.5.5 Future work

4.5.5.1 Observations

The two CO-dark gas candidates need to be followed up with ^{12}CO observations at higher sensitivity to verify their status beyond the sensitivity limitations in the CO survey data, which was used here.

4.5.5.2 Technical improvements

On the calibration side, the phase calibration of the interferometric measurements (visibilities) can be improved by using self-calibration. Our dataset is quite suitable for this technique, as our sources are strong continuum sources, which are also the requirement for a successful self-calibration, as shown in other studies (e.g., [Murray et al. 2015](#)).

The nature of interferometric measurements is that they recover emission only on spatial scales traced by the interferometer (Chapter 2). All other emission, especially constant backgrounds, is filtered out. We used this in the calculation of the optical depth, by applying the approximation that the emission of the OH and H I gas is effectively filtered out, i.e., by assuming that the measured signal is solely due to the attenuated background sources (Sect. 4.2.2). If the intensity of the background source varies significantly on the scales probed by the interferometer, we would effectively underestimate the optical depth of H I. The fact that we see complete saturation in many cases for H I gives some confidences that this effect is minor at most, since the $3\text{-}\sigma$ limit, which determines our

saturation limit, is at $T_{\text{sat}} \sim 40 - 60$ K.

However, as also the distribution of the emission is velocity dependent, this may not hold at all velocities. There are two possibilities to account for this. First, short baselines of the interferometer, which trace large spatial scales and are therefore most prone to showing emission can be excluded from the imaging (Murray et al. 2015). Alternatively, the interferometric spectrum can be compared to single-dish observations, which are not subject to spatial filtering. By smoothing the interferometric observations to the angular resolution of the single-dish observations, the difference between both spectra can be determined and accounted for in the analysis (Winkel et al. 2017).

Lastly, the spin temperature of the H I gas can be determined by obtaining emission spectra from locations close to the source by using H I emission surveys, e.g., from the combined THOR+VGPS³ dataset (Beuther et al. 2016, Wang et al., in prep.). By assuming that properties of the H I gas do not change significantly between the absorption and emission spectra from the vicinity of the continuum source, both optical depth and spin temperature can be determined simultaneously (see, e.g., Bühr et al. 2015, and references therein).

4.5.5.3 Future steps in the analysis

With new surveys of $^{12}\text{CO}(1-0)$ emission becoming available (e.g., the FUGIN survey used here), the excitation conditions of the CO emission can also be analyzed more accurately for the THOR OH sample, as done here for the VLA follow-up (Appendix C.2). Together with more detailed fitting approaches which account also for upper limits on the CO data, the relation between N_{OH} and N_{H_2} may be re-evaluated.

4.5.5.4 Excitation conditions

Clumps associated with dense gas show deviations from LTE in the main lines (see Sect. 4.4.2.2). Chapter 3 found that most of the satellite lines in the THOR survey were anomalously excited and show signs of population inversion. The satellite lines in the VLA follow-up observations show similar behaviour. This can be noted in Fig. 4.1, which shows many satellite line components at negative optical depths, which indicate masing. While the main lines are not necessarily affected by this (see Sect. 3.3.3), the morphology of the inversion points to either radiative or collisional pumping which are closely related to the environment. Models of radiative transfer of the OH main lines together with the information of the satellite lines may bring more information on the excitation conditions of these particular observations. The results may then be applied to this dataset and to the THOR dataset in a future analysis.

³The VLA Galactic Plane Survey; Stil et al. 2006.

4.6 Conclusion

We present high-sensitivity OH and H I absorption observations at cm-wavelengths with the VLA. These are follow-up observations of the THOR survey, in order to investigate the presence of low-optical depth OH absorption from diffuse interstellar clouds and cloud envelopes, as well as to estimate the maximum absorption depth of H I in the Galactic plane. Our main conclusions can be summarized as follows:

- We derive a maximum H I optical depth of $\tau_{\max} = 4.1$ with the VLA follow-up H I absorption measurements. Some of the saturated components in THOR ($\tau_{\max} \sim 3.0$) have optical depths of $\tau < 4.1$ in the new data, whereas some components still saturate. The true optical depths and column densities of such strong absorption features, which are likely to be associated to spiral arms and/or GMCs, still remain unknown.
- We characterize OH 1667 MHz optical depths at higher sensitivity and detect about 20 absorption components towards three lines of sight, with the majority of them at $\tau = 0.02 - 0.15$, in a range typical of diffuse clouds (e.g. Liszt & Lucas 1996).
- The OH detections complement the sample from the THOR survey at lower OH and H₂ column densities. Combining both datasets, we confirm the sublinear trend in $\log(N(\text{OH}))$ vs. $\log(N(\text{H}_2))$ found in Chapter 3. Subsequently, the column density averaged OH abundance with respect to H₂ shows a decrease with increasing H₂ column density in confirmation of the results of Chapter 3.
- At low OH column densities, the H I column densities are found to be comparable or larger than the H₂ column densities for a significant subset of the OH detections. This leads to an approximately constant OH column density averaged abundance with respect to the column density of the total number of hydrogen nuclei, $N_{\text{H}} = 2 \times N_{\text{H}_2} + N_{\text{H}}$, at different N_{H} .
- We find OH detections without CO emission in the available archival ¹²CO and ¹³CO emission surveys (8/19 non-detections in ¹³CO and 2/19 non-detections in ¹²CO), where the ¹²CO non-detections are possible candidates for CO-dark gas.
- Both the strong atomic gas fraction and the partial non-detections of CO indicate that the many of the OH components in the VLA follow-up sample emerge from partially atomic cloud regions.
- The OH detections are in good agreement in $\log(N_{\text{OH}})$ vs. $\log(N_{\text{13CO}})$ with a survey of absorption of strong cm-continuum sources (Li et al. 2018), which predominantly traces diffuse clouds. This gives confidence to the method of observation and analysis used here. However, we note that our VLA follow-up sample is yet sensitivity limited in both OH and CO observations.

Further observations at higher sensitivity in the CO(1-0) transitions are necessary to verify the status of the CO-dark gas candidates. Further steps have been identified to improve the calibration, imaging and analysis of the data.

Chapter 5

Stellar feedback in W49A with radio recombination lines

This chapter will be published in a refereed journal, “Feedback in W49 diagnosed with Radio Recombination Lines and Models”; M. R. Rugel, D. Rahner H. Beuther, et al., submitted to A&A, and was adapted for this thesis.

Overview: *We move the focus away from molecular gas in diffuse phases of the interstellar medium, and concentrate on the evolution of molecular clouds, which are currently forming stars. In this Chapter, we investigate feedback processes which have the potential to destroy molecular clouds (see Chapter 1) and address the question of how feedback affects evolution of a molecular cloud. We present images of radio recombination lines (RRLs) from THOR of the star-forming region W49A to determine the kinematics of ionized gas. We find a shell-like distribution of ionized gas as traced by RRL emission in the surrounding of the central cluster of OB stars in W49A. We used models of feedback-driven shells (WARPFIELD) to determine the evolution of this shell and find that it is re-collapsing. The shell may also have triggered star formation in other parts of W49A. We suggest that W49A is a potential candidate for star formation regulated by feedback-driven and re-collapsing shells.*

5.1 Introduction

Radiative and mechanical feedback from UV radiation and winds from OB stars and supernova explosions (see Chapter 1) alter the potential of molecular gas to fragment and form future generations of stars, but their precise role in star formation is yet to be clarified. Recent investigations of 30 Doradus in the Large Magellanic Cloud (LMC) indicate that feedback from the older stellar population in its main star cluster NGC 2070 has been unable to destroy its parent molecular cloud (Rahner et al. 2018). Rather, feedback-driven shells of ionized and molecular gas from these older cluster members may have

re-collapsed due to the gravitational attraction of the star cluster and the self-gravity of the shell, forming a second generation of stars. Only with these, the combined stellar feedback becomes strong enough to disperse the parent molecular cloud.

While star formation induced by re-collapsing shells may not change the total number of stars formed in a giant molecular cloud (GMC), such a process would naturally imply that star formation in at least some GMCs may occur episodically. As pointed out by [Rahner et al. \(2017\)](#), re-collapse of a feedback-driven shell can occur only in the most massive and densest GMCs. It is therefore an open question whether this also takes place in GMCs in the Milky Way.

In our search for a 30 Doradus analog in the Milky Way, we focus this study on W49A. It is one of the most massive and the most luminous young star-forming regions in the Galaxy, with one of the highest luminosity to molecular mass ratios, indicating a high star formation efficiency (it is responsible for 12% of all luminosity in the Galaxy; [Urquhart et al. 2018](#)). While regions like W49A lie within the statistical distribution of luminosity to molecular mass ratios of the Galaxy-wide sample of star-forming regions, the nature of the physical processes that causes this extreme star formation is still not fully understood. This makes it an ideal region to search for re-collapse of feedback-driven shells.

5.1.1 Overview of W49A

W49 was first discovered as a radio source by [Westerhout \(1958\)](#) and is located at a distance of 11.1 kpc from the Sun ([Zhang et al. 2013](#)). It is located in the Perseus spiral arm (e.g., [Moore et al. 2012](#)), at similar Galactocentric radius as the Solar system. It is associated with a GMC of mass $\sim 10^6 M_{\odot}$ ([Galván-Madrid et al. 2013](#)), which contains the supernova remnant W49B, and the massive H II region complex W49A ([Mezger et al. 1967](#)) with a molecular gas mass of $\sim 2 \times 10^5 M_{\odot}$ ([Urquhart et al. 2018](#); [Galván-Madrid et al. 2013](#)). An overview of W49A is shown in Fig. 5.1, with 8 μm emission (GLIMPSE; [Benjamin et al. 2003](#); [Churchwell et al. 2009](#)) as a tracer of ongoing star formation (e.g., [Stock et al. 2014](#)), and 870 μm emission (from ATLASGAL; [Schuller et al. 2009](#)) indicating the presence of cold and dense gas – the sites of future star formation. The main physical parameters are summarized in Table 5.1.

The W49A cloud harbors multiple ultracompact (UC) H II regions (e.g., [Dreher et al. 1984](#); [De Pree et al. 1997](#)), with a central condensation in a ring-like structure ([Welch et al. 1987](#)). The region has the highest concentration of UCH II regions in the Galactic disk (18 compact and UC H II; [Urquhart et al. 2013](#)). Four star clusters are detected by infrared imaging ([Alves & Homeier 2003](#)), amounting to a total stellar mass of $5 - 7 \times 10^4 M_{\odot}$ ([Homeier & Alves 2005](#)). The so-called ‘Cluster 1’ ([Homeier & Alves 2005](#)) in the central part of W49A ($r \lesssim 2.5$ pc) contains about 50 O stars with $M_* \geq 20 M_{\odot}$, and a total of ~ 270 O stars are found in and around W49A ([Homeier & Alves 2005](#)). Several of these candidate cluster members have masses between $20 - 250 M_{\odot}$, as determined from near-infrared spectroscopy and photometry ([Wu et al. 2016](#)).

The molecular gas of W49A shows a complex velocity structure, with blue- and red-shifted components with respect to the systemic velocity ($v_{\text{LSR}} = 8.6 \text{ km s}^{-1}$; [Quireza et al. 2006a](#)): There are two main velocity components at 4 km s^{-1} and 12 km s^{-1} (or at

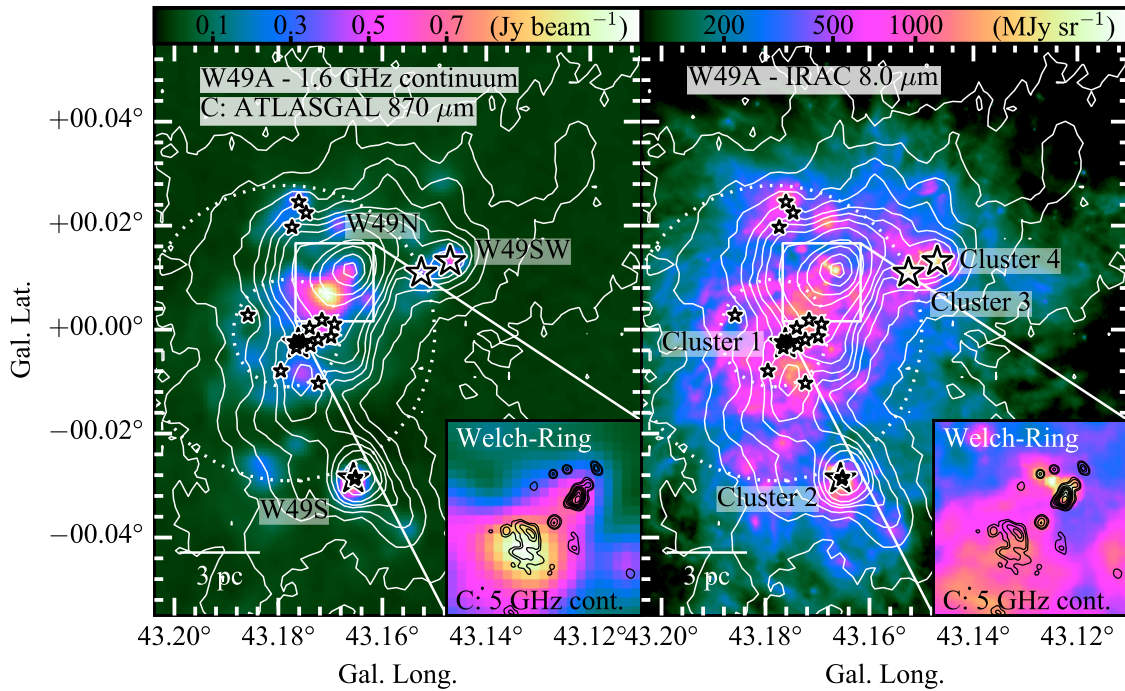


Figure 5.1: Overview of W49A in 1.6 GHz continuum emission shown in color scale (*left*; THOR; Wang et al., submitted) and GLIMPSE Spitzer IRAC 8.0 μm emission (*right*; Benjamin et al. 2003; Churchwell et al. 2009). On both panels: White contours indicate cold, dense dust in 870 μm emission (ATLASGAL, Schuller et al. 2009; at levels of -0.24, 0.24, 0.8, 1.6, 2.4, 3.2, 4.0, 5.2, 8.0, 16.0, 24.0, 40.0, 56.0 Jy beam^{-1}). Large stars indicate stellar clusters found with JHK imaging (Alves & Homeier 2003). Small stars indicate individual O stars observed by Wu et al. (2016). The insert shows the Welch-Ring of ultra-compact H II regions (UCH II regions, Welch et al. (1987)), represented here by 5 GHz continuum emission (CORNISH survey, Hoare et al. (2012); at levels of 0.01, 0.02, 0.05, 0.75, 0.1, 0.125, 0.15, 0.175, 0.2, 0.25 Jy beam^{-1}). The dotted inner ring indicates the shell structure found in this chapter (in good agreement with shells found by Peng et al. 2010); the outer ring indicates the approximate size of W49A. Labels in the left panel indicate main cm-continuum emission peaks (e.g., Dreher et al. 1984), and in the right panel indicate infrared star clusters (Alves & Homeier 2003).

Table 5.1: Cloud properties of W49A

Quantity	Assumed values	Comments	Reference
Cloud radius	$R \approx 6 \text{ pc}$	approximate distance from Cluster 1 to W49SW and W49S	Peng et al. (2010)
Molecular gas mass (W49A; $r \lesssim 6 \text{ pc}$)	$M_{\text{gas}} \approx 2_{-1}^{+2} \times 10^5 M_{\odot}$	assumed uncertainties of a factor of 2; used for modeling	Galván-Madrid et al. (2013) , Urquhart et al. (2018)
Molecular gas mass (W49 molecular cloud; $r \lesssim 60 \text{ pc}$)	$M_{\text{gas}} \approx 1 \times 10^6 M_{\odot}$		Galván-Madrid et al. (2013)
Stellar cluster mass (all infrared sub-clusters)	$M_{*} \approx 5 - 7 \times 10^4 M_{\odot}$		Homeier & Alves (2005)
Stellar cluster mass (Cluster 1)	$M_{*} \approx 1 \times 10^4 M_{\odot}$	used for modeling, assume that mass is possibly up to a factor of two higher	Homeier & Alves (2005)
Derived molecular gas density (W49A; $r \lesssim 6 \text{ pc}$)	$n \approx 4_{-2}^{+4} \times 10^3 \text{ cm}^{-3}$	assuming homogeneity and spherical symmetry	

-4.6 km s^{-1} and 3.6 km s^{-1} w.r.t. the systemic velocity) observed in many gas tracers on scales ranging from the entire W49A region ([Mufson & Liszt 1977](#); [Miyawaki et al. 1986](#); [Simon et al. 2001](#); [Miyawaki et al. 2009](#)) to the inner-most parts, towards W49N in CS (e.g., [Serabyn et al. 1993](#)). While CO transitions may be optically thick, the double-peaked structure appears to reflect the true dynamics of the molecular cloud, as it is persistent in optically-thin, high-density tracers such as $\text{H}^{13}\text{CO}^{+}(1-0)$ and $\text{CS}(2-1)$, Figure 3 in [Galván-Madrid et al. \(2013\)](#), also [Miyawaki et al. 2009](#)). The velocity components were attributed to background and foreground clouds, respectively, by [Serabyn et al. \(1993\)](#), as indicated by H_2CO absorption ([Goss & Tilanus 1985](#)). This spatial location would mean that the two clouds are moving towards each other, either as the collision of two clouds, or the inside-out collapse of one cloud ([Serabyn et al. 1993](#); [Welch et al. 1987](#)). Alternatively, the velocity components could be due to expanding motions ([Peng et al. 2010](#)). Other studies have suggested that the complexity of the H_2CO absorption, as well as of CS and HCO^{+} emission in this region, is connected to a complex arrangement of H II regions surrounded by dense and diffuse molecular gas, outflows and infall motions ([Dickel & Goss 1990](#); [Williams et al. 2004](#)).

5.1.2 Feedback and star formation in W49A

The number of ionizing photons from the stellar population in W49A ([Alves & Homeier 2003](#)), with the largest contribution being from the most massive of these stars ([Wu et al. 2016](#)), is sufficient, or may exceed that required to ionize the gas within W49A, as determined from low- ([Kennicutt 1984](#)) and high-resolution continuum observations (e.g. [De Pree et al. 1997](#)). The fraction of ionized to molecular gas mass is low ($\sim 1\%$; [Galván-](#)

Madrid et al. 2013), indicating that the molecular gas in W49A is not yet penetrated by this radiation. Estimates of the radiation pressure on dust particles indicate that radiative feedback alone from the star cluster is not yet strong enough to disperse W49A (Galván-Madrid et al. 2013; Reissl et al. 2018), while models with other feedback mechanisms (thermal pressure from the H II region and shocked winds, protostellar jets, radiation pressure, however not including wind-momentum) find feedback to be approximately strong enough to disrupt the cloud (Murray et al. 2010). It has been noted, however, that comprehensive modeling that includes all sources of feedback is needed to reliably predict its impact on cloud evolution (Rahner et al. 2017).

This poses the question of whether, and if so how, feedback from Cluster 1 affected star formation in W49A. W49A hosts H II regions and O/B associations which have different ages, with some having already dispersed some of the molecular gas around them (the O/B stars discovered in Alves & Homeier 2003), and others still deeply embedded (e.g., the UC H II regions in the Welch ring; e.g., Dreher et al. 1984; De Pree et al. 1997). Both single O stars and UC H II regions appear to be spread across W49A in small groups. While many studies focussed on the formation of the UC H II regions in the Welch-ring/W49N dust clumps (e.g., Welch et al. 1987; Serabyn et al. 1993; Williams et al. 2004), two main scenarios have been invoked to explain the star formation in W49A as a whole. One interpretation is causally-unrelated, sub-clustered star formation across W49A (Alves & Homeier 2003) along filamentary inflows of molecular gas from a larger reservoir of gas (Galván-Madrid et al. 2013). Alternatively, star formation and the dynamics of the region are causally connected to the feedback of the central star cluster. The central cluster of O stars drives expanding shells of molecular gas (Peng et al. 2010), which may have triggered star formation in the Welch ring (Alves & Homeier 2003). Feedback may also be responsible for the formation of W49S and W49NW, if they are interpreted as ejecta from the central star cluster. While previous interpretations of sub-clustered star formation may be a suitable description of the star formation activity in W49A, the dynamics show imprints of feedback (Peng et al. 2010).

In this chapter, we investigate the observational signatures of stellar feedback using emission from radio recombination lines (RRLs). Radio Recombination Lines have been used in numerous works to determine the physical conditions of ionized gas in H II regions (e.g., Hjellming & Davies 1970, Shaver 1980; see also review by Roelfsema & Goss 1992), in particular also for W49A (e.g. van Gorkom et al. 1980; Balser et al. 1999). In this chapter, we use RRLs to trace the kinematics of ionized gas. RRLs have been mapped also for different star forming regions in the Milky Way (e.g., Pankonin et al. 1979; Lang et al. 2001; Balser et al. 2001). We use our RRL data as constraints for models of the past and future evolution of a feedback-driven shell in a cloud with average physical properties corresponding to those of W49A.

After presenting the observations in Sect. 5.2, the RRL emission is analyzed and compared to molecular gas emission in Sect. 5.3 to characterize the density and velocity structure of different gas phases in W49A. We identify shell-like RRL emission at the interface between hot ionized gas and neutral gas. With the radius and velocity of the shell, we aim

to constrain its evolution with the 1D-code `WARPFIELD`¹ (Rahner et al. 2017) in Sect. 5.4. The results are discussed in the context of the previous interpretations of star formation in W49A, and compared to the feedback-driven star formation history of 30 Doradus in Section 5.5. In Sect. 5.6, we summarize our main findings.

5.2 Observations and Methods

5.2.1 Radio recombination lines at 1.6–1.9 GHz

The RRLs allow us to study the kinematics and structure of the ionized gas in W49A. The H151 α -H156 α and H158 α RRLs, which have frequencies between 1.6–1.9 GHz, were observed towards W49A within the THOR survey (The HI, OH, Recombination line survey in the first quadrant of the Milky Way; Beuther et al. 2016; Chapter 2). Observations of 5–6 minutes per pointing were conducted with the VLA C-configuration in L-band. Each line was observed with a bandwidth of 2 MHz and a spectral resolution of 15.63 kHz. This corresponds to a velocity resolution of 2.5 km s⁻¹ and 2.8 km s⁻¹ for the highest and lowest frequency transitions, respectively (the H151 α line at 1.891 GHz and the H158 α line at 1.651 GHz; see Table 2.1 and also table 2 in Beuther et al. 2016). Using CASA², the absolute flux scale and the bandpass were calibrated on the quasar 3C386 and the complex gain with the quasar J1925+2106.

With a significant detection of all RRLs, the data were gridded to a spectral resolution of 5 km s⁻¹ as opposed to 10 km s⁻¹ in the first data release of the THOR survey. All observations were continuum-subtracted, imaged and combined into mosaics of 3.75° × 2.5°, and deconvolved as described in Beuther et al. (2016). We only consider the seven lines in the frequency interval between 1.6–1.9 GHz to maintain higher spatial resolution (while higher order transitions from lower frequencies were included by Beuther et al. 2016). The angular resolution of the observations of the individual transitions is between 12''0 × 14''6 (H151 α) to 16''8 × 13''8 (H158 α). To improve the signal-to-noise, the different Hn α lines were stacked in velocity after regridding each individual line to a common angular resolution (using CASA task `imsmooth`). Our image of the stacked continuum-subtracted emission of the RRLs has an angular resolution of 16''8 × 13''8. The RMS noise of the stacked image in a line-free channel is 1.5 mJy beam⁻¹.

This study focusses on the continuum-subtracted RRL emission associated with W49A ($v_{\text{LSR}} = 8.6$ km s⁻¹; Quireza et al. 2006a). A likely unassociated component at 60 km s⁻¹, which has been found in other RRL observations (e.g., Liu et al. 2013; Liu et al., in prep.), is not significantly detected in our dataset and not discussed further here (faint emission (<3 σ) at 60 km s⁻¹ is seen in some of the spectra in Fig. 5.3). The integrated emission between -40 and 60 km s⁻¹ (moment 0) is presented in Fig. 5.2. Individual spectra are shown in Fig. 5.3, with their positions indicated in Fig. 5.2 and in the upper left panel of Fig. 5.4. Images of all channels between -10 and 25 km s⁻¹ are shown in Fig. 5.4.

¹<https://bitbucket.org/drahner/warpfield/>

²<http://casa.nrao.edu>; version 4.2.2

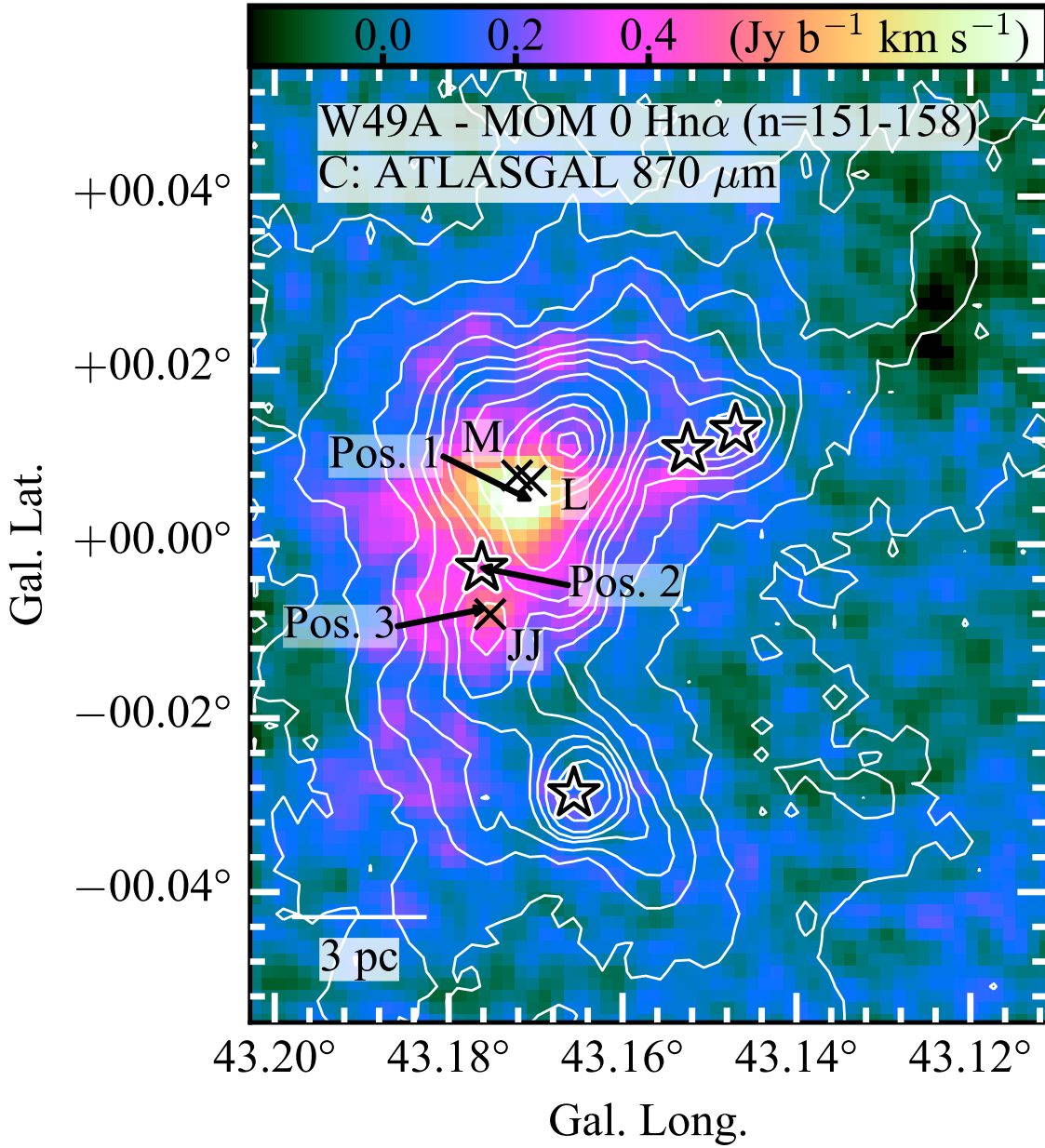


Figure 5.2: Integrated emission of stacked Hn α (n=151-158; angular resolution $16''.8 \times 13''.8$, 0.85 pc): The color scale shows velocity integrated intensity (between -40 and 60 km s^{-1}). Contours (white) show $870 \mu\text{m}$ emission (ATLASGAL survey; Schuller et al. 2009; contours as in Fig. 5.1). Stars indicate infrared star clusters (Alves & Homeier 2003). The positions of the spectra shown in Fig. 5.3 are marked, as well as the locations of the 3.6 cm continuum sources “M”, “L” and “JJ” (De Pree et al. 1997), which are mentioned in Sect. 5.3.1 and 5.5.1.

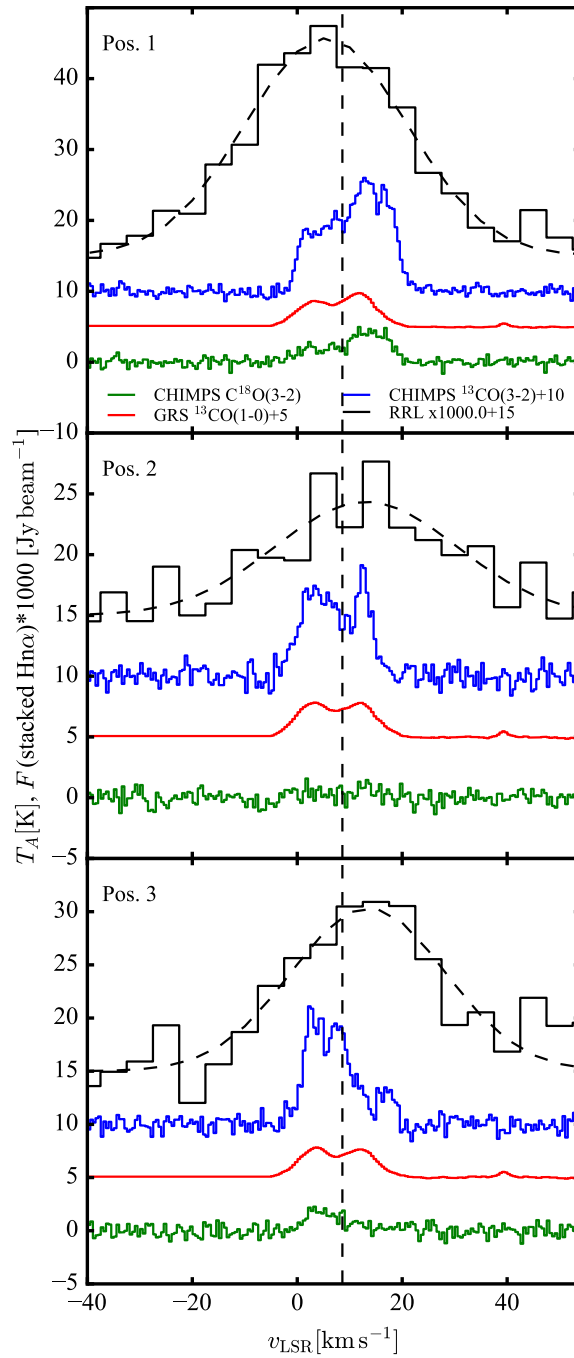


Figure 5.3: Spectra of $Hn\alpha$ ($n=151-158$; *black*), CHIMPS $^{13}\text{CO}(3-2)$ (*blue*), GRS $^{13}\text{CO}(1-0)$ (*red*) and CHIMPS $\text{C}^{18}\text{O}(3-2)$ (*green*), at selected locations in W49A, as indicated in Figs. 5.2 and 5.4. The RRL emission is scaled by a factor of 1000, and given in Jy beam^{-1} , while the antenna temperature (T_A) of the CO emission is given in K. The *black dashed* lines indicate the Gaussian fits to the RRL emission mentioned in Sect. 5.2.3. The channel spacing is 5 km s^{-1} for the RRLs, 0.5 km s^{-1} for CO spectra from CHIMPS, and 0.21 km s^{-1} for GRS.

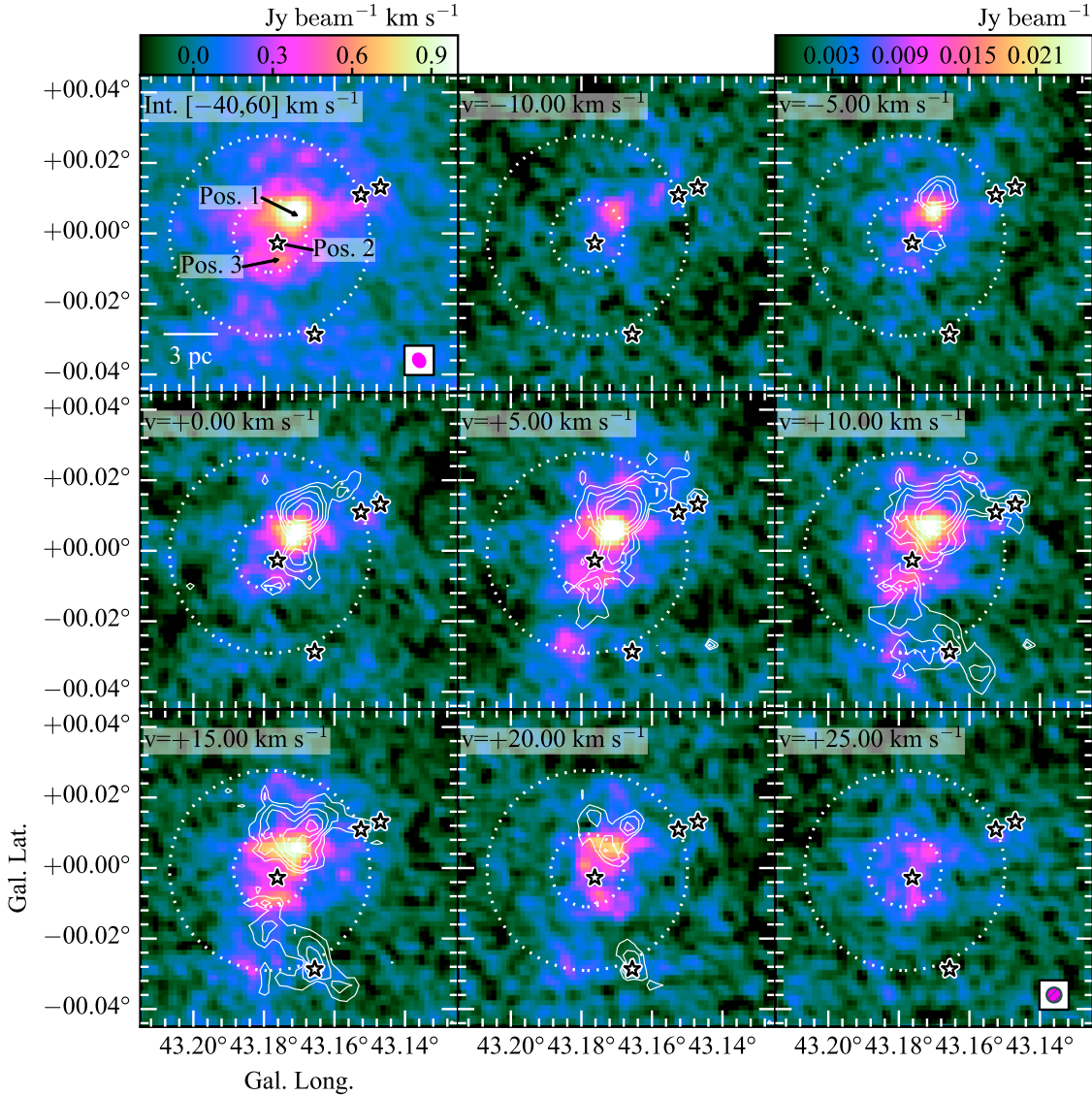


Figure 5.4: Channel maps of stacked $Hn\alpha$ $n=151-158$ shown in color scale. The *upper left panel* shows the moment 0 image (velocity integrated emission; Fig. 5.2), with the positions and numbers of the spectra in Fig. 5.3 overlaid. The remaining *panels* show the RRL emission between -10 and 25 km s^{-1} , with the corresponding contours of $C^{18}O$ emission (CHIMPS; Rigby et al. 2016; at levels of $T_A^* = 0.65, 1.03, 1.63, 2.59, 4.1 \text{ K}$) after binning to 5 km s^{-1} channels. The white dashed circles denote the shell of an expanding HII region (inner ring) and the assumed extent of W49A (outer ring) as described in Fig. 5.1. The center of both radii is $l = 43.1783^\circ$, $b = -0.0007^\circ$. Stars denote stellar clusters identified in Alves & Homeier (2003). The angular resolution of the RRL emission is shown in the lower right corner of the *left panel in the top row* (magenta). The angular resolution of the $C^{18}O$ emission is shown in the *right panel of the bottom row*, superposed as empty hatched circle in gray on the RRL beam.

5.2.2 Archival CO observations

To investigate the interplay between ionized and molecular gas, we use $^{13}\text{CO}(3-2)$ and $\text{C}^{18}\text{O}(3-2)$ emission (CHIMPS survey; Rigby et al. 2016) to trace the morphology and kinematics of molecular gas in W49A. Although ^{13}CO may be optically thick at the high column densities found towards W49A (Galván-Madrid et al. 2013), lines from high density tracers like CS and H^{13}CO^+ , as well as from the high column density tracer C^{18}O , show similar shapes in the same work. The ratio of main-beam brightness temperatures of the two CO isotopologues remains close to constant at ~ 0.11 across the peaks and troughs of the spectra, roughly in agreement with a ratio of 0.14 from Wilson & Rood (1994) in the solar neighborhood. This is expected as W49A has a similar Galactocentric radius as the Sun. Similar conclusions have been obtained by Miyawaki et al. (2009), based on investigations of $^{13}\text{CO}(J=1-0)$ and $\text{C}^{18}\text{O}(J=1-0)$ at $17''$ resolution. Hence, we assume ^{13}CO emission to be optically thin and use it with the $\text{C}^{18}\text{O}(3-2)$ emission for the kinematic analysis of the molecular gas in W49A.

Archival $^{13}\text{CO}(3-2)$ and $\text{C}^{18}\text{O}(3-2)$ data from the $^{13}\text{CO}/\text{C}^{18}\text{O}(J=3\rightarrow 2)$ Heterodyne Inner Milky Way Plane Survey (CHIMPS; Rigby et al. 2016) cover W49A with a half-power beam width (HPBW) of $\sim 15''$, and a channel spacing of $\sim 0.5 \text{ km s}^{-1}$. The standard deviation in the images is $\sigma(T_A) \sim 0.6 \text{ K}$ for $^{13}\text{CO}(3-2)$ and $\sigma(T_A) \sim 0.8 \text{ K}$ for the $\text{C}^{18}\text{O}(3-2)$. For comparison, also archival $^{13}\text{CO}(1-0)$ data from the Galactic Ring Survey (GRS; Jackson et al. 2006) are used, with a HPBW of $46''$, and a channel spacing of $\sim 0.2 \text{ km s}^{-1}$ (Simon et al. 2001). The standard deviation in the images is $\sigma(T_A) \sim 0.1 \text{ K}$. Spectra of all tracers are shown in Fig. 5.3 towards selected positions in W49A. Figure 5.4 shows emission contours of $\text{C}^{18}\text{O}(3-2)$ after smoothing to a spectral resolution of 5 km s^{-1} .

5.2.3 Gaussian line-fitting of the RRL data

To extract the kinematic properties of the RRL emission, maps of velocity centroids and line widths are derived for each tracer. The RRLs have typically a full width at half maximum (FWHM) of $25\text{--}45 \text{ km s}^{-1}$ in W49A. The RRL data are well described by a single Gaussian. We fit the stacked RRLs at each pixel with a Gaussian profile with the CASA task `specfit` to obtain maps of the peak velocity and FWHM (Fig. 5.5). Despite the large channel width of 5 km s^{-1} , the nominal uncertainty on the center of the Gaussian is $\lesssim 2.5 \text{ km s}^{-1}$ in all cases, and $< 1 \text{ km s}^{-1}$ towards the RRL emission peak.

5.3 Results

5.3.1 Spatial distribution of the RRL emission in comparison to other gas tracers

The emission in the stacked $\text{Hn}\alpha$ data between 1.6-1.9 GHz is spread over the entire W49A star-forming complex. The spectral indices of the continuum emission (α) fall between 0 and 1, indicating thermal, partially optically thick emission (Wang et al., sub-

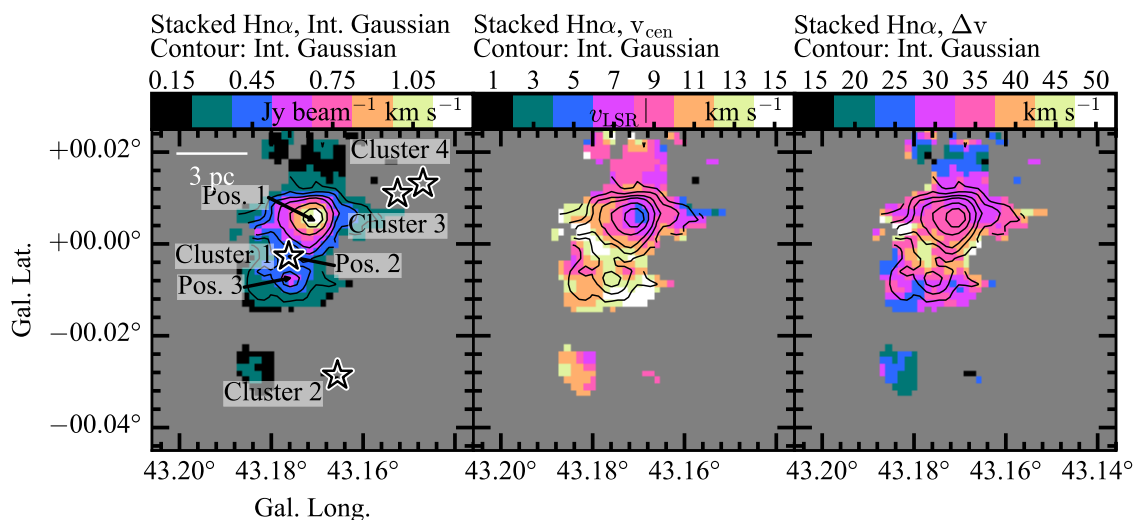


Figure 5.5: Integrated emission (*left panel*), peak velocity (*middle panel*) and full width at half maximum (*right panel*) of the Gaussian-decomposed, stacked H α ($n=151-158$) emission. The systemic velocity is marked in the colorbar of the middle panel ($v_{\text{LSR}} = 8.6 \text{ km s}^{-1}$; Quireza et al. 2006a). The contours represent integrated emission of the fitted Gaussian (shown in color in the *left panel*; at levels of 0.3, 0.4, 0.5, 0.6, 0.8, 1.0 and $1.2 \text{ Jy beam}^{-1} \text{ km s}^{-1}$).

mitted). It is similarly extended in W49A as the $8 \mu\text{m}$ continuum (Fig. 5.1) and the $870 \mu\text{m}$ continuum emission (Fig. 5.2).

The emission peaks of the different tracers are slightly different. The integrated 1.6–1.9 GHz RRLs peak offset from the $870 \mu\text{m}$ emission (Fig. 5.2). The offset between the peaks is $\sim 25''$ or $\sim 1.5 \text{ pc}$.

The peak in $870 \mu\text{m}$ emission corresponds to W49N, which harbors the “Welch-Ring” of UC H II regions (Welch et al. 1987), as indicated in Fig. 5.1 by the 5 GHz emission. The fact that the 1.6–1.9 GHz RRL emission (and the continuum emission at the same frequency) peaks slightly offset is likely due to optically thick continuum from the high-density ionized gas in the very compact UC H II regions at the location of the Welch-ring that lowers the flux at our longer wavelengths. A similar effect could be causing the relatively weak RRL emission towards W49S and W49NW, which also host UC H II regions (e.g. Dreher et al. 1984; De Pree et al. 1997).

The peak of the 1.6–1.9 GHz RRL emission occurs towards the more extended radio sources “L” and “M” at the edge of the Welch ring (e.g. Dreher et al. 1984, see Fig. 5.2 and inlay to Fig. 5.1). Since it is also offset from the dust emission peak, this H II region may have already cleared parts of its cocoon of gas and dust.

5.3.2 Shell-like distribution of RRL and CO emission around Cluster 1

At the center of W49A, the emission of stacked RRLs appears to have a shell-like morphology. The channel maps (Fig. 5.4) show that towards the position of Cluster 1 (Pos. 2

in Fig. 5.3), the RRL emission is suppressed. North and south of Cluster 1, the RRL emission increases, in parts resembling a ring-like structure. This emission is potentially indicative of an ionized bubble around Cluster 1 with a radius of $\sim 2 \pm 1$ pc, as indicated by the inner white ring in Fig. 5.4.

The radius of the bubble is in agreement with the shells found in 4.5 and 8.0 μm emission by Peng et al. (2010, 2-3 pc diameter). The RRL emission here agrees better with their shell 1, though this cannot be said with certainty due our the lower angular resolution of the RRL image. Extended emission at this position is seen in the broadband 1.6 GHz continuum image (Fig. 5.1) as well as in radio continuum at higher frequencies (e.g., De Pree et al. 1997).

Confirmation of this structure is seen in the $\text{C}^{18}\text{O}(3-2)$ data (Fig. 5.4), and less pronounced in $^{13}\text{CO}(3-2)$ and (1-0) emission (Fig. D.2). In Fig. 5.4 at 5 km s^{-1} , the C^{18}O emission resembles an arc around Cluster 1. Channel maps at 10 km s^{-1} and 15 km s^{-1} show elongated emission edges around Cluster 1, together with a lack of emission towards the center of the bubble (see also spectrum of Pos. 2 in Fig. 5.3). To a lesser degree, this can also be seen in $^{13}\text{CO}(3-2)$ and (1-0) emission in Fig. D.2. At 10 km s^{-1} and 15 km s^{-1} the emission is lower towards Cluster 1 than to the north and the south of it.

We do not observe a full ring in RRL or CO emission. RRL emission appears towards the north, south and west of Cluster 1 only, as confirmed by the CO observations. Together with arcs in 8 μm emission reported east of Cluster 1 by Peng et al. (2010, see also Fig. 5.1), we attribute the RRL emission to this ring-like structure around Cluster 1.

5.3.3 Kinematics of RRLs and ^{13}CO

5.3.3.1 Velocity distribution

The $^{13}\text{CO}(3-2)$ emission shows two components at similar strength towards Cluster 1 (Pos. 2). Blue-shifted with respect to the systemic velocity of W49A ($v_{\text{LSR}} = 8.6 \text{ km s}^{-1}$; Quireza et al. 2006a) lies a broad component with a peak at $\sim 4 \text{ km s}^{-1}$ (or multiple blended narrow components between 1–7 km s^{-1}). The other component is a narrow, red-shifted emission peak at $\sim 13 \text{ km s}^{-1}$. The RRL emission at this position is located between the CO components, albeit the peak occurs closer towards the red-shifted CO component, with a fitted peak of $13.6 \pm 2.7 \text{ km s}^{-1}$, which has high uncertainties due to the weak RRL emission at Pos. 2.

Across W49A, the stacked RRL emission shows variations in peak velocity from the north to the south. The peak velocity distribution of the RRL data (Fig. 5.5) indicates a peak velocity at the latitude of W49N (Pos. 1 and higher) of $6.2 \pm 0.7 \text{ km s}^{-1}$. At lower latitudes towards Pos. 3, velocities of $12.6 \pm 1.2 \text{ km s}^{-1}$ are observed.

The $^{13}\text{CO}(3-2)$ emission extends between 0–20 km s^{-1} in W49A. Towards Pos. 1, a red-shifted peak, while towards Pos. 3 a blue-shifted peak dominates the emission. In both positions, the ^{13}CO peak velocity appears anti-correlated with the peak velocity observed in the RRL emission at the same positions. At the RRL peak velocities, the ^{13}CO emission seems to be suppressed. The $\text{C}^{18}\text{O}(3-2)$ emission shows similar profiles and confirms the location of the ^{13}CO peaks. This confirms the assumption that the ^{13}CO emission profiles

are not affected by optical depth effects. The lower-angular resolution GRS $^{13}\text{CO}(1-0)$ emission shows two smooth peaks towards all three positions, which are mainly a result of averaging over variations within the $46''$ GRS beam.

To summarize, towards the position of Cluster 1, the RRL emission is located in between or aligned with one of the two ^{13}CO emission components. The two ^{13}CO components are separated by $\sim 9 \text{ km s}^{-1}$. If these are attributed to fore- and background parts of the shell bubble (Peng et al. 2010), the expansion or collapse velocity of this shell would be approximately between $5\text{--}10 \text{ km s}^{-1}$, depending on whether both parts of the shell are moving, or one of them is at rest with respect to the star cluster. To the north and south of the center of the shell bubble (Peng et al. 2010), the RRL and CO emission show one main component, with the peaks at each position anti-correlated with respect to the rest velocity of W49A ($v_{\text{LSR}} = 8.6 \text{ km s}^{-1}$; Quireza et al. 2006a). For the following modelling (Sect. 5.4) of this ionized bubble, we assume a spherical structure with a shell radius of $1\text{--}3 \text{ pc}$ radius from the RRL emission data and a relative velocity of the shell components of $5\text{--}10 \text{ km s}^{-1}$.

5.3.3.2 Distribution of the FWHM of the RRL emission

It is intrinsically difficult to see expansion or infall signatures in the RRL line profiles, due to their large line widths of up to 50 km s^{-1} . The large line width itself, especially towards Cluster 1 (note the increase of line widths up to 45 km s^{-1} in Fig. 5.5), however, may point to unresolved dynamical motions. Contributions to the line width are thermal broadening, pressure broadening and non-thermal motions. Assuming an electron temperature for W49A of $T_e \sim 8300 \text{ K}$ (Quireza et al. 2006b), the thermal line width is approximately 20 km s^{-1} . An estimation of the pressure broadening requires observations of lower-order RRLs, as pressure broadening depends on transition level to the seventh power (e.g., Keto et al. 1995). Observations of mm- $\text{H}\alpha$ lines ($n = 39 - 42$) are available at an angular resolution of $\sim 20''$ towards the ATLASGAL dust emission peaks in W49A (Kim et al. 2017). For W49N (source AGAL043.166+00.011), a line width of $37.0 \pm 0.2 \text{ km s}^{-1}$ is reported for the mm-RRLs, while the cm-RRLs presented here have a line width of $31.4 \pm 3.3 \text{ km s}^{-1}$. Since the widths are larger or comparable at most, we conclude that dynamical broadening dominates the emission, which is expected due to the large number of UCH II regions at this location. Towards Pos. 3 (source AGAL043.178-00.011), the line width of the cm-RRL is larger than the mm-RRL ($29.7 \pm 0.5 \text{ km s}^{-1}$ and $33.5 \pm 4.0 \text{ km s}^{-1}$, respectively). Using equations 4 and 5 from Nguyen-Luong et al. (2017) and a thermal line width of 20 km s^{-1} , we derive line widths of dynamical and pressure broadening of 23 km s^{-1} and 6 km s^{-1} , respectively. Again, this indicates that dynamical broadening dominates the RRL line width. While this is likely to be true for most of W49A due to its high star formation activity, pressure broadening is certainly present and may be dominant towards some positions. Especially for large line widths in Fig. 5.5 (e.g., Pos. 2), observations of RRLs with lower quantum numbers at the same angular resolution as the cm-RRLs are necessary to verify the role of pressure broadening (see, e.g., Nguyen-Luong et al. 2017).

An investigation of the spectra for double peaked structures which would be indicative

for relative motions of front and back of a shell is not conclusive: Figure 5.4 shows slightly more emission in Pos. 2 at 5 km s^{-1} and 15 km s^{-1} , compared to 10 km s^{-1} . The variation, however, is only at a $2\text{-}\sigma$ level and the spectrum is not fitted well by two Gaussians. Also, two distinct Gaussian components with such a small velocity separation are not expected to be distinguishable in the RRL data from a single Gaussian due to their large intrinsic, thermal line widths.

5.4 Stellar feedback models for W49A

How has star formation progressed in W49A? We will now use the presented data to answer important questions about W49A: What influence has the formation of high mass stars had on the cluster's subsequent evolution? To explore possible scenarios of the evolution of W49, we employ models of an expanding shell around star formation to compare with our observations.

In the following, we compare our data to models of an expanding shell of star cluster inside a molecular cloud to constrain the evolution of the shell around Cluster 1, which was discussed in Section 5.3.2. Given its complexity in terms of currently ongoing star formation and density distribution, we do not aim here to reproduce the RRL emission in W49A directly. Rather we aim to use the radius at which the RRL emission peaks to constrain the evolutionary history of the shell. As discussed below, we use literature values on the stellar mass in Cluster 1, the molecular cloud mass and the average density of W49A (see Table 5.1) as initial conditions and constrain the evolutionary stage of the shell with the observed radius of the shell and age of the stellar cluster.

As introduced briefly in Chapter 1, Rahner et al. (2017) have developed feedback models (WARPFIELD) describing the expansion of a hydrostatic, spherical shell due to radiative feedback from young stars, including the energy and momentum input from stellar winds and supernovae, while also accounting for the effects of the gravity of the cluster and the self-gravity of the cloud. Models with the physical prescription for the hydrostatic shell, which is used in WARPFIELD, have been successfully compared to observations in previous works (e.g., M17; Pellegrini et al. 2007). In the models by Rahner et al. (2017), the expansion of the shell is initially governed by adiabatic expansion due to wind-shocked gas from the stellar winds of O/B stars in the massive star cluster. Once cooling becomes comparable to the wind-energy input, a second phase starts, and momentum driven expansion from radiation and winds dominate. A potential third phase of expansion is reached as the entire molecular cloud is swept up and the system freely expands into the (low-density) ambient medium.

These models are applied here due to their advantage in efficiently probing large parameter spaces in molecular cloud mass, density and star formation efficiency. Since this requires a simplified model to remain computationally feasible, the models assume a 1D geometry (i.e., spherical symmetry of the H II region). While this is certainly a limitation, especially for determining detailed dynamics and morphologies of H II regions, they allow us to trace the general evolution of feedback-driven shells. The models also incorporate all relevant physical aspects of feedback, in particular for very massive and luminous regions

in which the initial mass function should be fully sampled, with masses of individual stars of up to $120 M_{\odot}$. In the sub-region of W49A relevant for this investigation, Cluster 1, the most massive star has a mass of $M = 130 \pm 30 M_{\odot}$ (Wu et al. 2016), which is within the uncertainties of the highest mass of sampled stars in the models. Therefore, since W49A is one of the most massive and luminous regions in the Milky Way, it is an ideal target for such an investigation (Urquhart et al. 2018).

5.4.1 Initial conditions

The input parameters for the models are listed in Table 5.1. Galván-Madrid et al. (2013) find a molecular gas mass of $M_{\text{gas}} \approx 2 \times 10^5 M_{\odot}$ for W49A within a radius of 6 pc, which we adopt for the modeling in the following. The value is in agreement with the cloud mass derived from dust emission (Sievers et al. 1991; Urquhart et al. 2018). As a side note, W49A is embedded within a larger molecular cloud complex, which has a total mass (including W49A) of $1 \times 10^6 M_{\odot}$ within 60 pc (Galván-Madrid et al. 2013). Hence, free expansion of the feedback-driven shell into the low-density ISM would only occur far beyond a radius of 6 pc. Since the shells in the models considered here do not expand beyond this point during the first expansion (see Sect. 5.4.2), we treat the molecular cloud mass as fixed at $M_{\text{gas}} \approx 2 \times 10^5 M_{\odot}$ in the models. Low-density channels, in which free expansion would occur earlier, could exist in the true initial density distribution. Such channels could influence the expansion of the shell in the energy-driven phase, i.e. in the initial stages of the expansion. The momentum-driven expansion phase of the shell is not significantly affected.

Assuming a homogenous medium and spherical geometry for $r < 6$ pc, the average initial molecular density of W49A is estimated as $n \sim 4 \times 10^3 \text{ cm}^{-3}$. To address uncertainties of at least a factor of two in the molecular gas mass, multiple models are computed to explore a parameter space in density³ of $n = (2 - 10) \times 10^3 \text{ cm}^{-3}$, in steps of $1 \times 10^3 \text{ cm}^{-3}$. The initial radial gas density profile of the models is assumed to be flat. It has to be noted that in reality, the cloud density might evolve as a function of time due to inflow of gas onto the cloud (e.g., Fukui et al. 2009; Seifried et al. 2017; Ibáñez-Mejía et al. 2017). This is currently not taken into account in WARPFIELD.

With literature constraints on the mass of the stellar clusters in W49A (Alves & Homeier 2003) and the above assumption on the molecular cloud mass, we constrain the star formation efficiency (SFE). The mass of the central O/B-star cluster, Cluster 1 (Fig. 5.1), is $M_* = 1 \times 10^4 M_{\odot}$ (Homeier & Alves 2005), but may potentially be higher due to the large visual extinction in the region. Therefore, we choose SFEs of $\epsilon = 0.05$ and 0.09 , to account for star cluster masses of $M_* \approx (1 - 2) \times 10^4 M_{\odot}$.

For these parameter ranges in density and SFEs the cluster does not disperse its cloud in the first 2 Myr, assuming a cloud mass of $M_{\text{cl}} = 2 \times 10^5 M_{\odot}$ (see Table 5.1; Galván-Madrid et al. 2013; Urquhart et al. 2018), nor does it drive feedback shells beyond the outer radii of W49A (see Sect. 5.4.2). The total cloud mass is only of dynamical importance once free expansion into the ambient ISM sets in. Since this stage is not reached in any of the

³Mass densities chosen as input to WARPFIELD are: $\rho \approx (8-40) \times 10^{-24} \text{ g cm}^{-3}$, in steps of $4 \times 10^{-24} \text{ g cm}^{-3}$.

models in the first 2 Myr, the important parameters are the density and SFE. We choose not to vary the initial molecular cloud mass of $M_{\text{cl}} = 2 \times 10^5 M_{\odot}$, which is the mass in W49A within $r < 6$ pc. The shell will encounter the ambient ISM only at $r > 60$ pc, since W49A is embedded into the larger molecular cloud complex W49. Therefore, the assumption of a fixed initial cloud mass is reasonable, as the phase of free expansion of the shell is likely to start only at larger radii, and after accumulating more mass than assumed here.

5.4.2 Models of stellar feedback indicate collapse of an initially expanding shell

The time evolution of the shell radius in each model is shown in Fig. 5.6, with $t = 0$ at the beginning of the expansion of the shell. For simplicity, we neglect the (ultra)-compact H II-region phase of the high-mass stars, which is assumed to occur before the shell expansion and is considerably smaller than the stellar ages (3×10^5 yr; Mottram et al. 2011). The shell is expected to have a similar age as the O stars, i.e. 1-2 Myr (Wu et al. 2016). This time range is highlighted in Fig. 5.6 in gray, together with the adopted current expansion radius of 1-3 pc (in comparison, the angular resolution of the RRL images is ~ 0.8 pc), in agreement with both the RRL emission (see Sect. 5.3.2) and the $8 \mu\text{m}$ emission (Peng et al. 2010). For reference, the approximate radius of the entire W49A region is shown as gray-shaded region C in Fig. 5.6.

These conditions are met by several models: For a large range of densities, shells fall within the limits of the radius after an evolution of 1-2 Myr. In all models in Fig. 5.6, the observed shell size agrees with the simulated shell size at two distinct times – once during collapse and again during re-expansion. For three models ($n = 2.5, 4.0, 7.5 \times 10^3 \text{ cm}^{-3}$), the radius and range in time at which the observational constraints are met are indicated schematically in Fig. 5.6 (by a colored bar which is labeled “now”). If the double-peaked velocity profile in the ^{13}CO data is attributed to relative motions of the back and the front of the shell, it would be expanding or collapsing at a speed of $5\text{--}10 \text{ km s}^{-1}$ (see Sect. 5.3.3). This agrees well with the modeled velocities of the re-collapsing shells. For each model, the formation period of the O/B-stars is highlighted as between 1 and 2 Myr before $t = \text{“Now”}$ (Wu et al. 2016). Similarly, the presence of UCH II regions in W49A indicates a more recent episode of star formation (a few $\times 10^5$ yr ago or even more recent; Kawamura & Masson 1998; Wood & Churchwell 1989; Mottram et al. 2011). The formation period of the UCH II regions is marked as a time span of 3×10^5 yr before the current time in Fig. 5.6.

All three models which are discussed here show the same qualitative evolution. A shell, triggered by the formation of a star cluster (*left panel* of Fig. 5.7), expands to a certain radius inside the molecular cloud (*middle panel* of Fig. 5.7), at which point the self-gravity of the shell and the gravity of the star cluster start to dominate the force balance. The shell would re-collapse to form a new star cluster. Using the observed shell radius and star cluster age as constraints, we infer that the shell is either at the end of re-collapse or at the beginning of a new expansion (*right panel* of Fig. 5.7).

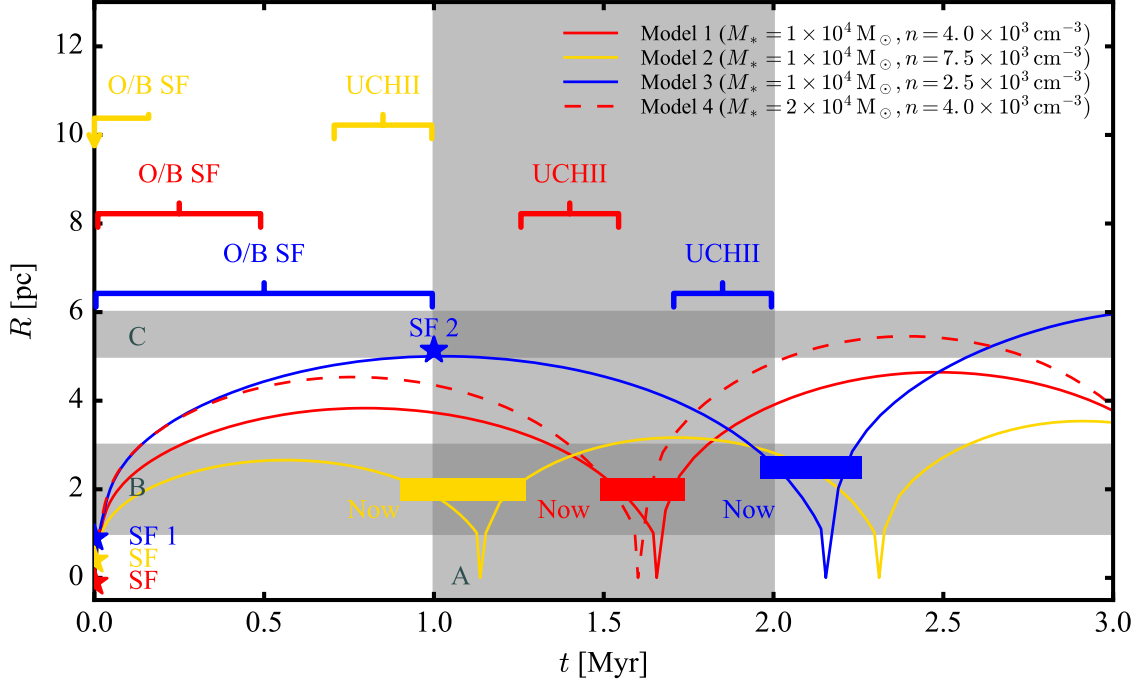


Figure 5.6: Expansion radius vs. time for models of stellar cluster feedback (WARPFIELD; Rahnner et al., 2017) in W49A. $t = 0$ denotes the formation of the first stellar cluster. Observational constraints on stellar cluster age (A), shell size (B) and extent of W49A (C) are shown in gray. Models 1-3 were computed with molecular gas densities of $n = (4.0, 7.5, 2.5) \times 10^3 \text{ cm}^{-3}$, respectively, and a stellar cluster mass of $M_* = 1 \times 10^4 M_\odot$. Model 4 used a molecular gas density of $n = 4.0 \times 10^3 \text{ cm}^{-3}$ and a stellar cluster mass of $M_* = 2 \times 10^4 M_\odot$. Each model agrees best with the observations at the expansion radius indicated by a *filled bar* (“Now”), which then defines the elapsed time. The stars with labels “SF” or “SF 1” denote the time of the formation of the first stellar cluster in the model. To put the models into perspective, the observational constraints from the perspective of the today (*filled bars*) on the age of the O/B cluster and the UCH II regions are highlighted by brackets in the top part of the plot (“O/B SF” or “UCH II”). The later bound of the observational constraints on the O/B star formation in Model 2 (indicated by a *yellow arrow*) coincides approximately with the formation of the first star cluster in the model. For Model 3, “SF 2” marks the radius and time at which the model reaches the outskirts of W49A (no additional star formation is input to the model at this point).

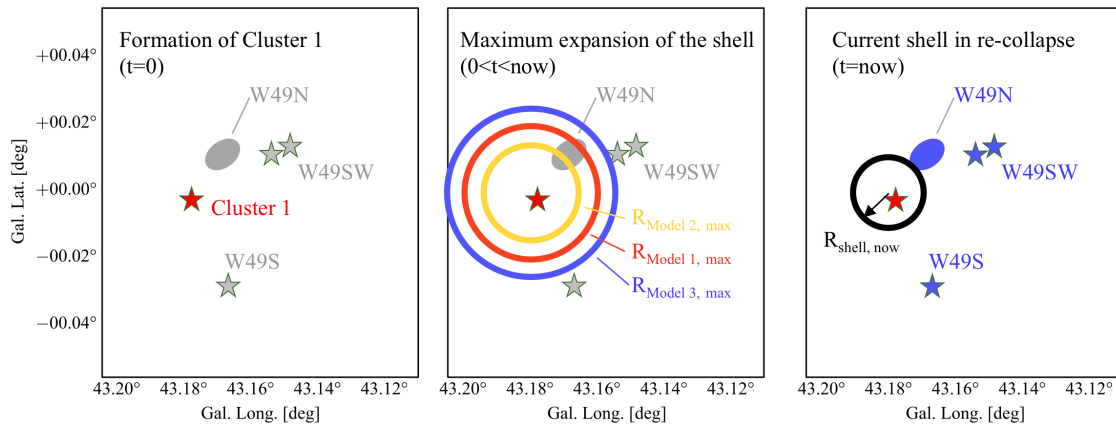


Figure 5.7: Sketch of the evolution of the feedback-driven shell around Cluster 1 in W49A (see text for details). At $t = 0$, Cluster 1 (red) is formed in the models (left panel). The feedback from Cluster 1 drives a shell into the molecular gas of W49A (middle panel). The radii of maximum extension from Fig. 5.6 are highlighted (Model 1, 2, 3 in red, yellow and blue, respectively). The shell re-collapses to its observed extent. The other stellar sub-clusters, as well as the Welch-Ring, are highlighted in blue in the right panel, to indicate their relative position. In the left and middle panels, these objects are highlighted in gray to indicate that, depending on the model, they may not have formed yet and that their formation may have been triggered by the feedback-driven shell around Cluster 1. The stellar clusters/Welch ring are not to scale.

All models predict that Cluster 1 is not powerful enough to disperse the molecular cloud. Rather the dispersal would only happen after repeated collapse, which would trigger more star formation. Additionally, feedback-triggered star formation in the outskirts of W49A (i.e., fragmentation of the shell or shell collision with outer dense clumps) could increase the total amount of stellar feedback which might eventually become sufficient enough to disperse the cloud.

As can be seen from Models 1-3 in Fig. 5.6, the shell expands farther in surroundings of lower densities, and will also take a longer time to re-collapse for models with lower initial cloud densities. For a given stellar cluster mass with the same strength of feedback, this is expected, since the shell has piled up more material at a given radius in a denser medium. At even lower densities, feedback from the first cluster would be sufficient to destroy the cloud. However, such low densities are ruled out by the observations. Similarly, increasing the stellar cluster mass (within the masses probed here) allows the model to push to larger radii, while the timescales for re-collapse are not strongly affected. More massive stellar clusters provide stronger feedback forces, which accelerate the shell to higher velocities and therefore cause the larger expansion. This is shown in Model 4 in Fig. 5.6, for $M_* = 2 \times 10^4 M_\odot$ at a constant density of $n = 4 \times 10^3 \text{ cm}^{-3}$.

The radius of maximum expansion varies among the different models between the currently observed radius (gray-shaded region B in Fig. 5.6; Model 2) and the projected radius of W49A (gray-shaded region C; Model 3). Radial, monotonically decreasing density profiles would imply denser material in the center of W49A. The acceleration of the shell would be lower within the maximum expansion radii of the models considered here,

since the material which is swept-up in the shell grows faster with radius. Also, feedback due to thermal pressure in phase 1 (see above) would be lower, as dense gas cools faster. Both effects would lead to smaller radii of maximum expansion.

For all densities probed here, the models confirm that shells driven by Cluster 1 may have at least affected the Welch ring and possibly triggered star formation there (in agreement with [Alves & Homeier 2003](#); [Peng et al. 2010](#)). They have in common that the feedback-driven shell underwent re-collapse. On the lower end of the density range justified by the observations, shells have pushed to the outskirts of W49A in the past, and may have affected star formation all across W49A.

5.5 Discussion

5.5.1 Dynamics of re-collapse in W49A

The stellar feedback models predict a shell in contraction, which is about to induce or may have already induced a new star-formation event. From an observational perspective, the double-peaked emission of molecular gas towards Pos. 2 (Cluster 1) is consistent with the presence of a moving shell. Both peaks are $\sim 4.5 \text{ km s}^{-1}$ offset from the systemic velocity of $v_{\text{LSR}} = 8.6 \text{ km s}^{-1}$ ([Quireza et al. 2006a](#)). This indicates expansion or contraction of $\sim 4.5 \text{ km s}^{-1}$, if the star cluster, which drives the shell, is at the systemic velocity. It is not possible to determine from CO and RRL emission alone, whether the shell is expanding or collapsing. The RRL emission appears to be associated more with the high velocity peak. However, the exact peak position is uncertain, due to the low signal-to-noise of the RRL emission at this position. Optically thick continuum emission at 18 cm (spectral index $\alpha = 0-1$; Wang et al., submitted) may additionally influence the emission shape, by hiding (or substantially weakening) specific spectral sub-components. Depending on the rest velocity of the star cluster, it may further be possible that expansion or collapse are asymmetric and that one part of the shell is at rest.

Anti-correlation between molecular and ionized emission in velocity is seen towards Pos. 1 and Pos. 3, offset from Cluster 1. At the peak velocities of the ionized gas emission in both positions, the strength of molecular gas emission is weaker in comparison to emission at other velocities. If both gas phases at a given velocity are spatially connected, this emission may be weaker as the molecular gas is destroyed.

The emission structure at both positions can also be affected by local star formation and does not have to be dominated by the shell dynamics alone. Pos. 3 harbors the cm-continuum emission source “JJ”, while Pos. 1 the sources “M”, and “L” (see Fig. 5.2; all three sources are characterized with low-cm continuum emission in [De Pree et al. 1997](#)). Pos. 1 is also located at the edge of the Welch-Ring. Towards this sub-region of W49A, dense gas tracers such as CS show evidence for collisions between dense gas clouds (see e.g., [Serabyn et al. 1993](#)), although this interpretation is not unambiguous (e.g., [Williams et al. 2004](#)). The velocity signature therefore may not only be shaped by large-scale motions, such as the expanding bubbles, but also by the small-scale dynamics.

The precise time of the formation of the second generation of stars postulated by the

models is difficult to constrain since the shell is either close to the end of the re-collapse or at the beginning of the second expansion phase. Towards the center of Cluster 1, we do not see evidence of UC H II regions, many young stars or enhanced dust opacities (compared to the rest of W49A), which would be indicative of recently new stars having been formed there. However, high foreground extinction towards W49A ($A_V > 30$ mag; [Alves & Homeier 2003](#)) and high uncertainties in stellar ages make it impossible to rule out that a second generation of stars has already formed at this position.

Furthermore, as W49A is clearly not spherically symmetric, it is also possible that Cluster 1 did not form at the center of mass and the shell may collapse to a different center. In the idealized case of a 1D geometry the cloud is forced to re-collapse onto the same cluster. Depending on the stellar mass distribution, which is intrinsically difficult to measure for the region, the re-collapsing gas may fall more towards W49N, which is 3 pc offset from Cluster 1 in projection ([Alves & Homeier 2003](#)) and therefore may be within the maximum radius of expansion for large parts of the range of densities in agreement with the observations. The youngest clusters dominate feedback. So long as the shell expands to a radius which encompasses both populations the models will be valid in the future. Hence, without clear evidence of the presence nor of the absence of a new population of stars at the center of the shell, the molecular cloud is either shortly before, after or even within a new episode of star formation.

Most likely, W49A is currently in the phase of the formation of this second star cluster. Indication of this is the large number of compact and UC H II regions surrounding Cluster 1, including the Welch-Ring. These may have been triggered during the re-collapse of the shell. Since some of them are extended (i.e. source "L"; [De Pree et al. 1997](#)), they may already be contributing to the feedback of the bubble. These sources may provide the feedback to halt the re-collapse of the shell in the future, or may have already started the second expansion period of such a shell.

5.5.2 Effect of feedback on the molecular gas in W49A

The WARPFIELD models were used in Sect. 5.4.2 to characterize the expansion of the shell radius. This section discusses to what extent other parts of W49A were affected by it and where star formation may have been triggered by feedback, e.g., via triggering of clumps of molecular gas into gravitational collapse (e.g., [Elmegreen & Lada 1977](#); [Whitworth et al. 1994a](#); [Preibisch et al. 2002](#); [Preibisch & Zinnecker 2007](#)).

For all models highlighted in Fig. 5.6, the expanding shell remains confined to the inside of W49A (<6 pc). The radius of maximum expansion is between 2.5-5 pc. This implies that feedback of Cluster 1 has affected molecular gas in W49N. The Welch-ring harbors UC H II regions, which have an approximate lifetime of 3×10^5 yr ([Mottram et al. 2011](#)). Therefore, these need to have formed after the O/B stars in Cluster 1. Feedback may have triggered the star formation in the Welch ring, either at the point of maximum expansion (Model 2; $n \sim 7.5 \times 10^3 \text{ cm}^{-3}$), or during contraction at re-collapse (Models 1,3,4; $n \lesssim 7.5 \times 10^3 \text{ cm}^{-3}$). Also, as discussed in Sect. 5.5.1, these UC H II regions may already be part of the second episode of star formation after re-collapse.

Towards the lower bound of the considered range of densities (Model 3; $n \approx 2.5 \times$

10^3 cm^{-3}), feedback could have pushed to the outskirts of the cloud. During the expansion, it may have triggered star formation in molecular clumps in the swept-up molecular gas, which could be the reason for the formation of O stars and UC H II regions outside of Cluster 1, as well as larger star forming sites such as W49S and W49NW (Fig. 5.1). Shell fragmentation could be a possible cause for these clumps to be decoupled from the bulk collapse of the shell. This may occur especially when the expansion of the shell has considerably slowed down (e.g., McCray & Kafatos 1987, see eq. 14 therein). This is expected at the expansion maximum and could explain why we observe them today at projected distances from Cluster 1 of $\sim 5 - 6$ pc.

We note that for Models 1 and 2, the molecular clumps W49S or W49NW at the edge of W49A, would not have been affected by the star formation in Cluster 1; they were of independent origin. Their formation may be connected to global motions, like cloud-cloud collisions (Serabyn et al. 1993) or fragmentation of filamentary inflow (Galván-Madrid et al. 2013). This may fit in the picture of sub-clustered star formation, which does not require a causal connection between individual events of star formation in W49A (e.g., Alves & Homeier 2003).

For the models in Sect. 5.4, we assumed a homogeneous density profile. If the density instead increased towards the molecular cloud center, the evolution of the shell would have a smaller radius of maximum expansion. However, the models would still predict a re-collapsing shell similar to Model 1 and 2.

It needs to be stated that the models do not predict any ejecta at distances $d > 12$ pc, as discussed by Peng et al. (2010). In the picture of re-collapsing shell models, these would need to be formed independently, at least if feedback were driven only by Cluster 1. In principle, strong inhomogeneities in the molecular cloud could have allowed feedback to channel out of the surrounding molecular cloud. However, as mentioned by Peng et al. (2010), high energies would be necessary to drive these ejecta (few $\times 10^{50}$ erg).

To summarize, the WARPFIELD models show that the feedback shell has affected different subsections of the molecular cloud and potentially triggered star formation, depending on the assumed density distribution of the molecular cloud. Star formation in parts of the cloud which were not affected by feedback, need to have occurred in different ways. Therefore, these models do not necessarily rule out other hypotheses on the formation scenario of stars in W49, such as sub-clustered star formation or cloud-cloud collisions, which had been discussed so far in the literature.

5.5.3 Star formation rate and multiple generations of stars

Re-collapsing shells induce episodic events of star formation in a molecular cloud. At each re-collapse event, stars are formed at a certain instantaneous star formation efficiency (SFE),

$$\epsilon = M_*/M_{\text{cloud}}, \quad (5.1)$$

with M_* the mass of the star cluster originating from a single star formation event, and M_{cloud} the cloud mass prior to the formation of a cluster (e.g., Murray 2011). If star

clusters continue to form with a fixed SFE for each star formation event (we adopt values of $\epsilon = 0.05$ and 0.09), it would take multiple re-collapse events (each of which leads to a new star formation event) to disperse the cloud. Since the main focus of the model comparison was to follow the first expansion cycle of the feedback shell from Cluster 1, we assume here for simplicity that the SFE at future collapse events is the same as at the initial cluster formation. Changes in the SFE, however, are expected (as, e.g., in 30 Dor; [Rahner et al. 2018](#)), since the SFE depends on the physical conditions of the re-collapsing gas, which are likely to be different than during the first episode of star formation.

Re-collapsing shells change the star formation rate as they govern the timescale at which star formation occurs. It is given by

$$\dot{M}_* = M_*/t_{\text{SF}}, \quad (5.2)$$

with M_* the mass of the stellar cluster and t_{SF} the time, over which star formation occurs. In the case of re-collapsing feedback shells, an estimate of t_{SF} is given by the time between two feedback events. As mentioned in Sect. 5.1, the star formation efficiency evaluated over the entire lifetime of the cloud is self-regulated (i.e., the total number of stars per cloud lifetime). It may not strongly depend on how star formation in a molecular cloud proceeded in detail, and therefore may not be affected. It is given by

$$\epsilon_{\text{GMC}} = M_{*,\text{total}}/M_{\text{cloud}}, \quad (5.3)$$

with ϵ_{GMC} being the cumulative star formation efficiency, $M_{*,\text{total}}$ the mass of stars formed over the GMC lifetime, and M_{cloud} the cloud mass prior to the formation of a cluster at each re-collapse.

Re-collapse models generally yield a star formation per free-fall time of about 1% (see [Rahner et al. 2017](#), section 7). The star formation efficiency per free-fall time ϵ_{ff} is given by (e.g., [Krumholz & McKee 2005](#))

$$\epsilon_{\text{ff}} = (\dot{M}_*/M_{\text{cloud}}) \times \tau_{\text{ff}}, \quad (5.4)$$

with M_{cloud} the cloud mass prior to cluster formation. The free-fall time for W49A is ~ 0.5 Myr, assuming a density $n = 4.0 \times 10^3 \text{ cm}^{-3}$. Considering Cluster 1 in isolation, we obtain $\epsilon_{\text{ff}} = 1 - 2\%$ for W49A. The star formation efficiency per free-fall time for the entire W49A star-forming region is likely to be different, as Cluster 1 amounts to only 20% of the stellar mass in W49A. Also, if the recently formed stars will eventually power a common feedback shell, it will affect the evolution of this shell and change the time-scale between re-collapse events.

Models of re-collapsing shells have implications for the age distribution of the future star cluster. Different generations of stars would be expected in W49A, induced by recurring collapse events and the subsequent formation of a new star cluster. Their age difference in the case of W49A will however be small compared to other star forming regions, such as 30 Doradus (see Sect. 5.5.4). The models for Cluster 1 predict only a small age difference of 1-2 Myr. The wide-spread star formation in W49A suggests that stars may form also in between (see Sect. 5.5.2). The age differences are therefore likely

to be lower than 1 Myr, which is well within typical uncertainties of the ages derived for O stars, and therefore intrinsically difficult to differentiate observationally.

5.5.4 W49A in comparison to the massive star-forming region 30 Doradus

One of the most prominent prototypes for an extreme high-mass star-forming region can be found in 30 Doradus, which is located in the Large Magellanic Cloud (LMC). It has the observational advantage of being visible in the optical, which is not possible for W49A, due to the obscuration of the dust by the Milky Way. There are obvious differences between both regions in molecular gas mass (depending on method and radius: $10^{6-7} M_{\odot}$ for 30 Doradus; e.g., Dobashi et al. 2008; Faulkner 1967; Sokal et al. 2015; vs. $10^{5.3-6}$ for W49A; e.g., Galván-Madrid et al. 2013) and stellar cluster mass ($7 \times 10^4 - 5 \times 10^5 M_{\odot}$ for 30 Doradus; Selman et al. 1999; Bosch et al. 2001, 2009; Cignoni et al. 2015; vs. $5 - 7 \times 10^4 M_{\odot}$ for W49A; Homeier & Alves 2005). Here, we focus the discussion on feedback-related star formation in both star-forming regions.

The star cluster NGC 2070 in 30 Doradus contains a sub-cluster, R136, which is younger (~ 1 Myr) than the older stellar population of NGC 2070 (~ 5 Myr; Brandl et al. 1996; Walborn & Blades 1997; Massey & Hunter 1998; Selman et al. 1999; Sabbi et al. 2012; Cignoni et al. 2015; Crowther et al. 2016). Rahner et al. (2018) found that the formation of R136 can be naturally connected to the formation of NGC 2070 by the re-collapse of an expanding shell from the first star formation event, and the subsequent formation of R136. While the stars in W49A are of similar age as R136, there is no distinct older population. Rather, there seems to be only an even younger population of UCHII regions present in W49A, with an age difference to the O-star population of 1-2 Myr (see Sect. 5.5.2). The model confirms this difference in star formation history: While for 30 Dor, the models find re-collapse events 3-4 Myr after the initial event of star formation, the re-collapse is predicted earlier for W49A, within 2 Myr after initial star formation.

The larger re-collapse interval in 30 Doradus is due to a combination of different cloud density, stellar cluster mass and metallicity. The models require higher initial molecular gas densities in W49A to satisfy the observational constraints ($n \gtrsim 2.5 \times 10^3 \text{ cm}^{-3}$) than have been found for 30 Doradus ($n \gtrsim 5 \times 10^2 \text{ cm}^{-3}$). The mass of the first cluster of stars is a factor of a few higher in 30 Doradus and its metallicity is lower at $Z \approx 0.5 Z_{\odot}$ (Lebouteiller et al. 2008; Choudhury et al. 2016).

The lower metallicity in 30 Doradus changes the shell evolution in a nontrivial manner. While Lopez et al. (2011) suggest weaker winds in low-Z systems, Rahner et al. (2017) finds that the longer cooling time can lead to winds being more important, as the expansion of the shell stays in phase 1, the energy-driven phase, for a longer time. Pellegrini et al. (2011) finds that the shell structure is over pressured near the cluster by X-ray bubbles over radiation pressure, consistent with the results by Rahner et al., and in opposition to Lopez et al. (2011). In turn, accelerations of the shell in phase 2 the momentum-driven phase may decrease. Low metallicities imply weaker stellar wind lu-

minosities (e.g., Lopez et al. 2011) and affects the coupling of radiation to the shell by changing the shell structure (Rahner et al. 2017): The confining pressure from the winds of the shell is weaker, which leads to lower densities in the shell (see Rahner et al. 2017, eq. 14). In turn, these lower densities result in a decrease in radiation pressure on a given part of the shell, as it absorbs less ionizing radiation than a high density shell, because the absorption of ionizing radiation by hydrogen depends on the recombination rate and is proportional to n^2 . The effect of metallicity is therefore complicated and it depends on the details of the investigated model whether there is faster or slower expansion. Further, Pellegrini et al. (2011) found significant fractions of the 30 Doradus region to be dominated by optically thin (fully ionized gas) further leading to a decoupling between radiation and the gas, a result that can only be explained by a complete accounting for feedback and ISM coupling and cooling, and not from simple scaling relations.

These models provide a framework with which to understand how feedback (both positive and negative) regulates star formation and the associated timescales. The fact that models with re-collapse of a feedback shell are compatible with observations in W49A indicates that re-collapse may not be a phenomenon that is unique to 30 Doradus. This would imply that feedback is not only responsible for cloud dispersal, but could also be the means of star formation to regulate the rate of stellar birth by introducing a timescale for subsequent cluster-formation events. The timescale would be much shorter (<2 Myr) in W49A than in 30 Doradus and consequently, it would also be harder to observe (see Sect. 5.5.3). Other clusters besides 30 Doradus and potentially W49A may be affected by feedback-regulated star formation episodes. According to Rahner et al. (2018), these need to have a star formation efficiency of $\lesssim 10\%$ and average densities of $n \geq 5 \times 10^2 \text{ cm}^{-3}$. It remains for investigation of clusters which meet these criteria, if this may be a common scenario in the formation of massive star clusters.

5.5.5 Future investigations

Detailed observations of the morphology of the molecular gas, as well as the stellar content as seen in infrared wavelengths are needed in order to shed more light on the physical processes dominating the dynamics and evolution of W49A. While much work has been done on W49N, more studies focussing on the connection of the large-scale dynamics inside and outside of the region are necessary. With the Atacama Large Millimeter/sub-millimeter Array (ALMA⁴), kinematics of molecular and ionized gas can be mapped at significantly higher resolution than the observations of ionized and molecular gas applied here. Due to the high extinction towards W49A of $A_V > 30$ mag (Alves & Homeier 2003), soft, diffuse X-ray emission from wind bubbles (Townsley et al. 2003, 2014, 2018) are difficult to observe. Chandra observations of hard X-rays for W49A exist, and have been discussed for W49N, including both wind-driven bubbles and other possible formation scenarios (Tsujimoto et al. 2006). An interpretation of these in the light of wind driven feedback is therefore non-trivial, and remains to be explored for Cluster 1. The

⁴<http://www.almaobservatory.org>

James Webb Space Telescope (JWST⁵) will yield high sensitivity imaging of many star-forming regions in the Galaxy. This will provide a better insight in the most embedded populations of O stars in regions like W49A.

The 1D models from [Rahner et al. \(2017\)](#) are well suited for exploring a large parameter space in molecular cloud mass, star formation efficiency and density. While these models contain all the necessary physics to describe the expanding shell, modeling a shell in three spatial dimensions is necessary. 3D models can better account for escape routes for feedback in the energy driven phase in the beginning of the expansion, as well as for instabilities in the shell, even though the effect of instabilities on the escape fraction of ionizing radiation, which may affect the effectiveness of feedback ([Dale et al. 2014](#)), is accounted for in the 1D models. More importantly, it is the density structure which affects most the geometry and the timescales of the expansion. As seen in W49A, many star-forming regions appear not to be spherically symmetric, and expansion will not occur isotropically into a uniform medium. These models are naturally more computationally intensive. Such studies have been carried out (e.g., [Howard et al. 2016](#); [Peters et al. 2010](#)), even though not including all the relevant physics yet. However, given that with the 1D models we can explore the parameter spaces very well, the results from this chapter may provide the average initial cloud parameters for more detailed modeling.

5.6 Conclusions

The study presented here investigates hydrogen radio recombination line emission of the $H151\alpha$ - $H156\alpha$ and $H158\alpha$ transitions at frequencies between 1.6–1.9 GHz with the VLA in C-configuration towards W49A, as well archival CO observations from the CHIMPS and GRS surveys ([Rigby et al. 2016](#); [Jackson et al. 2006](#)). We find shell-like RRL emission around the infrared star cluster at the center of W49A, Cluster 1. We find double peaked $^{13}\text{CO}(3-2)$ emission towards Cluster 1, again indicative of emission from shell-like geometries. The RRL emission is rather broad over all velocities between the two CO components, but peaking towards the redshifted one. Towards positions at the edges of the shell-like bubble, the velocities of the ionized and molecular gas emission are anti-correlated. This anti-correlation may be a signature of interaction of the ionized shell with the molecular envelope.

One-dimensional models of expanding shells around massive star clusters ([WARPFIELD, Rahner et al. 2017](#)) are used to investigate its evolution. Given the observational initial conditions of stellar cluster mass, age of the O-star population and the current radius of the shell, all models predict re-collapse of the shell after the first star formation event. Feedback of the first formed cluster is therefore not strong enough to disperse the cloud in the first instance.

The evolution of the shell, however, strongly depends on the assumed densities. In some of the models, the shell has expanded to the outskirts of W49A. With this, it could have affected molecular gas in the entire region of W49A. In this case, a causal connection

⁵<https://www.jwst.nasa.gov>

between feedback from cluster 1 and star formation all across W49A is possible. However, for most of the models in the range of the assumed densities, the feedback shell did not expand to the outskirts of W49A. Hence, it is more likely that only limited parts of W49A were affected by feedback from the central stellar cluster, while stars in the outer parts of W49A formed independently. To what extent it altered the physical conditions in the surroundings and nurtured star formation (i.e. “triggered”), needs to be left to future studies.

This modeling presents another alternative to sub-clustered star formation and cloud-cloud collision models, without ruling out any of the latter. In comparison to the star-forming region 30 Doradus, indications for re-collapse are less clear, due to difficulties of identifying two distinct stellar populations. On the other hand, as W49A is younger, it is likely to continue to form stars, possibly in an episodic mode.

Chapter 6

Conclusions & Outlook

6.1 Conclusions

This thesis presents the analysis of hydroxyl radical (OH) absorption observations with the THOR survey (Chapter 3) and with high-sensitivity VLA follow-up observations (Chapter 4), as well as a case study of radio recombination lines (RRLs) from THOR in the star-forming region W49A (Chapter 5).

For this analysis, we used data from the THOR survey (The H I, OH, Radio recombination line survey of the Milky Way; [Beuther et al. 2016](#)), which was conducted to map a plethora of tracers of different phases of the interstellar medium (ISM), in the first quadrant of the Milky Way, with the Very Large Array (VLA) between 1 and 2 GHz. My contributions to the data reduction are described in Chapter 2.

We characterize the OH abundance with respect to molecular gas (Chapters 3 and 4). These investigations have led to the following main conclusions:

- The OH abundance ($X_{\text{OH}}(N_{\text{H}_2}) = N_{\text{OH}}/N_{\text{H}_2}$) shows a decreasing trend with increasing H_2 column density (Chapter 3). This trend is confirmed after including additional OH detections from Chapter 4 at lower N_{OH} and N_{H_2} (Figs. 4.11 and 4.12). We speculate that at higher column densities, this decrease is either due to depletion of OH from the gas phase or due to variations in the excitation conditions of OH (Sect. 3.4.2).
- As low molecular column densities may contain significant amounts of atomic gas, the OH abundance ($X_{\text{OH}}(N_{\text{H}}) = N_{\text{OH}}/N_{\text{H}}$) is compared to the column density of the total number of hydrogen nuclei ($N_{\text{H}} = 2 \times N_{\text{H}_2} + N_{\text{H I}}$). In this case, we find the OH abundance to be approximately constant with N_{H} (Fig. 4.14). This is confirmed after the inclusion of cloud components at low N_{OH} measured with VLA follow-up observations (Sect. 4.5.2).
- With high-sensitivity follow-up observations (Chapter 4), we detect two OH absorption features without corresponding ^{12}CO emission components, which are “CO-dark” gas candidates. A large fraction of the OH absorption components (8/19) are not detected in ^{13}CO emission (Sect. 4.5.4). We probe significantly deeper in OH column density ($N_{\text{OH}} \sim 10^{13.5-14.5}$) than in the THOR sample ($N_{\text{OH}} \sim 10^{14.5-15.5}$), and find a large number of OH velocity components tracing gas which is not predominantly molecular.

We conclude that the OH abundance can be used to study diffuse regions of molecular clouds; in particular, as a tracer of the column density of the total number of hydrogen nuclei. Our data, however, also show that the abundance shows large scatter. Nonetheless, the derived empirical relation between $\log(N_{\text{OH}})$ and $\log(N_{\text{H}_2})$ in Sect. 3.3.2.6 and Sect. 4.4.4.1, may be applied in future studies (e.g., in magnetic field studies of Zeeman splitting of the OH ground state transitions; e.g., Crutcher 2012) with their large scatter kept in mind.

The detections of OH at velocities which are not accompanied by CO emission, are an indication that indeed OH exceeds CO in its ability to trace diffuse regions. Follow-up observations are needed to see if CO emission is absent in observations at even lower sensitivities. These results are promising indications that the characterization of the CO-dark gas phase will be possible with future OH investigations and surveys.

To better understand the impact of stellar feedback from star clusters on their parent molecular cloud, our investigation in Chapter 5 of the RRLs from the THOR survey in W49A, combined with models, led to the following results:

- We detect ring-like emission of radio recombination lines around the infrared star cluster in the center of W49A (Sect. 5.3.2; Fig. 5.4), in agreement with previously determined shells in $8\ \mu\text{m}$ emission (Peng et al. 2010). We attribute this to a signature of feedback in the ionized gas component.
- We compare the radius of the shell to the WARPFIELD models (Rahner et al. 2017), which describe the evolution of feedback-driven shells and include all relevant types of stellar feedback (Sect. 5.4). We find that feedback is likely not to be strong enough to disperse the molecular cloud after the first epoch of star formation (Sect. 5.5.1; Fig. 5.6). The shell is currently re-collapsing or has recently re-collapsed to form a second generation of stars, as also indicated by the large amount of ultra-compact H II regions present in W49A.

This indicates that RRLs can be used to study stellar feedback in the rest of the THOR survey. Especially, it will be interesting to investigate the kinematic signatures found here – an anti-correlation of the velocity of the molecular and ionized gas is visible in W49A (Sect. 5.5.1) – and to test if this is a common property to feedback around star clusters.

W49A has been the first Milky Way object, on which WARPFIELD has been tested. W49A is a difficult object for modelling due to its complexity, but also due to the very short timescales involved (with an age of the stellar population of $\sim 1\text{-}2$ Myr; Wu et al. 2016). We note that the full impact of the density structure on the evolution of the feedback shell needs to be investigated by comparing with 3D-simulations in the future.

Even so, as in 30 Doradus (Rahner et al. 2018), the models indicate for W49A that it did not disperse its molecular cloud in the first feedback expansion event, and that star formation occurs episodically on timescales of the re-collapse of the shell. Rahner et al. (2018) find that a necessary condition for re-collapse of a feedback driven shell is an average cloud density of $> 500\ \text{cm}^{-2}$. This holds for W49A and other regions need to be

investigated to see if re-collapse of feedback shells is a common scenario in molecular clouds.

At the end of this work, many open questions remain. Regarding the diffuse regions of molecular clouds, among these are: What are the properties of the (CO-)dark gas? What can we learn from it about the formation of molecular clouds and about the structure of the ISM in general? And regarding feedback from star clusters: What are the best kinematic signatures to trace feedback? What is the influence of feedback on the stellar population of star clusters and the star formation history in statistical terms in the Milky Way?

In the following, I will address how these questions can be investigated from an observational perspective, as well as indicate future studies with the data presented in this work and the THOR survey in general.

6.2 Outlook

6.2.1 Further characterization of the gas phase of OH

We plan to compare the OH absorption observations with observations of the far-infrared transition of ionized carbon [C II] towards two of the lines of sight discussed in Chapter 4, which were observed with the SOFIA telescope in July 2018. Ionized carbon (C^+) is present in both atomic and molecular gas, until photodissociating radiation is sufficiently shielded such that carbon becomes atomic and eventually forms CO. Specifically, C^+ is abundant in such regions in which H_2 has already formed but CO is not yet present. [C II] emission has been used to estimate the CO-dark gas fraction in the Galactic plane with the *Herschel* space telescope, within the GOT C^+ survey (Pineda et al. 2013), and has been found to correlate with OH emission (Tang et al. 2017). A comparison of these measurements with the results of Chapter 4 will deepen our understanding of the gas phase traced by the OH measurements.

As shown in Chapter 3, extended continuum sources allow us to spatially map OH absorption, and we found OH variations on small scales (Sect. 3.3.4; Fig. 3.11). This analysis of OH in W43 can be extended also to H I absorption, and to other regions. For example, the surroundings of the strong continuum source G29.96–0.02 studied in Chapter 4 shows large patches of strong continuum emission, which are covered by the VLA follow-up observations presented in Chapter 4. The high spectral resolution and high sensitivity VLA follow-up observations are an excellent starting point for such a study. Comparing the extended OH and H I absorption to CO emission will allow us to investigate the interplay of atomic and molecular gas – not only spectrally, but also spatially.

6.2.2 Satellite lines as indicators of physical properties of OH gas

The OH satellite lines (at 1612 MHz and 1720 MHz) bear the potential to study the physical properties of the OH gas. As discussed in Chapter 3, the satellite line inversions are determined by their environment. To further understand this relation, additional studies, relying on both observations and simulations, will be needed. From an observational perspective, a systematic comparison of satellite line emission properties with other tracers, such as maps of infrared emission, is needed to identify sources for radiative pumping. Chapter 3 gives a first step in this direction by presenting a sample of satellite line emission sources, which can be compared to publicly available surveys of infrared emission in the future. This information can then be used to compare with radiative transfer calculations. The goal is to identify signatures, which are indicative of the environment, and the properties of the cloud itself.

6.2.3 Future surveys on OH and H I absorption observations

The THOR survey can serve as a primer for future surveys. One of them is the Galactic plane survey with the SKA precursor telescope ASKAP (GASKAP; [Dickey et al. 2013](#)). It will probe the H I emission on scales between 30'' and 60'', to trace small-scale structure and dynamics in the atomic gas, to ultimately understand how gas is channeled from warm, low-density, atomic gas over the CNM to dense molecular gas. The H I observations from the THOR survey will provide initial results on this comparison, which can be extended with GASKAP.

More importantly for the results of this thesis, GASKAP will observe the OH ground state transitions. As shown in Chapter 4, with high-sensitivity observations of only three lines of sight, the THOR sample of OH absorption detections in Chapter 3 can be significantly increased to detections at lower optical depths. With the GASKAP survey being conducted in the near future, many more of these high-sensitivity absorption observations will be in place to extend the THOR sample to lower optical depths. Similar observations towards specific point sources will also be conducted with the FAST telescope (The Five-hundred-meter Aperture Sphere Telescope), which will further add to the available emission-absorption measurements of OH ([Li et al. 2018](#)). Finally, these new surveys will allow us to have a continuous coverage in OH column density from the CO-dark gas to the dense molecular gas.

6.2.4 RRL emission in other regions

The analysis for W49A (Chapter 5) will be expanded to other RRL emission sources within the THOR survey for a statistical analysis of the impact of feedback on molecular gas. Since spectral signatures can be particular to W49A itself and a property of its dynamics, a larger sample is needed to distinguish unique signatures of feedback. The THOR survey provides such a sample, with ~ 40 RRL emission sources and a part of them spatially resolved.

This analysis can be extended to a multi-wavelength study of ionized gas by combining

both continuum and RRL emission from THOR with surveys at higher frequencies. The GLOSTAR survey (A Global view on star formation in the Galaxy with the VLA between 4 and 8 GHz) observes the radio continuum and RRLs between 4 and 8 GHz and is therefore excellently suited for such an extension. A combination will lead both a continuum coverage between 1 and 8 GHz as well as selected RRLs from the H96 α to the H186 α line to study the properties of ionized gas in greater detail.

Together with a comparison to the WARPFIELD models (Rahner et al. 2017; Chapter 5), a larger sample of evolution histories of star forming regions in the Galaxy can be determined. As mentioned before, a statistical sample can be built-up to determine if re-collapsing feedback shells are a common phenomena in massive star forming regions in the Milky Way and to evaluate their impact on the star formation in particular clouds and in the Galaxy as a whole.

Appendix A

Supplementary material for Chapter 2

In this appendix, we present an overview on the calibration quality of the second half of the THOR survey (Fig. [A.1](#)), as well as an overview of the flux variations of all test sources described in Sect. [2.5.3](#) (Fig. [A.2](#)).

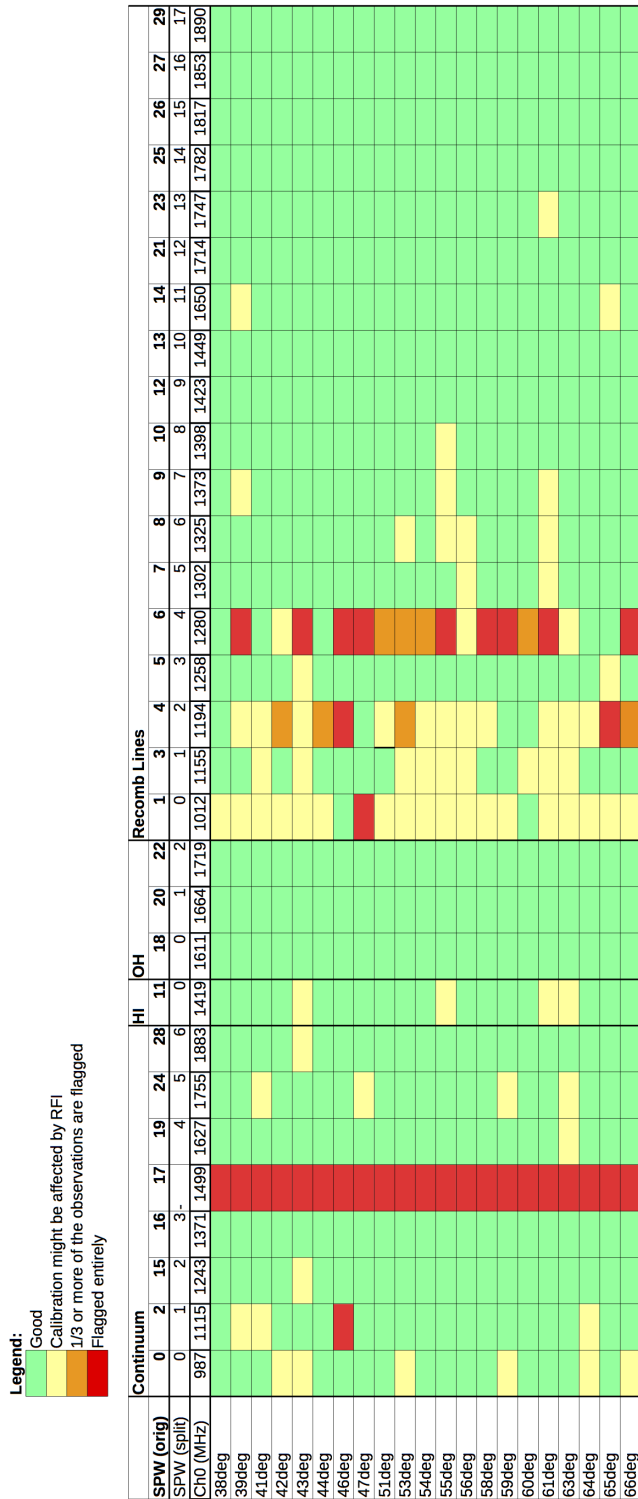


Figure A.1: Overview of the calibration quality of the observations in the second half of the THOR survey.

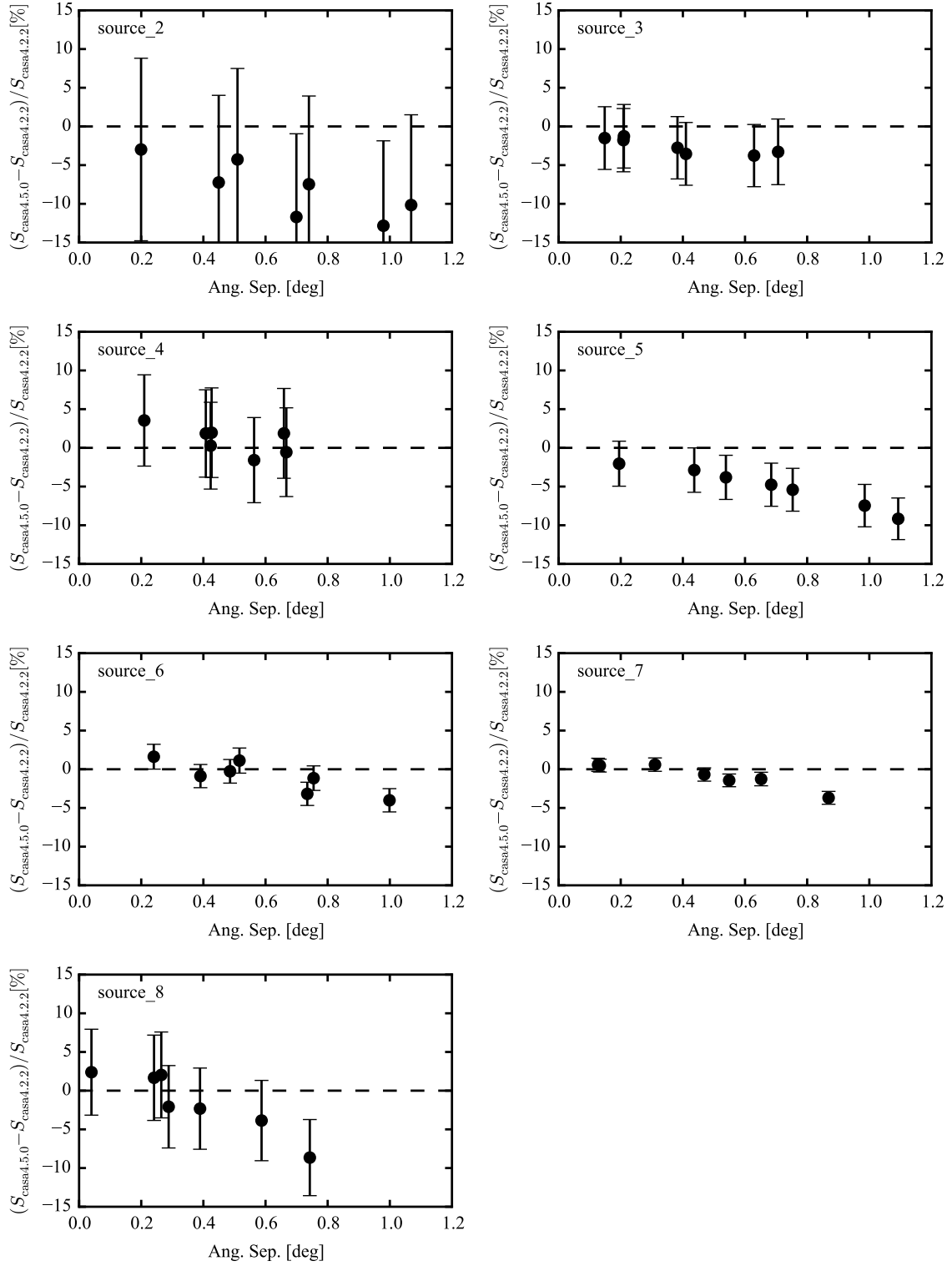


Figure A.2: Deviations of the flux of the continuum test sources between CASA versions 4.5.0 and 4.2.2 vs. angular separation from phase center.

Appendix B

Supplementary material for Chapter 3

B.1 Detection of OH main line absorption – notes on individual sources

- G23.956+0.150, +81.0 km s⁻¹: One velocity channel is above 4- σ and two above 3- σ . There is a corresponding ¹³CO(1-0) counterpart.
- G26.609–0.212, –33.0 km s⁻¹: One velocity channel is detected at 4- σ , another at 3- σ . The ¹³CO(1-0) data do not cover these velocities.
- G28.806+0.174, +79.5 km s⁻¹: One velocity channel is detected at 4- σ , a ¹³CO(1-0) counterpart exists that matches well in velocity.
- G28.806+0.174, +103.0 km s⁻¹: One velocity channel is detected at 4- σ , a ¹³CO(1-0) counterpart exists that contains blended components.
- G29.935–0.053, +51.0 km s⁻¹: This object is detected at 4- σ . Also, a ¹³CO(1-0) counterpart exists.
- G29.935–0.053, +7.5 km s⁻¹: This object is detected in one velocity channel at 3- σ and in one at 5- σ after smoothing to 46'' resolution. The detection is not picked up in the 1665 MHz transition. There is no ¹³CO(1-0) emission at this velocity.
- G30.535+0.021, +45.0 km s⁻¹: This feature shows one velocity channel at 4- σ and three at 3- σ in the 1667 MHz transition. We compare this feature to ¹³CO(1-0), after smoothing to 46''. The feature peaks at 43.5 km s⁻¹. In comparison, the ¹³CO(1-0) shows two distinct peaks at 40.3 and 47.3 km s⁻¹. Interestingly, the trough between both features occurs at the position of the OH peak. The trough could be a sign of CO self-absorption, i.e. the absorption by cold CO gas of the line emission from a warmer background source (e.g., [Phillips et al. 1981](#)). A possible heating source of the background CO gas could be the H II-region G30.539–00.024, which emits RRLs at 46 km s⁻¹ ([Table 3.1](#); [Anderson et al. 2014](#)).
- G30.535+0.021, +92.0 km s⁻¹: This feature shows one velocity channel at 4- σ and three at 3- σ in the 1667 MHz transition. The feature peaks at 92 km s⁻¹ and we compare it to ¹³CO(1-0) emission, after smoothing to 46''. The ¹³CO(1-0) seems to have blended components. In the 1665 MHz transition the feature is weakly

detected (at $3\text{-}\sigma$). However, it has a different shape to the 1667 MHz transition – most likely due to its weak detection – and so we do not include it for fitting the line width, but instead merely use it for the column density comparison.

- G32.272–0.226, $+22.5 \text{ km s}^{-1}$: In this feature, three velocity channels are detected at $4\text{-}\sigma$. There is a corresponding feature in $^{13}\text{CO}(1\text{-}0)$ that spreads over a similar velocity range but the line profile is not centrally peaked. This is confirmed by investigating the $^{13}\text{CO}(1\text{-}0)$ emission around this position, with the strongest individual peak being located at 22.7 km s^{-1} . The noise was checked a few arc minutes away from the emission and did not show any anomalies in this velocity range.
- G32.928+0.607, -34.5 km s^{-1} : This feature contains one pixel at $3\text{-}\sigma$ in the 1665 MHz transition. No $^{13}\text{CO}(1\text{-}0)$ data are available for comparison at this velocity.
- G35.467+0.139, $+78.0 \text{ km s}^{-1}$: This feature consists of two velocity channels close to a signal-to-noise ratio of $4\text{-}\sigma$. There exists $^{13}\text{CO}(1\text{-}0)$ emission that peaks at a similar velocity.
- G60.882–0.132, $+22.5 \text{ km s}^{-1}$: OH absorption in the 1667 MHz transition is detected, with one velocity channel at $3\text{-}\sigma$, $4\text{-}\sigma$ and $5\text{-}\sigma$, respectively. In the 1665 MHz transition, one velocity bin is detected at $5\text{-}\sigma$. Also, we find a $^{13}\text{CO}(1\text{-}0)$ counterpart at similar velocity.

B.2 Estimation of the correlation between N_{OH} and N_{H_2}

We provide additional information on the estimation of the correlation between N_{OH} and N_{H_2} from Sect. 3.3.2.6. For numerical stability, we center all data on the mean of the measured column densities, $\overline{N_{\text{OH}}}$ and $\overline{N_{\text{H}_2}}$. We perform the linear regression on $\log(N_{\text{OH}}/\overline{N_{\text{OH}}}) = m \times \log(N_{\text{H}_2}/\overline{N_{\text{H}_2}}) + t_{\text{centered}}$. The parameter t from Sect. 3.3.2.6 relates to the sampled t_{centered} as $t = t_{\text{centered}} + \log(\overline{N_{\text{OH}}}) - m \times \log(\overline{N_{\text{H}_2}})$. The median, 16%, and 84%-percentiles are $m = 0.33^{+0.14}_{-0.13}$, $t_{\text{centered}} = -0.06^{+0.06}_{-0.06}$ and $t = 7.91^{+2.86}_{-2.95}$. Fig. B.1 shows the histogram of the marginalized distributions of m and t_{centered} .

B.3 Individual sources – transitions of the OH ground state

This appendix shows the spectra of the OH ground state transitions.

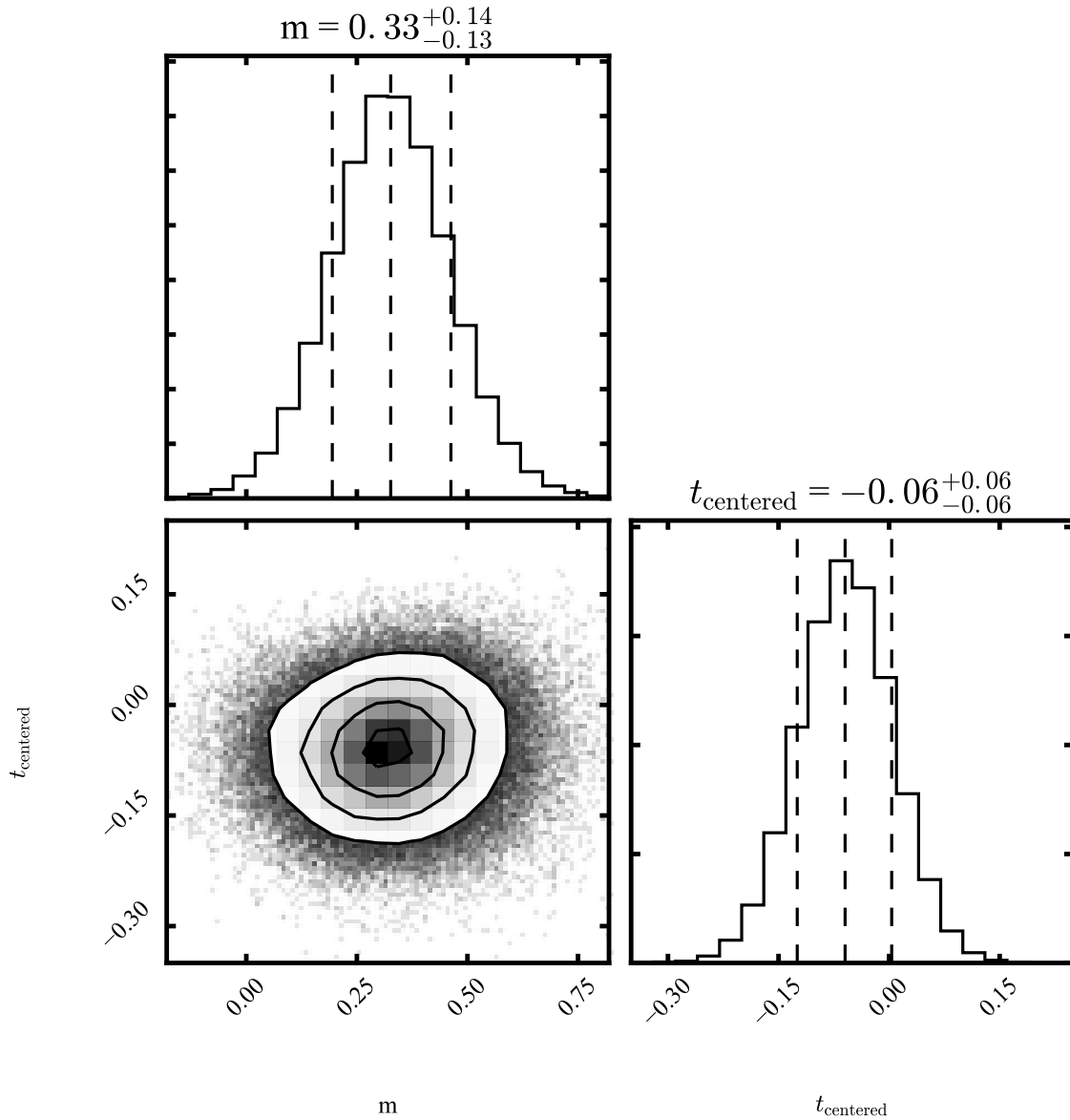


Figure B.1: Marginalized distributions of m and t_{centered} . These are obtained after centering all datasets by normalizing with the mean N_{OH} and N_{H_2} . The uncentered t is given by $t = t_{\text{centered}} + \log(\overline{N_{\text{OH}}}) - m \times \log(\overline{N_{\text{H}_2}})$, as $t = 7.91^{+2.86}_{-2.95}$.

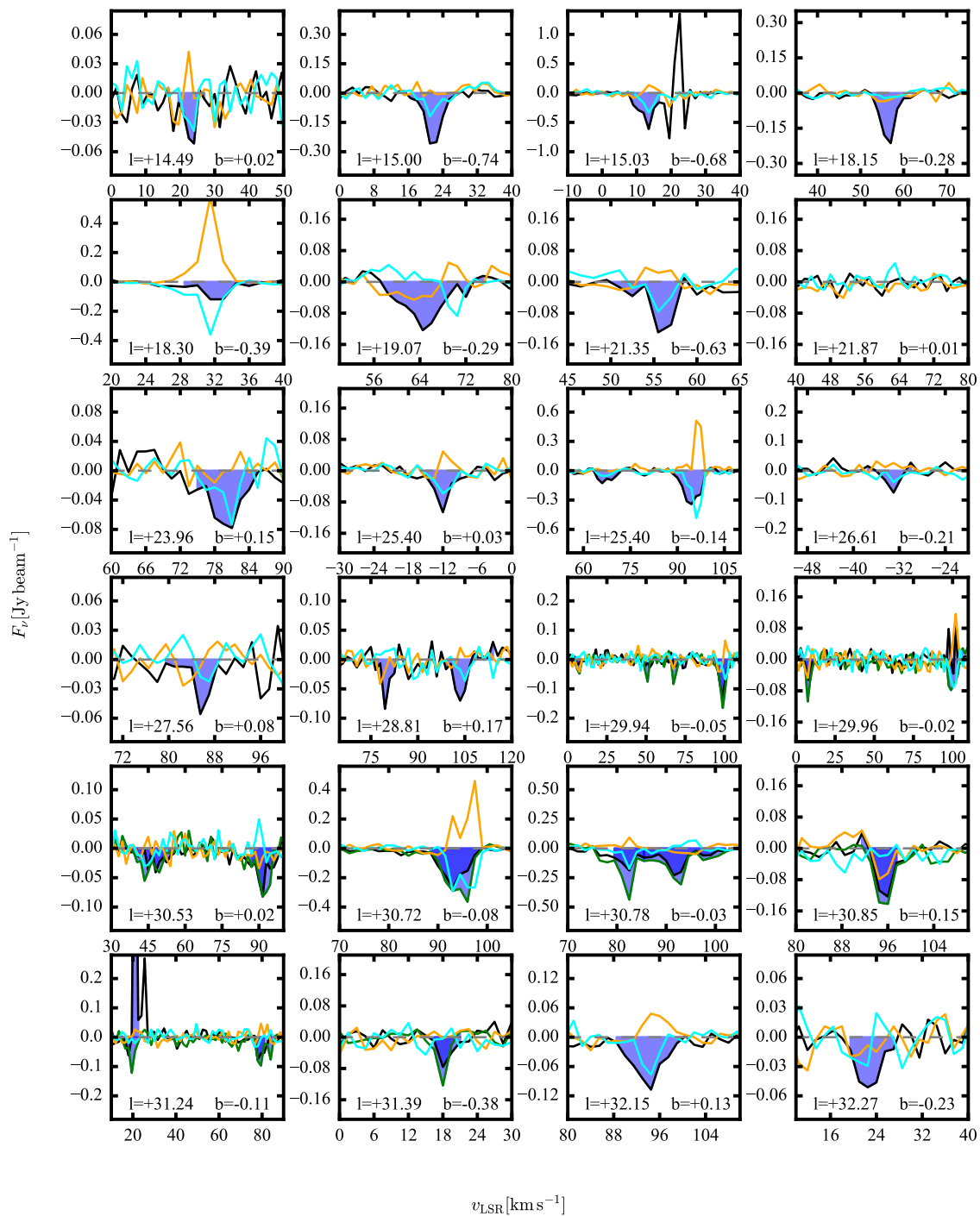


Figure B.2: Spectra of OH ground state transitions, especially also of the satellite lines, along lines of sight that show a detection in 1665 MHz or 1667 MHz absorption. The spectra are extracted from data cubes that have been smoothed to 46'' resolution. The transitions at 1665 MHz (black), 1612 MHz (orange) and 1720 MHz (cyan) are shown for all sources. The 1667 MHz (green) transition is displayed if available. OH absorption detections in the main line transitions are shaded in blue.

B.3 Individual sources – transitions of the OH ground state

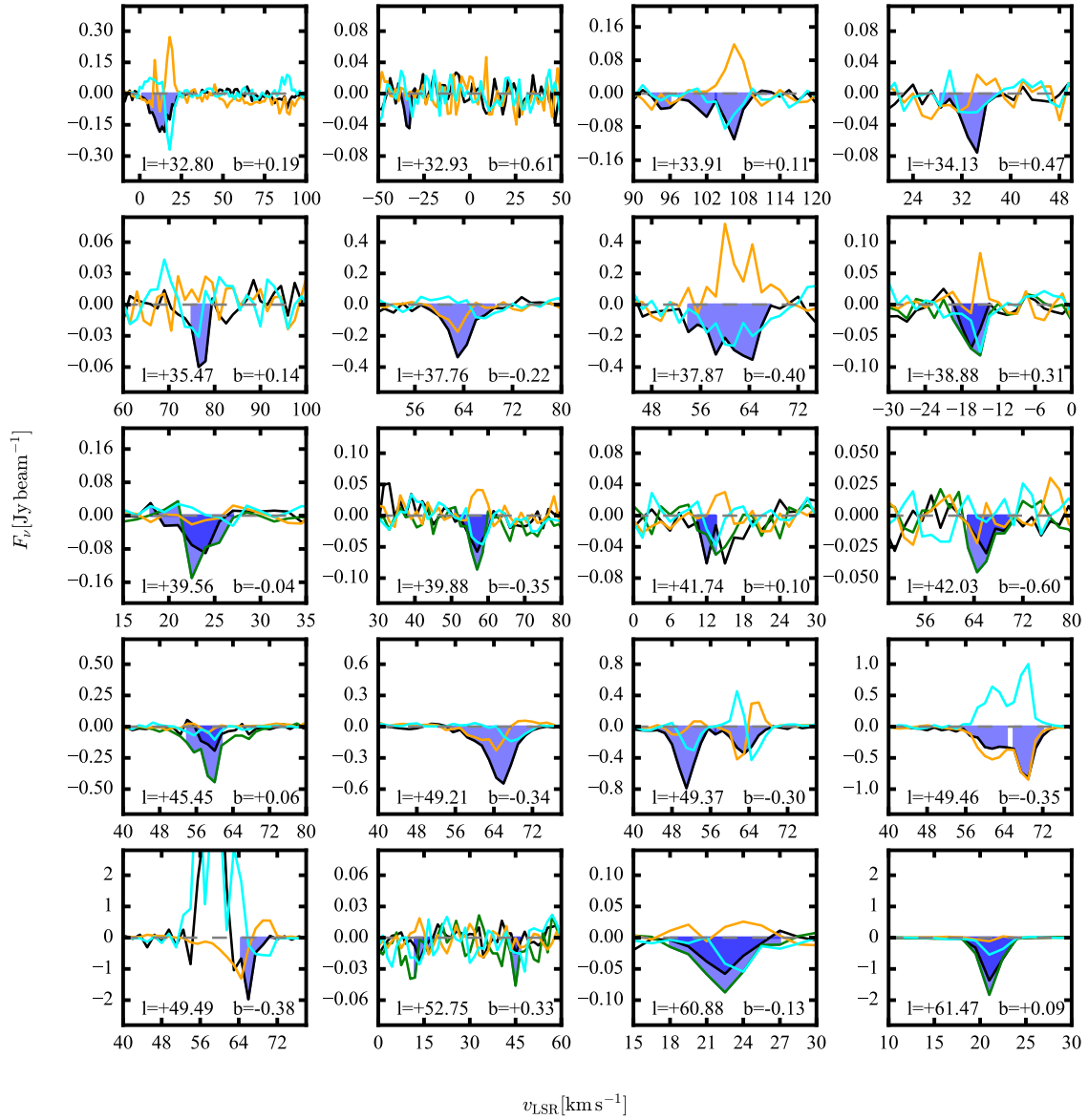


Figure B.3: As Fig. B.2.

B.4 Individual sources - OH and H_I optical depth and ¹³CO(1 – 0) emission

The appendix shows the OH and H_I optical depth profiles for each source, as well as the ¹³CO(1-0) emission.

B.5 OH absorption towards W43

Moment zero map of the optical depth of the 1667 MHz transition for different velocity intervals towards W43.

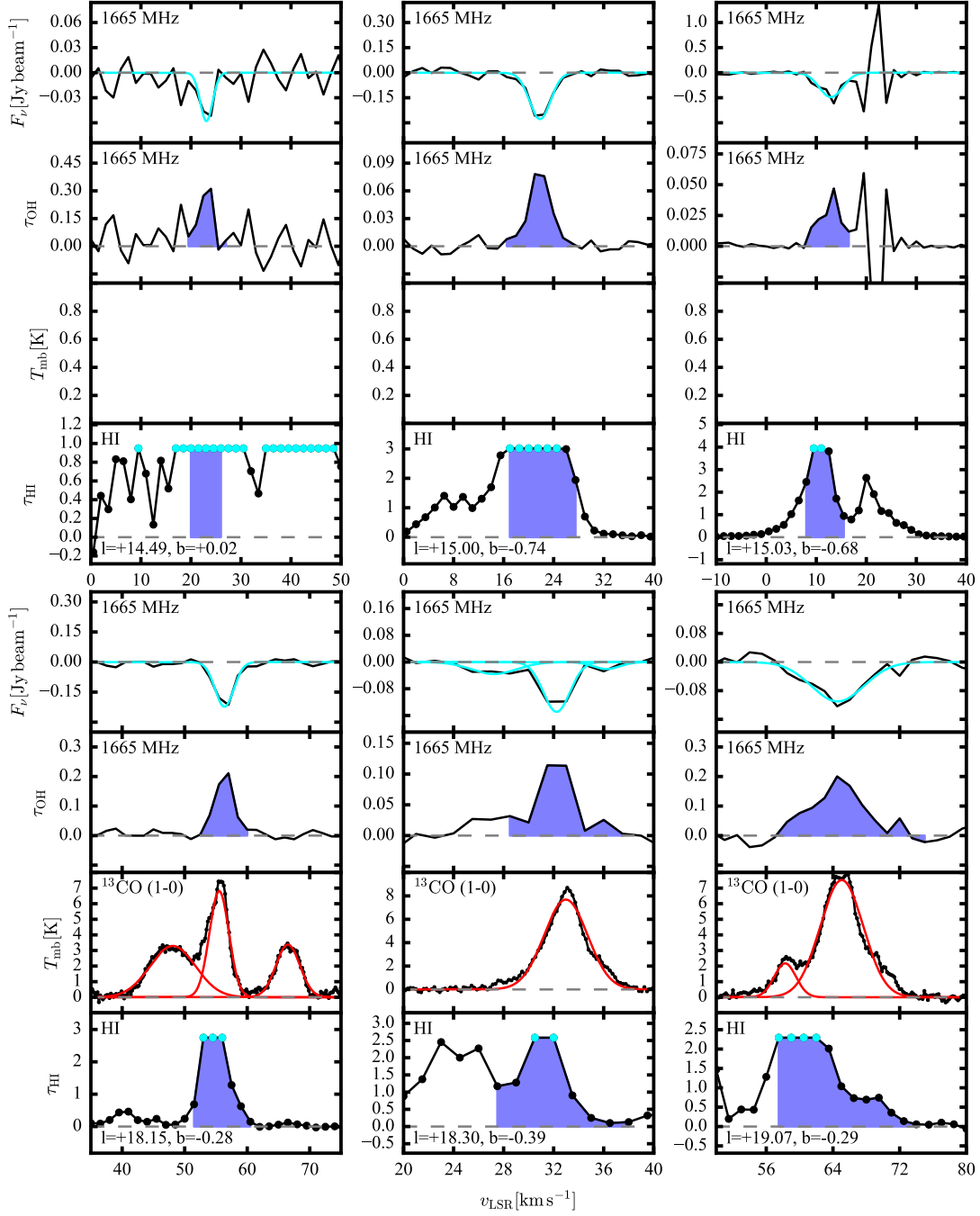


Figure B.4: Analyzed 1665 and 1667 MHz OH absorption features. The topmost panel shows 1665 MHz (black) and 1667 MHz (green) absorption features. The second panel from the top shows the spectrum converted to optical depth for the 1665 MHz (black) and 1667 MHz (green) transition. The third panel from the top shows $^{13}\text{CO}(1-0)$ emission in T_{mb} (data from the GRS survey ($l < 60^\circ$) and Exeter FCRAO CO survey ($l > 60^\circ$); Jackson et al. 2006, Mottram & Brunt 2010). The line widths were determined by fitting Gaussian profiles to the 1665 MHz (cyan) and 1667 MHz (orange) absorption, and the $^{13}\text{CO}(1-0)$ emission (red). The lowermost panel shows the H I absorption converted to H I optical depth. Measured bins are denoted by black dots, while we quote lower limits (cyan) for saturated bins. The 1667 MHz transition was observed only towards selected regions and is therefore shown only for a subset of lines-of-sight (see Sect. 3.2). The line-of-sight coordinates are given in degrees of Galactic coordinates. The blue shaded area in the lower three panels shows the line integrals. All data were smoothed to a spatial resolution of $46''$.

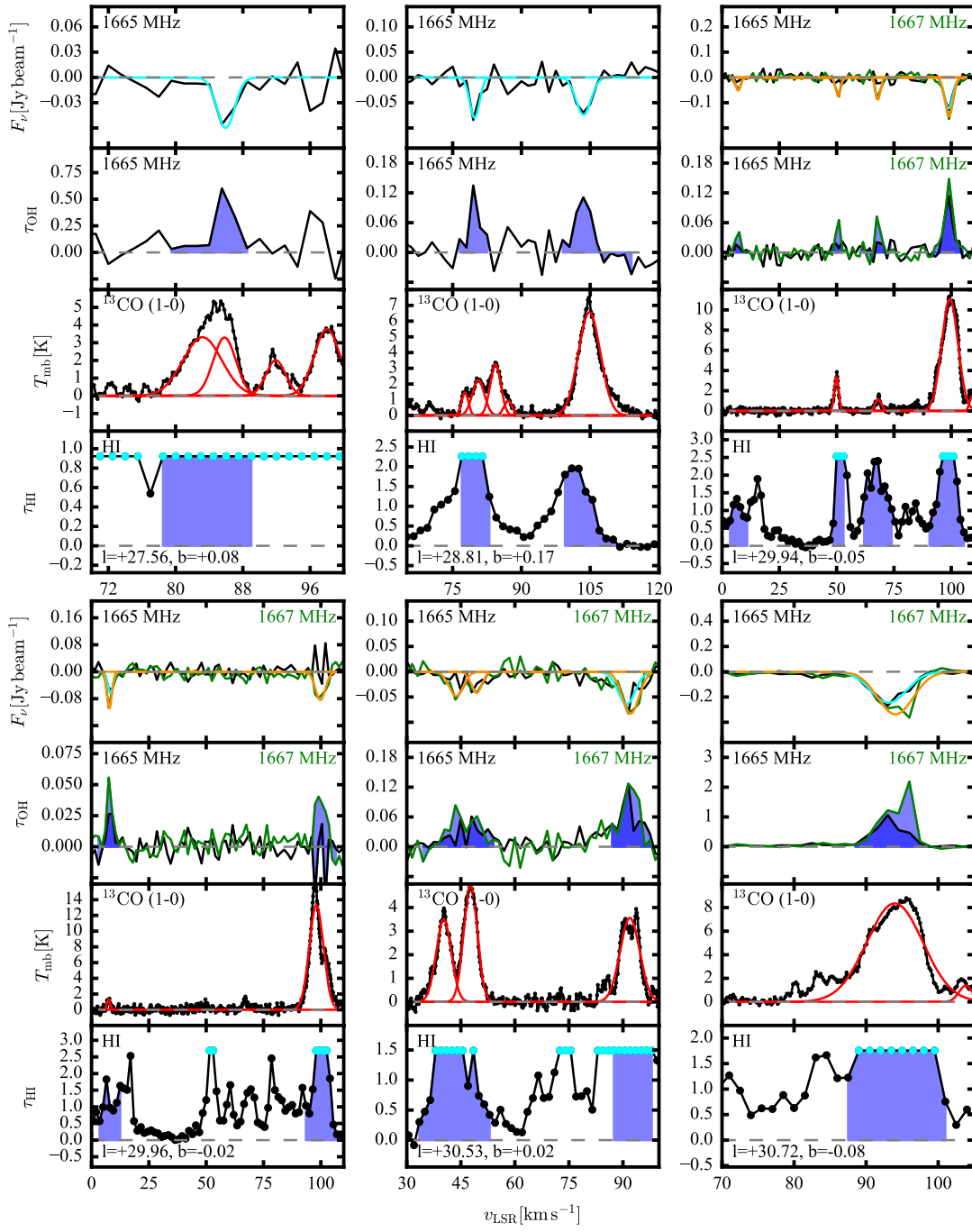


Figure B.6: As Fig. B.4.

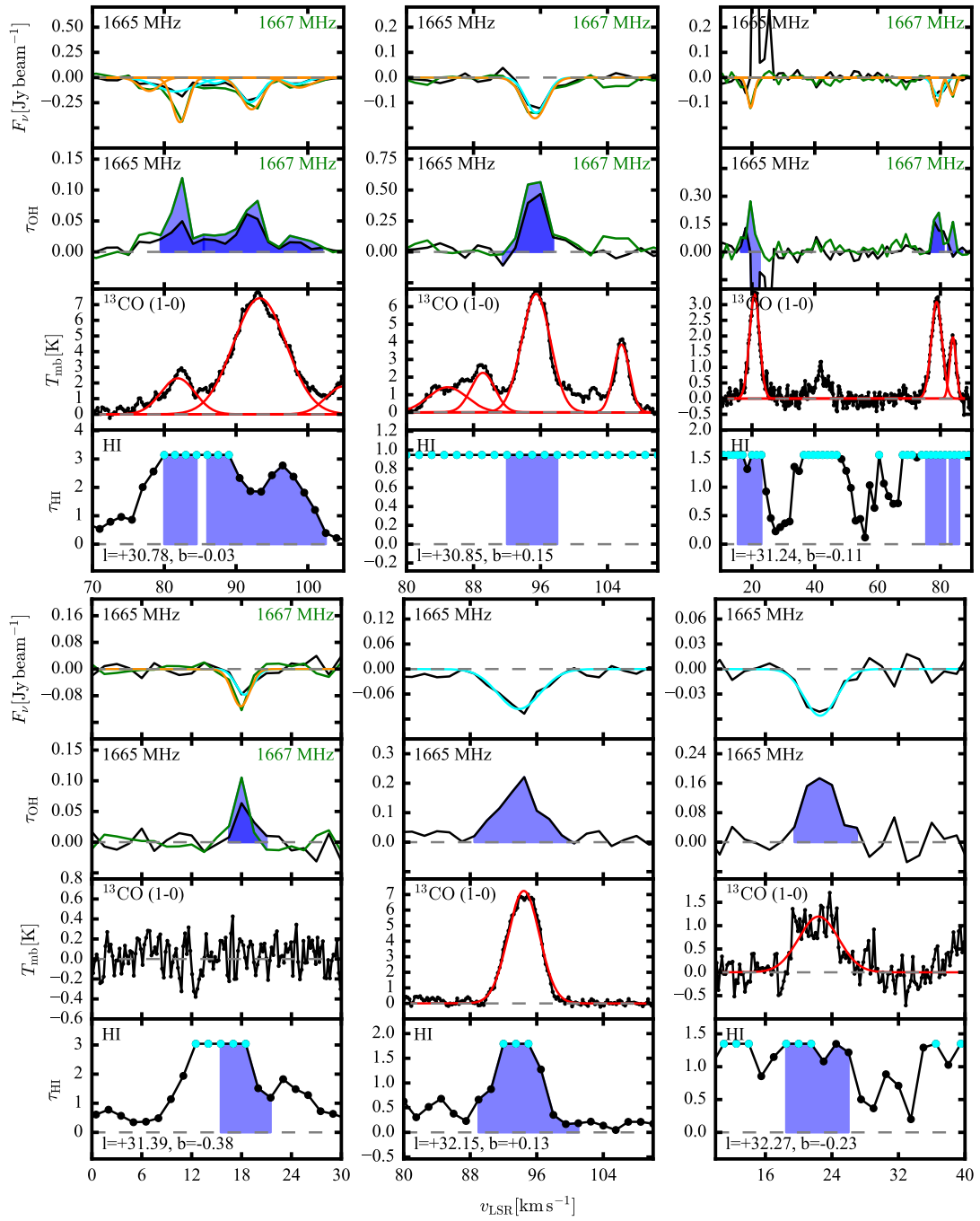


Figure B.7: As Fig. B.4.

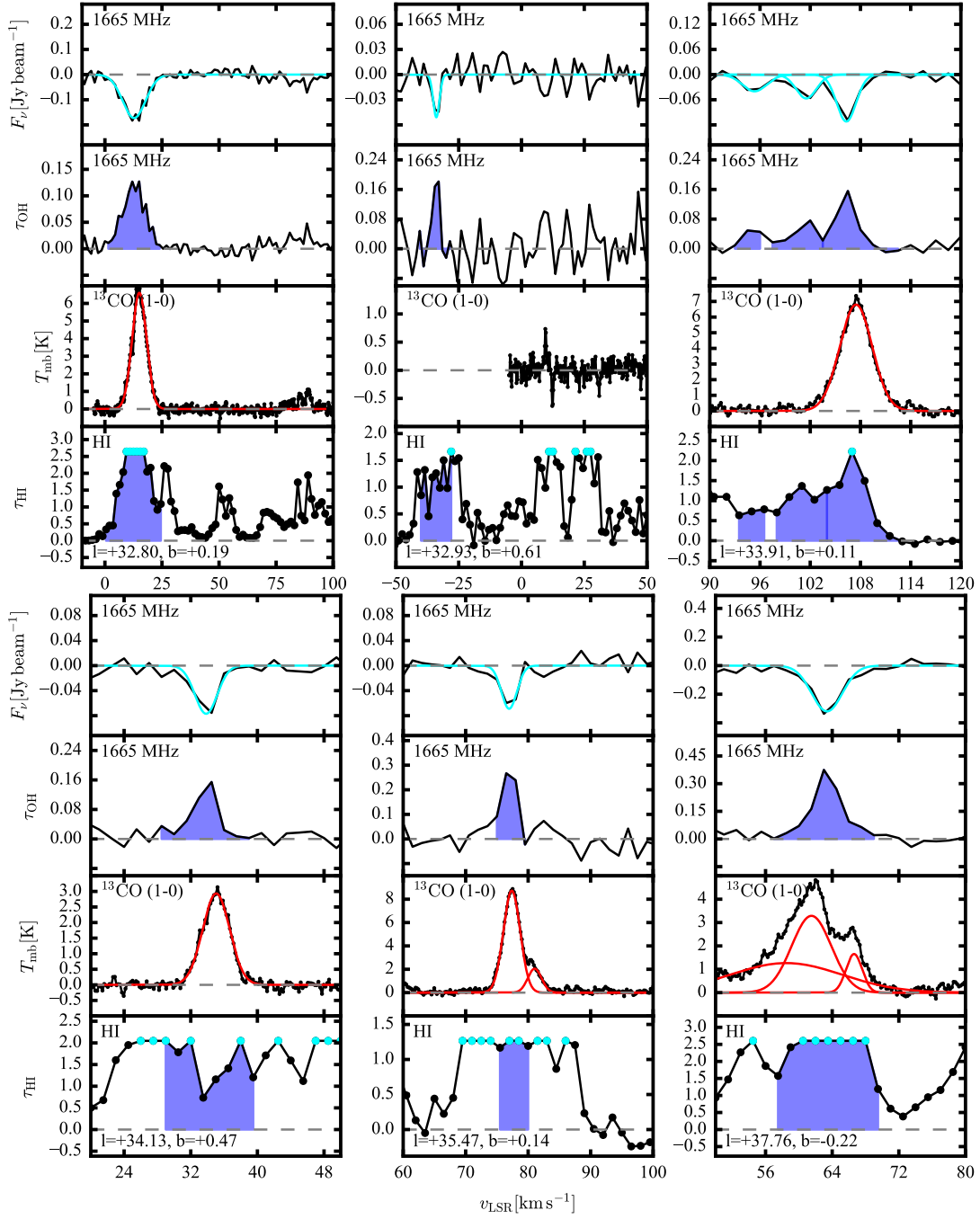


Figure B.8: As Fig. B.4.

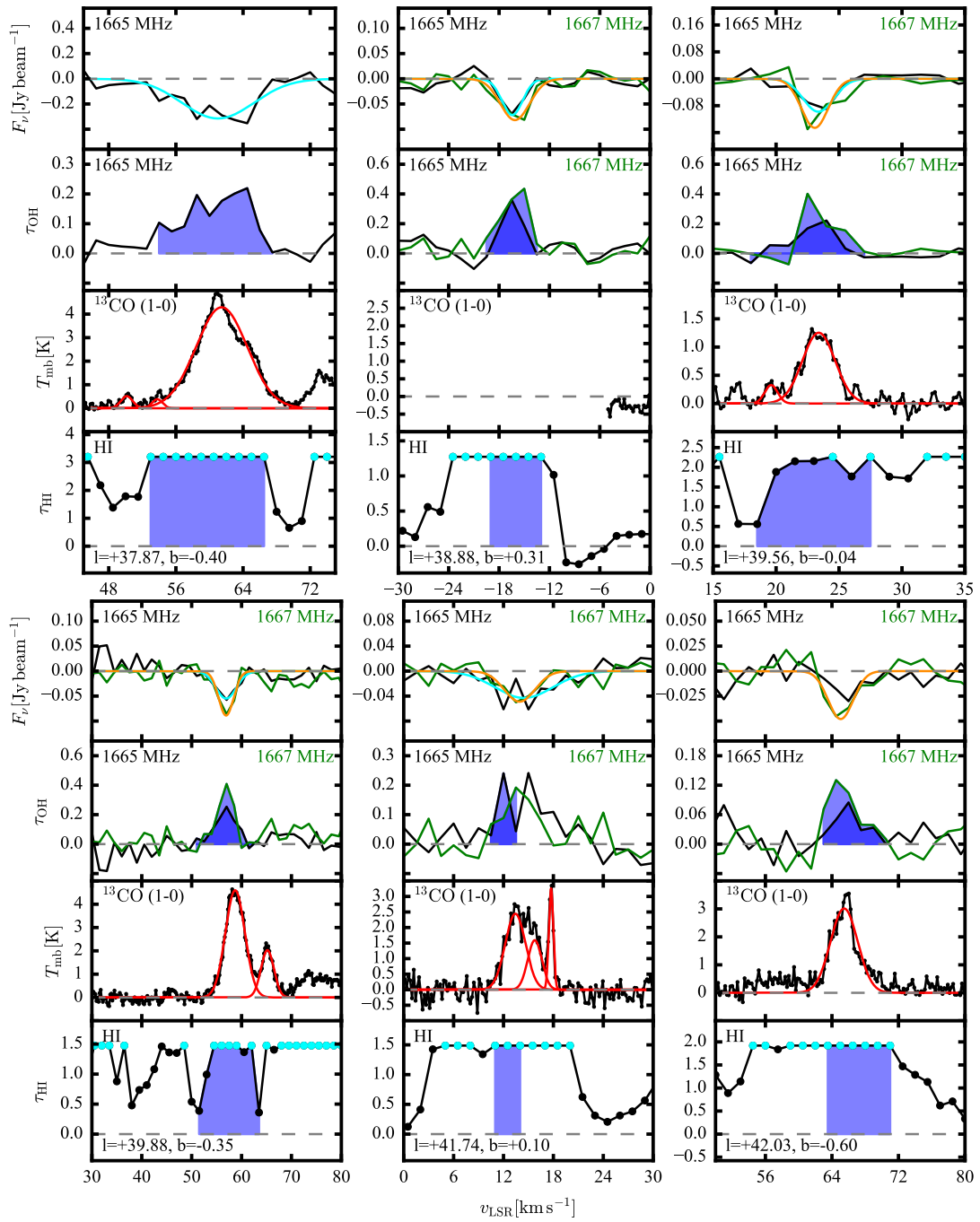


Figure B.9: As Fig. B.4.

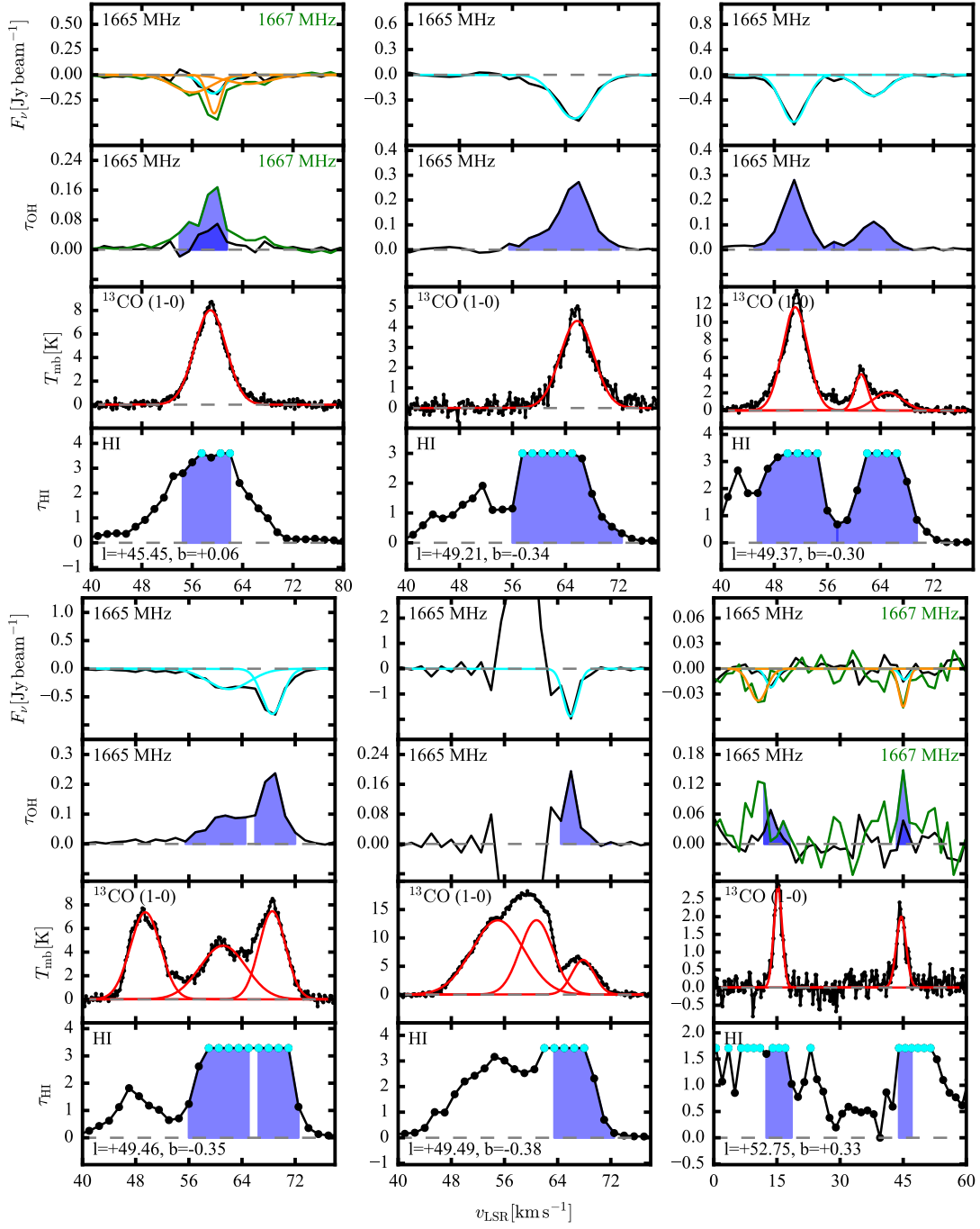


Figure B.10: As Fig. B.4.

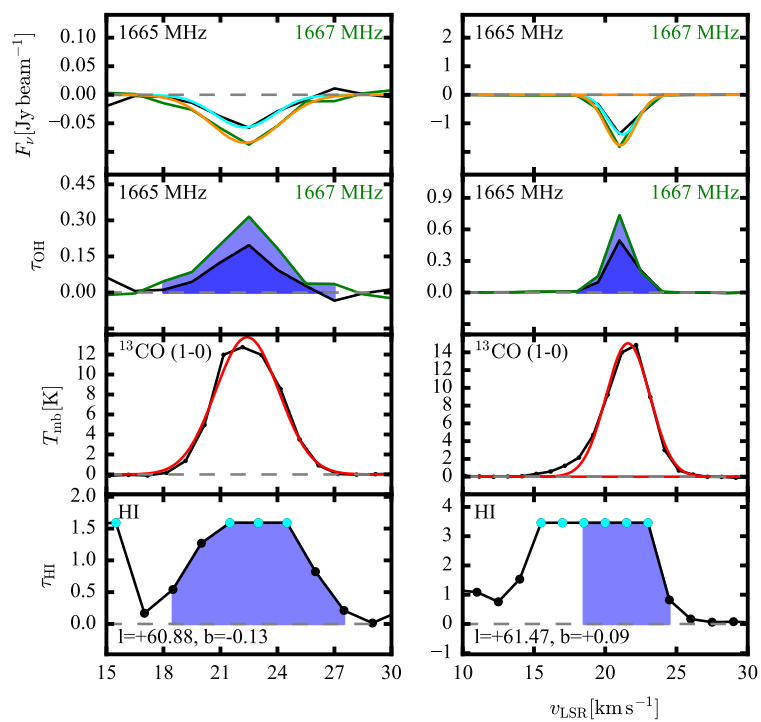


Figure B.11: As Fig. B.4.

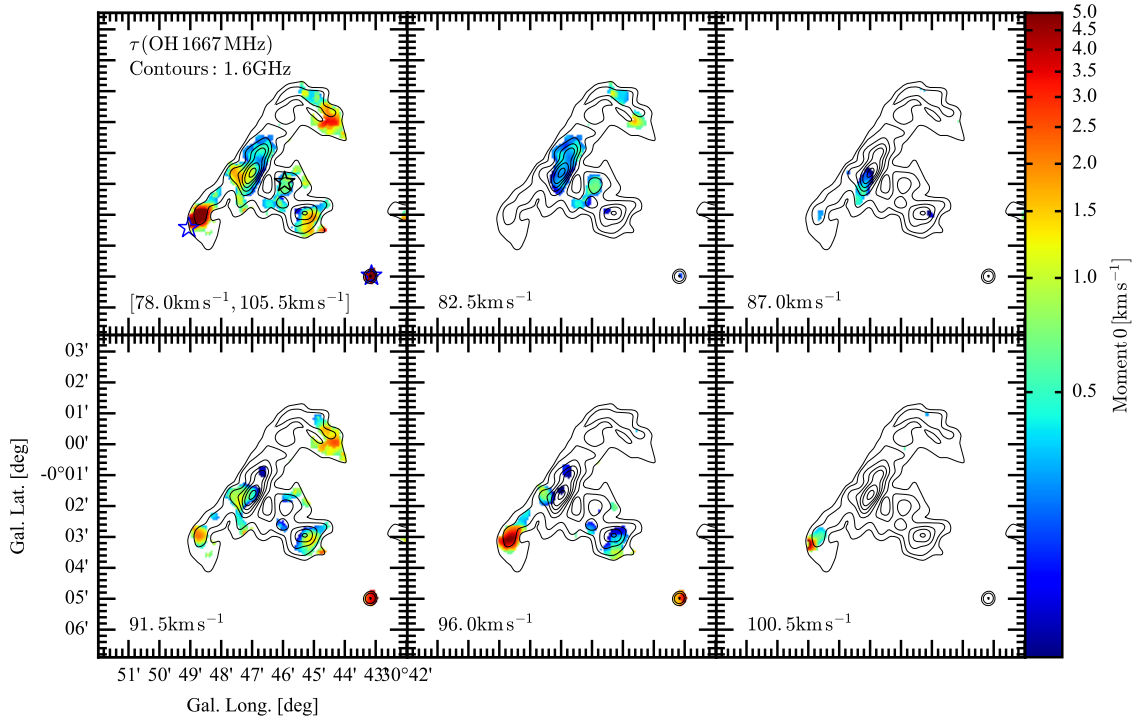


Figure B.12: Integrated optical depth of the OH 1667 MHz line in the W43 star-forming region. In the top-left panel, τ is integrated over the same velocity range as in Fig. 3.10. The other panels show τ around the indicated velocities after integrating over three channels of 1.5 km s^{-1} width. For each pixel, only channels that are detected at a $3\text{-}\sigma$ level or higher contribute to the integrated τ -map. The optical depth map is overlaid with contours of the 18 cm continuum emission (black, in levels of 0.1, 0.2, 0.4, 0.6, 0.8, 1.0, 1.25, 1.5 and $1.75 \text{ Jy beam}^{-1}$). Symbols as in Fig. 3.10.

Appendix C

Supplementary material for Chapter 4

C.1 Estimation of the correlation between N_{OH} and N_{H_2}

This appendix lists the complete fit results of $\log(N_{\text{OH}})$ vs. $\log(N_{\text{H}_2})$ to the combined VLA follow-up and THOR data (Sect. 4.4.4.1). For further details, see also Sect. 3.3.2.6 and B.2.

$\overline{N_{\text{OH}}}$ and $\overline{N_{\text{H}_2}}$ denote the mean of the measured column densities. The linear regression is performed on $\log(N_{\text{OH}}/\overline{N_{\text{OH}}}) = m \times \log(N_{\text{H}_2}/\overline{N_{\text{H}_2}}) + t_{\text{centered}}$. The parameter t depends on t_{centered} as $t = t_{\text{centered}} + \log(N_{\text{OH}}) - m \times \log(N_{\text{H}_2})$. The median, 16%- and 84%-percentiles have determined as $m = 0.52^{+0.09}_{-0.09}$, $t_{\text{centered}} = -0.06^{+0.07}_{-0.07}$ and $t = 3.67^{+1.92}_{-1.93}$. Fig. C.1 presents the histogram of the marginalized distributions.

C.2 Details on the derivation of $N_{^{13}\text{CO}}$ for Sect. 4.5.3

To compare the OH measurements from this chapter to the measurements of OH in diffuse clouds by Li et al. (2018) in Sect. 4.5.3, we provide an alternative derivation of the CO column density by using an excitation temperature determined from the peak temperature of the $^{12}\text{CO}(1-0)$ transition. This is possible due to the availability of ^{12}CO emission observations at similar angular resolution for all three lines of sight. For the sample presented in Chapter 3, only the ‘‘Massachusetts-Stony Brooks CO survey of the Galactic plane’’ of $^{12}\text{CO}(1-0)$ (Sanders et al. 1986) was available at the time when the majority of the analysis was conducted, which has similar beam size as the GRS survey, but is only sparsely sampled (180’). Therefore, we decided not to use it in order not to underestimate the ^{12}CO peak emission, and instead to assume an excitation temperature. With the FUGIN survey and a similar survey at PMO available now, we have measurements of $^{12}\text{CO}(1-0)$, $^{13}\text{CO}(1-0)$ and $\text{C}^{18}\text{O}(1-0)$ emission available for all three sources discussed here (see also Sect. 4.2.3).

C.2.1 Formalism

The excitation temperature of $^{12}\text{CO}(1-0)$ can be derived from the solution to the equation of radiative transfer (following equation 3-6 in Pineda et al. 2008; see also chapter 15.4.1 and equation 15.29 and 15.30 in Wilson 2009), which describes the measured intensity

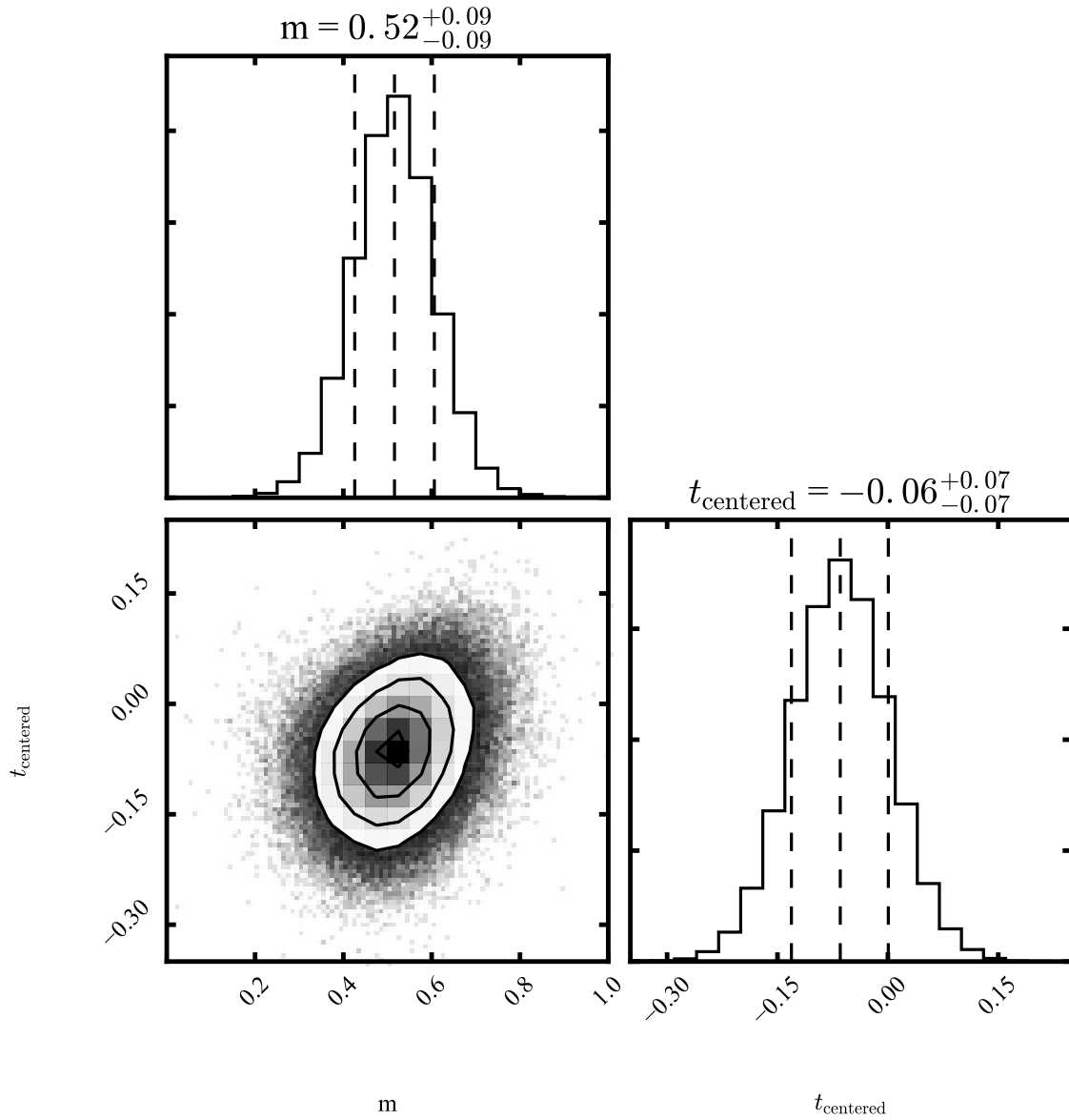


Figure C.1: Marginalized distributions of m and t_{centered} for VLA follow-up+THOR data. The distributions were derived from fitting the relation $\log(N_{\text{OH}}/\overline{N_{\text{OH}}}) = m \times \log(N_{\text{H}_2}/\overline{N_{\text{H}_2}}) + t_{\text{centered}}$. See text for further details.

by

$$I_{\text{line}} = (S - I_0)(1 - e^{-\tau}), \quad (\text{C.1})$$

with I_0 the intensity of the background radiation, S the source function and τ the optical depth. The radiation temperature (or brightness temperature) is defined as

$$T_R = I_\nu \frac{c^2}{2\nu^2 k}, \quad (\text{C.2})$$

with I_ν the intensity at a given frequency ν , c the speed of light and k the Boltzmann constant. Assuming a blackbody distribution for the density distribution $I_{0,\nu}$ at the background temperature T_{bg} and for the source function at T_{ex} , this can be written as

$$T_R = T_0 \left(\frac{1}{e^{T_0/T_{\text{ex}}} - 1} - \frac{1}{e^{T_0/T_{\text{bg}}} - 1} \right) (1 - e^{-\tau}), \quad (\text{C.3})$$

with $T_0 = h\nu/k$. It should be noted that for $T_0 \ll T_{\text{ex}}, T_{\text{bg}}$ (i.e., for the OH hyperfine transitions in the ground state), this equation reduces to

$$T_R = (T_{\text{ex}} - T_{\text{bg}})(1 - e^{-\tau}). \quad (\text{C.4})$$

The equation can now be solved for the excitation temperature, with

$$T_{\text{ex}} = \frac{T_0}{\ln \left(1 + T_0 / \left[\frac{T_p}{1 - e^{-\tau}} + \frac{T_0}{e^{T_0/T_{\text{bg}}} - 1} \right] \right)}, \quad (\text{C.5})$$

with T_p being the peak emission, which, in the case of the assumption of $\tau \gg 1$, the background given by the cosmic microwave background radiation (CMB) of $T_{\text{bg}} = 2.7$ K and $T_0 = 5.5$ K for the $^{12}\text{CO}(1-0)$ transition reduces to

$$T_{\text{ex}}(^{12}\text{CO}(1-0)) = \frac{5.5 \text{ K}}{\ln \left(1 + 5.5 \text{ K} / \left[T_p(^{12}\text{CO}) + 0.82 \text{ K} \right] \right)}. \quad (\text{C.6})$$

The excitation temperature may then be used to determine the optical depth in the ^{13}CO emission, if both CO transitions are in LTE. To do this, we solve Eq. (C.3) for τ and substitute $T_{\text{bg}} = 2.7$ K and $T_0(^{13}\text{CO}) = 5.3$ K (see eq. 15.31 in Wilson 2009):

$$\tau(^{13}\text{CO}(1-0)) = -\ln \left(1 - \frac{T_{\text{MB}}(^{13}\text{CO})}{5.3 \text{ K}} \left[\left(e^{5.3 \text{ K}/T_{\text{ex}}} - 1 \right)^{-1} - 0.16 \right]^{-1} \right) \quad (\text{C.7})$$

With this, the column density of ^{13}CO can be determined as (Wilson 2009, eq. 15.37)

$$N(^{13}\text{CO}) = 3.0 \times 10^{14} \frac{T_{\text{ex}} \int \tau^{13}(v) dv}{1 - e^{-5.3 \text{ K}/T_{\text{ex}}}}, \quad (\text{C.8})$$

which can be approximated (Wilson 2009, eq. 15.39) as

$$N(^{13}\text{CO}) = 3.0 \times 10^{14} \frac{\tau_0}{1 - e^{-\tau_0}} \frac{\int T_{\text{MB}}(v) dv}{1 - e^{-5.3 \text{ K}/T_{\text{ex}}}}. \quad (\text{C.9})$$

In the approximation of optically thin ^{13}CO emission, the expression reduces to

$$N(^{13}\text{CO}) = 3.0 \times 10^{14} \frac{\int T_{\text{MB}}(v) dv}{1 - e^{-5.3 \text{ K}/T_{\text{ex}}}}. \quad (\text{C.10})$$

C.2.2 Column densities of ^{13}CO with T_{ex} derived from ^{12}CO observations

We assume that the $^{12}\text{CO}(1-0)$ and $^{13}\text{CO}(1-0)$ transitions are in local thermodynamic equilibrium, i.e., share the same excitation temperature. Equation (C.9) then allows us to determine $T_{\text{ex}}(^{12}\text{CO})$ from the $^{12}\text{CO}(1-0)$ peak emission, in assumption that it is optically thick (Eq. C.6). We test this assumption by using equation 14 from Pineda et al. (2008) to determine the optical depth of the $^{12}\text{CO}(1-0)$ line, $\tau(^{12}\text{CO}) = a \times \int T_{\text{mb}}(^{13}\text{CO}) dv$, with the parameter a being derived from fitting a *curve-of-growth* to the integrated emission of the $^{12}\text{CO}(1-0)$ and $^{13}\text{CO}(1-0)$ lines. Pineda et al. (2008) find values between $a = 0.1$ and 0.6 in the Perseus molecular cloud complex. For most CO components, this relation only indicates moderate optical depths ($\tau \leq 1 - 3$) in the $^{12}\text{CO}(1-0)$ transition, with excitation temperatures between 3 and 10 K, if the excitation temperature was derived in the optical thick assumption. This is an indication that in these cases the assumption of optical thickness is likely not valid and would underestimate T_{ex} . Therefore, we assume an excitation temperature of 10 K whenever T_{ex} falls below this value.

The second correction of the ^{13}CO column density with respect to the optically thin assumption is to correct for the optical depth of the $^{13}\text{CO}(1-0)$ emission using Eq. (C.9). The optical depth is calculated with Eq. (C.7), using the peak emission of $^{13}\text{CO}(1-0)$. The integral over $T_{\text{mb}}(^{13}\text{CO}(1-0))$ in Eq. (C.9) is given in Table 4.3. The $^{13}\text{CO}(1-0)$ column densities are listed in Table 4.5.

C.2.3 Derivation of N_{OH}

A recent investigation of diffuse lines of sights (Li et al. 2018) find a lognormal distribution for the excitation temperatures of the OH main lines with a peak at 3.3 K (average between 3.4 K for the OH 1665 MHz transition and 3.2 K for the OH 1667 MHz transition). In order to compare our results with the sample of from Li et al. (2018) in Section 4.5.3, we list the OH column densities and abundances for an excitation temperature of 3.3 K in Table 4.5.

Table C.1: Abundances and column densities for comparison in Sect. 4.5.3

Source	Feature	v [km s ⁻¹]	N_{OH} [$\times 10^{14}$ cm ⁻²]	$\tau_{^{12}\text{CO}}^{\mu=0.3}$	$\tau_{^{12}\text{CO}}^{\mu=0.6}$	$T_{\text{ex},^{12}\text{CO}}$ [K]	$\tau_{^{13}\text{CO}}$	$N_{^{13}\text{CO}}$ [$\times 10^{15}$ cm ⁻²]	N_{H_2} [$\times 10^{21}$ cm ⁻²]	$X_{\text{OH}}(N_{\text{H}_2})$ [$\times 10^{-7}$]	$X_{\text{OH}}(N_{\text{H}})$ [$\times 10^{-7}$]
G21	1	+7.4	1.06±0.05	0.29	0.57	+10 (+9.13±0.44)	0.17	0.76±0.13	0.29±0.05	3.70±0.66	0.57±0.04
	2	+56.5	3.61±0.05	2.92	5.83	+13.15±0.43	0.78	12.68±1.98	4.82±0.75	0.75±0.12	0.31±0.04
	3	+66.6	0.34±0.04	1.13	2.26	+10 (+4.69±0.47)	0.10	<0.92	<0.35	>0.99	>0.42
	3	+68.8	0.36±0.04	1.13	2.26	+10 (+4.26±0.48)	0.10	<0.92	<0.35	>1.03	>0.44
	3	+73.5	0.94±0.07	1.13	2.26	+10 (+5.83±0.45)	0.10	<0.92	<0.35	>2.69	>0.45
G29	4	+6.5	1.30±0.07	0.64	1.29	+10 (+8.03±0.41)	0.21	1.74±0.40	0.66±0.15	1.97±0.47	0.59±0.09
	4	+9.7	0.56±0.06	1.25	2.50	+10 (+5.84±0.42)	0.11	<1.01	<0.39	>1.46	>0.49
	5	+67.5	0.80±0.10	1.29	2.57	+10 (+9.33±0.41)	0.31	3.64±1.26	1.38±0.48	0.58±0.21	0.19±0.05
	6	+102.4	1.47±0.05	9.16	18.31	+24.77±0.40	0.45	59.08±15.21	22.45±5.78	0.07±0.02	0.03±0.01
G31	7	-4.8	0.47±0.04	1.03	2.06	+10 (+4.57±0.39)	0.09	<0.84	<0.32	>1.47	>0.63
	7	-3.5	0.29±0.03	0.10	0.21	+10 (+4.22±0.39)	0.12	0.27±0.03	0.10±0.01	2.80±0.42	1.02±0.13
	8	+17.5	1.35±0.06	0.32	0.65	+10 (+5.62±0.14)	0.06	0.81±0.13	0.31±0.05	4.38±0.73	0.32±0.03
	9	+37.0	0.15±0.02	0.40	0.81	+10 (+3.22±0.17)	0.04	<0.33	<0.12	>1.18	>0.27
	10	+71.9	0.51±0.05	0.18	0.36	+10 (+5.49±0.14)	0.05	0.45±0.07	0.17±0.03	3.03±0.56	0.18±0.02
	10	+75.5	0.29±0.04	0.21	0.43	+10 (+5.22±0.15)	0.05	0.53±0.07	0.20±0.03	1.45±0.26	0.22±0.03
	10	+78.1	0.87±0.04	0.21	0.41	+10 (+4.43±0.15)	0.05	0.51±0.06	0.19±0.02	4.47±0.60	0.70±0.04
	10	+81.8	0.37±0.05	0.40	0.81	+10 (+4.85±0.15)	0.04	<0.33	<0.12	>2.96	>0.13
	10	+85.1	0.68±0.04	0.40	0.81	+10 (+4.82±0.15)	0.04	<0.33	<0.12	>5.48	>0.32
	10	+92.0	0.42±0.05	0.29	0.58	+10 (+5.43±0.15)	0.06	0.73±0.10	0.28±0.04	1.50±0.26	0.22±0.03

Notes: The excitation are assumed as follows (see text for details): $T_{\text{ex}}(\text{OH } 1667 \text{ MHz}) = 3.3 \text{ K}$, $T_{\text{ex}}(^{13}\text{CO})$ was derived from ^{12}CO and $T_{\text{ex}}(\text{H I}) = 100 \text{ K}$. The optical depths of ^{12}CO and ^{13}CO are described in the text. The column density averaged abundances are defined as $X_{\text{OH}}(N_{\text{H}_2}) = N_{\text{OH}}/N_{\text{H}_2}$ and $X_{\text{OH}}(N_{\text{H}}) = N_{\text{OH}}/N_{\text{H}}$.

C.2.4 Systematic uncertainties

For the comparison to the Millennium dataset in Sect. 4.5.3 (Li et al. 2018), the excitation conditions are modified with respect to Chapter 3. Even though the excitation temperature is no longer assumed to be the same for all measurements since it is derived from $^{12}\text{CO}(1-0)$ emission, in practice, it still is. We apply a lower bound on T_{ex} of 10 K, as for lower excitation temperatures, it is not clear if $^{13}\text{CO}(1-0)$ is simply sub-thermally excited or the $^{12}\text{CO}(1-0)$ transition is optically thin. This implies that the true excitation temperature could be lower by a factor of two. For this reason, we assume the systematic uncertainty of the excitation temperature to be of a factor of two.

We also modified the assumption on the excitation temperature of OH and use $T_{\text{ex}} = 3.3 \text{ K}$. This value is the peak of the lognormal distribution of all excitation temperatures in Li et al. (2018). We assume a systematic error on the excitation temperature of a factor of two in this case, as it overlaps in reasonable fashion with the probability distribution of $T_{\text{ex}}(\text{OH})$ in Li et al. 2018 (see, e.g., their figure 6). This assumption may be slightly restrictive, given that the probability distribution of T_{ex} has a longer tail towards higher excitation temperatures (it does not decrease by a factor of two with respect to the peak until $T_{\text{ex}} \sim 10 \text{ K}$). For simplicity, we adopt the same uncertainty on the OH excitation as in Sect. 4.3.2.4, leaving a more rigorous determination of the uncertainties for future studies.

G21 Feature 2

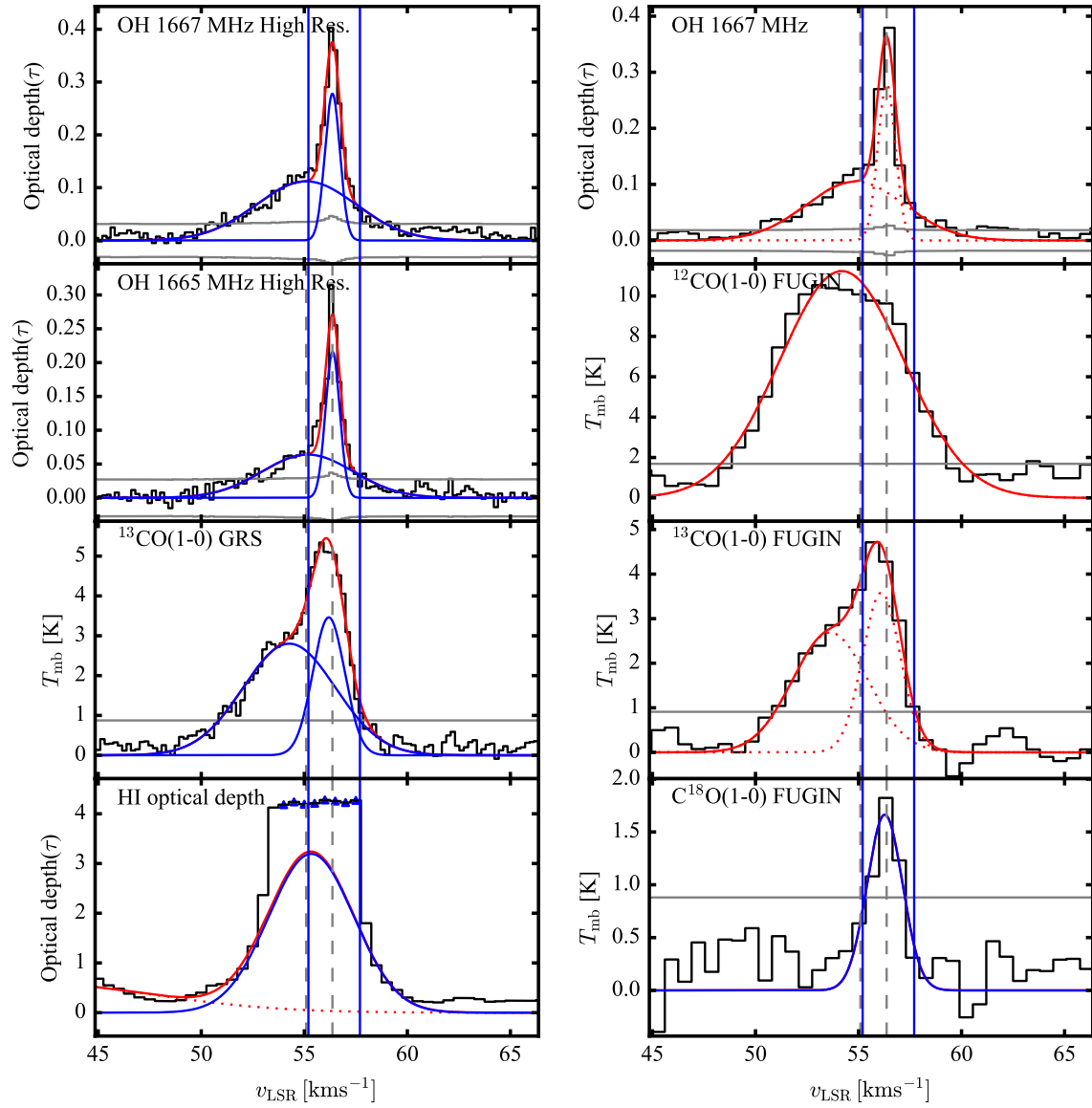


Figure C.2: Fig. 4.2, cont'd

G21 Feature 3

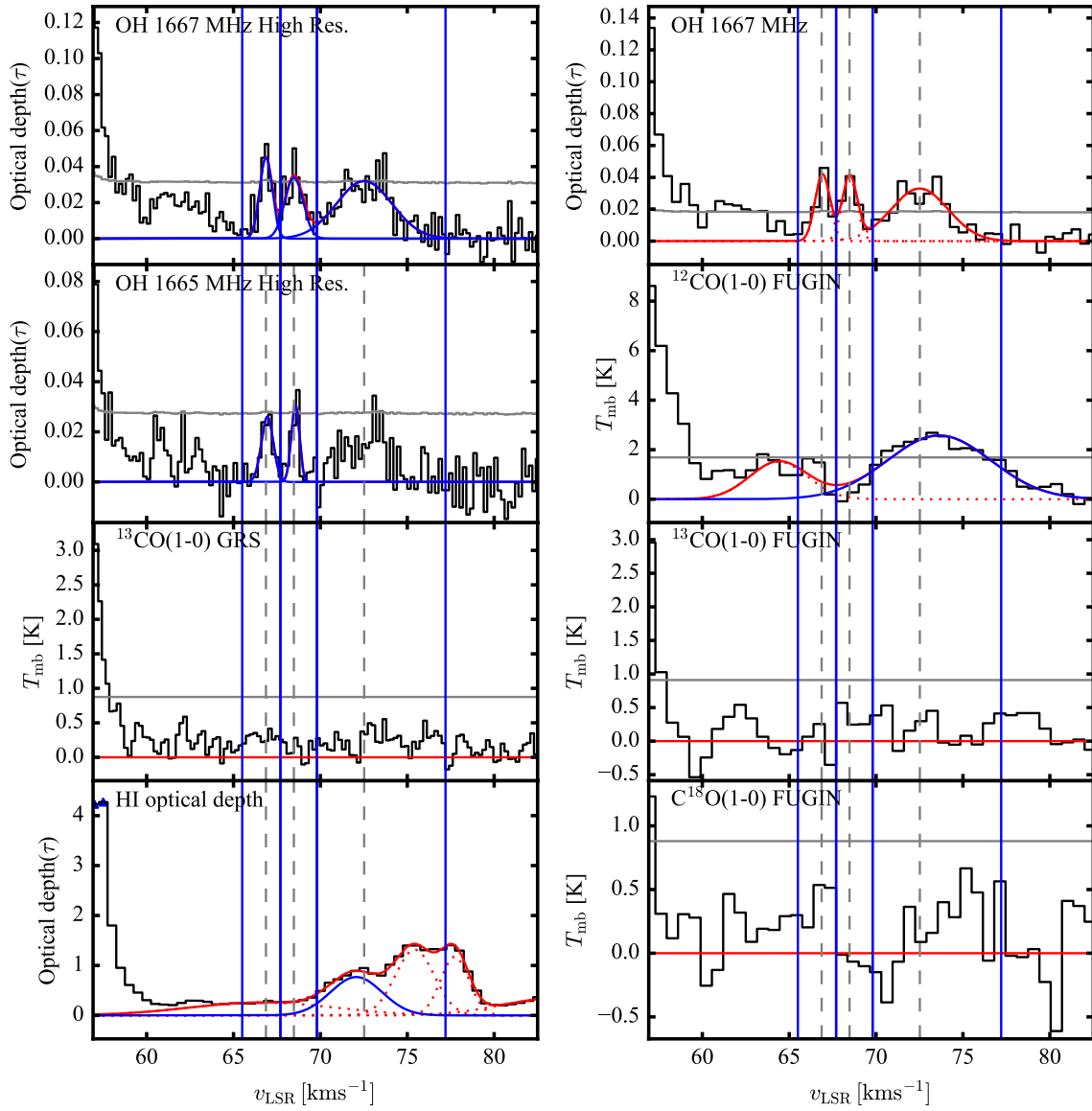


Figure C.3: Fig. 4.2, cont'd

G29 Feature 4

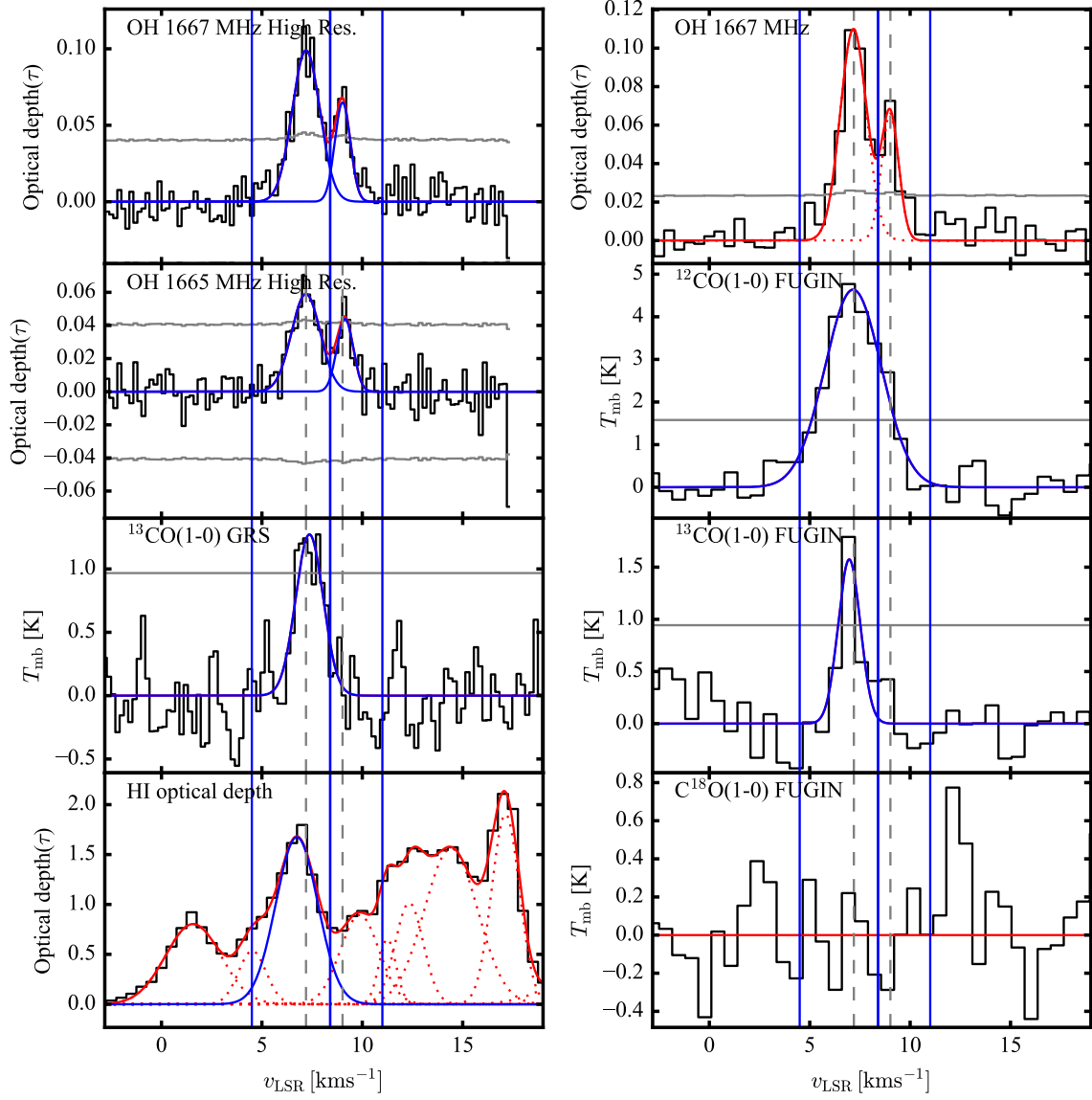


Figure C.4: Fig. 4.2, cont'd

G29 Feature 5

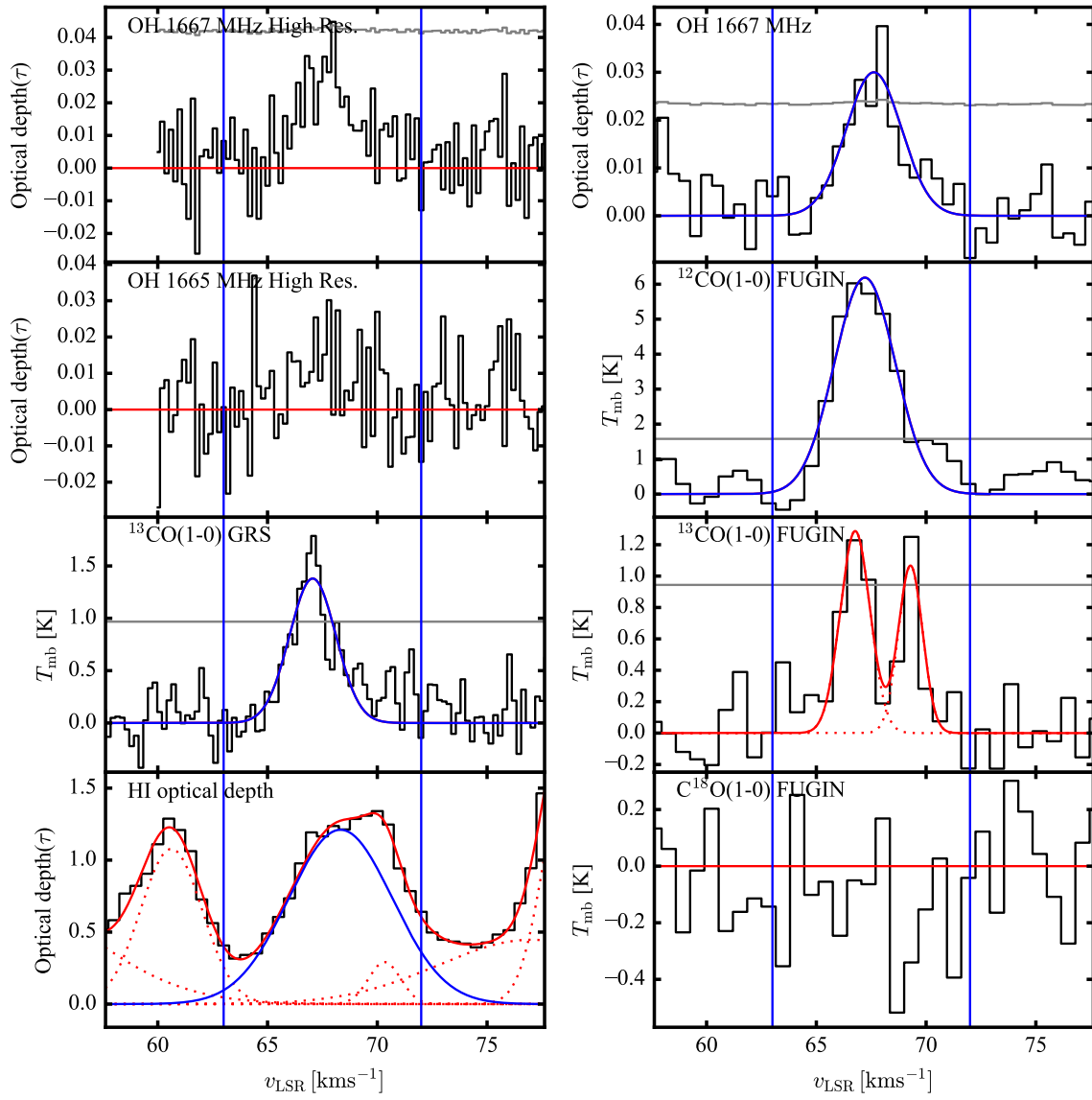


Figure C.5: Fig. 4.2, cont'd

G29 Feature 6

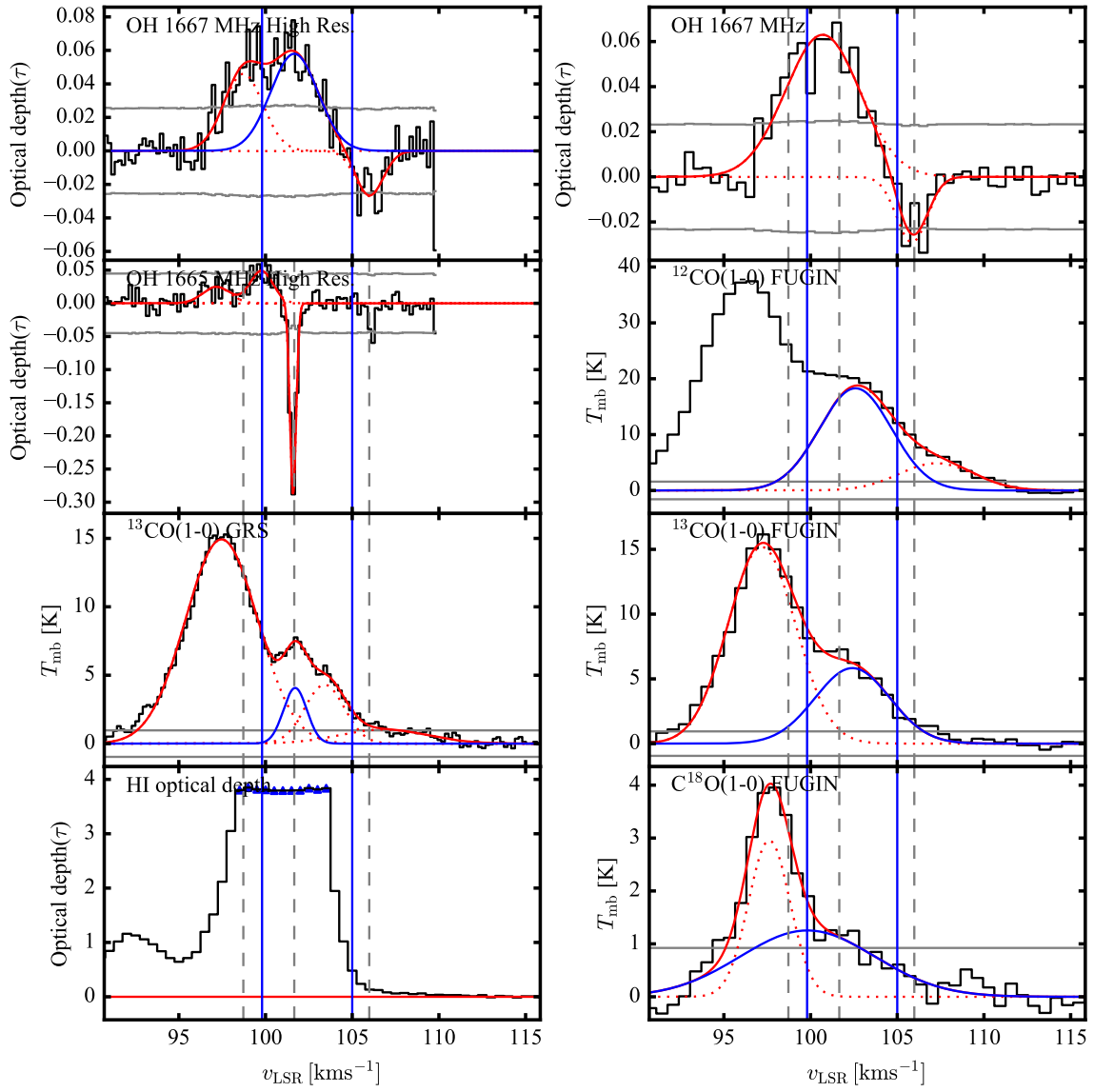


Figure C.6: Fig. 4.2, cont'd

G31 Feature 7

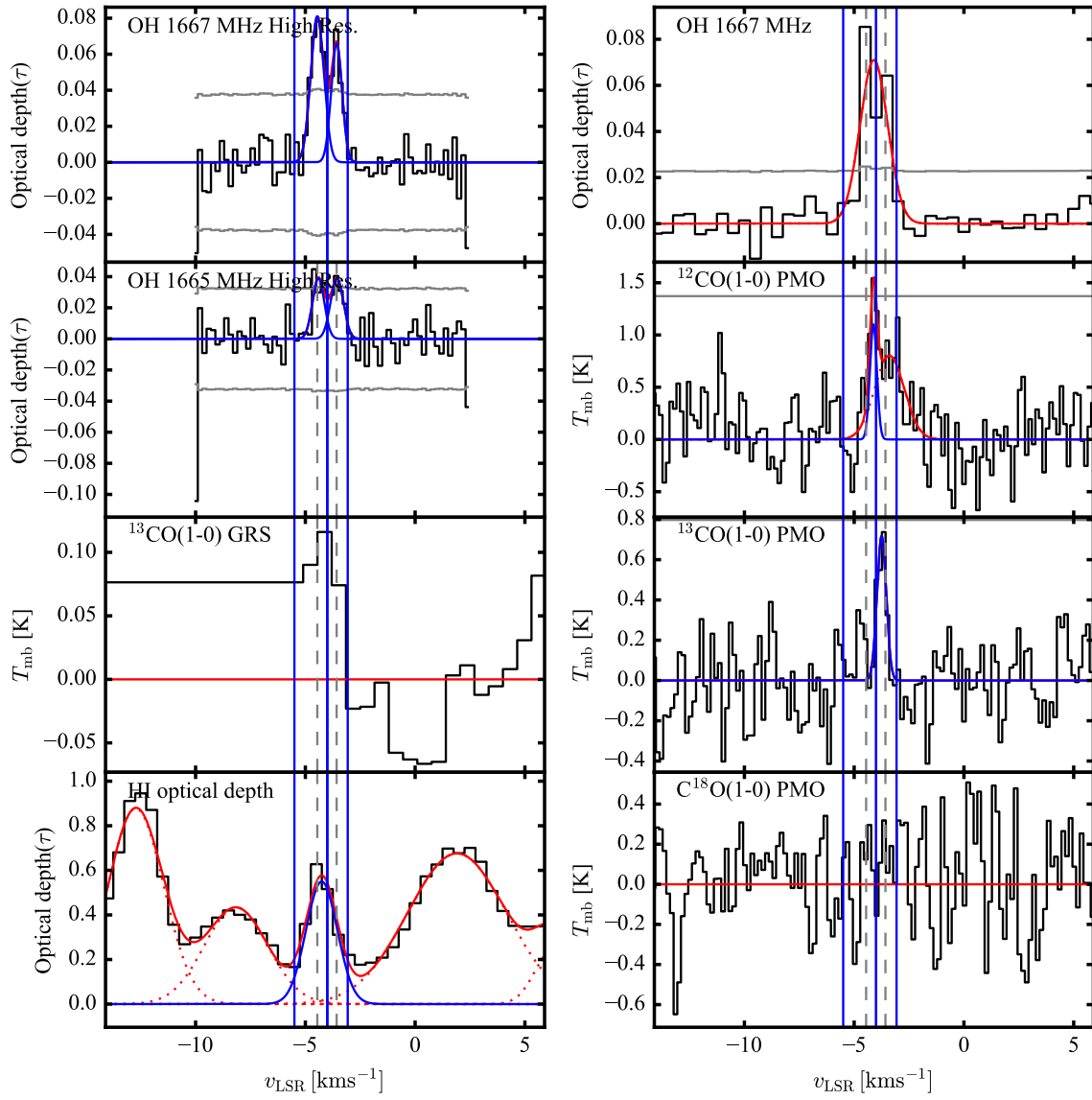


Figure C.7: Fig. 4.2, cont'd

G31 Feature 8

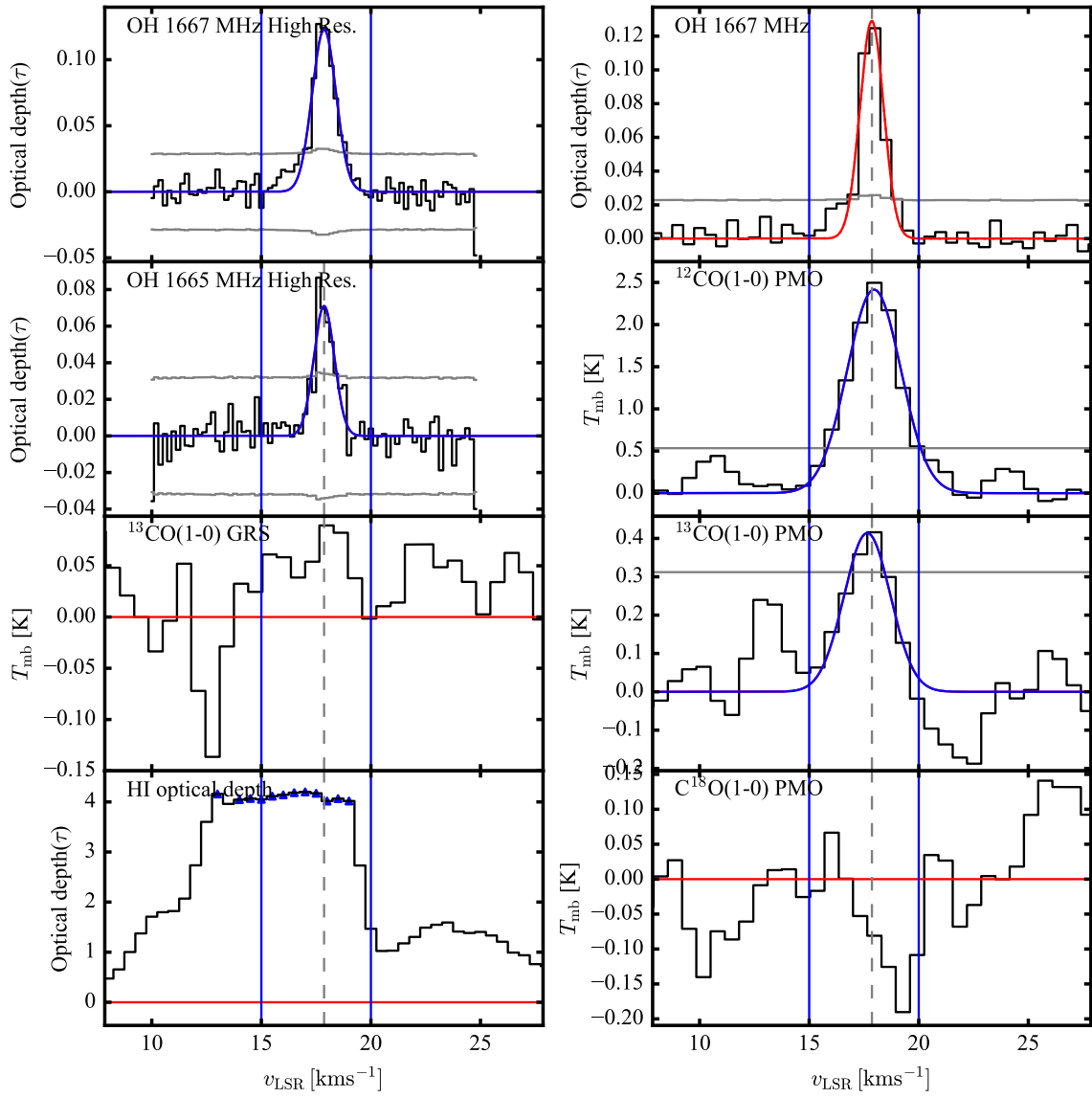


Figure C.8: Fig. 4.2, cont'd

G31 Feature 9

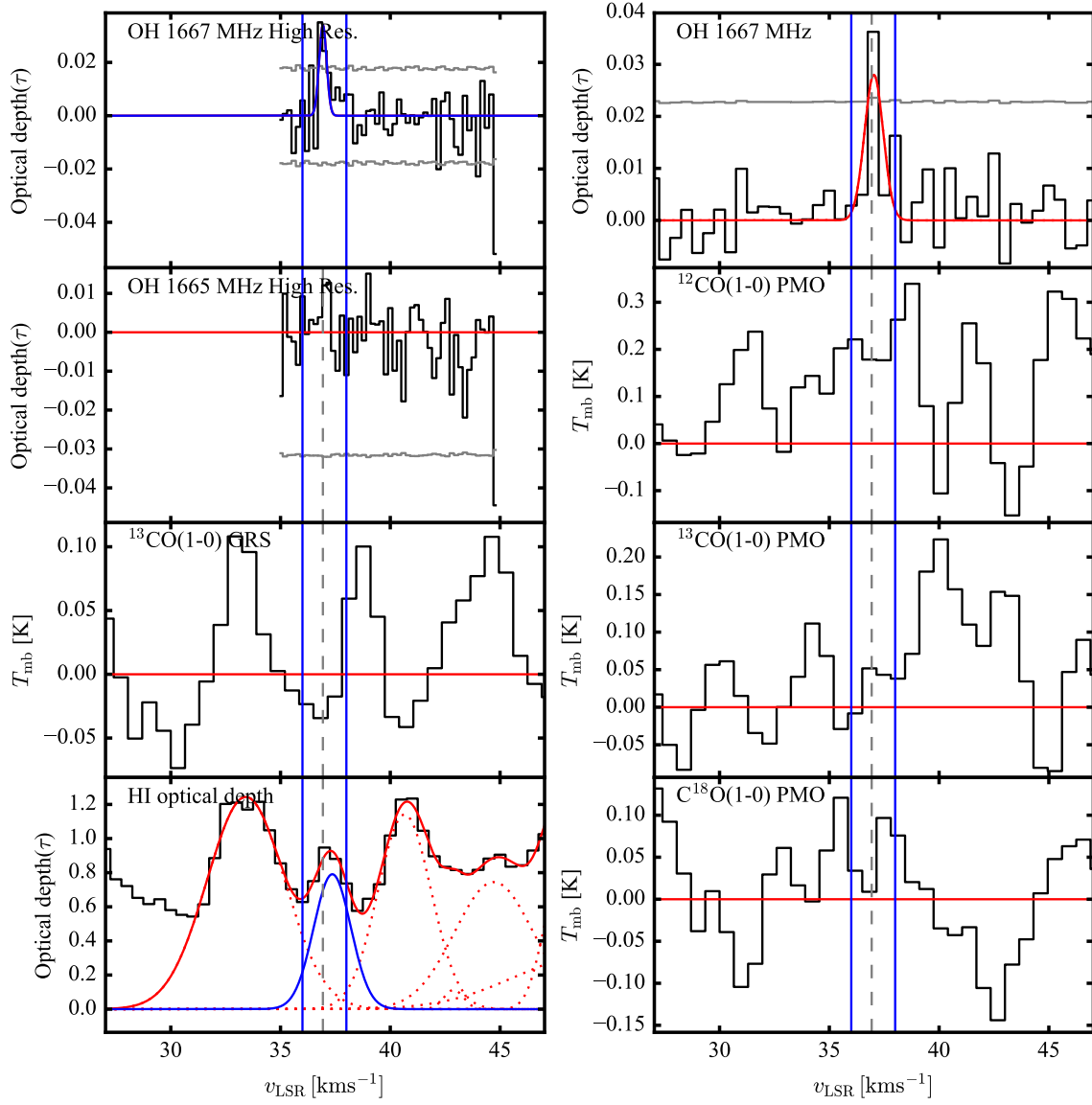


Figure C.9: Fig. 4.2, cont'd

G31 Feature 10

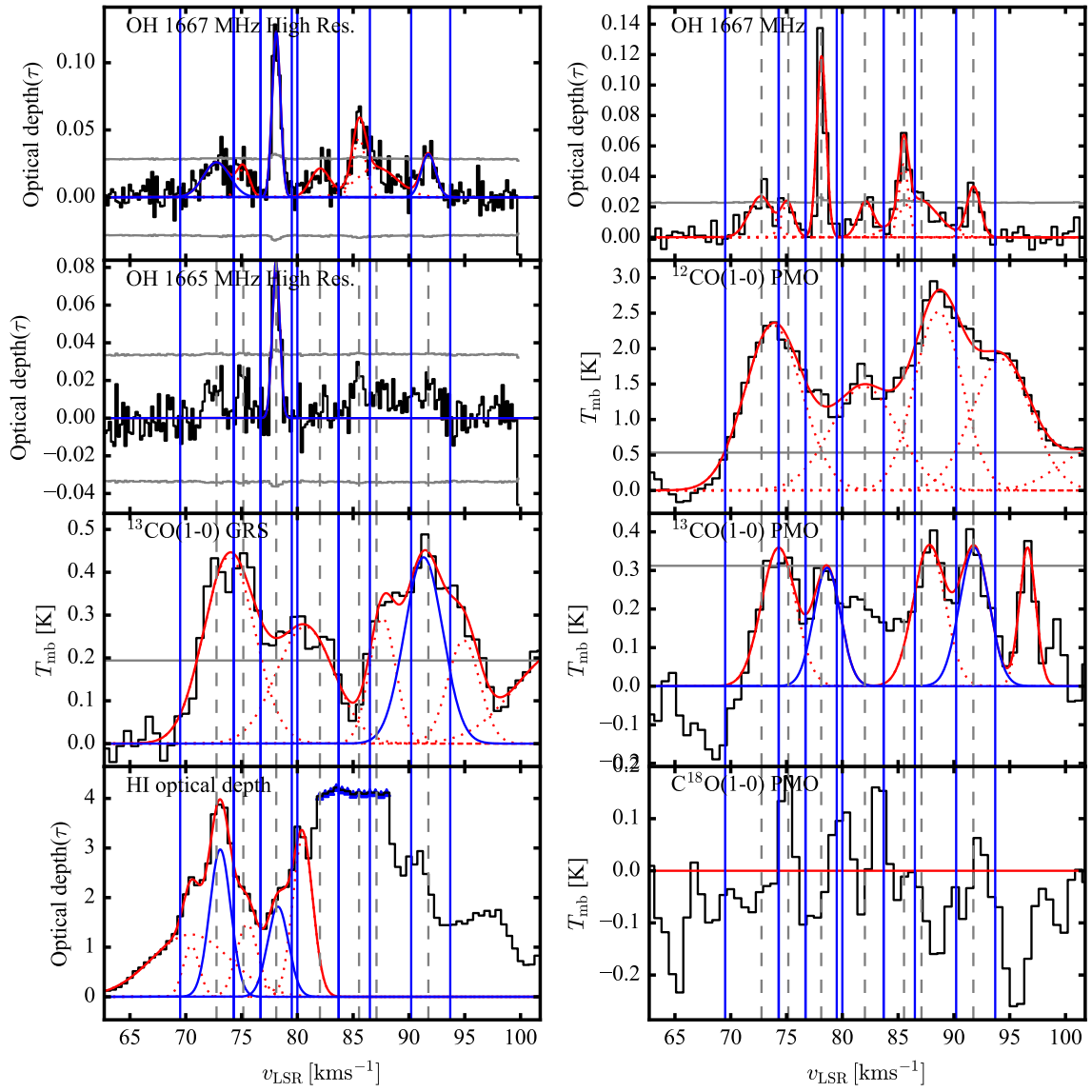


Figure C.10: Fig. 4.2, cont'd

C.3 Overview plots of each transition

C.4 Tables

We present in this Appendix a table with a detailed description of all OH and H I datasets in the VLA follow-up observations.

Appendix C Supplementary material for Chapter 4

Table C.2: Overview of data products of the VLA follow-up observations

Source	Transition	Frequency [GHz]	Δv [km s ⁻¹]	BMAJ [$''$]	BMIN [$''$]	BPA [$^\circ$]	v_{\min} [km s ⁻¹]	v_{\max} [km s ⁻¹]	F_{cont} [Jy beam ⁻¹]	$\sigma(F_{\text{cont}})$ [Jy beam ⁻¹]	$\sigma(\tau)$
G21	H _I	1.420	0.50	17.2	12.8	57.0	-100.00	+159.50	0.912	0.006	0.006
G21	OH1612	1.612	0.50	15.1	11.5	58.9	-100.00	+159.50	0.908	0.004	0.005
G21	OH1612	1.612	0.20	15.2	11.5	57.4	-7.50	+17.30	0.905	0.009	0.009
G21	OH1612	1.612	0.20	15.0	11.5	62.5	+32.50	+84.90	0.906	0.006	0.006
G21	OH1665	1.665	0.50	14.3	10.8	59.1	-100.00	+159.50	0.900	0.005	0.006
G21	OH1665	1.665	0.20	14.6	10.9	57.3	-7.50	+17.30	0.902	0.008	0.009
G21	OH1665	1.665	0.20	14.3	11.0	62.4	+32.50	+84.90	0.897	0.006	0.007
G21	OH1667	1.667	0.50	14.6	11.0	58.8	-100.00	+159.50	0.908	0.004	0.005
G21	OH1667	1.667	0.20	14.5	11.0	59.8	-7.50	+17.30	0.895	0.008	0.009
G21	OH1667	1.667	0.20	14.6	10.9	57.3	+32.50	+84.90	0.902	0.007	0.008
G21	OH1720	1.721	0.50	14.0	10.7	60.3	-100.00	+159.50	0.899	0.004	0.005
G21	OH1720	1.721	0.20	14.2	10.7	60.6	-7.50	+17.30	0.898	0.008	0.009
G21	OH1720	1.721	0.20	14.3	10.7	57.9	+32.50	+84.90	0.901	0.007	0.008
G29	H _I	1.420	0.50	16.1	13.8	52.6	-100.00	+159.50	1.029	0.007	0.007
G29	OH1612	1.612	0.50	14.0	12.3	47.1	-100.00	+159.50	1.044	0.007	0.007
G29	OH1612	1.612	0.20	14.3	12.3	52.5	-7.50	+17.30	1.044	0.010	0.009
G29	OH1612	1.612	0.20	14.2	12.3	51.5	+60.00	+79.80	1.047	0.013	0.013
G29	OH1612	1.612	0.20	14.2	12.3	50.1	+90.00	+109.80	1.039	0.007	0.007
G29	OH1665	1.665	0.50	13.5	11.9	38.9	-100.00	+159.50	1.048	0.008	0.008
G29	OH1665	1.665	0.20	13.7	11.9	50.7	-7.50	+17.30	1.043	0.011	0.010
G29	OH1665	1.665	0.20	13.6	11.9	46.3	+60.00	+79.80	1.041	0.014	0.013
G29	OH1665	1.665	0.20	13.5	11.9	43.9	+90.00	+109.80	1.047	0.012	0.011
G29	OH1667	1.667	0.50	13.7	11.9	52.1	-100.00	+159.50	1.048	0.006	0.006
G29	OH1667	1.667	0.20	13.6	11.8	50.7	-7.50	+17.30	1.038	0.010	0.010
G29	OH1667	1.667	0.20	13.7	11.9	51.1	+60.00	+79.80	1.048	0.011	0.010
G29	OH1667	1.667	0.20	13.7	11.9	51.6	+90.00	+109.80	1.046	0.007	0.006
G29	OH1720	1.721	0.50	13.3	11.4	50.3	-100.00	+159.50	1.048	0.007	0.007
G29	OH1720	1.721	0.20	13.5	11.4	54.8	-7.50	+17.30	1.051	0.009	0.009
G29	OH1720	1.721	0.20	13.4	11.4	54.0	+60.00	+79.80	1.059	0.031	0.030
G29	OH1720	1.721	0.20	13.4	11.4	53.0	+90.00	+109.80	1.054	0.010	0.009
G31	H _I	1.420	0.50	15.1	13.8	47.4	-100.00	+159.50	1.344	0.006	0.004
G31	OH1612	1.612	0.50	13.2	12.3	42.7	-100.00	+159.50	1.183	0.006	0.005
G31	OH1612	1.612	0.20	13.5	12.3	50.6	-10.00	+2.40	1.182	0.008	0.006
G31	OH1612	1.612	0.20	13.5	12.3	50.6	+10.00	+24.80	1.179	0.009	0.008
G31	OH1612	1.612	0.20	13.5	12.3	50.4	+35.00	+44.80	1.179	0.009	0.008
G31	OH1612	1.612	0.20	13.4	12.3	48.6	+60.00	+99.80	1.181	0.007	0.006
G31	OH1665	1.665	0.50	12.8	11.7	36.8	-100.00	+159.50	1.135	0.008	0.007
G31	OH1665	1.665	0.20	12.9	11.8	44.4	-10.00	+2.40	1.136	0.009	0.008
G31	OH1665	1.665	0.20	12.9	11.8	43.8	+10.00	+24.80	1.132	0.009	0.008
G31	OH1665	1.665	0.20	12.9	11.8	43.1	+35.00	+44.80	1.133	0.009	0.008
G31	OH1665	1.665	0.20	12.8	11.7	40.7	+60.00	+99.80	1.130	0.010	0.008
G31	OH1667	1.667	0.50	13.1	11.9	44.0	-100.00	+159.50	1.139	0.006	0.006
G31	OH1667	1.667	0.20	12.9	11.8	41.8	-10.00	+2.40	1.130	0.011	0.009
G31	OH1667	1.667	0.20	12.9	11.8	42.7	+10.00	+24.80	1.131	0.008	0.007
G31	OH1667	1.667	0.20	12.9	11.9	43.6	+35.00	+44.80	1.128	0.005	0.004
G31	OH1667	1.667	0.20	13.0	11.9	44.6	+60.00	+99.80	1.138	0.008	0.007
G31	OH1720	1.721	0.50	12.8	11.5	49.4	-100.00	+159.50	1.095	0.005	0.005
G31	OH1720	1.721	0.20	12.7	11.5	49.7	-10.00	+2.40	1.092	0.013	0.012
G31	OH1720	1.721	0.20	12.7	11.5	49.8	+10.00	+24.80	1.092	0.007	0.007
G31	OH1720	1.721	0.20	12.7	11.5	49.6	+35.00	+44.80	1.096	0.006	0.005
G31	OH1720	1.721	0.20	12.6	11.5	48.1	+60.00	+99.80	1.088	0.009	0.008

Notes: Columns 5–7 show major axis, minor axis and position angle of the angular resolution element. Columns 8–9 give the velocity coverage. The continuum flux in Col. 10 is extracted from the pixel at peak emission, and the noise in Cols. 11 and 12 derived from the line-free channels in the spectrum.

Appendix D

Supplementary material for Chapter 5

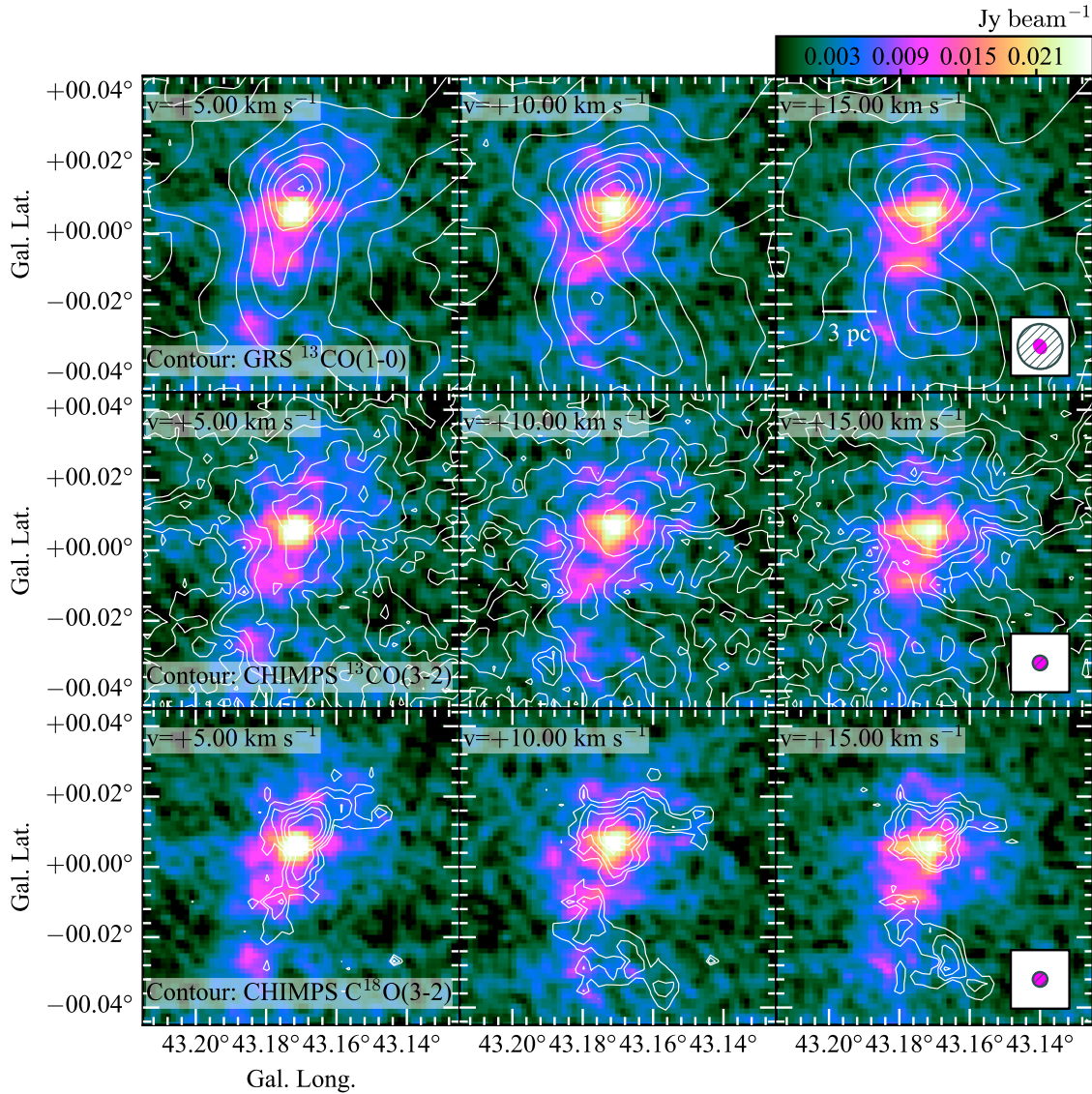


Figure D.2: RRL emission as in Fig. 5.4 for $5\text{--}15 \text{ km s}^{-1}$. Overlaid as contours are GRS $^{13}\text{CO}(1-0)$, CHIMPS $^{13}\text{CO}(3-2)$ and $\text{C}^{18}\text{O}(3-2)$. The contours are shown for the GRS $^{13}\text{CO}(1-0)$ emission at levels of 0.075, 0.125, 0.25, 0.5, 1.0, 1.5, 2.0, 2.5, 3.0, 3.5, 4.0, 4.5, 5.0 K, for the CHIMPS $^{13}\text{CO}(3-2)$ emission at levels of 0.45, 0.9, 1.79, 3.57, 7.13, 14.23 K, and for the $\text{C}^{18}\text{O}(3-2)$ emission at levels of 0.65, 1.03, 1.63, 2.59, 4.1 K. The angular resolution of the data is shown in the right column. The colored beam indicates the resolution of the RRL data ($16''8 \times 13''8$), with the beam of the CO emission overlaid in gray ($46''$ for GRS $^{13}\text{CO}(1-0)$ emission and $15''$ for CHIMPS $^{13}\text{CO}(3-2)$ and $\text{C}^{18}\text{O}(3-2)$ emission).

Bibliography of own publications used in this thesis

- *OH absorption in the first quadrant of the Milky Way as seen by THOR*, Rugel, M. R., Beuther, H., Bihr, S., et al., A&A, in press. Chapter 3 is based on this publication. This research was conducted in a large collaboration. I led part of the calibration and imaging of the data. I led the analysis, the discussion, the writing of the manuscript and the publication of the project.
- *Feedback in W49A diagnosed with Radio Recombination Lines and Models*, Rugel, M. R., Rahner, D., Beuther, H., et al., A&A, submitted. Chapter 5 is based on this publication. This research was conducted in a large collaboration. I led the calibration and part of the imaging of the data. I also led the analysis, the model application, the discussion, the writing of the manuscript and the publication of the project.

Bibliography

- Albertsson, T., Indriolo, N., Kreckel, H., et al. 2014, *ApJ*, 787, 44
- Allen, R. J., Hogg, D. E., & Engelke, P. D. 2015, *AJ*, 149, 123
- Alves, J. & Homeier, N. 2003, *ApJ*, 589, L45
- Anderson, L. D., Bania, T. M., Balsler, D. S., et al. 2014, *ApJS*, 212, 1
- Anderson, L. D., Bania, T. M., Jackson, J. M., et al. 2009, *ApJS*, 181, 255
- Argon, A. L., Reid, M. J., & Menten, K. M. 2000, *ApJS*, 129, 159
- Bally, J., Anderson, L. D., Battersby, C., et al. 2010, *A&A*, 518, L90
- Balsler, D. S., Bania, T. M., Rood, R. T., & Wilson, T. L. 1999, *ApJ*, 510, 759
- Balsler, D. S., Goss, W. M., & De Pree, C. G. 2001, *AJ*, 121, 371
- Barnard, E. E. 1910, *ApJ*, 31
- Beccari, G., Petr-Gotzens, M. G., Boffin, H. M. J., et al. 2017, *A&A*, 604, A22
- Benjamin, R. A., Churchwell, E., Babler, B. L., et al. 2003, *PASP*, 115, 953
- Beuther, H., Bihr, S., Rugel, M., et al. 2016, *A&A*, 595, A32
- Beuther, H., Schilke, P., Sridharan, T. K., et al. 2002, *A&A*, 383, 892
- Beuther, H., Tackenberg, J., Linz, H., et al. 2012, *A&A*, 538, A11
- Bialy, S., Bihr, S., Beuther, H., Henning, T., & Sternberg, A. 2017, *ApJ*, 835, 126
- Bihr, S., Beuther, H., Ott, J., et al. 2015, *A&A*, 580, A112
- Bihr, S., Johnston, K. G., Beuther, H., et al. 2016, *A&A*, 588, A97
- Blaauw, A., Gum, C. S., Pawsey, J. L., & Westerhout, G. 1960, *MNRAS*, 121, 123
- Blum, R. D., Damini, A., & Conti, P. S. 1999, *AJ*, 117, 1392
- Bohlin, R. C., Savage, B. D., & Drake, J. F. 1978, *ApJ*, 224, 132
- Bolatto, A. D., Wolfire, M., & Leroy, A. K. 2013, *ARA&A*, 51, 207
- Bosch, G., Selman, F., Melnick, J., & Terlevich, R. 2001, *A&A*, 380, 137
- Bosch, G., Terlevich, E., & Terlevich, R. 2009, *AJ*, 137, 3437
- Bourke, T. L., Myers, P. C., Robinson, G., & Hyland, A. R. 2001, *ApJ*, 554, 916
- Brandl, B., Sams, B. J., Bertoldi, F., et al. 1996, *ApJ*, 466, 254
- Brooks, K. J. & Whiteoak, J. B. 2001, *MNRAS*, 320, 465
- Carlhoff, P., Nguyen Luong, Q., Schilke, P., et al. 2013, *A&A*, 560, A24
- Cesaroni, R. & Walmsley, C. M. 1991, *A&A*, 241, 537
- Choudhury, S., Subramaniam, A., & Cole, A. A. 2016, *MNRAS*, 455, 1855
- Churchwell, E., Babler, B. L., Meade, M. R., et al. 2009, *PASP*, 121, 213
- Churchwell, E., Povich, M. S., Allen, D., et al. 2006, *ApJ*, 649, 759
- Churchwell, E., Watson, D. F., Povich, M. S., et al. 2007, *ApJ*, 670, 428
- Cignoni, M., Sabbi, E., van der Marel, R. P., et al. 2015, *ApJ*, 811, 76
- Colgan, S. W. J., Salpeter, E. E., & Terzian, Y. 1989, *ApJ*, 336, 231
- Contreras, Y., Schuller, F., Urquhart, J. S., et al. 2013, *A&A*, 549, A45
- Cornwell, T., Braun, R., & Briggs, D. S. 1999, in *Astronomical Society of the Pacific*

Appendix D Bibliography

- Conference Series, Vol. 180, Synthesis Imaging in Radio Astronomy II, ed. G. B. Taylor, C. L. Carilli, & R. A. Perley, 151
- Crowther, P. A., Caballero-Nieves, S. M., Bostroem, K. A., et al. 2016, *MNRAS*, 458, 624
- Crutcher, R. M. 1977, *ApJ*, 216, 308
- Crutcher, R. M. 1979, *ApJ*, 234, 881
- Crutcher, R. M. 2012, *ARA&A*, 50, 29
- Csengeri, T., Menten, K. M., Wyrowski, F., et al. 2012, *A&A*, 542, L8
- Dale, J. E. & Bonnell, I. 2011, *MNRAS*, 414, 321
- Dale, J. E., Haworth, T. J., & Bressert, E. 2015, *MNRAS*, 450, 1199
- Dale, J. E., Ngoumou, J., Ercolano, B., & Bonnell, I. A. 2014, *MNRAS*, 442, 694
- Dame, T. M., Hartmann, D., & Thaddeus, P. 2001, *ApJ*, 547, 792
- Dawson, J. R., Walsh, A. J., Jones, P. A., et al. 2014, *MNRAS*, 439, 1596
- De Pree, C. G., Mehringer, D. M., & Goss, W. M. 1997, *ApJ*, 482, 307
- Dempsey, J. T., Thomas, H. S., & Currie, M. J. 2013, *ApJS*, 209, 8
- Dickel, H. R. & Goss, W. M. 1990, *ApJ*, 351, 189
- Dickey, J. M., Crovisier, J., & Kazes, I. 1981, *A&A*, 98, 271
- Dickey, J. M., McClure-Griffiths, N., Gibson, S. J., et al. 2013, *PASA*, 30, 3
- Dobashi, K., Bernard, J.-P., Hughes, A., et al. 2008, *A&A*, 484, 205
- Dobbs, C. L., Krumholz, M. R., Ballesteros-Paredes, J., et al. 2014, in *Protostars and Planets VI*, ed. H. Beuther, R. S. Klessen, C. P. Dullemond, & T. Henning, 3–26
- Donate, E. & Magnani, L. 2017, *MNRAS*, 472, 3169
- Draine, B. T. & Bertoldi, F. 1996, *ApJ*, 468, 269
- Dreher, J. W., Johnston, K. J., Welch, W. J., & Walker, R. C. 1984, *ApJ*, 283, 632
- Dulieu, F., Congiu, E., Noble, J., et al. 2013, *Scientific Reports*, 3, 1338
- Ebisawa, Y., Inokuma, H., Sakai, N., et al. 2015, *ApJ*, 815, 13
- Elitzur, M. 1992, *Astrophysics and Space Science Library*, Vol. 170, *Astronomical masers* (Dordrecht: Kluwer Academic Publishers)
- Elmegreen, B. G. 1993, in *Protostars and Planets III*, ed. E. H. Levy & J. I. Lunine, 97–124
- Elmegreen, B. G. & Lada, C. J. 1977, *ApJ*, 214, 725
- Faulkner, D. J. 1967, *MNRAS*, 135, 401
- Field, G. B., Goldsmith, D. W., & Habing, H. J. 1969, *ApJ*, 155, L149
- Fomalont, E. B. & Perley, R. A. 1999, in *Astronomical Society of the Pacific Conference Series*, Vol. 180, *Synthesis Imaging in Radio Astronomy II*, ed. G. B. Taylor, C. L. Carilli, & R. A. Perley, 79
- Frayser, D. T., Seaquist, E. R., & Frail, D. A. 1998, *AJ*, 115, 559
- Frerking, M. A., Langer, W. D., & Wilson, R. W. 1982, *ApJ*, 262, 590
- Fukui, Y., Kawamura, A., Wong, T., et al. 2009, *ApJ*, 705, 144
- Galván-Madrid, R., Liu, H. B., Zhang, Z.-Y., et al. 2013, *ApJ*, 779, 121
- Ginsburg, A., Bressert, E., Bally, J., & Battersby, C. 2012, *ApJ*, 758, L29
- Glover, S. C. O. & Clark, P. C. 2012, *MNRAS*, 421, 9
- Goldsmith, P. F. & Li, D. 2005, *ApJ*, 622, 938
- Goodman, A. A., Alves, J., Beaumont, C. N., et al. 2014, *ApJ*, 797, 53
- Goss, W. M. 1968, *ApJS*, 15, 131

- Goss, W. M. & Tilanus, R. P. J. 1985, *MNRAS*, 215, 197
- Gould, R. J. & Salpeter, E. E. 1963, *ApJ*, 138, 393
- Grenier, I. A., Casandjian, J.-M., & Terrier, R. 2005, *Science*, 307, 1292
- Guelin, M. 1985, in *Molecular astrophysics: State of the art and future directions*, ed. G. H. F. Dierksen, W. F. Huebner, & P. W. Langhoff, *Proceedings of the Advanced Research Workshop, Bad Windsheim, West Germany, July 8-14, 1984 (A86-39726 18-90)* (Dordrecht: D. Reidel Publishing), 23–43
- Guibert, J., Rieu, N. Q., & Elitzur, M. 1978, *A&A*, 66, 395
- Hales, C. A., Murphy, T., Curran, J. R., et al. 2012, *MNRAS*, 425, 979
- Heiles, C., Goodman, A. A., McKee, C. F., & Zweibel, E. G. 1993, in *Protostars and Planets III*, ed. E. H. Levy & J. I. Lunine, 279–326
- Heiles, C. & Troland, T. H. 2003, *ApJS*, 145, 329
- Herschel, W. 1785, *Philosophical Transactions of the Royal Society of London Series I*, 75, 213
- Heyer, M. H., Carpenter, J. M., & Snell, R. L. 2001, *ApJ*, 551, 852
- Hjellming, R. M. & Davies, R. D. 1970, *A&A*, 5, 53
- Hoang-Binh, D. & Walmsley, C. M. 1974, *A&A*, 35, 49
- Hoare, M. G., Purcell, C. R., Churchwell, E. B., et al. 2012, *PASP*, 124, 939
- Hollenbach, D., Kaufman, M. J., Bergin, E. A., & Melnick, G. J. 2009, *ApJ*, 690, 1497
- Hollenbach, D., Kaufman, M. J., Neufeld, D., Wolfire, M., & Goicoechea, J. R. 2012, *ApJ*, 754, 105
- Hollenbach, D. J. & Tielens, A. G. G. M. 1997, *ARA&A*, 35, 179
- Homeier, N. L. & Alves, J. 2005, *A&A*, 430, 481
- Howard, C. S., Pudritz, R. E., & Harris, W. E. 2014, *MNRAS*, 438, 1305
- Howard, C. S., Pudritz, R. E., & Harris, W. E. 2016, *MNRAS*, 461, 2953
- Ibáñez-Mejía, J. C., Mac Low, M.-M., Klessen, R. S., & Baczynski, C. 2017, *ApJ*, 850, 62
- Jackson, J. M., Rathborne, J. M., Shah, R. Y., et al. 2006, *ApJS*, 163, 145
- Kawamura, J. H. & Masson, C. R. 1998, *ApJ*, 509, 270
- Kendrew, S., Beuther, H., Simpson, R., et al. 2016, *ApJ*, 825, 142
- Kendrew, S., Simpson, R., Bressert, E., et al. 2012, *ApJ*, 755, 71
- Kennicutt, Jr., R. C. 1984, *ApJ*, 287, 116
- Keto, E., Zhang, Q., & Kurtz, S. 2008, *ApJ*, 672, 423
- Keto, E. R., Welch, W. J., Reid, M. J., & Ho, P. T. P. 1995, *ApJ*, 444, 765
- Kim, W.-J., Wyrowski, F., Urquhart, J. S., Menten, K. M., & Csengeri, T. 2017, *A&A*, 602, A37
- Klessen, R. S. & Glover, S. C. O. 2016, *Saas-Fee Advanced Course, Vol. 43, Physical Processes in the Interstellar Medium*, ed. Y. Revaz, P. Jablonka, R. Teyssier, & L. Mayer (Springer Berlin Heidelberg), 85–249
- Krumholz, M. R., Bate, M. R., Arce, H. G., et al. 2014, *Protostars and Planets VI*, 243
- Krumholz, M. R. & McKee, C. F. 2005, *ApJ*, 630, 250
- Lang, C. C., Goss, W. M., & Morris, M. 2001, *AJ*, 121, 2681
- Langer, W. D. & Graedel, T. E. 1989, *ApJS*, 69, 241
- Langer, W. D., Velusamy, T., Pineda, J. L., Willacy, K., & Goldsmith, P. F. 2014, *A&A*,

- 561, A122
- Lebouteiller, V., Bernard-Salas, J., Brandl, B., et al. 2008, *ApJ*, 680, 398
- Lester, D. F., Dinerstein, H. L., Werner, M. W., et al. 1985, *ApJ*, 296, 565
- Li, D. & Goldsmith, P. F. 2003, *ApJ*, 585, 823
- Li, D., Tang, N., Nguyen, H., et al. 2018, ArXiv e-prints [arXiv:1801.04373]
- Liszt, H. & Lucas, R. 1996, *A&A*, 314, 917
- Liszt, H. & Lucas, R. 1999, in *Astronomical Society of the Pacific Conference Series*, Vol. 156, *Highly Redshifted Radio Lines*, ed. C. L. Carilli, S. J. E. Radford, K. M. Menten, & G. I. Langston, 188
- Liszt, H. & Lucas, R. 2002, *A&A*, 391, 693
- Liszt, H. S. 1995, *AJ*, 109, 1204
- Liu, B., McIntyre, T., Terzian, Y., et al. 2013, *AJ*, 146, 80
- Lopez, L. A., Krumholz, M. R., Bolatto, A. D., Prochaska, J. X., & Ramirez-Ruiz, E. 2011, *ApJ*, 731, 91
- Louvet, F., Motte, F., Gusdorf, A., et al. 2016, *A&A*, 595, A122
- Magnani, L. & Shore, S. N. 2017, *Astrophysics and Space Science Library*, Vol. 442, *A Dirty Window* (Springer-Verlag)
- Massey, P. & Hunter, D. A. 1998, *ApJ*, 493, 180
- McClure-Griffiths, N. M., Stanimirovic, S., Murray, C., et al. 2015, *Advancing Astrophysics with the Square Kilometre Array (AASKA14)*, 130
- McCray, R. & Kafatos, M. 1987, *ApJ*, 317, 190
- McKee, C. F. & Ostriker, E. C. 2007, *ARA&A*, 45, 565
- McKee, C. F. & Ostriker, J. P. 1977, *ApJ*, 218, 148
- McKellar, A. 1940, *PASP*, 52, 187
- Mezger, P. G., Schraml, J., & Terzian, Y. 1967, *ApJ*, 150, 807
- Milam, S. N., Savage, C., Brewster, M. A., Ziurys, L. M., & Wyckoff, S. 2005, *ApJ*, 634, 1126
- Miville-Deschênes, M.-A., Murray, N., & Lee, E. J. 2017, *ApJ*, 834, 57
- Miyawaki, R., Hayashi, M., & Hasegawa, T. 1986, *ApJ*, 305, 353
- Miyawaki, R., Hayashi, M., & Hasegawa, T. 2009, *PASJ*, 61, 39
- Molinari, S., Schisano, E., Elia, D., et al. 2016, *A&A*, 591, A149
- Moore, T. J. T., Urquhart, J. S., Morgan, L. K., & Thompson, M. A. 2012, *MNRAS*, 426, 701
- Motte, F., Nguyen Luong, Q., Schneider, N., et al. 2014, *A&A*, 571, A32
- Motte, F., Schilke, P., & Lis, D. C. 2003, *ApJ*, 582, 277
- Mottram, J. C. & Brunt, C. M. 2010, in *Astronomical Society of the Pacific Conference Series*, Vol. 438, *The Dynamic Interstellar Medium: A Celebration of the Canadian Galactic Plane Survey*, ed. R. Kothes, T. L. Landecker, & A. G. Willis, 98
- Mottram, J. C., Hoare, M. G., Davies, B., et al. 2011, *ApJ*, 730, L33
- Mufson, S. L. & Liszt, H. S. 1977, *ApJ*, 212, 664
- Murray, C. E., Stanimirović, S., Goss, W. M., et al. 2015, *ApJ*, 804, 89
- Murray, N. 2011, *ApJ*, 729, 133
- Murray, N., Quataert, E., & Thompson, T. A. 2010, *ApJ*, 709, 191
- Neufeld, D. A., Kaufman, M. J., Goldsmith, P. F., Hollenbach, D. J., & Plume, R. 2002,

- ApJ, 580, 278
- Neufeld, D. A., Lepp, S., & Melnick, G. J. 1995, ApJS, 100, 132
- Nguyen-Luong, Q., Anderson, L. D., Motte, F., et al. 2017, ApJ, 844, L25
- Nguyen Luong, Q., Motte, F., Carlhoff, P., et al. 2013, ApJ, 775, 88
- Nguyen Luong, Q., Motte, F., Schuller, F., et al. 2011, A&A, 529, A41
- Nishimura, A., Tokuda, K., Kimura, K., et al. 2015, ApJS, 216, 18
- Offer, A., van Hemert, M., & van Dishoeck, E. . 1994, J. Che. Phys., 100
- Palmeirim, P., Zavagno, A., Elia, D., et al. 2017, A&A, 605, A35
- Pankonin, V., Walmsley, C. M., & Harwit, M. 1979, A&A, 75, 34
- Paradis, D., Dobashi, K., Shimoikura, T., et al. 2012, A&A, 543, A103
- Pellegrini, E. W., Baldwin, J. A., Brogan, C. L., et al. 2007, ApJ, 658, 1119
- Pellegrini, E. W., Baldwin, J. A., & Ferland, G. J. 2011, ApJ, 738, 34
- Peng, T.-C., Wyrowski, F., van der Tak, F. F. S., Menten, K. M., & Walmsley, C. M. 2010, A&A, 520, A84
- Perley, R. A., Chandler, C. J., Butler, B. J., & Wrobel, J. M. 2011, ApJ, 739, L1
- Peters, T., Banerjee, R., Klessen, R. S., et al. 2010, ApJ, 711, 1017
- Phillips, T. G., Knapp, G. R., Huggins, P. J., et al. 1981, ApJ, 245, 512
- Pihlström, Y. M., Fish, V. L., Sjouwerman, L. O., et al. 2008, ApJ, 676, 371
- Pineda, J. E., Caselli, P., & Goodman, A. A. 2008, ApJ, 679, 481
- Pineda, J. L., Goldsmith, P. F., Chapman, N., et al. 2010, ApJ, 721, 686
- Pineda, J. L., Langer, W. D., Velusamy, T., & Goldsmith, P. F. 2013, A&A, 554, A103
- Planck Collaboration, Ade, P. A. R., Aghanim, N., et al. 2011, A&A, 536, A19
- Pratap, P., Megeath, S. T., & Bergin, E. A. 1999, ApJ, 517, 799
- Preibisch, T., Brown, A. G. A., Bridges, T., Guenther, E., & Zinnecker, H. 2002, AJ, 124, 404
- Preibisch, T. & Zinnecker, H. 2007, in IAU Symposium, Vol. 237, Triggered Star Formation in a Turbulent ISM, ed. B. G. Elmegreen & J. Palous, 270–277
- Quireza, C., Rood, R. T., Balsaer, D. S., & Bania, T. M. 2006a, ApJS, 165, 338
- Quireza, C., Rood, R. T., Bania, T. M., Balsaer, D. S., & Maciel, W. J. 2006b, ApJ, 653, 1226
- Ragan, S. E., Henning, T., Tackenberg, J., et al. 2014, A&A, 568, A73
- Rahner, D., Pellegrini, E. W., Glover, S. C. O., & Klessen, R. S. 2017, MNRAS, 470, 4453
- Rahner, D., Pellegrini, E. W., Glover, S. C. O., & Klessen, R. S. 2018, MNRAS, 473, L11
- Reid, M. J., Dame, T. M., Menten, K. M., & Brunthaler, A. 2016, ApJ, 823, 77
- Reid, M. J., Menten, K. M., Brunthaler, A., et al. 2014, ApJ, 783, 130
- Reifenstein, E. C., Wilson, T. L., Burke, B. F., Mezger, P. G., & Altenhoff, W. J. 1970, A&A, 4, 357
- Reissl, S., Klessen, R. S., Mac Low, M.-M., & Pellegrini, E. W. 2018, A&A, 611, A70
- Remy, Q., Grenier, I. A., Marshall, D. J., & Casandjian, J. M. 2018, A&A, 611, A51
- Rigby, A. J., Moore, T. J. T., Plume, R., et al. 2016, MNRAS, 456, 2885
- Roelfsema, P. R. & Goss, W. M. 1992, A&A Rev., 4, 161
- Rubin, R. H. 1968, ApJ, 154, 391
- Russeil, D., Pestalozzi, M., Mottram, J. C., et al. 2011, A&A, 526, A151

Appendix D Bibliography

- Sabbi, E., Lennon, D. J., Gieles, M., et al. 2012, *ApJ*, 754, L37
- Sanders, D. B., Clemens, D. P., Scoville, N. Z., & Solomon, P. M. 1986, *ApJS*, 60, 1
- Sault, R. J. & Conway, J. E. 1999, in *Astronomical Society of the Pacific Conference Series*, Vol. 180, *Synthesis Imaging in Radio Astronomy II*, ed. G. B. Taylor, C. L. Carilli, & R. A. Perley, 419
- Schöier, F. L., van der Tak, F. F. S., van Dishoeck, E. F., & Black, J. H. 2005, *A&A*, 432, 369
- Schuller, F., Menten, K. M., Contreras, Y., et al. 2009, *A&A*, 504, 415
- Seifried, D., Walch, S., Girichidis, P., et al. 2017, *MNRAS*, 472, 4797
- Selman, F., Melnick, J., Bosch, G., & Terlevich, R. 1999, *A&A*, 347, 532
- Serabyn, E., Guesten, R., & Schulz, A. 1993, *ApJ*, 413, 571
- Shaver, P. A. 1980, *A&A*, 90, 34
- Sievers, A. W., Mezger, P. G., Bordeon, M. A., et al. 1991, *A&A*, 251, 231
- Simon, R., Jackson, J. M., Clemens, D. P., Bania, T. M., & Heyer, M. H. 2001, *ApJ*, 551, 747
- Simpson, R. J., Povich, M. S., Kendrew, S., et al. 2012, *MNRAS*, 424, 2442
- Smith, L. F., Biermann, P., & Mezger, P. G. 1978, *A&A*, 66, 65
- Smith, R. J., Glover, S. C. O., Clark, P. C., Klessen, R. S., & Springel, V. 2014, *MNRAS*, 441, 1628
- Snow, T. P. & McCall, B. J. 2006, *ARA&A*, 44, 367
- Sokal, K. R., Johnson, K. E., Indebetouw, R., & Reines, A. E. 2015, *AJ*, 149, 115
- Stanimirović, S., Weisberg, J. M., Dickey, J. M., et al. 2003, *ApJ*, 592, 953
- Stecher, T. P. & Williams, D. A. 1967, *ApJ*, 149, L29
- Stil, J. M., Taylor, A. R., Dickey, J. M., et al. 2006, *AJ*, 132, 1158
- Stock, D. J., Peeters, E., Choi, W. D.-Y., & Shannon, M. J. 2014, *ApJ*, 791, 99
- Swings, P. & Rosenfeld, L. 1937, *ApJ*, 86, 483
- Szűcs, L., Glover, S. C. O., & Klessen, R. S. 2016, *MNRAS*, 460, 82
- Tang, N., Li, D., Heiles, C., et al. 2017, *ApJ*, 839, 8
- Thompson, A. R. 1999, in *Astronomical Society of the Pacific Conference Series*, Vol. 180, *Synthesis Imaging in Radio Astronomy II*, ed. G. B. Taylor, C. L. Carilli, & R. A. Perley, 11
- Thompson, M. A., Urquhart, J. S., Moore, T. J. T., & Morgan, L. K. 2012, *MNRAS*, 421, 408
- Tielens, A. G. G. M. 2010, *The Physics and Chemistry of the Interstellar Medium* (Cambridge, UK: Cambridge University Press)
- Towle, J. P., Feldman, P. A., & Watson, J. K. G. 1996, *ApJS*, 107, 747
- Townsley, L. K., Broos, P. S., Garmire, G. P., et al. 2018, *ApJS*, 235, 43
- Townsley, L. K., Broos, P. S., Garmire, G. P., et al. 2014, *ApJS*, 213, 1
- Townsley, L. K., Feigelson, E. D., Montmerle, T., et al. 2003, *ApJ*, 593, 874
- Tsujimoto, M., Hosokawa, T., Feigelson, E. D., Getman, K. V., & Broos, P. S. 2006, *ApJ*, 653, 409
- Turner, B. E. 1966, *Nature*, 212, 184
- Turner, B. E. 1973, *ApJ*, 186, 357
- Turner, B. E. 1979, *A&AS*, 37, 1

Turner, B. E. & Heiles, C. 1971, *ApJ*, 170, 453
Umamoto, T., Minamidani, T., Kuno, N., et al. 2017, *PASJ*, 69, 78
Urquhart, J. S., Csengeri, T., Wyrowski, F., et al. 2014, *A&A*, 568, A41
Urquhart, J. S., König, C., Giannetti, A., et al. 2018, *MNRAS*, 473, 1059
Urquhart, J. S., Thompson, M. A., Moore, T. J. T., et al. 2013, *MNRAS*, 435, 400
van Dishoeck, E. F. & Black, J. H. 1986, *ApJS*, 62, 109
van Dishoeck, E. F., Herbst, E., & Neufeld, D. A. 2013, *Chemical Reviews*, 113, 9043
van Gorkom, J. H., Goss, W. M., Shaver, P. A., Schwarz, U. J., & Harten, R. H. 1980, *A&A*, 89, 150
van Langevelde, H. J., van Dishoeck, E. F., Sevenster, M. N., & Israel, F. P. 1995, *ApJ*, 448, L123
Walborn, N. R. & Blades, J. C. 1997, *ApJS*, 112, 457
Walsh, A. J., Beuther, H., Bühr, S., et al. 2016, *MNRAS*, 455, 3494
Wannier, P. G., Andersson, B.-G., Federman, S. R., et al. 1993, *ApJ*, 407, 163
Weinreb, S., Barrett, A. H., Meeks, M. L., & Henry, J. C. 1963, *Nature*, 200, 829
Welch, W. J., Dreher, J. W., Jackson, J. M., Terebey, S., & Vogel, S. N. 1987, *Science*, 238, 1550
Weselak, T., Galazutdinov, G. A., Beletsky, Y., & Krełowski, J. 2010, *MNRAS*, 402, 1991
Westerhout, G. 1958, *Bull. Astron. Inst. Netherlands*, 14, 215
Whitworth, A. P., Bhattal, A. S., Chapman, S. J., Disney, M. J., & Turner, J. A. 1994a, *A&A*, 290, 421
Whitworth, A. P., Bhattal, A. S., Chapman, S. J., Disney, M. J., & Turner, J. A. 1994b, *MNRAS*, 268, 291
Wiesemeyer, H., Güsten, R., Heyminck, S., et al. 2016, *A&A*, 585, A76
Wiesemeyer, H., Güsten, R., Heyminck, S., et al. 2012, *A&A*, 542, L7
Williams, J. A., Dickel, H. R., & Auer, L. H. 2004, *ApJS*, 153, 463
Wilson, T. L. 2009, *ArXiv e-prints* [[arXiv:0903.0562](https://arxiv.org/abs/0903.0562)]
Wilson, T. L., Rohlfs, K., & Hüttemeister, S. 2009, *Tools of Radio Astronomy* (Springer-Verlag)
Wilson, T. L. & Rood, R. 1994, *ARA&A*, 32, 191
Winkel, B., Wiesemeyer, H., Menten, K. M., et al. 2017, *A&A*, 600, A2
Wolfire, M. G., Hollenbach, D., & McKee, C. F. 2010, *ApJ*, 716, 1191
Wood, D. O. S. & Churchwell, E. 1989, *ApJ*, 340, 265
Wu, S.-W., Bik, A., Bestenlehner, J. M., et al. 2016, *A&A*, 589, A16
Xu, D. & Li, D. 2016, *ApJ*, 833, 90
Xu, D., Li, D., Yue, N., & Goldsmith, P. F. 2016, *ApJ*, 819, 22
Yusef-Zadeh, F., Wardle, M., & Roberts, D. A. 2003, *ApJ*, 583, 267
Zhang, B., Moscadelli, L., Sato, M., et al. 2014, *ApJ*, 781, 89
Zhang, B., Reid, M. J., Menten, K. M., et al. 2013, *ApJ*, 775, 79

Acknowledgements

First and foremost, I would like express my gratitude to my supervisor Prof. Dr. Henrik Beuther, for being a referee of my thesis, for the positive way of guiding me in all aspects of scientific work, for always being available for questions and discussions and especially for his continuous encouragement and enthusiasm to tackle new challenges and projects, which let me grow both as a scientist, as well as personally.

I would like to thank the entire THOR group at MPIA, Dr. Yuan Wang, Dr. Juan Soler, and Dr. Simon Bihr, for all the lively discussions, the suggestions and help. I would like to extend my thanks to all members of the THOR team, for the collaboration and, in particular, the insightful and detailed comments on my manuscripts, which taught me a lot. I am very thankful for the inspiring discussions with Prof. Dr. Malcolm Walmsley at the beginning of the OH absorption project. I would like to thank Daniel Rahner and Dr. Eric Pellegrini for the intensive collaboration on the RRL study on W49A.

I am thankful for the guidance of Prof. Dr. Thomas Henning and Prof. Dr. Simon Glover as members of my thesis committee – the committee meetings always helped me to see my work from a new and wider perspective.

I would like to express my thanks to Prof. Dr. Cornelis Dullemond for the availability and time to be the second referee of my thesis, as well as Prof. Dr. Ralf Klessen and Prof. Dr. Mario Trieloff for being members on my thesis defense committee.

I would like to thank Dr. Juergen Ott and NRAO for hosting me during my stay at NRAO in Socorro, as well as him and the other staff at NRAO for the intensive discussions on how to deal with THOR and VLA data in general.

I would like to thank IMPRS and Christian Fendt for organizing the seminars and retreats of the doctoral school!

I am very grateful for all the support during the writing phase of the thesis. Especially to Prof. Dr. Henrik Beuther, Dr. Juan Soler, Dr. Yuan Wang and Dr. Joe Mottram for the interesting and very insightful discussions in the last months, for reading parts of my thesis and their suggestions and corrections. I would also like to thank Dr. Iskren Georgiev, Dr. Chiara Mazzucchelli, Daniel Rahner, Felix Bosco, Micah Klettke and Dr. Gesa Bertrang for reading parts of the thesis and the helpful comments.

Also, I would like to extend my thanks to all colleagues, officemates and friends at MPIA for their continuous support and the enjoyable working environment at MPIA.

Furthermore, I would like to thank all my friends in Heidelberg for their support and company over the past years.

Ein letzter Dankesgruß gilt meinen Eltern - vielen Dank für Eure Unterstützung!

Declaration:

I hereby declare that I have written the submitted dissertation myself and in this process have used no other sources or materials than those expressly indicated.

Heidelberg, den